UNIVERSIDAD COMPLUTENSE DE MADRID
FACULTAD DE CIENCIAS FÍSICAS

TESIS DOCTORAL

Interacción entre estrellas evolucionadas de alta masa y su medio circunestelar: una visión (SUB) milimétrica de la pérdida de masa en variables luminosas azules

Interplay between evolved massive stars and their circumstellar medium: a (SUB) millimetre view of luminous blue variable mass loss

MEMORIA PARA OPTAR AL GRADO DE DOCTOR

PRESENTADA POR

Cristóbal Bordiú Fernández

Director

José Ricardo Rizzo Caminos

Madrid

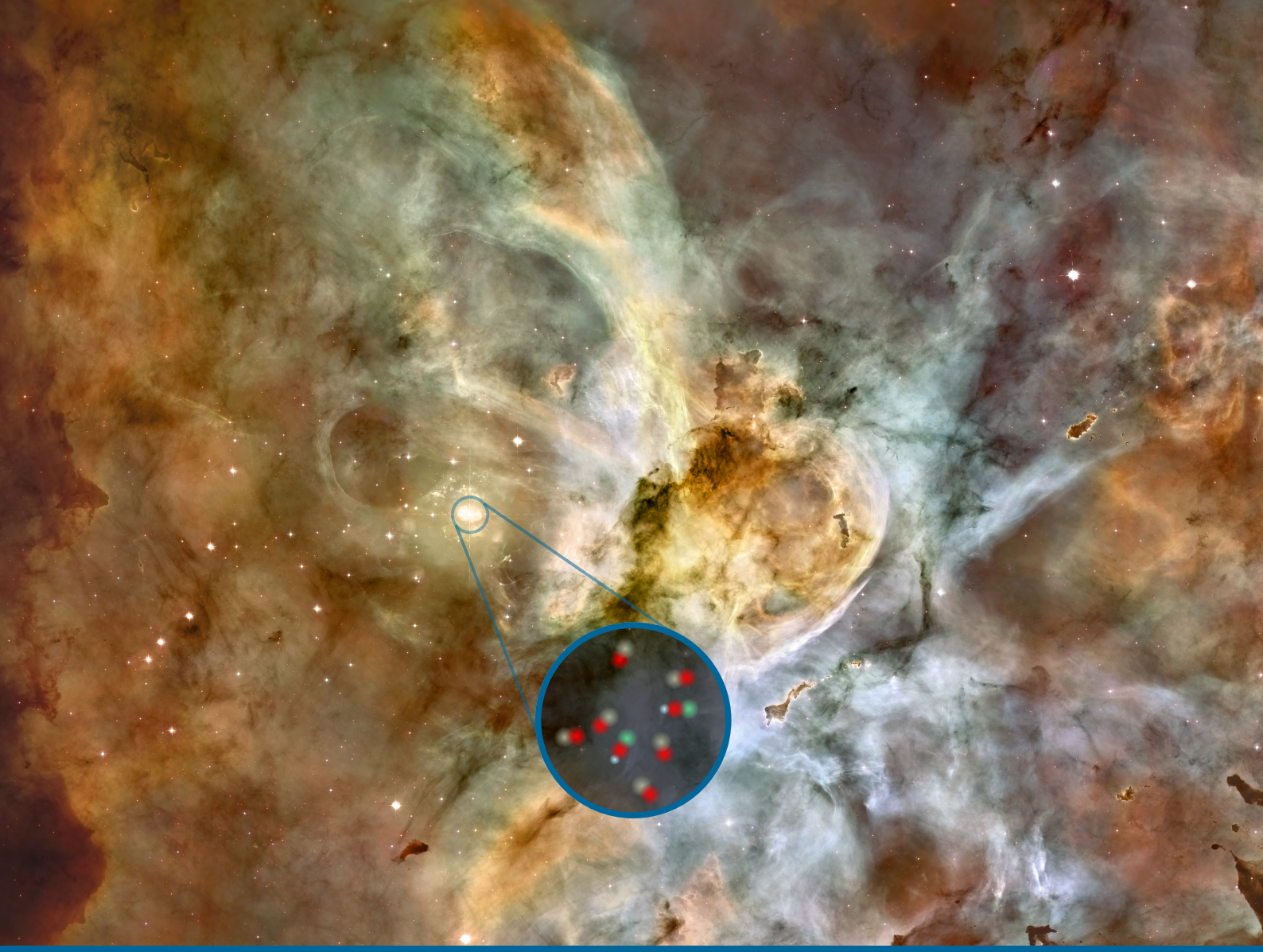

INTERPLAY BETWEEN EVOLVED MASSIVE STARS AND THEIR CIRCUMSTELLAR MEDIUM

A (SUB) MILLIMETRE VIEW OF LUMINOUS BLUE VARIABLE MASS LOSS

INTERACCIÓN ENTRE ESTRELLAS EVOLUCIONADAS DE ALTA MASA Y SU MEDIO CIRCUNESTELAR

UNA VISIÓN (SUB) MILIMÉTRICA DE LA PÉRDIDA DE MASA EN VARIABLES LUMINOSAS AZULES

Universidad Complutense de Madrid
Facultad de Ciencias Físicas

Cristóbal Bordiú Fernández

Supervisor:
Dr. José Ricardo Rizzo Caminos (CAB)

Madrid, Septiembre 2021

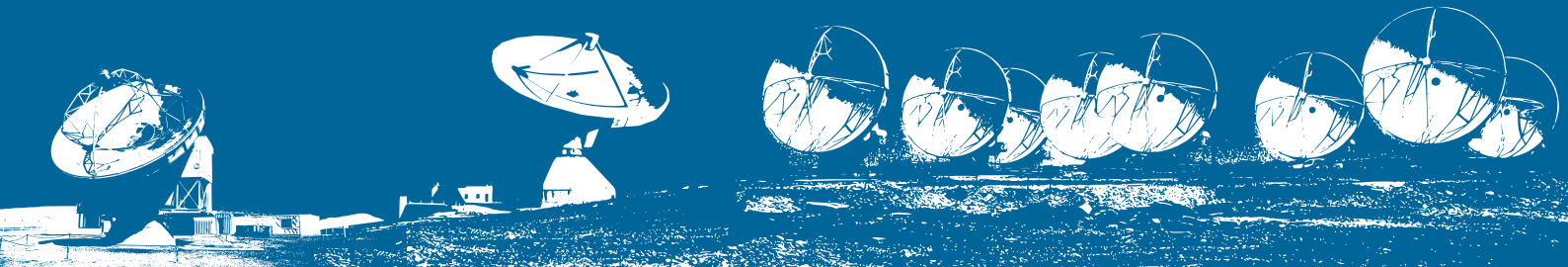

UNIVERSIDAD COMPLUTENSE DE MADRID

FACULTAD DE CIENCIAS FÍSICAS

TESIS DOCTORAL

INTERACCIÓN ENTRE ESTRELLAS EVOLUCIONADAS DE ALTA MASA Y SU MEDIO CIRCUNESTELAR: UNA VISIÓN (SUB) MILIMÉTRICA DE LA PÉRDIDA DE MASA EN VARIABLES LUMINOSAS AZULES

INTERPLAY BETWEEN EVOLVED MASSIVE STARS AND THEIR CIRCUMSTELLAR MEDIUM: A (SUB) MILLIMETRE VIEW OF LUMINOUS BLUE VARIABLE MASS LOSS

MEMORIA PARA OPTAR AL GRADO DE DOCTOR

PRESENTADA POR

Cristóbal Bordiú Fernández

DIRECTOR

Dr. José Ricardo Rizzo Caminos

Do not go gentle into that good night,
Old age should burn and rave at close of day;
Rage, rage against the dying of the light.
Though wise men at their end know dark is right,
Because their words had forked no lightning they
Do not go gentle into that good night.

Dylan Thomas

ABSTRACT

Massive stars play a significant role in the shaping and evolution of the Galaxy. Their stellar winds and strong UV fields continuously alter the structure, dynamics and chemical composition of the surrounding ISM. Still, their impact becomes even more relevant once they leave the main sequence. They turn unstable and progressively lose a significant fraction of their initial mass, evolving through a series of transitional phases toward their inevitable end as core-collapse supernovae.

Among these post-main sequence stages, the luminous blue variable (hereafter LBV) phase acquires a particular relevance. Short-lived ($\sim 10^4$ yr) and intrinsically variable, the LBV phase exhibits the highest mass-loss rates –with values up to 10^{-4} or 10^{-3} $M_\odot$ yr^{-1}–, by virtue of dense and steady winds often accompanied by violent outbursts that expel the outer stellar layers into the ISM. These processes lead to the formation of large and heterogeneous circumstellar nebulae of dust and gas, in which the mass-loss record of the central star is written. Despite having been exhaustively studied for decades at optical, infrared, and radio continuum wavelengths, the LBV phase still poses some of the most challenging questions of stellar astrophysics: which is the evolutionary role of these objects? what drives their instability? which factors determine the shaping of the nebulae?

In the last decade, a series of pioneering spectroscopic works at sub-mm and mm wavelengths opened a new window to learn about the LBV phenomenology, eventually allowing for tackling all these questions from a complementary perspective. Significant amounts of molecular gas were detected in the outskirts of η Car and G79.29+0.46, unveiling a "missing" mass component, not visible at other wavelengths, that provides new clues about LBV mass loss.

This thesis presents a comprehensive study of the LBV mass-loss processes at sub-mm and mm wavelengths. Combining molecular spectroscopy and continuum observations from state-of-the-art facilities such as the IRAM 30m, APEX and ALMA, we have portrayed an accurate picture of the circumstellar environment of the canonical LBV stars AG Car, η Car, AFGL2298, [GKF2010] MN48 and HD168607, as well as the candidates [GKF2010] MN101, [GKF2010] MN87, G79.29+0.46 and HD168625. Around AG Car and [GKF2010] MN101, we have discovered analogous ring-like structures traced by CO gas, warm (~ 50 K) and not very dense ($\sim 10^3$ cm^{-3}) on average. These rings likely arise from a mass-loss event that occurred some 10^4 years ago, as inferred from their morpho-kinematic features and chemical abundances. Likewise, on

η Car, we have found the HCN, $H^{13}CN$ and HCO^+ counterparts of a more compact, younger torus associated with the Great Eruption in the 1840s. We also reported the detection of inner structures that lie very close to the star: an expanding cloud of ejecta only seen in HCO^+ and continuum, plus hot bullets of HCN, possibly related to the lesser outburst suffered in the 1890s. These findings, which constitute the pillars of this thesis, are further supported by promising –yet not definitive– results in some of the other observed sources. We have found several molecular structures that, together with the surprisingly negative spectral indices of the central stars, shed new light on the formation and destruction of molecular gas in such hostile environments.

Taken altogether, the results of this thesis demonstrate that molecular gas is a crucial ingredient of the CSM of LBV stars. We show that it may account for more than 30% of the total mass loss budget, which has far-reaching implications in stellar evolution models, particularly sensitive to the adopted mass loss recipes. Our results also support that the surroundings of LBV stars can indeed harbour a rich molecular chemistry, despite the hot temperatures, strong UV fields and shocks. Finally, in an effort to provide a satisfactory explanation for the observed ring-like structures, we devise an evolutionary scenario in which binarity and fast rotation are the driving factors of the interaction between the stars and their circumstellar environment, eventually determining the shaping of the molecular ejecta.

This thesis will hopefully become a reference for future studies of molecular gas associated with LBV stars, and, more generally, evolved massive stars. The results of this work pave the way for follow-up observations targeting new promising sources and searching for new molecular tracers, in order to provide better answers to the long-standing questions of this elusive phase.

RESUMEN

Las estrellas masivas desempeñan un papel fundamental en la evolución de la Galaxia. Sus vientos estelares e intensos campos UV modifican continuamente la estructura, dinámica y composición química del medio interestelar. Sin embargo, su impacto se vuelve más evidente aún cuando dejan atrás la secuencia principal. En ese momento, las estrellas masivas se vuelven inestables, y pierden, progresivamente, una fracción importante de su masa inicial, evolucionando a través de una serie de etapas intermedias hacia su inevitable fin como supernovas por colapso de núcleo.

Entre estas fases posteriores a la secuencia principal, la fase de variable luminosa azul (LBV, por sus siglas en inglés) adquiere una especial relevancia. De corta duración ($\sim 10^4$ años), e intrínsecamente variable, la fase LBV exhibe las tasas de pérdida de masa más altas –hasta 10^{-4} o 10^{-3} $M_\odot$ yr^{-1}–, gracias a sus densos y constantes vientos estelares, en ocasiones acompañados por violentos estallidos que expulsan las capas más externas de la estrella al medio circundante. Estos procesos provocan la formación de enormes y heterogéneas nebulosas de gas y polvo, en las cuales está escrita la historia de pérdida de masa del objeto central. A pesar de haber sido estudiadas durante varias décadas en el óptico, infrarrojo y radio continuo, las estrellas LBV aún presentan algunas de las preguntas más desafiantes de la astrofísica estelar. ¿Cuál es el rol evolutivo de estos objetos? ¿Qué es lo que produce su inestabilidad? ¿Cuáles son los factores que determinan la forma de las nebulosas?

En la última década, una serie de trabajos pioneros de espectroscopía en longitudes de onda milimétricas y sub-milimétricas han abierto una nueva vía para estudiar la fenomenología LBV, permitiendo abordar estas preguntas desde un punto de vista complementario. La detección de cantidades sustanciales de gas molecular alrededor de η Car y G79.29+0.46 ha revelado una masa "ausente", invisible en otras longitudes de onda, que aporta nueva información sobre la pérdida de masa en estrellas LBV.

Esta tesis presenta un extenso estudio de los procesos de pérdida de masa en estrellas LBV en longitudes de onda milimétricas y submilimétricas. Combinando espectroscopía molecular y observaciones de continuo en instalaciones punteras como el telescopio de 30m de IRAM, APEX y ALMA, hemos obtenido una representación precisa del entorno circunestelar de las LBV canónicas AG Car, η Car, AFGL2298, [GKF2010] MN48 y HD168607, así como de las candidatas [GKF2010] MN101, [GKF2010] MN87, G79.29+0.46 y HD168625. En AG Car y [GKF2010] MN101, hemos descubierto

sendas estructuras en forma de anillo, formadas por gas CO, templado ($\sim$ 50 K) y no muy denso ($\sim 10^3$ cm^{-3}) en promedio. Probablemente, estos anillos trazan eventos de pérdida de masa ocurridos unas decenas de miles de años atrás, según se infiere de sus propiedades morfológicas y dinámicas, y de sus abundancias químicas. De igual manera, en η Car hemos detectado la contrapartida de HCN, H^{13}CN y HCO$^+$ de un anillo más joven y compacto relacionado con la Gran Erupción ocurrida en torno a 1840. También reportamos la detección de estructuras internas, más próximas a la estrella: una nube en expansión, visible solo en HCO$^+$ y continuo, y unos proyectiles calientes de HCN. Estas estructuras interiores están posiblemente asociadas a la erupción menor sufrida por η Car alrededor de 1890. Estos hallazgos, que constituyen los pilares de esta tesis, se complementan con otros resultados prometedores –si bien no concluyentes– en los otros objetos estudiados. Hemos encontrado varias estructuras moleculares que, junto a los índices espectrales sorprendentemente negativos de las estrellas centrales, proporcionan nuevas pistas sobre la formación y destrucción de gas molecular en entornos tan hostiles.

Vistos en conjunto, los resultados de esta tesis demuestran que el gas molecular es un ingrediente fundamental del material circunestelar de las estrellas LBV. Demostramos que puede representar más de un 30% del balance de pérdida de masa, lo cual tiene profundas consecuencias para los modelos de evolución estelar, que son especialmente sensibles a la pérdida de masa. Nuestros resultados sugieren que las proximidades de las estrellas LBV albergan una química molecular compleja, a pesar de las altas temperaturas, los intensos campos UV y los ocasionales choques. Finalmente, con el fin de proporcionar una explicación satisfactoria para la formación de las estructuras en forma de anillo, hemos propuesto un escenario en el cual binaridad y rotación rápida son los factores más relevantes de la interacción entre estas estrellas y su entorno circunestelar, determinando la estructura de la eyecta molecular.

Esta tesis servirá como referencia para estudios futuros de gas molecular asociado a estrellas LBV, y en general, estrellas de alta masa evolucionadas. Los resultados de este trabajo allanan el camino para futuras observaciones de nuevas fuentes prometedoras y nuevos trazadores moleculares, con el fin de proporcionar mejores respuestas a las preguntas que plantea esta desafiante fase evolutiva.

AGRADECIMIENTOS

Embarcarse en una tesis doctoral es un salto al vacío. Implica emprender un camino plagado de compromisos y sacrificios, sin tener muy claro a dónde te va a llevar y, en realidad, sin garantía de éxito. Por eso, ahora que llego al final, no puedo dejar de acordarme de todas aquellas personas que, especialmente en los momentos más difíciles, me brindaron su apoyo. Gracias a todos, de corazón.

En primer lugar, a mi director, Ricardo. Gracias por tu confianza, por haber apostado por mí, asumiendo la responsabilidad de guiar mis primeros pasos en el mundo de la ciencia, sin conocerme de nada y a pesar de mi situación laboral. Gracias por tu dedicación, por tantas tardes "cerrando" juntos el CAB, por esas llamadas atendidas a cualquier hora, incluso en fin de semana y vacaciones, que siempre desembocaban en larguísimas y fructíferas conversaciones. En definitiva, gracias por todo lo que me has enseñado, que va mucho más allá de lo meramente profesional. Mentor, referente y amigo.

A Miriam García, Paco Najarro, Christian Henkel, Alessia Ritacco, y a todos los demás excelentes científicos con los que he tenido la oportunidad de colaborar y aprender en estos años. Quiero asimismo agradecer a Jaime Zamorano, David Montes, Elisa de Castro, y a todo el personal de la UCM, su amabilidad y presteza a la hora de resolver mis dudas.

A mis ex-compañeros de Telefónica, Óscar, Marcos, Marina, Juanlu. A mis jefes, Dani y Pako, por vuestra comprensión y respeto, y por ponerme siempre las cosas tan fáciles. Sin vuestra ayuda, sacar adelante esta tesis habría sido mucho más difícil. Y muy especialmente, a Ioseba, Iván, Isa y Julia. Qué decir de vosotros. Gracias por vuestros ánimos, vuestro apoyo y vuestra paciencia. Echo mucho de menos esos cafés a media mañana.

No me olvido de mis italianos. A Grazia, Corrado, Carla, Paolo, Adriano, Sara, Francesco, Simone, Eva e Matteo, grazie per avermi fatto sentire a casa dal primo giorno a Catania. È veramente un piacere lavorare con voi. E particolaremente, a Milena, la mia "sorella" italiana. Hiciste que mi estancia en Catania fuese mucho mejor de lo que podía imaginar. Por tu ayuda, tu simpatía, tu sentido del humor. Por estar ahí en todo momento y por todo lo que has hecho por mí –¡y sigues haciendo!–, grazie mille. Eres muy top.

Gracias también a mis profesores del Máster de la VIU, por abrirme las puertas de un mundo nuevo. Especialmente, a Elisa Nespoli, por su inestimable ayuda y apoyo con aquel ya lejano trabajo sobre TW Hya. Y no puedo olvidarme de mi compañero

Fran. Me alegro de haber tenido la oportunidad de trabajar contigo y aprender de ti en el Máster. Gracias, también, por invitarme a aquel seminario en el CAB, y por hablarle de mí a Ricardo. Si hoy estoy aquí, es en gran medida gracias a ti.

Y, por supuesto, a mis amigos. Pablo, Marta, Juan, Diego, Andrea, Nico, Miguel, Paulina, Maldo, Rodri, Paula, Sandro, Vir, Ole, Belén, Cynthia, Ana, Juanra, Rubén, Leti, Rubén, Aitana. En Asturias, Alicante, o Madrid, más cerca o más lejos, pero siempre habéis estado ahí. Gracias por aguantarme, que no es fácil, y por sacar lo mejor de mí. Qué suerte tengo de teneros.

Por último, quiero agradecer a mi familia su cariño y apoyo. En especial, a mis padres, mi tía, y mi abuela, quienes siempre han creído en mí y han estado a mi lado en lo bueno y en lo malo. Y por supuesto, a ti, Laura. Por recorrer este camino conmigo, haciéndome sentir tu apoyo incondicional en todo momento. A tu lado todo es más fácil. Por todo el amor y el cariño que me demuestras cada día. Por saber cómo hacerme sonreír en los momentos más difíciles. Nadie sabe mejor que tú los sacrificios que conlleva pelear un doctorado mientras se trabaja. No sabes cuánto te admiro. Ahora que los dos estamos llegando a la meta, que las tardes de agobio y los fines de semana encerrados trabajando quedan atrás, es el momento de celebrar. Lo mejor está por venir.

Desde muy pequeño he sentido fascinación por el espacio. Pronto tuve claro que, de una forma u otra, quería dedicarme a estudiar el Universo. Ahora tengo la oportunidad de cumplir ese sueño. Uno nunca sabe lo que deparará el futuro, y menos en estos tiempos convulsos en los que es tan difícil hacer predicciones. Lo que sí tengo claro es que con vosotros al lado, todo será más fácil. Como dijo un hombre sabio una vez, la derrota es rendirse, el resto es camino.

CONTENTS

LIST OF FIGURES

LIST OF TABLES

LIST OF ABBREVIATIONS

ACA	Atacama Compact Array
ALMA	Atacama Large Millimetre-Submillimetre Array
APEX	Atacama Pathfinder EXperiment
ASKAP	Australian SKA Pathfinder
ATCA	Australia Telescope Compact Array
BSG	Blue SuperGiant
CASA	Common Astronomy Software Applications
CNO	Carbon, Nitrogen and Oxygen
CSE	CircumStellar Envelope
CSM	CircumStellar Medium
ESO	European Southern Observatory
EVLA	Extended Very Large Array
FIR	Far InfraRed
FOV	Field Of View
FUV	Far UltraViolet
FWHM	Full Width at Half Maximum
HPBW	Half-Power Beam Width
HR	Hertzsprung-Russell
IAU	International Astronomical Union
IRAM	Institut de Radiastronomie Millimétrique
IRDC	InfraRed Dark Cloud
ISM	InterStellar Medium
LAMDA	Leiden Atomic and Molecular DAtabase
LBV	Luminous Blue Variable
LIME	LIne Modelling Engine
LMC	Large Magellanic Cloud
LSR	Local Standard of Rest
LVG	Large Velocity Gradient
LTE	Local Thermodynamical Equilibrium
MB	Main Beam
MIPS	Multiband Imaging Photometer for Spitzer
MIPSGAL	MIPS Galactic Plane Survey
NIKA2	New IRAM Kids Array

NIR	Near InfraRed
NOEMA	NOrthern Extended Millimeter Array
OTF	On-The-Fly
PAH	Polycyclic Aromatic Hydrocarbon
PDR	Photodissociation Region
PSF	Point Spread Function
pwv	Precipitable Water Vapour
rms	Root Mean Square
RSG	Red SuperGiant
SED	Spectral Energy Distribution
SEST	Swedish ESO Submillimetre Telescope
SINFONI	Spectrograph for INtegral Field Observations in the Near Infrared
SKA	Square Kilometre Array
SN	SuperNova
SNR	SuperNova Remnant
SMA	SubMillimetre Array
SMC	Small Magellanic Cloud
SMT	SubMillimetre Telescope
TE	Thermodynamical Equilibrium
UV	UltraViolet
VLA	Very Large Array
VLT	Very Large Telescope
WISE	Wide-field Infrared Survey Explorer
WR	Wolf Rayet
YSG	Yellow SuperGiant
ZAMS	Zero Age Main Sequence
2MASS	2-micron All Sky Survey

PHYSICAL CONSTANTS AND UNITS

Speed of Light (in vacuum)	$c_0 = 2.99792458e10$ cm s^{-1}
Planck's constant	$h = 6.626070040(81) \times 10^{-27}$ erg s
Reduced Planck's constant	$\hbar = 1.054571800(13) \times 10^{-27}$ erg s
Boltzmann's constant	$k = 1.38064852(79) \times 10^{16}$ erg K^{-1}
Stefan-Boltzmann constant	$\sigma = 5.670367(13) \times 10^{5}$ erg cm^{-2} K^{-4}s^{-1}
Gravitational constant	$G = 6.67408(31) \times 10^{8}$ cm^{3} g^{-1}s^{-2}
Electron volt	$eV = 1.6021766208(98) \times 10^{-12}$ erg
Mass of electron	$m_e = 9.10938356(11) \times 10^{-28}$ g
Mass of proton	$m_p = 1.672621898(21) \times 10^{-24}$ g
Mass of neutron	$m_n = 1.674927471(21) \times 10^{-24}$ g
Mass of hydrogen	$m_H = 1.6733 \times 10^{-24}$ g
	=
Astronomical unit	au $= 1.495979 \times 10^{13}$ cm
Parsec	pc $= 3.085678 \times 10^{18}$ cm
Solar mass	$\mathrm{M}_\odot = 1.98855 \times 10^{33}$ g
Solar radius	$R_\odot = 6.95660 \times 10^{10}$ cm
Solar luminosity	$L_\odot = 3.8270 \times 10^{33}$ erg s^{1}
Jansky	Jy $= 10^{-23}$ erg cm^{-2} s^{-1} Hz^{-1}

A mi familia.

CHAPTER 1
INTRODUCTION

This thesis aims at studying the interplay between evolved high mass stars in the Luminous Blue Variable phase and the interstellar medium. Our research focuses on the mass-loss processes that trigger the formation and destruction of molecular material, giving rise to multiple circumstellar structures that allow for tracing back the history of the parent star. In this chapter, we describe the importance of massive stars in the galactic context, briefly summarising the major issues of current evolutionary models. Finally, we present the Luminous Blue Variable phase and describe its main properties.

1.1 Massive stars

1.1.1 Relevant properties

Massive stars are usually considered as those stellar objects with zero-age main-sequence masses or $M_{\rm ZAMS}$ –i.e. 'initial' masses– above 8 $M_\odot$ (e.g., Heger et al. 2003, Poelarends et al. 2008), which is the minimum mass required for a single star to explode as a supernova. Similarly, stars with masses between 2 and 8 $M_\odot$ are 'intermediate-mass' stars, and stars below 2 $M_\odot$ are 'low-mass stars'. However, beyond these theoretical thresholds, we can define massive stars strictly in terms of energetic, structural and evolutionary criteria.

Main sequence stars produce energy by fusing hydrogen into helium in their cores. Two different chain reactions may account for this process: the proton-proton chain (pp-chain, Bethe & Critchfield 1938), and the CNO cycle, in which carbon (C), nitrogen (N) and oxygen (O) act as catalysers for the nuclear reaction (von Weizsacker, 1937). These two reactions operate at different temperature regimes: the pp-chain is efficient at temperatures between 4 and 16 MK, whereas the CNO-cycle starts to become efficient only above 17 MK. Thus, the CNO cycle is the primary fusion reaction in stars with masses > 2 $M_\odot$ which have higher core temperatures, and the pp-chain dominates energy production in less-massive stars (Bethe, 1939). These differences in the energy production mechanisms translate into structural differences as well. The CNO cycle is extremely sensitive to temperature ($\propto T^{16}$) compared to the pp-chain ($\propto T^4$). Consequently, in massive stars, the energy generation zone is exceptionally

compact, and the temperature gradient so steep that energy transport occurs mainly by convection. Hence, massive stars have convective cores surrounded by radiative envelopes, while low-mass stars have radiative cores with convective envelopes.

Finally, from an evolutionary perspective, another crucial difference emerges when the stars run out of hydrogen: low-mass stars develop a degenerate helium core and undergo the so-called 'helium flash'; intermediate-mass stars, on the other hand, develop a non-degenerate core and enter a thermally stable helium-burning phase. In both cases, when helium is exhausted, the stars expel their outer layers, exposing their cores and ending their lives as white dwarfs. Contrarily, massive stars keep burning heavier elements in thermal equilibrium (carbon, oxygen, neon, silicon) until their core is entirely composed of iron. As the iron is an extremely stable element and its fusion reaction is endothermic, energy generation stops, the core shrinks and the star collapses into a violent supernova explosion (Iben, 1967).

1.1.2 The role of massive stars in the Galaxy and the Universe

Low-mass stars largely dominate the galactic stellar population. Massive stars, on the other hand, represent only a tiny fraction of this population, because of two main reasons: first, low-mass stars are more likely to form than their massive counterparts; and second, the lifetime of a star is inversely proportional to its initial mass; thus low-mass stars are much longer-lived. Therefore, at any given time, massive stars are broadly outnumbered.

Despite their relative scarcity, massive stars play a pivotal role in the galactic evolution, ever since the farthest cosmological epochs (e.g., Mac Low et al. 2005), to the point that some authors refer to them as 'cosmic engines' (Bresolin et al., 2008; Langer, 2012). From a qualitative point of view, massive stars continuously release vast amounts of ionising photons, thermal and mechanical energy through their strong UV fields and stellar winds. These winds (and occasional eruptive episodes) remove mass from the stars and contribute to the chemical enrichment of the stellar neighbourhood with substantial amounts of processed products. Therefore, massive stars have a profound impact on the structure, dynamics and composition of the interstellar medium. During their whole lifecycle, they erode their natal molecular clouds, create large wind-blown bubbles, circumstellar shells and other structures, and even trigger the formation of the next generation of stars.

Consequently, a quantitative approach to these processes is needed to understand their impact at a galactic scale, and their cosmological implications (e.g., chemical enrichment of the early Universe). In recent years, we have witnessed a notable improvement in our understanding of massive stars. Such progress has been possible thanks to the ever-increasing spectroscopic capabilities of new observing facilities, including ground-based observatories –like the Atacama Large Millimetre-Submillimetre Array (ALMA)–, and space-born telescopes –like *Herschel*–; and the development of much more sophisticated codes that allow for precise simulations of the stellar interiors, atmospheres and their radiative transfer properties. Even so, multiple questions remain still unanswered regarding the physics, structure and mass-loss properties of massive stars (Langer, 2012).

1.1.3 A look at evolutionary models

Massive stars produce strong and steady stellar winds owing to their high luminosities. These winds, driven by radiation pressure and occasionally enhanced by sporadic eruptive episodes, remove mass and angular momentum from the stars (Vink et al., 2010). This alters their rotational properties and strongly influences their evolutionary pathway (Meynet & Maeder, 2000; Brott et al., 2011). Indeed, massive stars sustain extremely high mass-loss rates for long periods, stripping their outermost layers and losing a large fraction of their initial mass (up to 50% in some extreme cases, Yusof et al. 2013; Köhler et al. 2015) during their journey from the main sequence to core-collapse supernovae. Therefore, mass loss is generally accepted as the primary driving mechanism in massive star evolution.

Mass-loss rates, however, depend strongly on the stellar wind properties (e.g., density, velocity, clumpiness), which are heavily influenced by factors such as binarity, rotation, magnetic fields and even metallicity (e.g., Vink 2011; Vink et al. 2011). Thus, mass-loss rates show substantial fluctuations across the different evolutionary stages, and empirical estimates involve significant uncertainties. For that reason, our current understanding of massive star evolution is somewhat limited, especially in the post-main sequence phases, where important discrepancies arise between theory and observations.

The standard picture of massive star evolution depicts a spectroscopic transition in which an H-burning O star evolves off the main sequence into one or more transitional stages before reaching the terminal, He-burning Wolf-Rayet phase (e.g., Maeder 1983).

The first attempts to build a common evolutionary framework for massive stars prescribed several tracks depending on the initial mass regime (e.g., Chiosi & Maeder 1986). Such tracks involved a series of transitions between intermediate red, blue and yellow supergiant (RSG, BSG and YSG) and luminous blue variable (LBV) phases. The nature and duration of these transitions, as well as the terminal pre-SN state, were exclusively determined by the properties of their radiatively-driven winds, disregarding other factors. In short, according to this model, stars with $M_{\rm ZAMS}$ below 25 $M_\odot$ followed an O→BSG→RSG→SN track, relatively insensitive to the mass-loss rate; stars with masses comprised between 25 and 60 $M_\odot$ ended their lives as WR, in case of high $\dot{M}$, or as RSG otherwise; and finally, the most massive stars, with $M_{\rm ZAMS}$ above 60 $M_\odot$, experienced a bluewards transition, such that O→BSG→LBV→WN/C/O→SN.

Although these models were valuable to clarify the relation between the different evolutionary stages, they soon proved incomplete and unable to account for many observational facts, and so they were gradually refined (e.g., Maeder & Meynet 1987). The glaring discrepancies between the models and observations were especially critical in the upper mass range, where inconsistent mass-loss rates, terminal wind velocities (Lamers & Leitherer, 1993), He-enrichments and luminosities were observed (Herrero et al., 1992). In an attempt to alleviate these disagreements, Langer et al. (1994) proposed a new evolutionary sequence, introducing a pulsationally enhanced mass-loss component during the core hydrogen-burning phase, such that O → H-rich WN → LBV → H-poor WN → H-free WN → WC → SN.

While this new scenario was able to overcome some of the issues of previous models, many inconsistencies between theory and observations persisted (Maeder, 1995). Issues concerning the predicted He- and N-excesses in OBA supergiants (Venn, 1995; Venn et al., 1996), the RSG/BSG ratio in galaxies (Langer & Maeder, 1995) and the

WN → WC transition (Langer, 1991), to name a few, highlighted the need for incorporating stellar rotation into the models. In a series of papers from 1997 to 2005, the Geneva group studied the evolutionary implications of stellar rotation and its effects on stellar structure, internal mixing, magnetism and mass-loss processes of massive stars (e.g., Meynet & Maeder 1997; Maeder 1997; Maeder & Zahn 1998 and related papers).

In parallel, notable progress in the identification of SN progenitors provided solid observational evidence that some massive stars can explode prematurely in intermediate post-main sequence phases (Smartt, 2009). In this sense, the work by Kotak & Vink (2006) and Smith (2007b) and Gal-Yam & Leonard (2009) have shown that LBV stars may be stellar endpoints and thereby direct SN progenitors. This paradigm shift has led to a further review of stellar evolution models.

The most recent Geneva models for single, rotating massive stars establish three different evolutionary paths (e.g., Maeder & Meynet 2008; Ekström et al. 2012; Georgy et al. 2012; Groh et al. 2013a, see Figure 1.1):

- Stars with initial masses in the range 10–25 $M_\odot$ expand to become RSG after core hydrogen exhaustion (e.g., Brott et al. 2011). Those with masses up to 17 $M_\odot$ are expected to end their lives at this stage, exploding as type IIP SN. Identification of SN progenitors in UV to mid-IR imagery has confirmed this track (Smartt, 2009). However, stars more massive than 17 $M_\odot$ seem to depart from this itinerary, resulting in an apparent lack of type IIP SN progenitors in the mass range 16–30 $M_\odot$. This is known as the "red supergiant problem", for which multiple tentative explanations have been proposed: distance and luminosity underestimates due to circumstellar extinction (Walmswell & Eldridge, 2012), or eventual blueward excursions toward a terminal BSG state (Meynet et al., 2013).

- Stars with initial masses in the range 25–30 $M_\odot$ experiment the so-called "blue loops": they burn a significant portion of their helium in the RSG stage, then move to the BSG stage, finish the helium burning, and go back to the RSG branch. This behaviour seems to depend strongly on internal mixing and core overshooting properties, as argued by Stothers & Chin (1991).

- Stars with $M_{\rm ZAMS}$ above 30 $M_\odot$ may evolve through various intermediate phases before becoming He-burning Wolf-Rayet stars and explode as type I supernovae. The factors determining the occurrence or not of each of these stages are unknown. Basically, stars with masses between 30–40 $M_\odot$ may evolve in a blue-red-blue fashion, such that O → BSG → RSG → WN → SNIb, possibly experimenting a short-lived LBV phase after RSG; or strictly bluewards, such that O→ BSG → LBV → WN → SNIbc. However, as noted above, the LBV phase may be the actual stellar endpoint, even for stars with $M_{\rm ZAMS}>$ 50 $M_\odot$.

Still, these tracks refer exclusively to single, isolated stars, but binarity is another fundamental aspect that must be taken into account when studying massive star evolution. Several observational campaigns have provided solid, direct evidence that a large fraction of all massive stars (possibly as high as ∼70%) are members of a binary –or higher order– system (Sana et al., 2008, 2009; Maíz Apellániz, 2010; Aldoretta et al., 2015). This condition has remarkable implications for the fate of these stars.

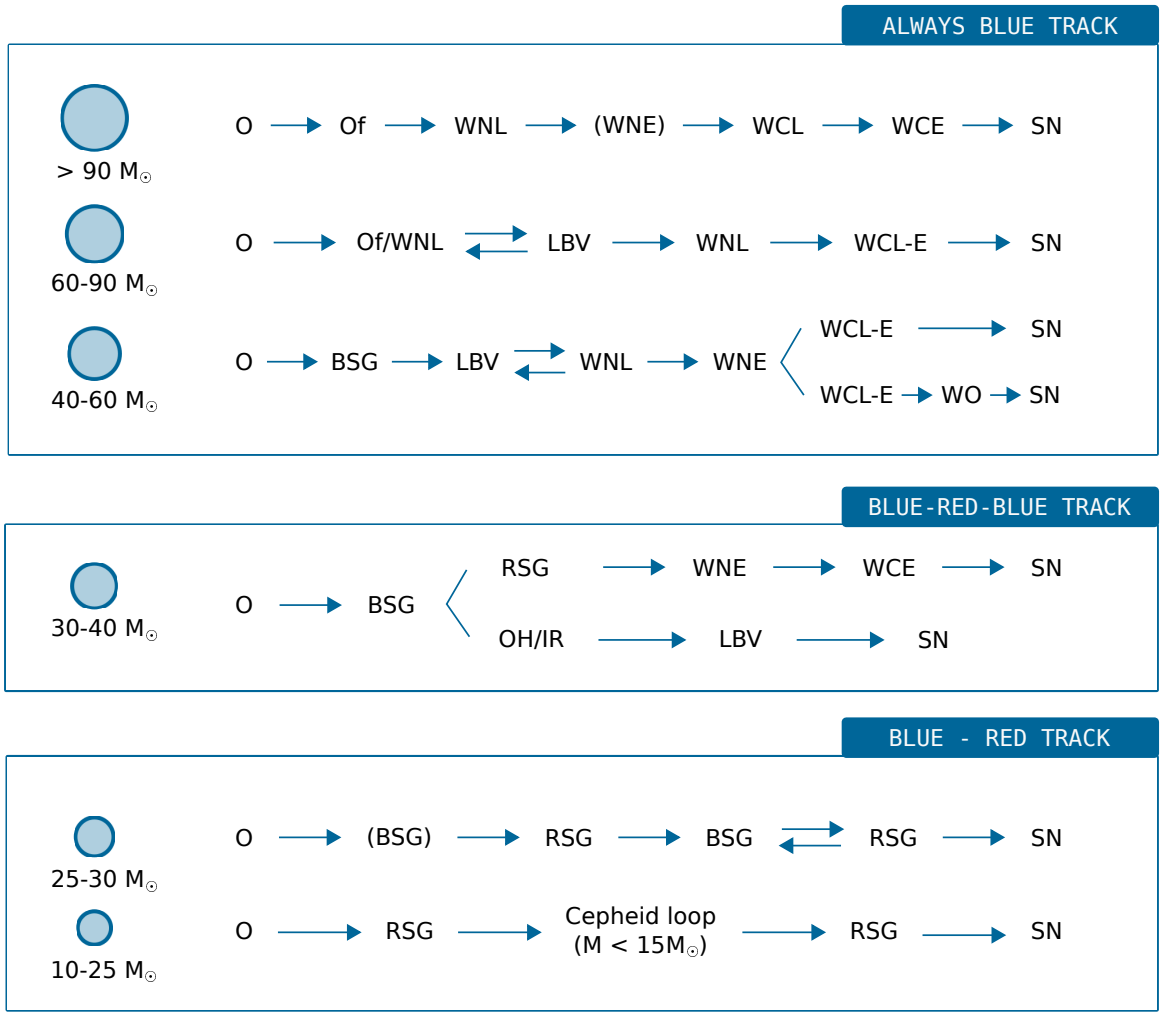

FIGURE 1.1: Massive star evolutionary paths at different mass regimes. Double arrows indicate transition loops. Adapted from Maeder & Meynet (2008).

Indeed, it is estimated that most O stars will eventually interact with a companion during their lifetime (Sana et al., 2012, 2013). Such interactions may lead to an exchange of mass and angular momentum, heavily altering the evolutionary tracks of these stars and triggering diverse phenomena, from stellar mergers to gamma ray bursts.

The post-main sequence evolution of massive stars is then driven by multiple concurrent factors, each one subject to different levels of uncertainty. A proper characterization of the post-main sequence phases is thus critical to reconcile theory and observations. In particular, constraining their mass-loss properties emerges as a necessary step, not only for fine-tuning of evolutionary models, but also for a quantitative understanding of the interplay between these objects and the ISM.

1.2 Luminous Blue Variables in a nutshell

1.2.1 Historical perspective

In the middle of the twentieth century, astronomers surveyed nearby galaxies looking for new variable stars to be used as distance calibrators. After a long monitoring campaign, Hubble & Sandage (1953) reported five new irregular variable stars in M31 and M33, namely Var 1, Var 2, Var A, Var B and Var C. These five sources shared some common properties: they had F-like spectral features, they were extremely luminous, and they had blue colour indices. They thus constituted a new variability class, being designated as "Hubble-Sandage variables".

Speculation over a possible link between Hubble-Sandage variables and other variability classes did not take long to appear. The striking similarity of their behaviour to that of S Dor in the LMC was soon pointed out by several authors (e.g., Feast et al. 1960). Years later, many other "bright irregular blue variables" were discovered in surveys of nearby spiral galaxies (e.g., Sandage & Tammann 1974). Independently, Humphreys (1975) suggested a tentative connection between the Hubble-Sandage variables, S Dor and the most luminous galactic stars, such as η Car, in view of their similar spectral properties.

The current term "Luminous Blue Variable" was coined ad hoc by Peter Conti, during a talk at the 1984 IAU Symposium (Conti, 1984), encompassing S Dor variables, Hubble Sandage variables, P Cyg and η Car-like objects under a common denomination, and thus giving birth officially to a new –and very special– class of stars.

1.2.2 Main properties

The luminous blue variable phase represents a brief transitional stage in the life of some massive stars. As discussed in the previous section, the passage through the LBV phase depends on many factors, including initial mass, mass loss, rotation and metallicity, but in principle, any star with $M_{\rm ZAMS} > 20$ M$_\odot$ can potentially experiment a LBV phase.

The characteristic duration of the LBV phase is just a few 10^4 years. Such a short timescale has a direct impact on the population of LBVs. At any given time, only a handful of massive stars are passing through the LBV phase, which makes them exceptionally scant. The most recent census of confirmed and candidate LBVs in the Local Group counts only a total of 61 members (19 confirmed) in the Milky Way, 27 (8 confirmed) in the LMC, 4 (2 confirmed) in the SMC, 16 (6 confirmed) in M31, 35 (5 confirmed) in M33 and 6 (1 confirmed) in other galaxies (Richardson & Mehner, 2018). Such a scarcity makes the study of LBVs quite challenging. Besides, distinguishing LBVs from other types of evolved massive stars is sometimes a complicated task. As their name suggests, LBVs are very luminous, very hot (blue), and variable supergiants. LBV luminosities can indeed exceed 10^6 L$_\odot$, making them some of the brightest stars known. The most luminous LBVs lie near the Eddington limit in the HR diagram, the maximum luminosity a star in hydrostatic equilibrium can reach. Regarding temperature and variability, though, the term LBVs becomes

slightly misleading: some LBVs may turn temporarily cooler and experiment long periods of quiescence. Therefore, these three characteristics fall short to properly define a stellar class.

LBV classification is, more than anything, phenomenological (Groh et al., 2013a). For an evolved star to be regarded as a *bona fide* member of the LBV class, at least one of the following conditions must be fulfilled: (1) the star must exhibit strong spectrophotometric variability in the form of S Dor cycles; or (2) the star must have suffered eruptive mass-loss events. Since the assessment of these phenomena usually requires long-term monitoring campaigns, a number of "LBV-like" supergiant stars are provisionally considered "candidate" LBVs.

Photometric and spectroscopic variability

LBV stars are intrinsically unstable, and thus present various types of variability that involve substantial changes in some stellar properties.

S Dor variability is a type of aperiodic, long-term variability, with cycles that last from years to several decades. During a S Dor cycle [1], LBVs traverse the HR diagram horizontally, at a roughly constant bolometric luminosity, moving towards lower effective temperatures (Humphreys & Davidson, 1994). In these redward excursions, the photospheric temperature typically drops from 15-30 kK to 8 kK, and consequently, the LBV spectra changes abruptly from an early type (resembling Of/WN stars, or, less often, B/Be/B[e] supergiants) to a late one (more similar to A or F supergiants). Such temperature variations shift the spectral energy peak from UV to visual wavelengths, causing brightenings of up to ∼1–2 visual magnitudes. Wolf (1989) demonstrated empirically that the decrease in effective temperature is directly proportional to the stellar luminosity. Since all LBVs show remarkably similar "cool" temperatures near their visual maxima, around 8–10 kK, this proportionality implies that their nominal hot temperatures scale with luminosity: more luminous LBVs are hotter during their visual minima. This defines the so-called "S Dor instability strip", a diagonal region in the upper part of the HR diagram where most –but not all– LBVs reside during their visual minima, as displayed in Figure 1.2.

Interestingly, an alternate explanation for the temperature drops observed during the S Dor cycle has been proposed (e.g., Lamers 1986; Davidson 1987). The spectral type changes may simply obey to the formation of an optically thick wind, hiding the actual photosphere, instead of tracing real variations of the effective temperature. In this scenario, this expanding "pseudo-photosphere" would also result in an apparent increase of the stellar radius.

van Genderen (2001) established a photometric classification of LBV stars, attending to their S Dor behaviour in the 20th century. LBVs were classified as "strongly active", with significant brightness variations of more than 0.5 mag, owing to complete S Dor cycles of short (<10 yr) or long duration (>20 yr); "weakly active", displaying less pronounced brightenings, smaller than 0.5 mag but still attributable to S Dor oscillations; and finally "dormant" or "quiescent", showing no hints of S Dor variability. However, all LBVs –even the dormant ones– may also show variability at shorter time scales, pretty much like other evolved massive stars, with microvariations of ∼

[1] Some authors in the literature refer to S Dor cycles as S Dor "eruptions" or "outbursts", that should not be confused with genuine eruptive mass-loss episodes.

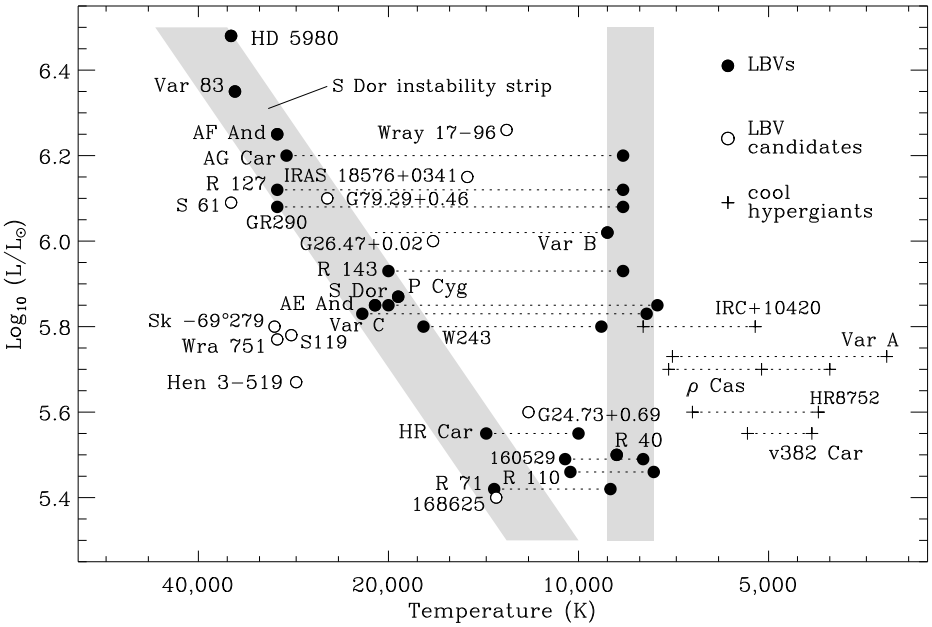

FIGURE 1.2: Hertzsprung-Russell diagram showing the location of the S Dor instability strip (diagonal band) and the visual maxima region at nearly constant temperature (vertical band). Some remarkable sources are highlighted (Credits: Smith et al. 2004).

0.1 mag or less, superimposed to the S Dor cycles (e.g., AG Car and HR Car, van Genderen et al. 1989).

Mass-loss rates

Stars in the LBV phase bear the highest mass-loss rates known among massive stars, with typical $\dot{M}$ values of 10^{-4}–10^{-5} $M_\odot$ yr^{-1}, and even reaching 10^{-3} $M_\odot$ yr^{-1} in the most extreme cases (Smith, 2014). These values are at least two orders of magnitude higher than those of average OB stars. Such a copious mass loss occurs principally through radiatively driven, slow ($\sim$100 km s^{-1}) and consequently dense stellar winds.

However, LBV mass-loss rates change notoriously across the S Dor cycle, and so do the stellar wind properties. These variations are likely associated with the bistability jump around 21 kK (Lamers et al., 1995). On the "hot" side of the jump, the wind is faster but less dense, but as the star crosses the bistability limit, the wind slows down and becomes much denser, resulting in a notable increase of the mass-loss rate, up to a factor of $\sim$5 near the visual maximum (e.g., Stahl et al. 2001).

The mechanisms behind the S Dor cycles and the extremely high mass-loss rates of LBV stars are yet to be well established from a theoretical perspective. Following Vink (2012), a number of possible causes must be considered: (1) radiation pressure-driven instabilities, due to the proximity to the Eddington limit and the possible role of stellar rotation on surpassing that limit; (2) turbulent pressure gradients, that may destabilise the outermost stellar layers –which become convective as the star approaches the Eddington limit–, leading to an effective increase of the mass-loss rate (de Jager, 1984); and (3) dynamical instabilities, such as strange sub-photospheric

vibration modes and pulsations (e.g., Guzik et al. 2005; Lovekin & Guzik 2014). Recent 3D hydrodynamic simulations also suggest that variations in the helium opacity could play a significant role in the observed phenomenology (Jiang et al., 2018).

Giant eruptions

Some LBVs occasionally exhibit another particular type of variability: the so-called giant eruptions, episodic outbursts that expel the outer stellar layers –several solar masses of processed material– into the surrounding medium. These unpredictable events are incredibly energetic, causing sudden luminosity increases of up to ∼5 mag that may last for several months. Detection of multiple giant eruptions in the last two decades outside the Milky Way evidences that some of these outbursts rival in luminosity with genuine supernovae, to the point that they are frequently denominated "supernovae impostors" –since the underlying star survives– (see, e.g., Van Dyk 2007; Kochanek et al. 2012). Besides, these eruptions further enhance mass loss, largely exceeding the rates expected for radiatively driven winds: during an outburst, LBVs can reach instantaneous $\dot{M}$ values of 10^{-1} $M_\odot$ yr^{-1} or even higher.

The prototype for these events is the eruption of η Car near 1843. In this outburst, nicknamed "the Great Eruption", η Car became the 2nd brightest star in the sky (de Vaucouleurs & Eggen, 1952), and, according to current estimates, it expelled more than 20 $M_\odot$ of gas and dust, producing the well-known Homunculus nebula (Davidson, 1989; Gomez et al., 2010).

The occurrence of giant eruptions during the LBV phase is puzzling, and their nature is far from clear: they could be explosive, shock wave-induced events; or radiatively enhanced steady winds owing to an episode of extreme luminosity (Smith, 2014). In any case, these sporadic events are crucial in determining the subsequent evolution of the star, since they contribute notoriously to the net mass-loss. Only a handful of galactic and extragalactic LBVs have *recorded* eruptions (Davidson & Humphreys, 2012; Pastorello & Fraser, 2019). Many of these events may have gone undetected, and sometimes the presence of ejected circumstellar nebulae is the only hint to trace them back. In this sense, a notable fraction of the known bona fide and candidate LBVs appear surrounded by dense, massive shells, possible vestiges of such past eruptions (Weis, 2001).

1.2.3 Circumstellar nebulae

Giant eruptions, conspicuous mass loss and interaction of different wind regimes during the S Dor cycle leave an unambiguous footprint in the stellar neighbourhood. As a consequence of these processes, many LBV stars are surrounded by dense circumstellar nebulae of dust and gas. These LBV nebulae have typical sizes ranging from 0.1 to 1 pc, with estimated masses between 0.1 to 10 $M_\odot$ (Smith & Owocki, 2006).

LBV nebulae expand rather slowly, with typical expansion velocities in the range 20–100 km s^{-1}, comparable to that of Wolf-Rayet nebulae (Weis, 2012). η Car is a notable exception to this rule, with its outer ejecta probably moving as fast as 3000 km s^{-1} (Smith et al., 2018c).

In terms of chemical composition, LBV nebulae are fundamentally made of stellar ejecta, sometimes mixed with swept-up ISM gas. Chemical abundances of the ejecta suggest the presence of ashes of the CNO cycle, that likely emerged on the stellar

surface due to rotational mixing. These CNO products typically manifest as strong emission lines of [NII] in nebular and wind spectra. Most nebulae also contain considerable amounts of dust, formed due to condensation of the expelled CNO-rich mixture (Gail et al., 2005). In fact, the detection of *dusty bubbles* at mid-infrared wavelengths constitutes one of the most prolific methods to spot new potential candidates. Using the Spitzer MIPSGAL survey, Mizuno et al. (2010) discovered more than 400 bright bubbles at 24 μm, distributed near the galactic plane. In many cases, these sources lacked optical counterparts or extended emission at other infrared wavelengths, and only a small fraction ($\sim$ 13%) presented central objects. Follow-up spectroscopy of those central objects (Wachter et al., 2010; Gvaramadze et al., 2010) revealed several of them as evolved massive stars, including new LBV candidates.

LBV nebulae display a wide variety of morphologies, and sometimes, the distribution of dust grains does not follow that of ionised and neutral gas. According to Weis (2012), 40% of LBV nebulae are roughly spherical, 10% have irregular morphologies, and 50% show a certain degree of bipolarity. The mechanisms that determine the shaping of LBV nebulae are not entirely understood. It is accepted, though, that stellar rotation, metallicity, possible binarity and interaction with pre-existing ambient material play a fundamental role, but to what extent, is still a topic of debate.

Study of LBV nebulae is crucial for our understanding of the LBV phase in particular, and massive star evolution in general. They hold the key to reconstruct the mass-loss history of their parent stars, allowing for reliable and accurate estimates of the total mass lost. Such estimates are essential for stellar evolution models in order to constrain the tracks of these sources and reproduce the transition from the main sequence to supernovae satisfactorily. Moreover, LBV nebulae contain valuable insights about the stellar chemistry. Study of the dust composition and the chemical abundances of the gas provides snapshots of the stellar interior at the moment of the ejection.

1.2.4 Evolutionary role

As said above, the LBV phase is a post-main sequence stage in the life of some massive stars, during which a substantial fraction of the total mass loss occurs. However, the exact *evolutionary role* of this phase is not entirely clear, due to the intrinsic uncertainties that affect stellar evolution models (e.g., mass loss, stellar rotation, metallicity, binarity) and the unknowns regarding the physical mechanisms that drive the LBV phenomenology.

The conventional theoretical standpoint, as described in Section 1.1.3, regards the LBV state as a mere transitional phase, always preceding a terminal, core He-burning, H-poor Wolf Rayet stage during which core-collapse occurs. However, this traditional view of LBVs as an "intermediate" evolutionary step is being challenged in the last few years. As thoroughly discussed by Smith (2017), observations of extragalactic SNe have unveiled a handful of cases with some traits strongly compatible with a LBV-like progenitor. In particular, dense pre-SN CSM inferred from the light curves, with velocity distributions similar to those observed in LBV winds and nebulae, support the hypothesis of a terminal LBV stage (e.g., SN 2005gl, Trundle et al. 2008, SN 2006gy, Smith et al. 2007b). In addition, the direct detection of a number of precursors,

some of them even displaying S Dor-like variability or eruptions, adds another piece of evidence in favour of this new scenario (e.g., SN 2006jc, Pastorello et al. 2007).

Finally, modelling work by Groh et al. (2013a) provides solid theoretical support for the pre-mortem LBV hypothesis, proposing a novel evolutionary track, in which rotating stars with initial masses comprised between 20 and 25 $M_{\odot}$, shed most of their mass in a RSG phase and then end their lives as LBVs. Despite the validity of this model is limited to the low-luminosity, low-mass LBV range, the evidence accumulated so far implies a deep paradigm shift in the general picture of massive star evolution, and stresses the need for a comprehensive characterization of pre-SN CSM.

1.3 The search for molecular gas in LBV nebulae

1.3.1 Tracing mass loss in evolved massive stars

The interplay between evolved massive stars and their surroundings is one of the most challenging topics in modern galactic astrophysics. Each evolutionary stage leaves a recognisable footprint in the ISM, in the form of cavities, bubbles, nebulae and other structures with different scales, kinematics and compositions. By reading these footprints, we can reconstruct the mass-loss records and learn about the chemical evolution of these stars. This sort of 'mass-loss archaeology' thus constitutes an excellent method to measure, quantitatively, the structural and dynamical impact of massive stars –and their feedback mechanisms– in the ISM. Moreover, obtaining accurate and reliable estimates of the mass-loss rates in each evolutionary stage is also essential for stellar evolution models, allowing to properly reproduce the transition from the main sequence to supernovae at different mass regimes.

Study of the environments of massive stars has been traditionally focused on two 'fronts': first, the observation, generally at optical wavelengths, of neutral and ionised structures, from main-sequence wind-blown bubbles and HII regions (e.g., Arnal et al. 1999) to Wolf-Rayet nebulae (e.g., Chu 1981 and related papers; Miller & Chu 1993). And second, the observations of warm dust shells around Wolf-Rayet and LBV stars, particularly bright at mid- and far-infrared wavelengths (e.g., Marston 1996), which also have proven useful to discover many new evolved sources (Mizuno et al., 2010). Furthermore, radio continuum observations exploiting the capabilities of new radio telescopes have provided complementary clues on stellar wind properties, current mass-loss rates and the predominant nebular emission mechanisms (e.g., Duncan & White 2002, 2003; Umana et al. 2005; Buemi et al. 2010; Umana et al. 2011).

On the contrary, the search for molecular structures around evolved massive stars has been somewhat overlooked. The reason for that is two-fold: the demanding technical requirements to accomplish such a search, in terms of sensitivity and resolving power; and most importantly, the common assumption that the strong UV fields of massive stars quickly destroy their parent molecular clouds. Consequently, massive stars were regarded as "sterilising sources", and their surroundings, as hostile places for the survival of noticeable amounts of molecular gas.

1.3.2 Looking for the missing gas: past and present

The search for molecular gas associated or interacting with evolved massive stars is a research field that developed slowly. The literature on the topic is indeed scarce before the late 90s. The first detection of molecular gas related to an evolved massive star was accomplished in the Wolf-Rayet nebula NGC2359, commonly known as the "Thor's helmet" nebula. Schneps et al. (1981) observed it in the light of the CO and ^{13}CO $J = 1 \rightarrow 0$ lines and reported several molecular clouds allegedly interacting with the stellar wind, as suggested by the velocity overlapping between the CO and the optical shell. Some years later, McGregor et al. (1988a) surveyed 13 early-type, high-luminosity galactic supergiants, detecting for the first time CO first-overtone emission at 2.3 μm arising from extended envelopes in six of them. In a second campaign, they surveyed 63 high-luminosity supergiants in the LMC. CO first-overtone emission was again detected in six of the sources, which were B[e] and O stars. None of the three S Dor variables included in the sample showed hints of molecular material (McGregor et al., 1988b).

These pioneering works paved the ground for further discoveries in the following decades. St-Louis et al. (1998) detected H_2 emission at 2.112 μm in NGC2359, the first direct detection of molecular hydrogen in the outskirts of an evolved massive star. Soon after, Marston et al. (1999), while studying the neutral gas around Wolf-Rayet stars, found that the ionised ring nebula around WR 16 (=HD 86161) presented a molecular counterpart. Analysis of spectra of the ionised gas revealed that the structure was rich in nitrogen, pointing to an ejection event in a prior evolutionary phase. The total mass of molecular gas was only loosely constrained to the range 5–78 $M_\odot$ due to large uncertainties regarding distance and chemical enrichment. Rizzo et al. (2001b) conducted the first thorough kinematic analysis of the molecular gas associated with NGC2359. Using the Kitt Peak 12-m radio telescope, they mapped the distribution of CO $J = 1 \rightarrow 0$ and CO $J = 2 \rightarrow 1$ and identified a component bounding the optical shell at the south and the east. This component was remarkably broader than other intervening components in the field, and also exhibited excitation conditions compatible with shocked gas. This scenario was later confirmed by the detection of warm ammonia towards this broad component (Rizzo et al., 2001a), perhaps released to gas phase from grain dust mantles due to stellar wind shocks. These results proved the existence of a mechanical interaction between the Wolf-Rayet star and the surrounding molecular gas.

At the same time, Smith & Davidson (2001) reported the detection of K-band H_2 emission arising from the poles of the Homunculus Nebula in η Car, along with strong shock-excited lines of [FeII]. This finding constituted the first detection of molecular gas associated with a LBV nebula, and provided valuable information on the density structure of the Homunculus. Similarly, Nota et al. (2002) investigated the molecular environment of the LBV star AG Car. Using the SEST telescope, they coarsely mapped the distribution of CO $J = 1 \rightarrow 0$ and CO $J = 2 \rightarrow 1$ around the optical nebula. The obtained spectra showed multiple contaminating clouds in the line of sight, but also a broad component peaking at the star's position that the authors interpreted as an expanding envelope or disk. However, the nature of this component was never confirmed with higher resolution imaging.

Following the successful detection of ammonia, Rizzo et al. mapped the southern region of NGC2359 with the IRAM-30m telescope, disentangling the kinematics of the

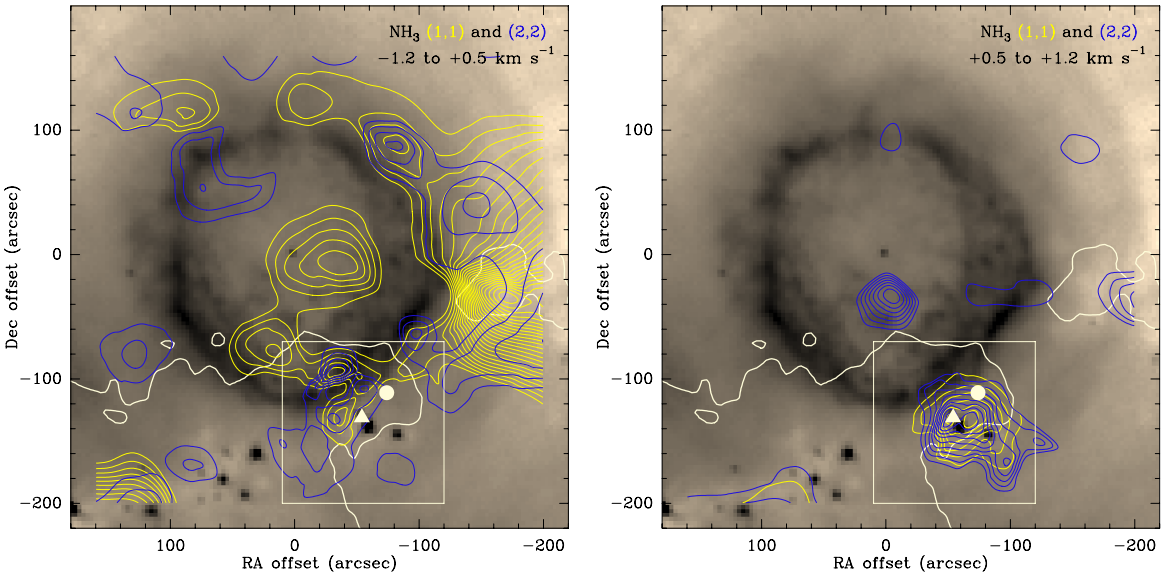

FIGURE 1.3: NH_3 integrated line emission maps towards G79.29+0.46, as contours, overlaid on a 70μm continuum image of the nebula (Herschel/PACS). The white contour traces the boundary of the IRDC, and the white box indicates the interaction region (Credits: Rizzo et al. 2014)

shocked gas (Rizzo et al., 2003a) and reporting four new molecules, namely CS, HCO^+, CN and HCN (Rizzo et al., 2003b). In η Car, further studies of its outer ejecta with the Hubble Space Telescope led to the detection of high-velocity absorption lines of CH and OH (Verner et al., 2005), and shortly after, observations with the Australia Telescope Compact Array (ATCA) yielded a tentative detection of NH_3 emission towards the Homunculus midplane (Smith et al., 2006) [2].

Rizzo et al. (2008) observed the ring LBV nebula G79.29+0.46 with the Submillimeter Telescope (SMT), detecting for the first time mid-J CO emission in this kind of environment. The detected emission traced a warm and relatively dense shell of molecular gas coincident with the infrared ring nebula, with a total mass of ~ 14 $M_\odot$. Parts of the shell with remarkably higher densities evidenced velocity broadenings consistent with a shock front. The results of this work were complemented with additional SMA and Spitzer observations, which revealed a second, previously unnoticed concentric outer shell as well as hints of photodissociation regions (PDR) –such as CO_2 ices and polycyclic aromatic hydrocarbons– (Jiménez-Esteban et al., 2010). In a subsequent campaign, Rizzo et al. (2014) found the ammonia counterpart of the CO shell, along with smaller, hot clumps toward the inner region of the nebula. The excitation conditions of the ammonia suggested a possible interaction between the nebula and a nearby infrared dark cloud (IRDC) located south of the star (see Figure 1.3). Such interaction was definitely confirmed through higher resolution Very Large Array (VLA) observations of ammonia and C_3H_2, which revealed that the effects of the LBV onto the IRDC were not only mechanical –i.e., shocks– but also radiative (Palau et al., 2014).

[2]Loinard et al. (2016) claimed that the observed emission corresponds to the H81β recombination line.

Using archival low resolution observations of ^{13}CO $J = 1 \rightarrow 0$ from the Galactic Ring Survey, Petriella et al. (2012) and Paron et al. (2012) studied the molecular environment of G24.73+0.69 and G26.47+0.02 respectively. In G24.73+0.69, a LBV star surrounded by two nested infrared shells, they found hints of interaction between the outer shell and several clumps of molecular gas, likely formed from ISM material piled up by the main-sequence wind. Similarly, they detected an incomplete and partially detached molecular shell east of the infrared nebula that surrounds G26.47+0.02, displaying spectral features that may be compatible with the turbulent motion of gas affected by the stellar wind.

In recent years, η Car has become the primary focus of attention due to its peculiar characteristics and its rich chemistry. The molecular inventory of η Car was substantially extended by Loinard et al. (2012), who surveyed the Homunculus with the Atacama Pathfinder Experiment (APEX) telescope and reported eight new species, namely CO, ^{13}CO, CN, HCO$^+$, HCN, H^{13}CN, HNC and N_2H^+. Follow up interferometric observations with ATCA at 5 arcsec resolution allowed Loinard et al. (2016) to study the morpho-kinematic features of HCN $J = 1 \rightarrow 0$ in detail. They measured a significant velocity gradient of $\sim$150 km s^{-1} and concluded that the main reservoir of molecular gas was located near the waist of Homunculus Nebula, protected from the intense UV radiation by the dusty cool ring reported by Smith et al. (2002). The relative chemical abundances in the gas indicated that both the dust and the molecules were formed out of stellar ejecta. This was later confirmed by Morris et al. (2017), who detected high-J transitions of CO towards the Homunculus and measured abundances compatible with CNO-processed material. Smith et al. (2018b) took one step further in the study of the molecular gas associated with η Car. Using ALMA, they analysed the spatial distribution of CO with an unprecedented resolution of $\sim$ 1 arcsec, unveiling a partially disrupted torus in the equatorial plane of the Homunculus. This structure, the molecular counterpart of the infrared ring, had a dynamical age of $\sim$ 170 years, compatible with the Great Eruption. This result demonstrated that molecules may arise from CNO-enriched ejecta in very short timescales.

1.3.3 Molecular gas: the last piece of the puzzle

All these results show that formation and survival of molecular gas is possible even in the outskirts of LBV stars and other evolved sources, as long as certain conditions are met. In particular, the gas must be dense enough to form molecules, and reside in regions sufficiently shielded from the intense stellar radiation fields, that otherwise would dissociate the molecules.

Reservoirs of molecular material around LBV stars may have diverse origins. Molecular gas may simply trace a relic of the parent molecular cloud where the star was born. For several Myr, the steady main sequence winds and the strong UV fields of the star would slowly erode the surrounding gas, creating a large cavity in the ISM. The cloud would end up almost entirely destroyed, but some dense clumps could survive relatively close to the star. Another possibility is that molecules arise from interstellar gas, swept-up, accumulated and compressed by the interaction of different wind regimes throughout the stellar lifecycle. Or molecules may form *in situ* out of stellar ejecta, either a stable wind that cools down and coagulates, or a past mass eruption. Generally, discriminating between these possible origins is a challenging

task, which relies on several morpho-kinematic and chemical criteria. Details on how to tackle this issue are provided in Chapter 2.

In either case, molecular gas is a powerful diagnostic tool that provides valuable complementary information about the parent star, its evolution and its relation with the surrounding medium. In particular, molecular gas:

- stores valuable kinematic information, that, regardless of its origin, allows us to estimate nebular expansion rates with precision, as well as identify dynamically affected regions such as shock fronts. With this information, one could accurately reconstruct the sequence of events that led to the formation of the observed circumstellar structures.

- traces different regions than ionised gas, and thereby allows to study the excitation conditions in these regions by independently determining densities, temperatures and opacities. This results in a more complete view of the stellar environment.

- may represent a significant contribution to the total mass of circumstellar gas. In the case of stellar ejecta, a proper characterization of the molecular component is crucial to obtain reliable and accurate mass-loss estimates. This has an evident impact on stellar evolution models, which are extremely sensitive to the mass-loss rates.

- provides complementary morphological information that, in combination with multiwavelength data of other components (dust, ionised gas), may shed light on the largely unknown mechanisms that determine the shaping of LBV nebulae.

- probes the chemistry of the parent star. If the molecular gas formed in situ, the measured abundances should reflect the chemistry of the stellar interior at the moment of the ejection. By measuring proxy ratios such as the $[^{12}CO/^{13}CO]$ ratio, we obtain valuable inputs about stellar chemistry, determining the relative abundances of CNO elements and tightly constraining the evolutionary track of the star.

- disentangles the chemical networks responsible for efficient molecular formation in the harsh surroundings of these stars, where conditions are very different from those in the ISM.

In other words, molecular spectroscopy toward LBV stars and their nebulae opens a novel window to learn about the physics and chemistry of these intriguing objects, allowing for better constraints on their mass-loss record and, therefore, providing a comprehensive picture of their evolution and their impact at a galactic scale.

1.4 Motivation and structure of this thesis

The work included in this thesis is framed in the study of the interplay between massive stars in their final stages and the interstellar medium, in terms of mass loss, energetic input and chemical enrichment. More precisely, this thesis aims at studying mass-loss phenomena in luminous blue variable stars from a molecular perspective.

As this thesis shows, molecular spectroscopy toward LBV nebulae provides invaluable morphological, kinematic and chemical information about the mass-loss processes

experimented by the parent stars throughout their lives. Furthermore, the combination of molecular data with infrared and radio continuum observations allows us to complete the mass-loss record as a whole, comparing current day mass-loss rates to those of past events. This kind of 'mass-loss archaeology' may have a significant impact on the current understanding of the LBV phase and its structural, dynamical and chemical effects on the ISM.

Objectives

The main goal of this research is to detect, characterise and analyse the molecular gas present in the outskirts of a sample of LBV stars which exhibit clear signposts of eruptive mass loss, i.e., circumstellar structures visible at optical or infrared wavelengths. The sample comprises the bona fide LBVs η Car, AG Car, [GKF2010] MN48, AFGL2298 and HD168607, and the candidates HD168625, [GKF2010] MN101 and [GKF2010] MN87. In this thesis, observations of continuum, CO, and other molecular species, acquired in state-of-the-art radio telescopes (e.g., IRAM 30m, APEX or ALMA) are combined with archival multi-wavelength imagery to accomplish the following specific objectives:

(i) Detect molecular emission arising from a sample of LBV sources with associated nebulae, analysing the morphology and kinematics of the gas and putting it in relation to already-known dust and ionised gas structures.

(ii) Estimate the physical properties of the molecular gas –density, temperature and opacity– by modelling its excitation conditions by means of radiative transfer codes.

(iii) Whenever possible, probe the chemistry of the observed structures, detecting molecules that trace different environments and physical processes, such as shocks and photo-dissociation regions.

(iv) Analyse the spatial distribution of molecular abundances and isotopic ratios in the nebulae, which trace different states in the chemical evolution of the parent stars.

(v) Study the continuum emission of the stars and their nebulae, identifying the radiation mechanisms at work –e.g., free-free emission, thermal dust and even non-thermal processes–, and quantifying their relative contribution to the global energetic balance.

(vi) Ultimately, improve the current understanding of the role that the LBV phase plays in the evolution of the most massive stars.

Structure

This thesis is mainly a compilation of peer-reviewed publications, extended with original unpublished material. It is divided in eight chapters and two appendices, written entirely in English. The general summary is also presented in Spanish. The thesis is structured as follows:

- Chapter 1 – scientific context of the thesis, an introduction of the LBV class and a brief literature review about the search for molecular gas in these sources.
- Chapter 2 – a review of the theoretical background of this work, the methods and tools used to analyse and interpret the data.
- Chapter 3 – a summary and discussion of the results obtained from IRAM 30m observations of CO and continuum toward the star [GKF2010] MN101, as detailed in Bordiu et al. (2019) and Rizzo et al. (2020) (hereafter Paper I and Paper II, respectively).
- Chapter 4 – a summary and discussion of the findings derived from the analysis of APEX and ALMA observations of the luminous blue variable AG Car, as reported in Bordiu et al. (2021) (hereafter Paper III)
- Chapter 5 – a summary and discussion of the outcomes of the analysis of archival ALMA observations η Car, published in Bordiu & Rizzo (2019) (hereafter Paper IV).
- Chapter 6 – a brief presentation and discussion of non-conclusive, unpublished findings in other promising sources, namely [GKF2010] MN48, G79.29+0.46, [GKF2010] MN87, HD168625, HD168607 and AFGL2298.
- Chapter 7 – general conclusions of this thesis, consolidating our findings into a unified global picture, that addresses the formation mechanisms and evolutionary implications of molecular structures around LBV stars.
- Chapter 8 – a brief description of our current activities and future, planned work to push this line of research forward.
- Appendix A – a preliminary reduction of near-infrared observations of [GKF2010] MN101 and a brief discussion about the rotational properties of this star.
- Appendix B – list of peer-reviewed publications and conference contributions related to this thesis.

CHAPTER 2
THEORY, METHODS AND TOOLS

This chapter introduces the theory, methods and tools that support this PhD thesis. In Section 2.1, we set the theoretical foundation of this work, following a "source to observer" approach. We describe the physics responsible for line and continuum emission at mm and sub-mm wavelengths, the propagation of the emitted electromagnetic radiation through space and its interaction with matter, and the basis and working principles of single-dish radio telescopes and interferometric arrays. In Section 2.2, we summarize the analytical methods used to extract significant physical information from the gathered line and continuum observations. In Section 2.3, we present the main pieces of software used throughout this work for analysis and modelling. Finally, in Section 2.4 we provide some remarks on the specific methodology employed in this thesis.

2.1 Theoretical framework

Radio astronomy is the science that studies the light emitted by astrophysical sources at radio wavelengths, which represents a significant portion of the electromagnetic spectrum. In this thesis, we analyse radiation in the millimetric and sub-millimetric range to study a sample of LBV stars and their associated nebular structures. This radiation manifests in the form of line emission due to changes in the rotational state of molecules, and also continuum emission from hot dust and ionized gas. It is then of paramount importance to understand 1) the physics behind these emission processes, 2) how the emitted radiation propagates through space and 3) how we can detect such radiation.

2.1.1 Line emission mechanisms

Molecular spectroscopy studies the energy changes that molecules experience as a consequence of their interaction with radiation and matter. Such interactions may alter the *electronic* configuration of the molecules, their *vibrational* state and also their *rotation*. Each one of these transitions involves energetic changes of very different orders of magnitude, manifesting across the entire electromagnetic spectrum. Broadly speaking, molecules emit radiation due to electronic transitions at UV and optical

wavelengths, due to vibrational transitions in the infrared, and due to rotational transitions at far-infrared and radio wavelengths.

Only molecules with asymmetric charge distributions present rotational transitions. These molecules are called *polar*, as they have a non-zero permanent electric dipole μ. When a polar molecule rotates at a constant velocity ω, its electric dipole moment, when projected normal to the line of sight, varies sinusoidally with a frequency equal to the rotation frequency. Therefore, a polar molecule emits radiation at its rotation frequency. This happens with all heteronuclear molecules, such as CO or NO.

Let us consider the simplest case, a diatomic rigid molecule with atomic masses m_1 and m_2 and internuclear distance $r = r_1 + r_2$, with r_i the distance from each atom to the centre of mass, as portrayed in Figure 2.1. The moment of inertia I for rotation around the centre of mass is given by:

$$I = \sum m_i r_i^2 = m_1 r_1^2 + m_2 r_2^2 \tag{2.1}$$

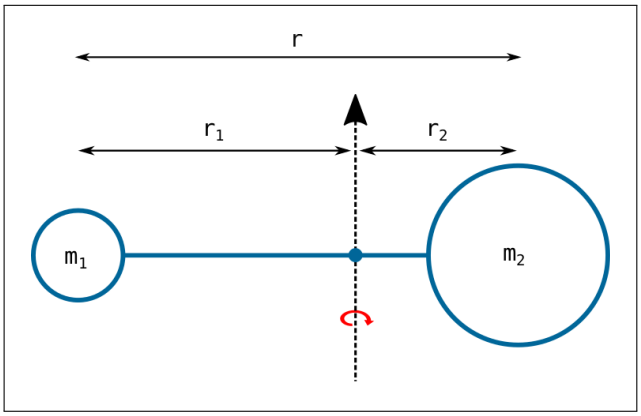

FIGURE 2.1: Schematic representation of a diatomic heteronuclear molecule rotating around its centre of mass.

Equation 2.1 can be rewritten in terms of the *reduced mass for rotation*:

$$m = \frac{m_1 m_2}{m_1 + m_2}, \tag{2.2}$$

so that

$$I = mr^2 \tag{2.3}$$

From a classical point of view, the rotational energy for a rotation velocity ω is given by:

$$E_{rot} = I\omega^2/2 \tag{2.4}$$

In an inertial reference frame, the angular momentum L of a rotating molecule is related to its moment of inertia I, so from equation 2.3, we have:

$$L = I\omega = mr^2\omega, \tag{2.5}$$

and thus the rotational energy becomes:

$$E_{rot} = \frac{L^2}{2I} \tag{2.6}$$

Quantum mechanics state that the angular momentum of a rotating molecule is quantized in discrete packets of $\hbar = \frac{h}{2\pi}$, where h denotes the Planck's constant. From Equation 2.6 it follows that the rotational energy is likewise quantized. As a consequence, the rotation velocity of a molecule is restricted to discrete values. The energy levels of a molecule behaving like a rigid rotor can be determined by solving the time-independent Schrödinger equation:

$$H\psi = -\frac{\hbar^2}{2m}\nabla^2\psi = E\psi \tag{2.7}$$

where ψ is the molecular wavefunction that describes the system, H is the hamiltonian operator and m the reduced mass of the molecule as in Equation 2.2. A detailed and rigorous treatment of this problem far exceeds the scope of this PhD thesis. We can take advantage of the Born-Oppenheimer approximation to express the total energy of the molecule as the sum of the electronic, vibrational, rotational and spin contributions, such that:

$$E_{tot} = E_{ele} + E_{vib} + E_{rot} + E_{spin} \tag{2.8}$$

with $E_{ele} \gg E_{vib} \gg E_{rot} \gg E_{spin}$. The relative magnitude of these energies is roughly $E_{ele} : E_{vib} : E_{rot} \sim 1 : 10^{-2} : 10^{-4}$ (e.g., 10 eV, 0.1 eV and 0.001 eV), and $E_{spin} \approx 0$, being sometimes neglected (Goodisman, 2012). The decomposition of the total energy in additive terms allows us to write the wavefunction as $\psi = \psi_{ele}\psi_{vib}\psi_{rot}$ and solve for each term independently. The eigenvalues of the rotational term are thus:

$$E_J = \frac{\hbar^2}{2I}J(J+1), \tag{2.9}$$

where E_J denotes the permitted energy levels of the molecule, and J is the rotational angular momentum quantum number. But the quantization of the energy levels inherently implies that the energy changes, i.e. the transitions between rotational energy levels, are also quantized, according to the quantum selection rule $\Delta J = \pm 1$ with $J = 0, 1...$

When a given molecule decays from level J to level $J-1$, the net loss in rotational energy results in the emission of a photon, whose energy is equal to:

$$\Delta E_{rot} = \frac{\hbar^2 J}{I}, \tag{2.10}$$

From Equation 2.10, we can determine the frequency of the photon by simply following Planck's energy-frequency relation:

$$\nu = \frac{\Delta E_{rot}}{h} = \frac{\hbar J}{2\pi I} \tag{2.11}$$

In other words, the emission frequency of a rotating molecule decaying from an excited state J is the $J-$th harmonic of a fundamental frequency, which depends only on the molecular moment of inertia.

Excitation mechanisms of rotational levels

Rotational transitions may be induced by radiative pumping, absorbing photons of energies determined by Equation 2.11; or by collisions with other molecules within a gas. We thereby speak of *radiative* excitation and *collisional* excitation.

The quantum processes involved in the radiative excitation of a molecule can be statistically described by the Einstein's coefficients (Einstein, 1917). Let us consider the simplest case, a molecule with two energy levels (a "two-level" system), as sketched in Figure 2.2, with energies E_2 and E_1, so that $E_2 > E_1$ and $\Delta E = E_2 - E_1 = h\nu$. The transition probabilities owing to radiative processes are described by:

- Spontaneous emission coefficient, A_{UL}, which represents the probability of a molecule emitting spontaneously a photon when decaying from the upper to the lower state.
- Absorption coefficient, B_{LU}, which represents the probability of a molecule absorbing a photon and transitioning from the lower to the upper state.
- Stimulated emission coefficient, B_{UL}, the probability of a molecule emitting a photon and decaying in a non-spontaneous (stimulated) way.

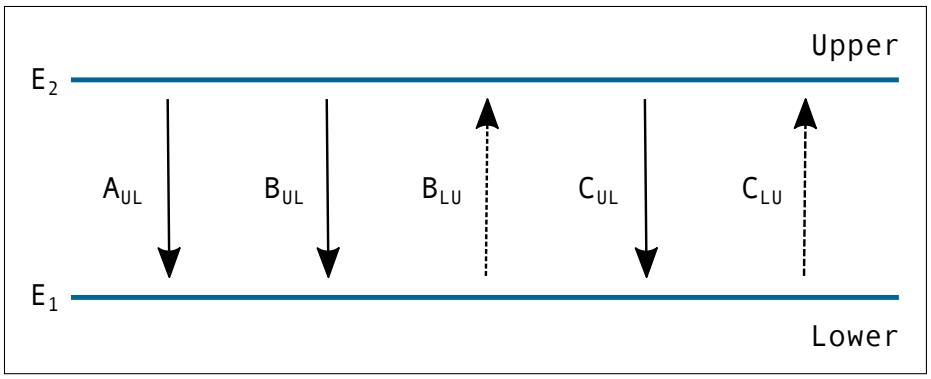

FIGURE 2.2: Diagram of the possible transitions in a two-level system, with their associated coefficients. Excitation processes are represented by dashed arrows.

Besides, collisional processes are accounted for by the collisional excitation (C_{LU}) and de-excitation (C_{UL}) coefficients, which relate to the transition probabilities through the number densities of the collision partners. The relation between the radiative and collisional coefficients constitute a fundamental piece of the radiative transfer problem, and will be derived in Section 2.2.

The minimum *excitation temperature* required for a molecule to undergo rotational transitions is:

$$T_{min} \sim \frac{E_{rot}}{k} \tag{2.12}$$

where k is the Boltzmann's constant. From this relation, in combination with equation 2.9, we can estimate the minimal kinetic temperature required in a parcel of gas to excite a certain $J \rightarrow J-1$ transition, which is:

$$T_{min} \sim \frac{\nu h(J+1)}{2k} \tag{2.13}$$

In many astrophysical environments, collisional excitation dominates over radiative excitation, as typically the kinetic temperature of the gas is significantly higher than the temperature of the cosmic microwave background. However, in low-density environments or near strong continuum sources, where large amounts of energetic photons are available, radiative excitation represents a significant contribution.

2.1.2 Continuum emission mechanisms

Unlike molecular line emission, which appears at very specific frequencies as a result of the quantized energy levels of the involved species, continuum emission is a broadband radiation spread over a wide range of frequencies, i.e. having a continuous energy distribution. When speaking of radio continuum emission, we distinguish between *thermal* and *non-thermal* processes.

Thermal emission

Thermal emission is the radiation emitted by a source (e.g., a parcel of gas) for the mere fact of having a temperature $T > 0$ K, due to the internal motions and collisions of its constituent particles (accelerating charged particles emit photons). Such particles follow a Maxwellian velocity distribution that depends on T, so that the higher the temperature, the faster the motions. Therefore, the emission spectrum of a thermal source is solely determined by its physical temperature (Condon & Ransom, 2016).

Blackbody emission is the simplest form of thermal radiation. Let us consider an ideal blackbody, i.e. a perfect absorber, a body that absorbs all incident radiation and reflects none. After reaching an arbitrary equilibrium temperature $T > 0$ K, the blackbody emits radiation with a spectrum that depends exclusively on its temperature T. Such blackbody spectrum is described by Planck's law:

$$B_\nu(T) = \frac{2h\nu^3}{c^2} \frac{1}{\exp\left(\frac{h\nu}{kT}\right) - 1} \tag{2.14}$$

with ν the frequency, c the speed of light and h the Planck's constant. This expression is general and valid for any ν. However, at low frequencies (i.e. radio wavelengths), $h\nu \ll kT$ and thus $\exp\left(\frac{h\nu}{kT}\right) \approx 1 + \frac{h\nu}{kT}$. This regime is known as the Rayleigh-Jeans limit, which allows us to simplify Planck's law:

$$B_\nu(T) = \frac{2kT\nu^2}{c^2} \tag{2.15}$$

Figure 2.3 compares the Planck's spectrum for several temperatures with the Rayleigh-Jeans approximation.

For a blackbody spectrum, the peak wavelength is inversely proportional to the temperature, meaning that hotter bodies radiate at shorter wavelengths and vice-versa. This relation is known as the Wien's displacement law, in which the peak wavelength λ_{peak} in units of m is given by:

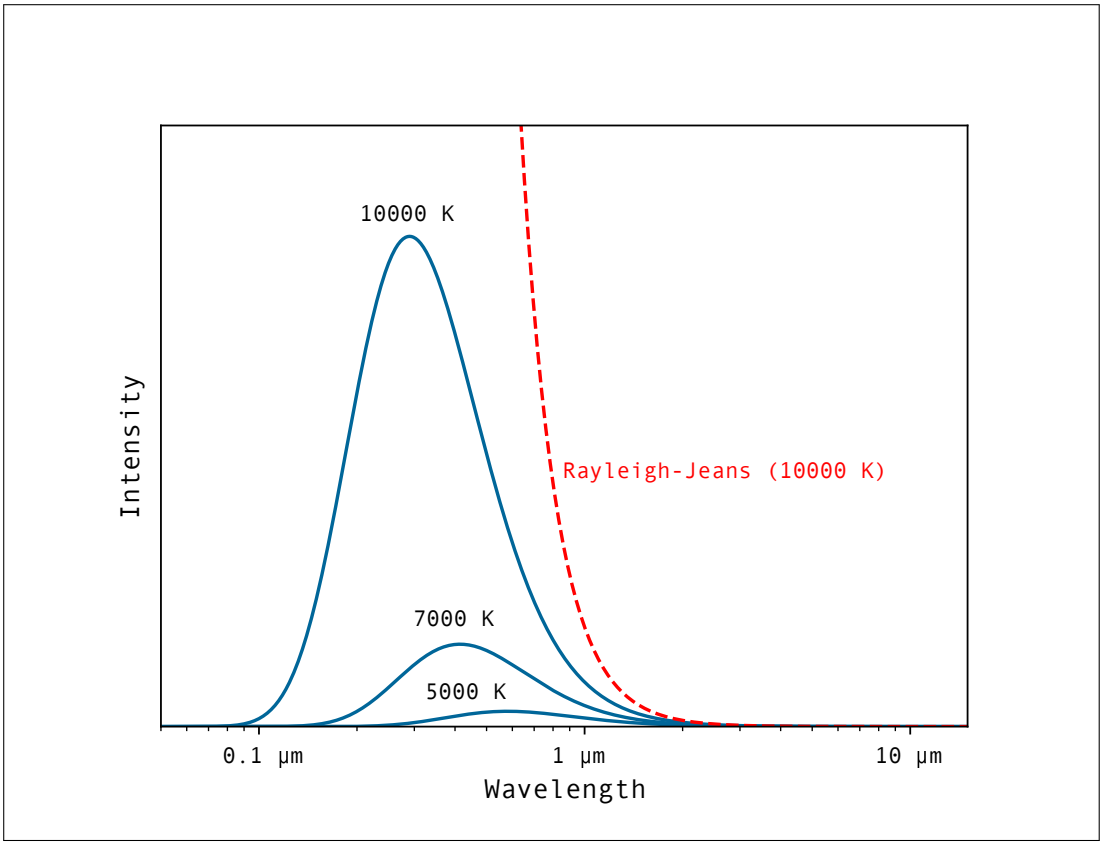

FIGURE 2.3: Intensity vs wavelength plot of Planck's spectra computed for 5000, 7000 and 10000 K (in blue) compared to the Rayleigh-Jeans approximation for 10000 K (in dashed-red). Note how the two 10000 K curves converge in the long-wavelength regime.

$$\lambda_{\text{peak}} = \frac{0.0028976}{T} \tag{2.16}$$

where the numerator is the Wien's displacement constant, in units of m×K, and T is the temperature in K. Many astrophysical sources behave *approximately* as blackbodies, e.g., the stars.

In the millimetre and submillimetre regime, thermal dust radiation is produced when small grains of silicates or graphites are heated, either by the interstellar radiation field or by energetic UV photons from nearby stars. However, dust grains are inefficient radiators in the radio band. In fact, their equilibrium temperature is hotter than it should be for a perfect blackbody in the same radiation field. We therefore speak of a *modified* blackbody spectrum (sometimes called *greybody*), whose general form, assuming a power-law behaviour for the optical depth of dust grains (Hildebrand, 1983), is given by:

$$B_{\nu,\text{dust}}(T) = \nu^{\beta} B_{\nu}(T) = \frac{2h\nu^{3+\beta}}{c^2} \frac{1}{\exp\left(\frac{h\nu}{kT}\right) - 1} \tag{2.17}$$

with β the dust emissivity index, which depends on physical properties of the dust grains, such as composition and size distribution.

Another essential type of thermal radiation in the radio band is the so-called free-free or *Bremsstrahlung* ("braking") radiation, which is caused by the interaction between free electrons and ions within a hot plasma. The name free-free comes from the fact that the electrons remain free after the interaction, i.e. they are not trapped by the ions.

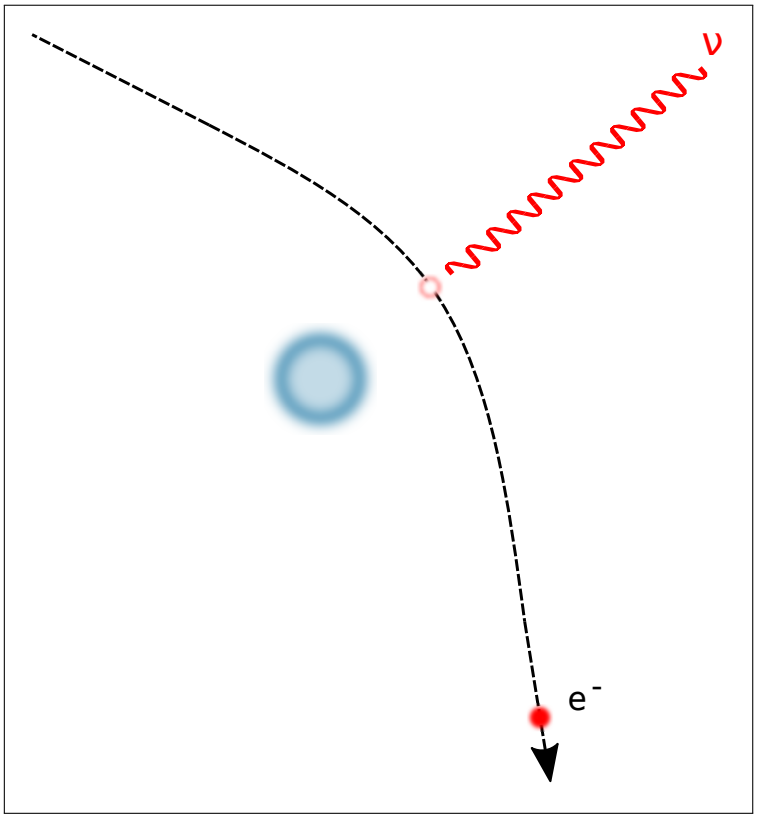

FIGURE 2.4: Scheme of free-free radiation. The large blue dot represents the atom, while the red spot represents a free electron, emitting a photon of frequency ν due to the change in trajectory, which has been exaggerated for clarity.

When an electron moving freely within a plasma passes nearby an ion, which is far more massive, the trajectory of the electron is deflected. Such deflection changes both the module and direction of the velocity vector of the electron, thereby decreasing its kinetic energy. The net result of this interaction is the emission of a single photon of energy equal to the energy lost by the electron, $\Delta E_e = h\nu$, as depicted in Figure 2.4. Since the electrons in the plasma span a broad range of energies, the resulting spectrum will be broad as well. In the radio band, the interactions responsible for free-free radiation are typically weak, in the sense that the change in energy is much smaller than the initial kinetic energy of the electron ($\Delta E_e \ll E_e$), to the point that sometimes it is considered that the trajectory does not vary at all (only the velocity module, hence the name of braking radiation). More energetic interactions would result in more energetic photons, even at X-ray wavelengths. Radio free-free emission

typically traces HII regions where the gas has been ionized by a nearby star, with typical temperatures around 10^4 K.

Continuum observations of astrophysical phenomena in the (sub) millimetre regime are especially interesting, since the relative contribution of thermal dust and free-free radiation to the total budget of thermal radiation is comparable at these wavelengths (Condon & Ransom, 2016).

Non-thermal emission

Different from thermal emission, non-thermal processes do not depend on the physical temperature of the emitting source. Non-thermal emission is influenced by other factors, such as the strength of magnetic fields. There are several types of non-thermal processes relevant to radio astronomy, e.g., non-thermal bremsstrahlung or synchrotron radiation (Ekers, 2014). The latter is particularly relevant to this PhD thesis.

Synchrotron radiation is emitted by charged particles accelerated to relativistic velocities, moving in the presence of strong magnetic fields. In such a scenario, an electron will traverse the magnetic field following a helical motion, as derived from the Lorentz's dynamical equation of motion, and releasing photons in the direction of the velocity. Therefore, synchrotron radiation is strongly beamed, i.e. collimated and enhanced (Rybicki & Lightman, 1986; Burke & Graham-Smith, 1997).

Synchrotron radiation is typically found in active galactic nuclei, supernova remnants and many other astrophysical environments. In the context of massive evolved stars, non-thermal synchrotron radiation is produced mainly in the colliding wind region of binary Wolf-Rayet systems (van der Hucht et al., 1992).

2.1.3 Radiation transport

The light produced by the processes described in the previous section usually travels a long way before reaching our detector devices. However, space is not empty, and during its journey, the emitted light interacts in many ways with matter (e.g., dust and gas clouds in the ISM, or the Earth's atmosphere). Understanding how such interactions alter the properties of the light is formally referred to as the *radiative transfer* problem, which we succinctly address in this section.

First, we need to characterize the strength of the electromagnetic radiation emitted. Using a classical ray optics approach, we define the *specific intensity* or *brightness* (I_ν) as:

$$I_\nu(\theta, \phi) = \frac{dE}{dS\, dt\, d\Omega\, d\nu} \tag{2.18}$$

which represents the amount of energy that passes through a differential area unit, per unit time, unit solid angle and within a narrow frequency range. It is thus measured in units of erg cm^{-2} s^{-1} sr^{-1} Hz^{-1}. Note that the specific intensity is a function of direction (θ, ϕ). In the particular case of blackbody emission, we have:

$$I_\nu(\theta, \phi) = B_\nu(T) \tag{2.19}$$

with $B_\nu(T)$ defined as in Equation 2.14, and therefore the intensity of radiation in any direction is the same. From the Rayleigh-Jeans approximation (2.15), it is possible to generalize that:

$$I_\nu = \frac{2kT_b\nu^2}{c^2} \tag{2.20}$$

where T_b is the equivalent *brightness temperature* of the source. This is a convention, valid even when $I_\nu(\theta,\phi) \neq B_\nu(T)$. Therefore, in a general case, T_b represents the temperature of an equivalent blackbody that would emit the same amount of radiation (at the same frequency) as the source.

If the emitting source subtends a certain solid angle, we can integrate I_ν over that solid angle to obtain the *flux density* of the source (S_ν), which is expressed as:

$$S_\nu = \int_{\Omega_{sou}} I_\nu(\theta,\phi)\,\cos\theta\, d\Omega \tag{2.21}$$

with units of erg cm^{-2} s^{-1} Hz^{-1}, or, more conveniently, Jansky (1 Jy = 10^{-23} erg cm^{-2} s^{-1} Hz^{-1}). Typically sources are much smaller than 1 rad, so the term $\cos\theta \approx 1$ and Equation 2.21 becomes:

$$S_\nu \approx \int_{\Omega_{sou}} I_\nu(\theta,\phi)\, d\Omega \tag{2.22}$$

Specific intensity has a very important property: it is constant along a ray if propagating through vacuum. For an arbitrary ray defined along the coordinate s:

$$\frac{dI_\nu}{ds} = 0 \tag{2.23}$$

This is known as the *conservation theorem*, and it essentially means that the brightness of a source is distance-independent. In other words, the brightness is the same at the source and the detector along a particular ray. The conservation theorem represents a fundamental piece of the radiative transfer theory, but it does not reflect the reality of radiation transport, where interaction with intervening matter plays a major role. Radiation-matter interaction can be explained as two separate processes:

- *absorption*, which involves the removal of radiation from a ray.
- *emission*, which involves the addition of radiation to a ray.

From a macroscopic point of view, when a ray goes through a medium able to absorb photons, photons in the ray will travel, on average, a frequency-dependent distance $l_{\nu,\text{free}}$ before being absorbed. This distance is known as the *photon mean free path*. We thus define the *optical depth* τ of a medium as its total length, expressed in terms of $l_{\nu,\text{free}}$. Intuitively, the optical depth can be understood as a measure of the *transparency* of a medium, directly related to its density and its ability to absorb radiation. Hence the distinction between *optically thin* mediums ($\tau \ll 1$), relatively transparent to radiation of a certain wavelength, and *optically thick* mediums ($\tau \gg 1$.) which are opaque. In general, the optical depth between two arbitrary points along a ray, s_0 and s_1 is given by:

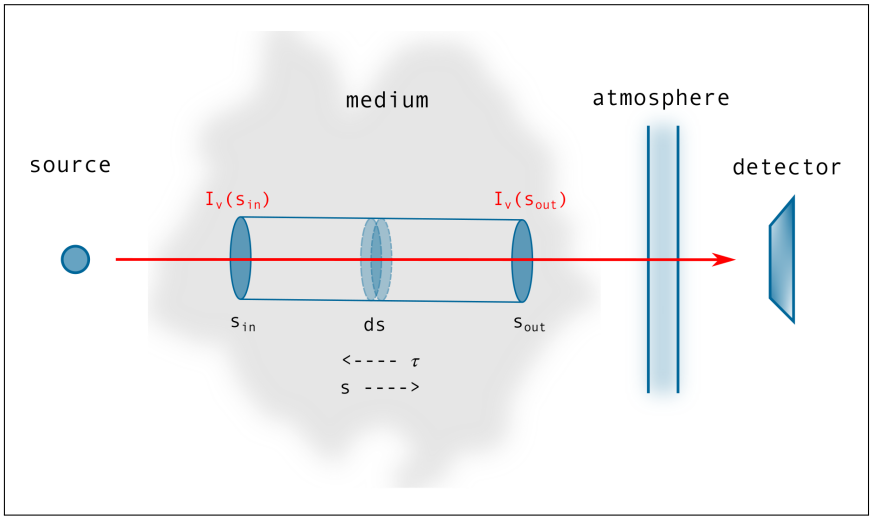

FIGURE 2.5: Radiation transport scheme, depicting a ray passing through an absorbing medium and the atmosphere before reaching the detector.

$$\tau_\nu(s_0, s_1) = \int_{s_0}^{s_1} \alpha_\nu \, ds \tag{2.24}$$

where α_ν is the inverse of the mean free path, in CGS units of cm^{-1}. This magnitude is known as the *opacity* of the medium, although opacity and optical depth are sometimes interchanged. Thus, one can use the optical depth to relate the intensity entering and leaving an absorbing medium through the equation:

$$\frac{I_\nu(s_{\mathrm{out}})}{I_\nu(s_{\mathrm{in}})} = \exp\left(-\tau\right) \tag{2.25}$$

as represented schematically in Figure 2.5. On the other hand, the medium may also add photons to the ray by virtue of some microscopic process. We define the emission coefficient j_ν as

$$j_\nu = \frac{dI_\nu}{ds} \tag{2.26}$$

This term is sometimes called emissivity and is measured in ergs s^{-1} cm^{-3} Hz^{-1} ster^{-1}. The combination of the absorption and emission terms yields the formal radiative transfer equation, which reads as:

$$\frac{dI_\nu}{ds} = j_\nu(s) - \alpha_\nu(s) I_\nu(s) \tag{2.27}$$

This relation, though, needs to be compliant with the laws of thermodynamics. If a ray goes through a medium in thermal equilibrium at a certain temperature T, then the intensity should remain the same at any point along the ray, because $I_\nu(s) = B_\nu(T)$ as in Equation 2.19. Mathematically, $\frac{dI\nu}{ds} = 0$, and, from Equation 2.27, this implies:

$$j_\nu(s) - \alpha_\nu(s) B_\nu(T) = 0 \tag{2.28}$$

or equivalently:

$$\frac{j_v}{\alpha_v} = B_\nu(T) \tag{2.29}$$

which essentially means that, whatever their values, the ratio of emissivity and extinction must equal the Planck's function in any medium in thermal equilibrium. This rule is known as the Kirchoff's law.

2.1.4 Radiation detection

Radio telescopes are the observing devices in the radio band. Most radio telescopes are ground-based [1] and therefore subject to the limitations imposed by the opacity of the Earth's atmosphere. Fortunately, the atmosphere is relatively transparent in the so-called *radio window*, similar to what occurs with visible light, so most of the radio photons reach the ground. However, the presence of some molecules in the atmosphere hampers observations in specific wavelength ranges, such as molecular oxygen (O_2) and water vapour (H_2O). Indeed, a critical parameter for radio astronomical observations is the precipitable water vapour column density along the vertical line of sight (abbreviated as pwv).

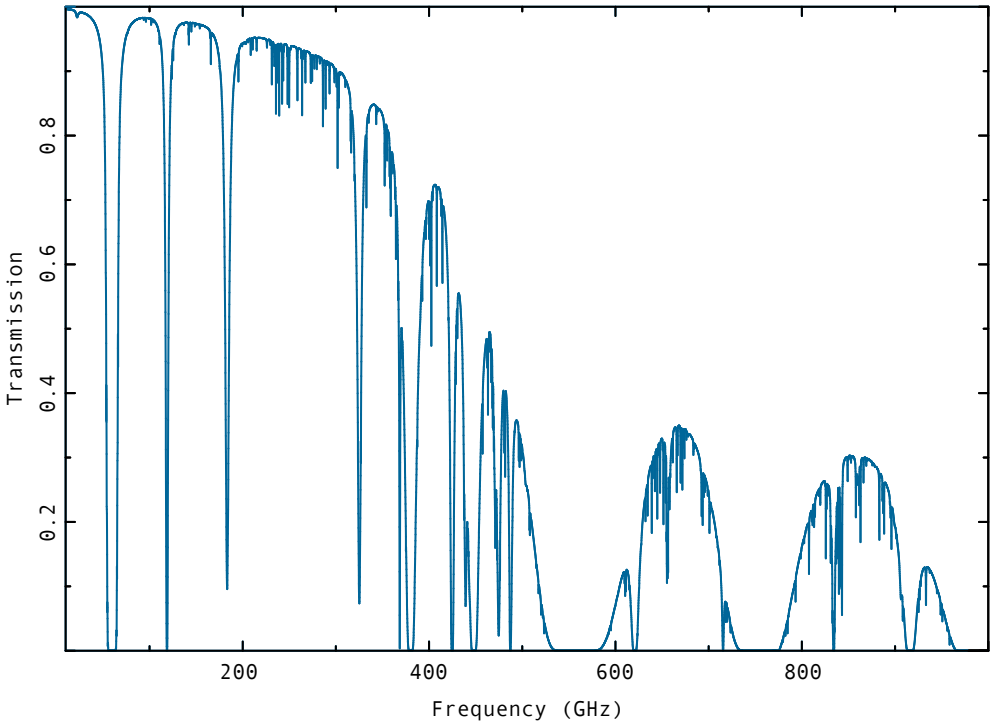

FIGURE 2.6: Model of zenith atmospheric transmission at ALMA (Llano de Chajnantor, Chile), computed between 10 and 960 GHz for 1 mm of pwv.

In order to minimize the impact of these molecules, some radio telescopes, specially those operating in the sub-millimetric range, are located in dry (i.e., less water vapour)

[1] The space-born radio telescope *RadioAstron* and the foreseen *Millimetron* are notable exceptions. See http://www.asc.rssi.ru/radioastron/description/intro$_e$*ng.htm* and https://www.millimetron.ru/en/ for further information.

and high sites (i.e., thinner atmosphere with low column densities of O_2). A prime example is the Atacama Large Millimeter/Submillimeter Array (ALMA), located $\sim$ 5000 m above sea level at the Llano de Chajnantor (Chile), one of the driest places on Earth. Figure 2.6 shows the zenith atmospheric transmission model between 10 and 960 GHz at the ALMA site, computed for a pwv of 1 mm.[2]

Antenna fundamentals

Nowadays, radio telescopes are generally built as parabolic antennas which work like any other optical device, collecting, focusing and amplifying the light coming from astronomical sources. In particular, the weak radio light waves are collected by a main dish, focused by a secondary sub-reflector, amplified and digitized for further analysis, as sketched in Figure 2.7. Like any other optical device, the defining properties of a radio telescope are its sensitivity and its angular resolution.

The resolution of a radio telescope depends on its response to the intensity of the incoming radiation, which is called *beam pattern* or PSF (point spread function). Mathematically it is expressed as the function that measures the ratio between the power received in a given direction (θ,ϕ) and the maximum power received P_{max}, such that:

$$P_n(\theta, \phi) = \frac{P(\theta, \phi)}{P_{max}} \tag{2.30}$$

where $P_n(\theta, \phi)$ denotes the normalized beam pattern or normalized power pattern, still a function of direction. The integral of the normalized beam pattern over all angles yields the beam solid angle:

$$\Omega_A = \iint_{4\pi} P_n(\theta, \phi) d\Omega \tag{2.31}$$

which is measured in steradians. A typical radio telescope has a highly directional power pattern, composed of a main lobe, where the value of Ω_A is high, and several secondary sidelobes, as depicted in Figure 2.8. This leads to the definition of the main beam solid angle Ω_{mb}, given by:

$$\Omega_{mb} = \iint_{mb} P_n(\theta, \phi) d\Omega \tag{2.32}$$

where the integral is limited to the main lobe. An antenna is said to be more efficient when most of the power pattern is contained in the main beam. Consequently, the so-called beam efficiency is defined as:

$$\eta_b = \frac{\Omega_{mb}}{\Omega_A} \tag{2.33}$$

Ideally, a perfectly efficient antenna ($\eta_b = 1$) would receive all the power through the main beam. The main beam determines the angular resolution of the telescope. For convenience, we define the half-power beam width (HPBW) as the angle subtended by the main beam of the antenna at the half of its maximum value, θ_{mb}.

[2] Adapted from the ALMA website https://almascience.eso.org/about-alma/atmosphere-model

This parameter is a direct measure of the resolving power of the telescope at a given frequency.

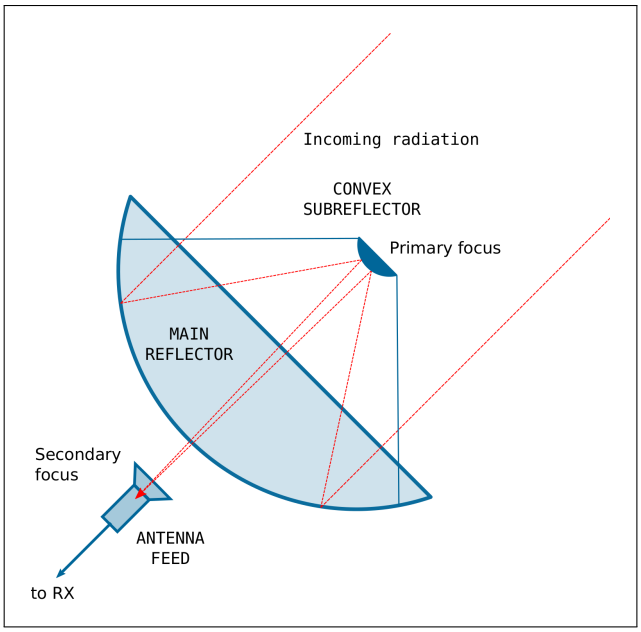

FIGURE 2.7: Schematic view of a Cassegrain single-dish radio telescope, highlighting the most important elements and the path of the incoming radiation.

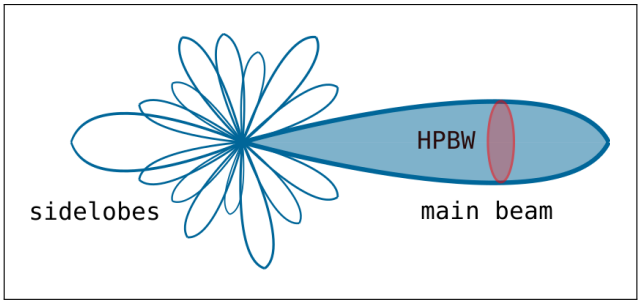

FIGURE 2.8: Typical antenna power pattern, with the main beam highlighted in blue, and the side lobes exaggerated for clarity. The red cross-section on the main beam represents the half-power beam width (HPBW).

At this point, it is needed to introduce the concept of *beam dilution*. If the observed source completely fills the antenna beam, $\theta_{sou} \geq \theta_{mb}$, the source is *resolved* by the beam; otherwise ($\theta_{sou} \leq \theta_{mb}$), the source is *unresolved*. In the former case, the measured brightness temperature is equivalent to the averaged specific intensity of the source within the beam. In the latter, the measured value must be corrected by a *beam filling factor*, F, which measures the fraction of the beam filled by the source, to obtain the actual brightness temperature.

F depends on the source geometry, which in many cases can be reasonably approximated by a gaussian. The resulting beam filling factor takes the form:

$$F = \frac{\theta_{sou}^2}{\theta_{sou}^2 + \theta_{mb}^2} \tag{2.34}$$

where θ_{sou} denotes the FWHM of a gaussian centred at the source position. The beam filling factor depends also on the frequency, and therefore is a critical parameter when working with line ratios.

Signal processing

Once the signal is collected by the dish and focused on the sub-reflector, it is redirected toward the receiver system, generally a heterodyne receiver. First, the input signal is filtered to select the frequencies of interest. Then, the filtered signal, of frequency ν_0, is sent through a low-noise amplifier (LNA). As the input frequency ν_0 may range from a few MHz to hundreds of GHz, it is conveniently down-converted to lower frequencies through a process known as heterodyning, i.e. mixing it with the signal of a local oscillator (e.g., a hydrogen maser) at a fixed frequency $\nu_{\rm LO} < \nu_0$. The mixing produces two signals, with frequencies $\nu_0 + \nu_{\rm LO}$ and $\nu_0 - \nu_{\rm LO}$ respectively. The former is filtered out in a low pass filter stage, and the latter, called the intermediate frequency (IF), is preserved and further amplified by additional stages. Finally, it is sent to the backend (spectrometers, correlators...) and transmitted to a computer for analysis. A schema of the heterodyning process is depicted in Figure 2.9.

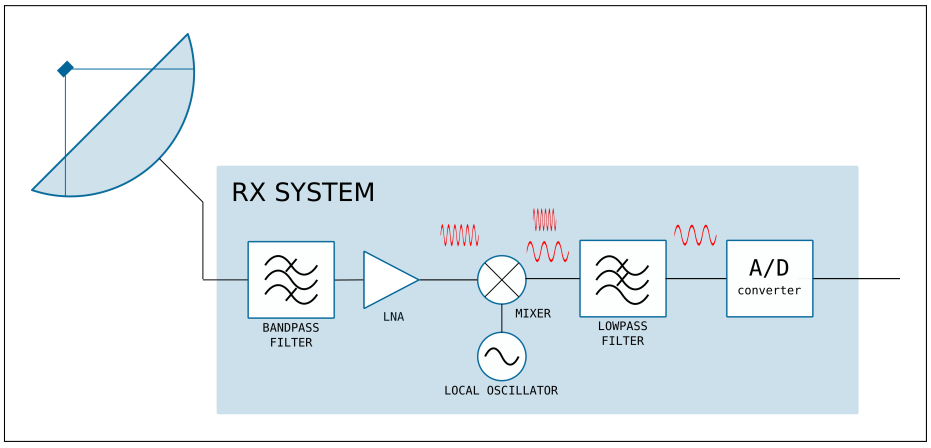

FIGURE 2.9: Block diagram of the elements that compose a classic heterodyne receiver.

Single-dish observations

Single-dish observations are carried out with a single antenna. Considering an antenna characterized by a certain beam pattern $P_n(\theta, \phi)$ and a geometric aperture A_g; when observing a source with a brightness distribution $I_\nu(\theta, \phi)$, the power received by the antenna is:

$$P_r(\theta, \phi) = \frac{1}{2} \int_\Omega A_e I_\nu(\theta, \phi) P_n(\theta, \phi) d\Omega, \tag{2.35}$$

where $A_e = \eta_A A_g$ is the effective aperture, which depends on the aperture efficiency η_A, always <1 as the antenna surface is not ideal. This power can be translated to a temperature scale by taking advantage of the Nyquist theorem, that states that any resistor at a temperature T produces a noise power $P = kT\Delta\nu$, where $\Delta\nu$ is the bandwidth and k is the Boltzmann's constant. Therefore, we define the *antenna temperature* as:

$$T_A(\theta,\phi) = \frac{1}{\Omega_A}\int_\Omega T_R(\theta,\phi)P_n(\theta,\phi)d\Omega, \tag{2.36}$$

By calibrating atmospheric effects, we can translate T_A into a *corrected antenna temperature* scale or T_A^*, representing the temperature that would be measured *outside* the Earth's atmosphere and considering the forward signal only. This conversion involves correcting for atmospheric opacity, such that:

$$T'_A = T_A e^{\tau_\nu} \tag{2.37}$$

and removing the contribution from the rear lobes, by applying the forward efficiency of the antenna, η_f, defined as the fraction of power received from the forward hemisphere:

$$T_A^* = \frac{T'_A}{\eta_f} \tag{2.38}$$

Note that T_A^* still depends on the power pattern of the telescope. It is thus convenient to express the received power in a temperature scale independent of the telescope parameters, so that:

$$T_{mb} = \eta_{mb} T_A^* \tag{2.39}$$

with T_{mb} denoting the *main beam temperature*, which is the scale used throughout this thesis in what respects to line intensities. $\eta_{mb} = \frac{\eta_f}{\eta_b}$ is the ratio between the forward efficiency and the main beam efficiency (Equation 2.33).

In the millimetric/sub-millimetric wavelength range, atmospheric properties are variable in very short timescales. The effects of these changes and other systematics must be properly calibrated. The standard calibration procedure is the so-called *chopper wheel* method, first described by Penzias & Burrus (1973) and discussed exhaustively by Ulich & Haas (1976) and Kutner & Ulich (1981). The chopper-wheel method characterizes the receiver by measuring the response to a hot and a cold load, and comparing the resulting power to the power obtained when measuring the sky. Observations are thus performed by alternating pointings on the target source and pointings on blank positions of the sky, i.e. ON and OFF positions. By doing so, it is possible to discriminate which fraction of the observed power comes from the source under study:

$$T^*_{A,ON} = T_{sou} + \{T_{bg} + T_{atm} + T_{rx} + T_{sw} + T_{loss} + T_{spill}\} \tag{2.40}$$

$$T^*_{A,OFF} = \{T_{bg} + T_{atm} + T_{rx} + T_{sw} + T_{loss} + T_{spill}\} \tag{2.41}$$

$$T^*_{A,ON} - T^*_{A,OFF} = T_{sou} \tag{2.42}$$

where T_{sou} is the source brightness, and the terms between brackets represent all the noise contributions through the whole signal path, caused by the cosmic microwave background, the Earth's atmosphere, the receiver electronics, potential standing wave patterns, ohmic losses in the feed, and ground radiation, respectively.

All possible sources of noise in the receiver may be described by a single system temperature $T_{\rm sys}$, so the rms achievable with the chopper-wheel method is determined by the radiometer equation, such that:

$$\Delta T \propto \frac{T_{sys}}{\sqrt{\Delta\nu t}} \tag{2.43}$$

where $\Delta\nu$ is the spectral resolution and t the total integration time considering both the ON and OFF positions.

After calibration of the receiver response, focus and pointing of the antenna need to be determined and adjusted to minimize flux losses. This is typically achieved by observing strong point sources, like planets or quasars. It is recommended to check pointing accuracy every one or two hours, or when the telescope moves a distance as long as to produce significant changes in the structural distribution of forces. On the other hand, focus is usually calibrated every two or three hours, and also at sunrise and sunset.

Concerning the observing strategy, there are several possible ON-OFF observing schemes:

1. Position switching, in which the ON signal is compared with an OFF signal from a nearby sky position. The selection of a proper OFF position is critical for line observations: the reference position should be devoid of the molecule of interest, and ideally at the same elevation as the ON position.

2. Wobbler switching, a variant from position switching in which only the secondary reflector wobbles from the ON position to an OFF position at a certain throw. This mode is appropriate for small sources, and it produces extremely flat baselines.

3. On-The-Fly mapping, in which the antenna is continuously driven at a constant speed, taking data every t_{dump} seconds. This mode is particularly tailored to map extended regions of the sky efficiently. The mapping is done in "scans" along a certain direction, with OFF pointings at the beginning and the end of each scan.

4. Frequency switching, which involves switching between two target frequencies while keeping the pointing on source. This technique is particularly useful for line observations, and only appropriate when the target lines lie within a relatively narrow bandwidth.

Interferometric observations

The maximum theoretical resolution of a telescope is determined by the size of the Airy disk, approximately $\theta = 1.22\frac{\lambda}{D}$, where θ denotes the angular resolution in radians, λ the wavelength and D the diameter of the telescope. In other words, the larger a telescope is, the better resolution it achieves. However, this relation implies that

the antenna dishes required to obtain arcsecond or sub-arcsecond resolutions in the radio band span from hundreds to thousands of meters, to the point that they become unpractical, and even impossible to build, for mechanical reasons.

Fortunately, this limitation can be overcome by taking advantage of interferometry, a technique that coherently combines the outputs of several antennas with a maximum separation (or *baseline*) B to obtain an approximate resolution of $\theta \approx \frac{\lambda}{B}$. In other words, several separated antennas working together synthesize a virtual dish as large as the maximum baseline. This technique is also called *aperture synthesis* for evident reasons.

Let us consider a simple two-element radio interferometer, with two antennas separated a distance B, pointing to a source with a brightness distribution $I(s)$, with s the direction of the incoming radiation such that $s = f(\theta, \phi)$. The schema is shown in Figure 2.10. For simplicity, we ignore the frequency dependency of $I(s)$, assuming a monochromatic wave. Since the observed source is at astronomical distances, the far-field regime applies, and the incoming wave-front can be considered planar. As a consequence, radiation from the source arrives at the antennas with a certain time delay τ, which depends on the projection of the baseline onto the direction of radiation.

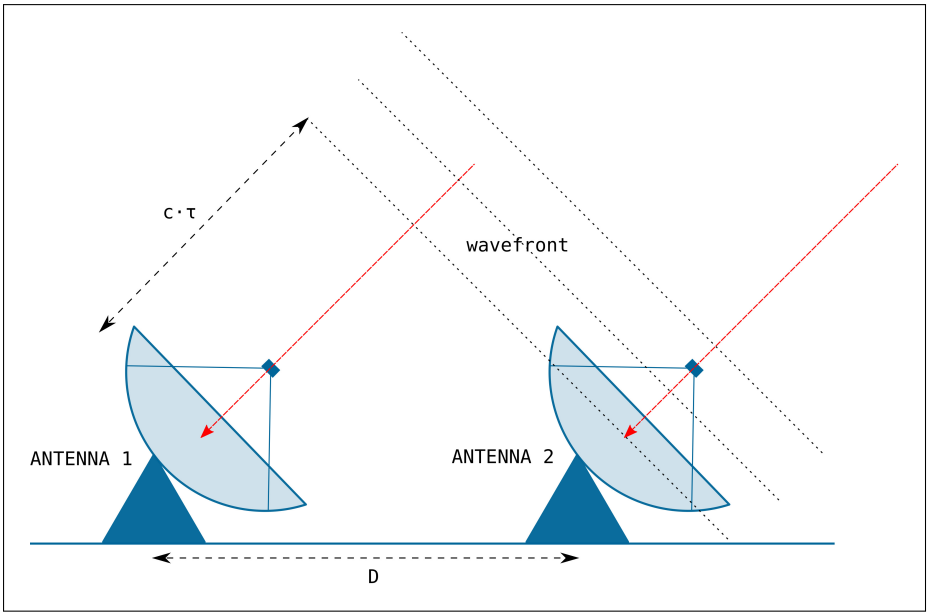

FIGURE 2.10: Schematic view of a radio interferometer.

The signals collected by the antennas are then sent to a correlator, which essentially computes their averaged product, producing a signal of the form:

$$R_C(\tau) =< V_1, V_2 >\propto I(s)e^{i\omega\tau}d\Omega \tag{2.44}$$

where V_i is the voltage induced in each antenna by the radiation coming from a differential source element $d\Omega$, and τ is the geometric delay. Note that $R_C(\tau)$ is indeed a periodic signal depending on τ: when the signals of the two antennas are in phase (τ=0), the correlator response is maximum. The delay can be written in terms of the baseline projection onto the radiation direction, expressed in wavelengths, such that:

$$\tau = \frac{b\vec{s}}{\lambda} \tag{2.45}$$

If we integrate 2.44 over all the source, we obtain the *complex visibility function*, which is a measure of the coherence of the source brightness distribution. For convenience, it is written as a function of the coordinates in the source plane (i.e. the sky), (x, y), and the coordinates of the baseline projection with respect to that plane, (u, v), such that $u = b_x/\lambda$ and $v = b_y/\lambda$:

$$V(u, v) = \iint_{sou} A(x, y)I(x, y)e^{2\pi i(ux+vy)}dxdy \tag{2.46}$$

By convention, the u and v coordinates run along the NS and EW directions respectively, defining what is known as the uv plane.

Intuitively, a visibility is the response of each pair of antennas to the brightness distribution of the source, i.e. one "sample" of the spatial frequencies of the source. However, the Van Cittert-Zernike theorem (van Cittert, 1934; Zernike, 1938) states that the visibility function is equivalent to the Fourier Transform of the brightness distribution of the source –as long as the source is incoherent, which happens to be the case for most astrophysical sources–. From this, it follows that Equation 2.46 can be inverted to reconstruct $I(x, y)$.

The accuracy of such reconstruction will depend on the number of visibilities observed, or, in other words, the number of spatial frequencies sampled and their distribution across the uv-plane. We define the uv-coverage as a measure of the completeness of the spatial frequency sampling. A perfect uv-coverage is not feasible, though, as only a discrete set of spatial frequencies can be sampled by a finite number of antennas. Consequently, interpolation is needed to reconstruct an approximate brightness distribution, such that $I'(x, y) \approx I(x, y)$. Likewise, different interferometers with different uv-coverages will recover slightly different brightness distributions.

Since the uv-plane and the image plane are conjugated spaces, high spatial frequencies, sampled by long baselines, correspond to sharp features or fine details in the image, whereas low spatial frequencies, sampled by short baselines, correspond to broad or extended features. The shortest baseline, b_{min}, limits the interferometer sensitivity to extended structures. We define the maximum recoverable scale as the size of the largest extended feature detectable by the interferometer. It can be approximated as:

$$MRS \sim \frac{\lambda}{b_{min}} \tag{2.47}$$

In this sense, given that two antennas cannot be located arbitrarily close, there will always be an "empty gap" in the origin of the uv-plane that cannot be sampled by an interferometer. For that reason, interferometric observations are sometimes complemented with single-dish observation, to avoid missing the lowest spatial frequencies.

Different strategies are possible to improve the sampling of the uv-plane: (1) changing the array configuration, i.e. the relative spatial distribution of the antennas; (2) increasing N, the number of elements of the array, as the number of visibilities is given by $N(N-1)/2$; and (3), taking advantage of the rotation of the Earth, sweeping

the *uv*-plane thanks to the apparent movement of the antennas from the source point of view. These strategies are usually combined together.

Due to their complex nature, interferometric observations are subject to three different sources of error, namely:

- Atmospheric effects, caused mainly by variations in the amount of precipitable water vapour. These effects are direction-dependent and include refractions, scintillation... that degrade both the pointing accuracy and sensitivity of continuum and line observations, producing *phase errors*.

- Effects derived from antenna positioning and usage of finite bandwidths, causing *delay errors*.

- Electronics-related issues, such as different system temperatures and gains, which cause *amplitude errors*.

As a consequence of these errors, interferometric observations involve more advanced calibration procedures than single-dish. In particular, the following steps are required:

1. *Bandpass calibration*, which aims at correcting the frequency-dependent receiver response. It is typically done by observing a very bright, compact source for which the telescope response is well known, e.g., a quasar.

2. *Gain calibration* (phase and amplitude), which accounts for time-varying amplitude and phase offsets produced by atmospheric variations or instrumental issues. It involves two separate corrections: (1) an atmospheric correction according to the readings provided by a Water Vapor Radiometer, and (2) the regular observation of a gain calibrator throughout the observing run. This gain calibrator should be a point-like source close to the science target, since these effects are strongly direction-dependent.

3. *Flux calibration*, which sets an absolute amplitude scale by determining system temperatures for each antenna (in a way analogous to what is done in single-dish) and observing a source whose flux is well determined.

As in single-dish, different observing strategies are possible in radio interferometry. The most common are:

- *Single field* imaging. Only a single target source is observed, so the phase centre of the array is fixed throughout the observation. To provide a more complete *uv*-coverage, the source may need to be tracked for a certain range of hour angles, and calibrators and target should be observed alternatively.

- *Mosaicking*, used to image sources larger than the primary beam. It involves observing a set of nearby positions, covering the field of interest, forming a *mosaic*. Adjacent pointings should overlap at half-power to ensure homogeneous sensitivity across the image.

The rms noise limit of an interferometer can be estimated, as for single-dish telescopes (Equation 2.43), resorting to the radiometer equation. Given an array of N identical antennas,with an effective aperture A_e, the flux density rms is given by the expression:

$$\Delta S_\nu \propto \frac{2kT_{sys}}{A_e\sqrt{2N\Delta\nu t}} \tag{2.48}$$

with k the Boltzmann constant, T_{sys} the receiver temperature that describes the system, $\Delta\nu$ the spectral resolution and t the integration time.

The brightness distribution of the source in the image plane, $I(x, y)$, has to be restored from a discrete collection of samples of spatial frequencies in the uv-plane. Such a collection can be written in terms of Kroenecker's delta functions, such that:

$$B(u, v) = \sum_{ij} \delta_{ij}(u, v) \tag{2.49}$$

with $\delta(u, v)$ a delta function sampling a specific coordinate of the uv-plane. We can then define the *dirty image* as the inverse Fourier Transform of the visibilities measured, which can be written as:

$$I^D(x, y) = \mathcal{F}^{-1}\{B(u, v) \times V(u, v)\} \tag{2.50}$$

with $V(u, v)$ the visibility function defined as in Equation 2.46. However, the convolution theorem states that the inverse Fourier Transform of a product is a convolution, and therefore Equation 2.50 can be rewritten as:

$$I^D(x, y) = b(x, y) * I(x, y) \tag{2.51}$$

where:

$$b(x, y) = \mathcal{F}^{-1}\{W(u, v)B(u, v)\} \tag{2.52}$$

is the point spread function or dirty beam, and $I(x, y)$ is the inverse Fourier Transform of the visibilities by virtue of the Van Cittert-Zernike theorem. In other words, the dirty image is just the convolution of the true brightness distribution of the source with the dirty beam.

The term $W(u, v)$ in Equation 2.51 is the weighting function. Including a weighting function allows for modulating the dirty beam sidelobes and provides more flexibility for image reconstruction. Depending on the science goals, there are several possible weighting schemes, namely: (1) natural weighting, which improves image sensitivity; (2) uniform weighting, which provides a finer resolution; (3) robust weighting, a compromise solution between natural and uniform; and (4) tapering, which increases sensitivity to extended structures.

The process to obtain the true brightness distribution $I(x, y)$ from the dirty image is known as deconvolution, since it involves deconvolving the dirty beam $b(x, y)$ from the dirty image $I^D(x, y)$. Most deconvolution algorithms look for a model of $I(x, y)$ that is compatible with the available data, starting from some a priori assumptions. The most widely adopted in radio astronomy is the CLEAN algorithm (Högbom,

1974), which relies on the assumption that the source is a collection of point sources. The CLEAN algorithm involves the following steps:

1. Initialize a "residual" map to the dirty image and a CLEAN component list.
2. Identify the strongest feature in the residual map as a point source.
3. Add a fraction g (the *iteration gain*, typically between 0.05-0.1) of this point source to the CLEAN component list, and subtract it times the dirty beam from the residual map.
4. Go back to 2 and repeat until reaching a convergence criterion, such as a noise limit or a maximum number of iterations.

As the last step of the algorithm, the CLEAN components are convolved with a CLEAN gaussian beam (also called *restoring beam*) and added to the residual map (pure noise at this point) to produce the final restored image, ready for scientific exploitation.

2.2 Analysis methods

2.2.1 Analysis of molecular line spectra

The ultimate objective of molecular spectroscopy is to derive meaningful physical information about the gas from the observed spectra. In this context, one of the fundamental quantities that describe a molecular gas distribution is the so-called column density, which measures the number of molecules per unit area along the line of sight. Computing this quantity is essential to constrain other physical properties of the gas, such as the excitation temperature or the volume density. Here we will briefly address the main considerations in the calculation of column densities from molecular line observations. However, a detailed treatment with further details can be found in Wilson & Hüttemeister (2000) and Mangum & Shirley (2015).

LTE regime

In a system in statistical equilibrium, population and depopulation rates of a given energy level are balanced, so that:

$$n_i \sum R_{ij} = \sum n_j R_{ji} \tag{2.53}$$

where n_i denotes the number density of the i-th level, and the transition rate R_{ij} is the sum of spontaneous radiative excitation, stimulated radiative excitation and de-excitation, and collisional excitation and de-excitation. These processes are described by the Einstein's coefficients A_{ij}, B_{ji}, B_{ij} and the collisional coefficients C_{ij} and C_{ji}, seen in Section 2.1.1. In other words, equation 2.53 implies that a system under LTE conditions absorbs and emits the same number of photons.

In Section 2.1.3, we treated the radiative transfer problem from a macroscopic point of view, i.e. considering macroscopic properties such as the emission and absorption coefficients. However, the Einstein's coefficients allow for linking these parameters to the quantum-scale properties of the transitions under study.

Let us consider again a two-level system in statistical equilibrium, as portrayed in Figure 2.2. Neglecting collisional excitation for now ($C_{ij} = C_{ji} = 0$) in order to derive the relation between A_{ij}, B_{ij} and B_{ji}, statistical equilibrium equation for radiative processes becomes:

$$n_1 B_{12} \bar{J} = n_2 B_{21} \bar{J} + n_2 A_{21} \tag{2.54}$$

where $\bar{J} = 4\pi/c \int_0^\infty I_\nu \phi(\nu) d\nu$ is the radiation field density, and $\phi(\nu)$ is line profile function, assumed equal for absorption and emission. Besides, if the system is in thermal equilibrium, $I_\nu = B_\nu(T)$, and level populations follow a Boltzmann distribution, so the number densities of each level are related through the expression:

$$\frac{n_2}{n_1} = \frac{g_2}{g_1} \exp\left(-\frac{h\nu}{kT}\right) \tag{2.55}$$

where g_i is the total degeneracy of each level. In the general case, $g_i = g_J g_K g_I$, the product of rotational and nuclear spin degeneracies, but for simple linear molecules $g_K = 1$ and often $g_I = 1$, so $g_i = g_J = 2J + 1$.

At this point we can rewrite Equation 2.27 in terms of A_{21}, B_{12} and B_{21}. Assuming that emitted photons are distributed over the full solid angle, now the radiative transfer equation reads:

$$\frac{dI_\nu}{ds} = \frac{h\nu}{4\pi} n_2 A_{21} \phi(\nu) - \frac{h\nu}{c}(n_1 B_{12} - n_2 B_{21}) \bar{J} \tag{2.56}$$

so putting the emission and absorption coefficients in relation to the Einstein coefficients is immediate:

$$\alpha_\nu = \frac{h\nu}{c}(n_1 B_{12} - n_2 B_{21}) \phi(\nu) \tag{2.57}$$

$$j_\nu = \frac{h\nu}{4\pi} n_2 A_{21} \phi(\nu) \tag{2.58}$$

Now, the interaction of a ray with a medium is expressed in terms of the quantum-scale properties of the medium, i.e. the transition rates between energy states. From Kirchoff's law (Equation 2.29), we obtain:

$$\frac{j_\nu}{\alpha_\nu} = \frac{2h\nu^3}{c^2} \left(\frac{g_2 n_1}{g_1 n_2} - 1\right) = B_\nu(T) \tag{2.59}$$

which directly yields the relation between number densities (Equation 2.55).

We can now extend Equation 2.54 incorporating the collisional coefficients, which in LTE fulfill:

$$n_1 C_{12} = n_2 C_{21} \tag{2.60}$$

The resulting relation is the (stationary) detailed balance equation for a two-level system:

$$n_1(B_{12} \bar{J} + C_{12}) = n_2(A_{21} + B_{21} \bar{J} + C_{21}) \tag{2.61}$$

However, the Einstein coefficients are still unknowns. To calculate the emission and absorption coefficients, we need an additional relation. If T in Equation 2.55 is the kinetic temperature T_k, we have:

$$T_{ex} = T_k \frac{T_b A_{21} + \frac{h\nu}{k} C_{21}}{T_k A_{21} + \frac{h\nu}{k} C_{21}} \tag{2.62}$$

where T_{ex} is the excitation temperature and T_b is the brightness temperature as in Equation 2.20. It is important to keep in mind that the excitation temperature does not always have a physical meaning: it is only a useful concept that describes the energy of a system (either kinetic, radiative, rotational...). Here we can distinguish two regimes, as briefly discussed in Section 2.1.1:

- If radiative excitation dominates (e.g., low-density environments), $A_{21} \gg C_{21}$ and therefore $T_{ex} \to T_b$.
- If collisional excitation dominates (e.g., high-density environments), $C_{21} \gg A_{21}$ and thus $T_{ex} \to T_k$.

In the general case, we define the *critical density* as the density when $A_{ij} \approx C_{ij}$. The critical density represents the minimal number density required for effective collisional excitation of a certain rotational transition.

We define the *column density* as the number of molecules in a certain energy level j integrated over a certain path (typically, the line of sight), such that:

$$N_j = \int n_j ds \tag{2.63}$$

where N_j is measured in units of $[\mathrm{cm}^{-2}]$. By virtue of Equations 2.54 and 2.57, and after some transformations not shown here for the sake of brevity, we obtain an expression that relates the column density in the upper energy level u to the optical depth:

$$N_u = \frac{3h}{8\pi^3 |\mu_{lu}|^2} \left[\exp\left(\frac{h\nu}{kT}\right) - 1 \right]^{-1} \int \tau_\nu d\nu \tag{2.64}$$

where $|\mu_{lu}|$ is the dipole matrix element in the definition of the Einstein spontaneous emission coefficient A_{ul}. We can further relate this magnitude with the intensity of the measured transition. To do so, we need to estimate the population of *all* energy levels, taking advantage that, under LTE, the level populations follow a Boltzmann distribution (Equation 2.55) and thus can be described by a single temperature T_{ex}. The total column density N considering all energy levels is then:

$$N = N_u \frac{Z}{g_u} \exp\left(\frac{E_u}{kT_{ex}}\right) \tag{2.65}$$

In this equation, we have introduced Z, the rotational partition function, which represents the sum over all energy states. It can be written as:

$$Z = \sum_J^\infty (2J+1) \exp\left(-\frac{hB_e J(J+1)}{kT}\right) \tag{2.66}$$

where the numerator in the exponential term is simply the energy of each rotational level as in Equation 2.9, but expressed in terms of the *rotation constant* $B_e = \frac{\hbar}{4\pi I}$, with I the moment of inertia of the molecule. If the temperature describing the system is large enough so that $hB_e \ll kT$, the partition function becomes:

$$Z \approx \frac{kT}{hB_e} \tag{2.67}$$

which is a useful and valid approximation in many cases. Combining Equations 2.64 and 2.65, we arrive at the formal expression for the total molecular column density:

$$N = \frac{3h}{8\pi^3|\mu_l u|^2}\frac{Z}{g_u}\exp\left(\frac{E_u}{kT_{ex}}\right)\left[\exp\left(\frac{h\nu}{kT_{ex}}\right)-1\right]^{-1}\int \tau_\nu dv \tag{2.68}$$

In the optically thin limit, i.e. when $\tau_\nu \ll 1$, we can simplify Equation 2.64 by replacing the integral term over τ with the integrated line intensity, such that:

$$N_u = \frac{3h}{8\pi^3|\mu_{lu}|^2}\exp\left(\frac{h\nu}{kT}-1\right)\int T_{mb}d\nu \tag{2.69}$$

where T_{mb} denotes the main beam temperature of the line. This equation represents a cornerstone for molecular spectroscopy, as it establishes a direct relationship between the measured line intensity and the column density of the molecular gas.

Non-LTE regime

The LTE regime is an ideal situation that greatly simplifies the radiative transfer problem, but, unfortunately, most astrophysical environments are not under this regime. This results in different transitions being characterized by different excitation temperatures. Besides, the collisional coefficients are directly proportional to the number densities of each level. In LTE, the relation between number densities given by Equation 2.55 greatly facilitates solving the system composed by Equations 2.56 and 2.61. This relation, however, is no longer valid under non-LTE conditions. Solving the radiative transfer equation thus becomes a challenging task.

The problem can still be simplified by taking advantage of the escape probability formulation, introduced by Sobolev (1960). We define β, the escape probability, as the chance of a photon escaping from the source (i.e., not being absorbed), so that $\beta = 0$ if the source is opaque, and $\beta < 1$ otherwise. This allows us to rewrite Equation 2.61 as:

$$n_2 = n_1 C_{12} - n_2 C_{21} - \beta n_2 A_{21} \tag{2.70}$$

thereby decoupling collisions from the radiation field $\bar{J}$ and the B_{ij} coefficients, which can be solved separately.

There exist several methods derived from the escape probability formulation that allow for solving the radiative transfer problem. By far, the most widely used is the Large Velocity Gradient (hereafter LVG) approximation, initially developed for collapsing molecular clouds. This approach assumes that any photons emitted escape quickly as a consequence of the macroscopic velocity gradient of the source, not interacting with nearby parcels of matter. In other words, the LVG premise means that emission produced at a certain point is completely decoupled from emission produced

at whatever other points in the source, which will have different velocities and thus a different Doppler shift $\delta\nu$. The escape probability can be derived from the optical depth in simple geometries (e.g., Elitzur 1992), such as a uniform collapsing sphere:

$$\beta = \frac{1 - e^{-\tau}}{\tau} \tag{2.71}$$

or a homogeneous slab:

$$\beta = \frac{1 - e^{-3\tau}}{3\tau} \tag{2.72}$$

Of course, the LVG method relies on rough geometrical simplifications and physical assumptions that may not be valid for all sources, but it is a good starting point to estimate the non-LTE global physical conditions of a gas from a set of line measurements, as it is done throughout this PhD thesis. More complex scenarios will require more sophisticated numerical methods to obtain approximate solutions of the radiative transfer equation.

2.2.2 Analysis of continuum data

To disclose the dominant emission mechanisms from radio continuum observations of a certain source, we use the *spectral index*, which measures the dependence of the flux density on frequency. In a given frequency regime, the spectral index represents the slope of the spectral energy distribution of the source, and it follows the convention:

$$S_\nu \propto \nu^\alpha \tag{2.73}$$

so that positive α values imply higher flux densities at higher frequencies. Spectral index is computed with at least two flux density measurements at two different frequencies, according to the expression:

$$\alpha = \frac{\log(S_1/S_2)}{\log(\nu_1/\nu_2)} \tag{2.74}$$

where S_1 and S_2 denote the flux density of the source measured at frequencies ν_1 and ν_2, respectively. The uncertainty associated with α depends on two factors: the intrinsic uncertainty of the flux density measurements, ΔS_i, and the frequency separation. The larger frequency separation, the more robust α becomes, as the impact of ΔS_i is less significant. We can compute $\Delta\alpha$ by propagating errors from Equation 2.74, such that:

$$\Delta\alpha = \frac{\sqrt{(\Delta S_1/S_1)^2 + (\Delta S_2/S_2)^2}}{\log(\nu_1/\nu_2)} \tag{2.75}$$

In this thesis, we usually work with spectral index *maps*, computed in a pixel-by-pixel basis when the signal-to-noise ratio is high enough, or *integrated* spectral indices, derived by integrating the flux density all over the source area.

The spectral index of a source provides useful insights on its emission mechanisms, allowing us to discriminate the contribution from thermal dust, free-free and non-thermal processes. In general:

- In the Rayleigh-Jeans limit (Equation 2.15), ideal thermal blackbody emission has a theoretical spectral index of $\alpha = 2$, directly derived from Equation 2.74 by applying Planck's law. For thermal dust, $\alpha = 2 + \beta$, with β, the dust emissivity index, typically ranging from 1 to 2.7 (Draine et al., 2007; Schnee et al., 2010).
- Free-free emission, e.g., arising from an HII region, presents α values spanning from -0.1 to 1.5. A case of particular interest within this range is the thermal stellar wind typical of evolved stars, with a characteristic value of $\alpha = 0.6$ (or higher if the wind is radiatively shocked) (Wright & Barlow, 1975).
- Non-thermal emission, e.g., synchrotron radiation, is characterized by negative spectral indices, with a canonical value of $\alpha = -0.7$. This is typically measured in extreme environments, e.g., the colliding wind region of close Wolf-Rayet binaries (Dougherty & Williams, 2000) or the relativistic jets of radio galaxies (Eckart et al., 1986).

Mass-loss rate estimates from flux density measurements

In the case of hot stars displaying a radio spectral index near 0.6, i.e. dominated by a thermal stellar wind, it is possible to estimate the current mass-loss rate from the measured flux density, by following the empirical relation described by Panagia & Felli (1975). This approach relies in a number of reasonable assumptions, namely that the star is surrounded by a spherically expanding, ionized envelope, extending a few stellar radii and characterized by a power-law electron density distribution of the form $n_e \propto r^{-2}$. Under this conditions, the expected radio flux S_ν emitted by such envelope at a certain frequency ν is given by:

$$S_\nu = 5.12 \left[\frac{\nu}{10\,\mathrm{GHz}}\right]^{0.6} \left[\frac{T_e}{10^4\,\mathrm{K}}\right]^{0.1} \left[\frac{\dot{M}}{10^{-5}\,\mathrm{M_\odot\,yr^{-1}}}\right]^{4/3} \left[\frac{\mu}{1.2}\right]^{-4/3} \left[\frac{v_{exp}}{10^3\,\mathrm{kms^{-1}}}\right]^{-4/3} \overline{Z}^{2/3} \left[\frac{d}{\mathrm{kpc}}\right]^{-2} \tag{2.76}$$

where T_e denotes the electron temperature of the plasma, $\dot{M}$ the mass-loss rate, μ the mean atomic weight, v_{exp} the terminal velocity of the stellar wind, $\overline{Z}$ the average ionic charge, and d the distance to the star. The expression above can be further simplified by assuming cosmic abundances and full ionization. For a measured flux density S_ν, the corresponding mass-loss rate according to Equation 2.76 is:

$$\dot{M} = 6.7 \times 10^{-4} v_{exp} S_\nu^{3/4} d^{3/2} (\nu \times g_{\mathrm{ff}})^{-1/2} \tag{2.77}$$

where the term g_{ff} accounts for the Gaunt factor, approximated as $g_{\mathrm{ff}} = 9.77(1 + 0.13 \log \frac{T_e^{3/2}}{\nu})$ (Leitherer & Robert, 1991).

2.3 Procedures and tools

Over the course of this thesis, we have surveyed a number of LBV sources looking for associated circumstellar structures. To do so, we analysed spectroscopic and continuum observations at millimetre wavelengths, obtained with both single-dish telescopes and interferometers. The typical pipeline to translate the raw data provided by these instruments into meaningful scientific results involved, at least, three steps: reduction and calibration; exploration and analysis; and modelling. Each of these steps required the use of specialized tools and software, as described below.

2.3.1 Data reduction and calibration

The first step of the data processing pipeline is data reduction. In the case of single-dish observations, reduction was principally done using the software package `GILDAS`[3]. This software is the standard reduction package for data obtained with the IRAM 30-m telescope and the NOEMA interferometer, although it is also able to deal with observations from other facilities (e.g., APEX).

`GILDAS` is a multi-purpose package that comprises a number of utilities to reduce, visualize and analyse spectral line and continuum data. For this work, the most relevant are:

- `CLASS`, a collection of tasks for single-dish data processing.
- `GREG`, a multi-purpose 2-D plotting and analysis tool.
- `ASTRO`, a tool for planning observing sessions.

After an observing run, single-dish telescopes typically provide a set of spectra already calibrated in frequency and antenna temperature (T_A^*). Further data reduction involves (1) flagging of bad channels or spectra, e.g., affected by spikes; (2) correction of other instrumental artefacts, such as rippling or platforming; (3) baseline fitting and subtraction –in the case of line observations; and (4) conversion to T_{mb} scale. The resulting spectra are the final data products, that can be averaged together to improve rms or combined to produce position-position-velocity cubes.

The procedure to reduce interferometric data is different and requires the use of other tools. The software package `CASA`[4] (Common Astronomy Software Applications) was employed to reduce data from ALMA and ATCA. Following the procedures thoroughly described in Section 2.1.4, the raw visibilities were flagged, calibrated and imaged to produce continuum maps and spectral cubes ready for analysis.

2.3.2 Data exploration and analysis

The final data products were inspected and analysed to extract physical information about the observed sources. The utilities from the `GILDAS` package were used for visual data exploration and measurement of observational parameters. In particular, we employed `CLASS` for line identification and component fitting, and also for generating

[3] https://www.iram.fr/IRAMFR/GILDAS/
[4] https://casa.nrao.edu/

data cubes from on-the-fly map spectra. Likewise, we used `GREG` for visual analytic tasks on the data cubes, including the computation of higher-level data products (moment maps and position-velocity diagrams) and the measurement of integrated fluxes over specific regions. The resulting values were later fed to the analytical methods presented in Sections 2.2.1 and 2.2.2 to derive first estimates of physical magnitudes, generally under ideal conditions (i.e., LTE).

Apart from the `GILDAS` package, a number of custom scripts written in Python (versions 3.6 and 3.8) were created to address specific needs of the analysis pipeline, such as convolving different maps to a common beam or computing line ratios. These scrips make extensive use of the `astropy`[5] library and the `SpectralCube`[6] package.

2.3.3 Data modelling

Finally, more reliable physical parameters under non-LTE conditions were estimated by means of radiative transfer modelling of the observed molecular emission lines. This requires the generation of a grid of models defined over a certain $n-$dimensional parameter space (depending on the specific needs of each science case), and the application of a reduced χ^2 minimization technique, so that the best-fitting model is determined through the metric:

$$\chi^2 = \left(\frac{X_{mod} - X_{obs}}{\Delta X_{obs}} \right)^2 \tag{2.78}$$

where X_{mod} represents the modelled magnitude, and X_{obs} and ΔX_{obs} are the observed value and its uncertainty, respectively.

The state-of-the-art radiative transfer codes `RADEX` and `LIME` were used to build the models.

RADEX

`RADEX` is a one-dimensional, non-LTE, excitation and radiative transfer code, originally written by J.H. Black and then rewritten and improved by F. van der Tak (van der Tak et al. 2010). `RADEX` uses the escape probability formalism to solve the radiative transfer problem, making a series of assumptions to simplify the calculation. For a given molecule and a set of physical parameters, namely the H_2 volume density $n(H_2)$, the molecular column density $N(X)$ and the kinetic temperature of the gas T_k, `RADEX` predicts the excitation temperature, the intensity and the optical depth of the corresponding rotational transitions. In this PhD thesis, `RADEX` is mainly used to obtain first-order estimates of the excitation conditions of the molecular gas in the surroundings of the observed LBV stars. To do so, we first compute large grids of models in the $\{n(H_2), N(X), T_k\}$ space, and then we look for the best-fitting model, i.e. the combination of physical parameters that better reproduces the observed line intensities and/or line ratios. The Python wrapper `ndradex` [7] provides built-in routines to perform these tasks.

[5] https://www.astropy.org/
[6] https://github.com/radio-astro-tools/spectral-cube
[7] https://pypi.org/project/ndradex/

However, RADEX has some limitations worth to be mentioned. First, it assumes a homogeneous, isothermal medium, with no large-scale velocity fields. This means that the code is entirely agnostic to source geometry and velocity gradients. As a consequence, the outputs of the code are line intensities, not fluxes, and thereby require a careful treatment: if the source under analysis is unresolved, RADEX intensities must be corrected by the corresponding beam-filling factor. Second, the radiative transfer is solved considering rectangular line shapes, which can be problematic in the optically thick regime, as RADEX does not account for changes in optical depth across the line profile.

RADEX source code can be downloaded from the website of Leiden University[8]. A simplified version of the program is also offered as an online tool[9], useful for quick calculations. The software makes use of the molecular data files available in the Leiden Atomic and Molecular Database (LAMBDA database, Schöier et al. 2005).

LIME

LIME, which stands for LIne Modelling Engine, is a non-LTE, 3D radiative transfer code that predicts line and continuum emission from 3D source models at millimetre and far-infrared wavelengths. The code, based on RATRAN, was created by C. Brinch (Brinch & Hogerheijde, 2010) and it is currently maintained by multiple developers. The source code of LIME is available in the corresponding GitHub repository[10].

In order to predict the rotational spectrum of a given molecule and transition, LIME randomly samples the input 3D model, generating a Delaunay-Voronoi lattice in which photon transport takes place. The principal advantage of LIME over other radiative transfer codes is that it does not impose any kind of predefined geometry. LIME works with user-provided model files, allowing for the representation of any kind of astrophysical source. Typically, a model file consists of a number of parameters to establish general properties of the model domain (e.g., physical size and resolution, grid density, target molecules...) and several source-specific model subroutines, describing:

- the density profile of the collision partners (e.g., H_2);
- the molecular abundance with respect to H_2;
- the temperature profile of the gas, and, optionally, the dust;
- the systematic velocity field of the gas;
- the turbulent motions of the gas, i.e. random dispersion from the velocity field;
- the magnetic field of the source;
- the gas-to-dust ratio;

[8] https://home.strw.leidenuniv.nl/~moldata/radex.html
[9] http://var.sron.nl/radex/radex.php
[10] https://github.com/lime-rt/lime

Most of these subroutines can be expressed as a function of (x, y, z), virtually enabling the representation of any arbitrary geometry. In this PhD thesis, we use `LIME` as a complement of `RADEX`, in particular, to evaluate how the source geometry and velocity fields affect the observed line profiles, allowing us to constrain gas kinematics in detail.

2.4 Final remarks on the methodology of this thesis

At the moment of starting this PhD thesis, only two LBV stars with unambiguously associated molecular structures were known, namely η Car and G79.29+0.46. There were also a handful of tentative detections, for which the relation between the star and the surrounding gas was not clear (e.g., AG Car or G26.47+0.02). Such a scarcity of positive detections highlights the inherent difficulties of this kind of research.

To successfully detect molecular gas in the outskirts of LBV stars, we need first to know what we are looking for. When speaking of structures *associated with* the stars, we expect one of these three scenarios:

- the remnants of the parent molecular clouds. In most cases, these clouds are partially –or even largely– destroyed by the strong FUV radiation of the star, and eroded by the continuous action of the stellar winds.
- interstellar gas, slowly swept-up and compressed by the steady stellar winds, possibly tracing the edges of a wind-blown bubble.
- molecular gas formed *in situ*, arising from stellar ejecta expelled in one or more mass-loss events, as in the case of η Car.

Despite their remarkable differences, discriminating these possible scenarios is a complex task, that becomes even more challenging owing to the fact that most LBVs reside near the Galactic Plane. At low Galactic latitudes, the unavoidable contamination by ambient clouds along the line of sight complicates the identification of abundant species like CO. However, we can establish a few loose criteria that may be helpful to disentangle the origin of the gas, namely:

- Morphological criteria. We generally look for structures that display a certain degree of symmetry with respect to the star, i.e. bipolar outflows, shells or ring-shaped structures.
- Kinematic criteria. We expect any gas affected by an evolved massive star, either ejected by the star itself or pushed away by the stellar wind, to move predominantly outwards. Similarly, any structure should in principle have a velocity distribution rather symmetric with respect to the systemic velocity of the star. We note, though, that in many cases the systemic velocity of these stars is poorly constrained due to their remarkable variability and atmospheric macroturbulence, which hamper the extraction of reliable kinematic information from optical or infrared spectroscopic measurements.

- Physical criteria. In principle, any gas in the outskirts of an evolved massive star should have physical conditions different from those of the quiescent ISM, in terms of density, temperature or optical depth. Besides, estimates of the total mass could be helpful, given that we expect different orders of magnitude depending on the origin (e.g., a few solar masses at most in the case of ejecta).

- Chemical criteria. For molecular gas formed in situ from ejecta, the abundances should reflect the chemistry of the stellar interior, therefore being compatible with CNO-processed matter, e.g., a $[^{12}C/^{13}C]$ isotopic ratio well below standard cosmic values. Besides, the detection of specific chemical tracers enables the identification of interaction regions such as shockfronts and PDRs.

Nonetheless, we underline that these are not strict rules, but rather a naive starting point to provide a meaningful interpretation for any detected structures. In consequence, by no means should any of these criteria be regarded as a necessary condition. Unlike the molecular envelopes around intermediate-mass stars, whose formation processes and physical and chemical properties are –to a certain extent– well characterized (e.g., Ziurys 2006), the search for molecular gas around evolved massive stars offers few certainties. It is almost impossible to know what to expect *a priori*, since the morphology, kinematics and chemistry of the gas are strongly influenced by the continuous evolution of the star –which is a constant source of radiative and kinetic energy– and its poorly constrained mass-loss history.

CHAPTER 3
THE CIRCUMSTELLAR ENVIRONMENT OF MN101

This chapter describes our findings concerning the LBV candidate MN101. We present molecular spectroscopy and millimetre continuum observations obtained with the IRAM 30m telescope, reporting for the first time a molecular structure associated with this source and identifying hints of non-thermal emission arising from the star and the infrared nebula. The content of this chapter has been adapted and extended from Paper I and Paper II.

3.1 Source details

MGE G042.0787+00.5084 (=IRAS 19040+0817; =[GFK2010] MN101; hereafter MN101 for the sake of brevity) is a bubble-like object first detected by visual inspection in the MIPSGAL legacy survey of the Galactic Plane (Carey et al., 2009), as part of an effort to unveil previously unnoticed evolved massive stars (Mizuno et al., 2010; Wachter et al., 2010). The bubble, visible only at 24 μm, has an approximate diameter of $\sim$24 arcsec, and enshrouds a central point-like source which is also detectable down to 2MASS wavelengths (=2MASS J19062457+0822015).

Wachter et al. (2011) obtained near-IR mid-resolution spectra of the central object and postulated it as a B[e]/LBV candidate, a claim which was later confirmed by Flagey et al. (2014). The infrared spectrum of MN101 exhibits strong hydrogen emission, including the Pfund and Brackett series, along with multiple metal lines characteristic of LBV spectra, such as FeII, MgII and NaII. Contrarily, the spectrum shows very weak HeII emission lines.

Ingallinera et al. (2014, 2016) studied the radio continuum emission associated with MN101 using the Very Large Array. At 5 GHz, the emission is remarkably coupled to the infrared, with a central point-like source surrounded by a clumpy nebula. The brightness profile of the nebular emission reveals an apparent limb brightening at about 11 arcsec from the star, which suggests a shell-like nature. The spectral index presents a remarkable radial variation, as shown in Figure 3.1: in the central object, it has a value of 0.70 ± 0.03, entirely consistent with the steady stellar wind of a LBV star. Conversely, it is mostly negative in the nebula, with values between -0.25 and -1.1, possibly due to the superposition of multiple emission mechanisms, such

as a thermal wind and a non-thermal emission component, as found in other evolved stars).

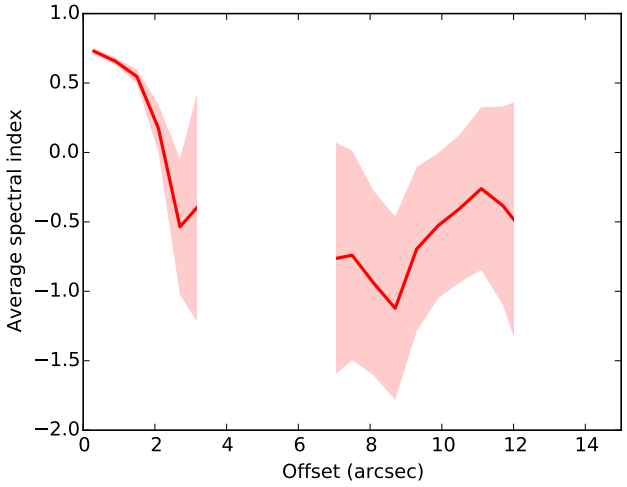

FIGURE 3.1: Radial profile of the spectral index of MN101, with its associated error, shaded (Credits: Ingallinera et al. 2016).

The presence of a roundish shell, probably tracing a recent mass eruption, together with a steady stellar wind acting upon the ejected material, makes of MN101 a fascinating opportunity to learn about the interaction between evolved massive stars and their surroundings, and thereby worth to be explored at mm and sub-mm wavelengths.

3.2 Observations

MN101 was observed in two consecutive campaigns at the IRAM 30m telescope in Pico Veleta (Granada, Spain). Spectroscopic observations of molecular gas were gathered as part of the project P043-17 (PI: C. Bordiu), aimed at probing the molecular environment of a sample of LBV stars visible from the Northern Hemisphere. Observations took place in July 2017, under good summer conditions (opacity ~ 0.25 at 225 GHz, corresponding to 4.2 mm of precipitable water vapour), with a total observing time of 3 hours. Two setups were used, targeting CO and its isotopologues ^{13}CO and C^{18}O in their $J = 1 \rightarrow 0$ and $J = 2 \rightarrow 1$ rotational transitions. The selected backend was the FTS spectrometer, providing an instantaneous bandwidth of 4 GHz per polarization and a velocity resolution of 0.26 and 0.52 km s^{-1} at 1 and 3 mm respectively. The source was observed in On-the-fly (OTF) mapping mode, obtaining $1.5' \times 1.5'$ maps around the star, using a position-switching strategy with a common reference for all sub scans. The final resolution of the maps corresponded to the telescope HPBW, which is ~ 11 and ~ 23 arcsec at 1 and 3 mm respectively.

Continuum observations were performed during the first open pool session of the NIKA2 instrument in October 2017. The source was observed during a survey of mm-continuum emission from a sample of five LBV stars, corresponding to project P044-17 (PI: J. R. Rizzo). Observations were carried out in daytime under excellent and stable weather conditions, with an average $\tau \sim 0.2$ measured at 225 GHz. The source was mapped using the OTF technique, adopting several independent scan

directions. A total of 60 scans were performed, which were later combined to minimize stripping effects. The total integration time was 2 hours. For individual scans, atmospheric opacity corrections were applied following the NIKA2 skydip standard procedure (Adam et al., 2018).

Data reduction and imaging were made using dedicated software: the `GILDAS` package for the spectroscopic data (Guilloteau & Lucas, 2000), and the NIKA2 standard IDL pipeline –developed by the NIKA2 collaboration– plus additional custom scripts for continuum background subtraction and noise map estimates.

3.3 Summary of results

After a thorough search in the molecular data cubes, we found significant emission of ^{12}CO and ^{13}CO in the field of MN101, arising from multiple velocity components in the range $(+10, +80)$ km s^{-1}. C^{18}O, on the contrary, was only detected as a single component at $\sim$ 26 km s^{-1} toward the SE. Field-averaged spectra of the observed transitions are shown in Figure 3.2.

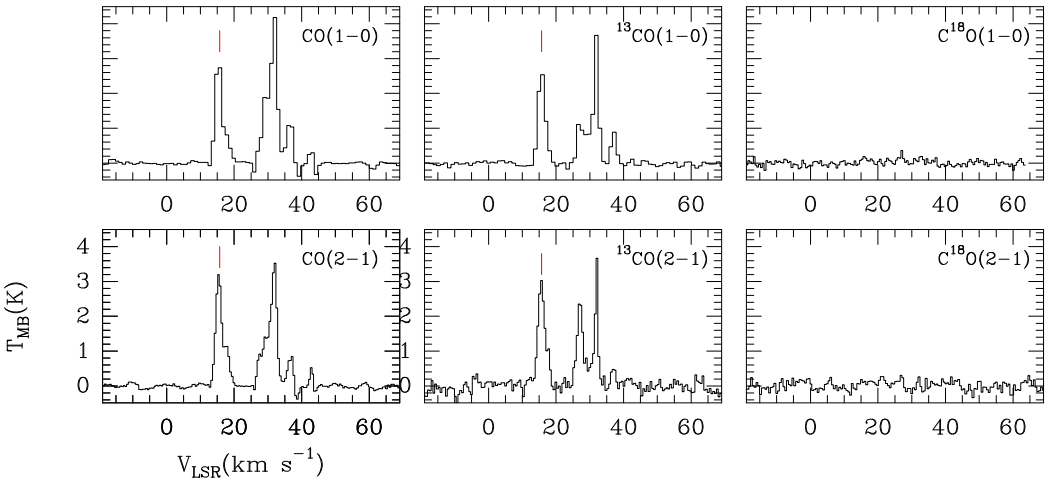

FIGURE 3.2: Field-averaged spectra of the observed transitions toward MN101. ^{13}CO and C^{18}O spectra have been scaled by a factor of 6 for easier comparison. The red marker indicates the velocity component at 15.4 km s^{-1}, associated with the LBV star.

We note that most of the observed velocity components present a widespread spatial distribution, showing no evident relation with the source and probably arising from contaminating clouds in the line of sight. However, a narrow component, extending in the velocity range $(+13, +19)$ km s^{-1}, with a central velocity of 15.4 km s^{-1} exhibits a remarkably symmetric pattern with respect to the star. As seen in the channel maps (Figs. 2 to 6 in Paper I), this component traces a series of arc-like features that surround the star from SW to NE as velocity increases. The integrated intensity map over this velocity range, as shown in Figure 3.3, reveals an elliptical closed structure that completely wraps the infrared bubble. We derive an angular size of 35 $\times$ 21 arcsec (P.A: 150°). The emission in this range is clumpy and mostly unresolved, probably tracing thin layers of gas smaller than the telescope beam. We identify at least four different regions: the main elliptical ring, the inner "cavity" that

roughly matches the infrared bubble, a partially detached clump toward the NW, and a contaminating cloud toward the SE.

Interestingly, the SE cloud seems to be chemically different from the main structure, as suggested by the detection of $C^{18}O$ exclusively towards this region (see Figure 3.4, and also Figure 7 in Paper I). This implies that chemical abundances and excitation conditions in the ring differ from those in the cloud. Careful inspection of individual spectra toward the elliptical ring also reveals a remarkable stratification near the eastern edge, where the emission splits into two separate components at 15.4 km s^{-1} and 17.8 km s^{-1}. This stratification, only visible in the ^{12}CO lines, could a signpost of a low-velocity shock ($\Delta v \sim 2$ km s^{-1}) or an interaction with an ambient component, possibly a fragment of the parent molecular cloud.

The NIKA2 continuum maps provided a complementary view of MN101 and its surroundings. The large instantaneous field of view of the instrument, of about 6.5 arcmin in diameter, allowed us to map a broader region around the source, exceeding the coverage of the molecular line observations. Figure 3.5 shows the maps at 150 and 260 GHz.

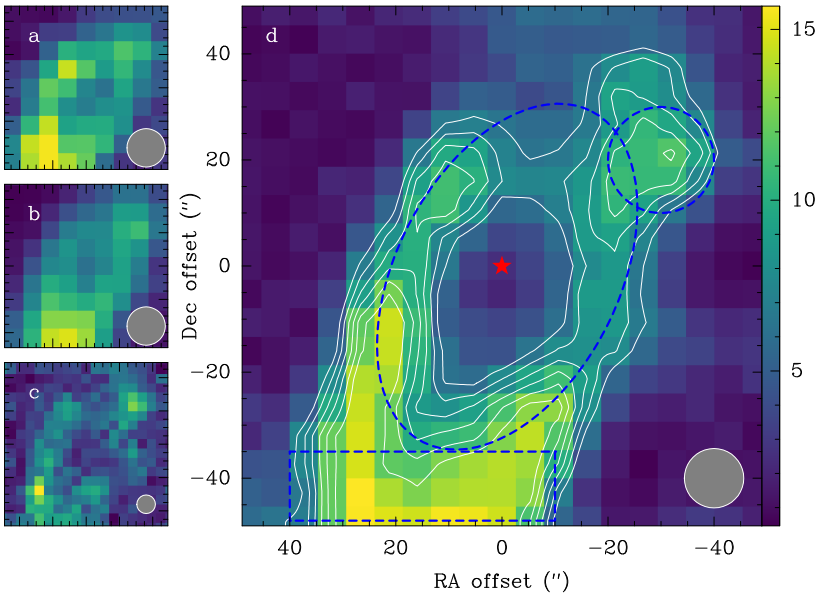

FIGURE 3.3: Velocity-integrated map of the observed transitions towards MN101 in the range (+13.4, +17.4) km s^{-1}. (a) ^{13}CO $J = 1 \rightarrow 0$ (b) ^{12}CO $J = 1 \rightarrow 0$ (c) ^{13}CO $J = 2 \rightarrow 1$ and (d) ^{12}CO $J = 2 \rightarrow 1$. In the latter, the dashed box indicates the contaminating SE cloud; the dashed circle indicates the NW clump, and the ellipse indicates the main ring-like structure. Contours starting at 6.5 K km s^{-1}, in steps of 1.2 K km s^{-1}. The position of the star is indicated by the red marker. The grey filled circle represents the IRAM 30m beam size.

Continuum emission from the star position is detected at both frequencies. The emission at 1 mm is rather extended, whereas at 2 mm is purely point-like, coincident with the beam size. The continuum counterpart of the CO cloud toward the SE, ~ 30 arcsec from the star, is also detected. Surprisingly, while the star is more intense at 2 mm, the cloud shows the opposite behaviour, being brighter at 1 mm, which indicates

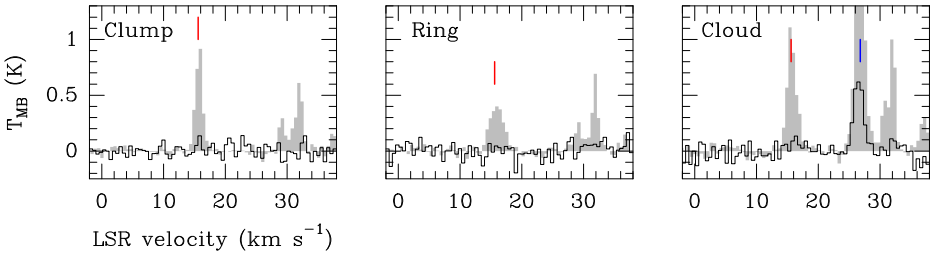

FIGURE 3.4: Spectra of $C^{18}O$ $J = 1 \rightarrow 0$ (black) and ^{13}CO $J = 1 \rightarrow 0$ (filled), averaged in the positions highlighted in Figure 3.3, panel d, namely the NW clump, the ring and the SE cloud. The vertical red line indicates the central velocity of the ring structure, and the blue one the central velocity of the prominent $C^{18}O$ emission.

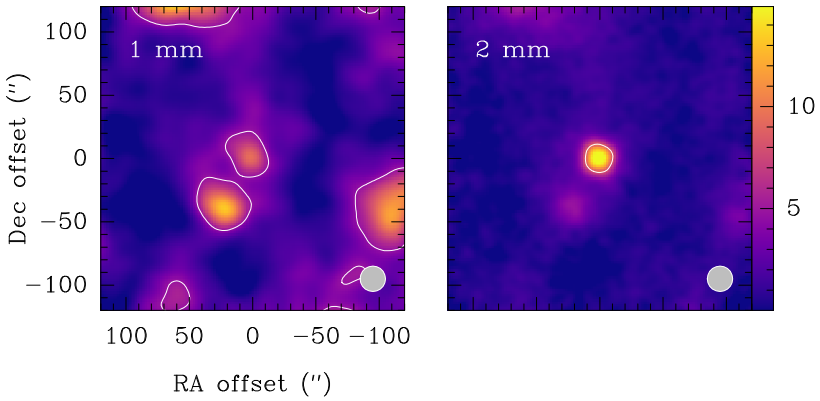

FIGURE 3.5: NIKA2 continuum maps at 1 and 2 mm of the field around MN101. The two maps have been convolved to a common angular resolution of 20 arcsec for easier comparison and have the same colour scale in mJy beam^{-1}. White contours depict the half-power level of the point source ($\sim$ 4.7 and 8.4 mJy beam^{-1}, respectively). The grey filled circle in the bottom right corner of each panel represents the approximate beam size. At 2 mm, the emission from the point-source matches the beam size, whereas at 1 mm there is a contribution from a more extended component.

the prevalence of a different emission mechanism. The two structures are immersed in a low-level plateau, more evident at 1 mm.

3.4 Analysis and interpretation

To disclose the nature of detected molecular structure and its association with MN101, we performed an in-depth analysis of its morphology, kinematics and excitation conditions, which involved several steps.

First, we conducted a detailed analysis of the observed kinematic features. Using position-velocity diagrams and the first-order moment maps of the lines (see Figs. 8 and 9 in Paper I), we analysed the motions of the gas in detail. We identified a clear velocity gradient from NE –where the gas is receding– to SW –where the

gas is approaching–, consistent with a dominant radial motion. According to such velocity gradient, we concluded that the observed emission can be explained by an expanding torus seen with a certain inclination angle –of about $53 \pm 6°$ if we consider the emission peaks–. Note, though, that this result assumes isotropic expansion into a homogeneous medium, which is an ideal situation. We also estimated the expansion velocity from the velocity difference measured in the position-velocity diagrams. After correcting for inclination, we obtain a remarkably low value of $v_{\rm exp} = 1.2 - 1.4$ km s^{-1}.

Subsequently, we analysed the excitation conditions of the gas in a LTE (local thermodynamic equilibrium) regime. Following the optically thin limit approximation described in Chapter 2, we analytically derived the average excitation temperature and column density of ^{12}CO and ^{13}CO in two regions: the main ring and the northwestern clump. We obtained excitation temperatures between 9 and 12 K, corresponding to column densities of 10^{15} cm^{-2} for ^{13}CO and 6×10^{15} cm^{-2} for ^{12}CO. To address a more realistic scenario and take into account non-LTE effects, we ran simulations with the non-LTE excitation and radiative transfer code `RADEX` over a grid of models parameterised by kinetic temperature, volume density and column density. We obtained the best fit for the measured line ratios, finding N(^{13}CO) $= 1.0 - 1.3 \times 10^{15}$ cm^{-2}, which agree within 20% with the LTE approximation. We also found a N(^{12}CO) between 5–7 times higher than N(^{13}CO), indicating a very low [^{12}C/^{13}C] isotopic ratio. The resulting volume densities are low, of a few 10^3 cm^{-3} and a factor of ~ 2 higher in the northwestern clump, thus consistent with the non-detection of high-density tracers. However, these are average values over the whole structures, so locally we could find substantially higher densities, arising from more compact clumps. Low densities somewhat limit the range of possible temperatures, with physically meaningful solutions up to 70 K in the torus and 100 K in the clump. Emission is found to be optically thin, with $\tau < 1$ in all cases.

Finally, we modelled gas kinematics using the pseudo-Monte Carlo 3D radiative transfer code `LIME` (Brinch & Hogerheijde, 2010), described in Section 2.3. We built a simple synthetic model of the structure to evaluate the impact of different velocity fields on the observed CO emission. Details on the modelling are provided in Annex II of Paper I. After exploring a range of possible ring inclinations and expansion velocities, we successfully reproduced the observed intensities and line widths with a torus expanding at $v_{\rm exp} = 3$ km s^{-1} and with an inclination of $i = 15°$. These values suggest that we initially overestimated the inclination of the structure due to the presence of the NE clump and the SE cloud.

3.4.1 On the origin of the structure

Considering the previous results, we conclude that the observed structure is a low-density, relatively warm and nearly face-on torus slowly expanding into the surrounding ISM. Such structure may have originated from a non-isotropic mass-loss process. Alternatively, it may be the relic of the parent molecular cloud, compressed by the steady action of a non-spherical wind. The mass and chemical composition of the structure could shed light on its origin, but unfortunately the distance to MN101 is unknown, hampering a reliable discrimination between the two scenarios.

To overcome this problem, first we derived two possible kinematic distances, namely 1.2 and 11.4 kpc, taking the central velocity of the CO line (15.4 km s^{-1}) as the systemic velocity of the star. Details on how we obtained these distances are provided in Annex 1 of Paper I. Qualitative arguments favour a near distance: the source is remarkably bright at near-IR wavelengths (Flagey et al., 2014), and the symmetry of the nebula is consistent with a rather young structure –hence closer–. Following the Bayesian approach described by Bailer-Jones et al. (2018), we inferred a geometric distance of 3.8 kpc from the Gaia DR2 parallax –which was affected by a significant uncertainty–. We thus adopted a compromise distance of $d = 2.5$ kpc.

The [^{12}CO/H_2] relative abundance is also a key factor in translating column densities into masses. We measured a low [^{12}CO/^{13}CO] ratio of 5–7. This could imply either a ^{12}CO depletion or a ^{13}CO enhancement. Since MN101 is an evolved massive star and the CNO cycle favours the formation of ^{13}C as a residual by-product (Berdyugina & Savanov, 1994)–, we conclude that the gas surrounding MN101 is of stellar origin, i.e., ejecta. This is further supported by the detection of C^{18}O in the SE cloud but not in the structure, as shown in Figure 3.4. Assuming a standard [CO/C^{18}O] ratio of $\sim$ 50 (e.g., Davis 2014), we would expect C^{18}O intensities in the ring comparable to the rms noise ($\sim$ 50 mK). Since in the SE cloud we have a similar rms and the intensity of the other isotopologues is comparable, the non-detection of C^{18}O toward the ring could imply an excess of ^{13}CO –especially since the [^{13}CO/C^{18}O] on the cloud, of $\sim$5.5, is close to the canonical value–, or a selective photodissociation of C^{18}O due to the strong UV field of the star. However, the latter should be a local effect rather than a global one, only observed towards the innermost and densest parts of the structure (Shimajiri et al., 2014).

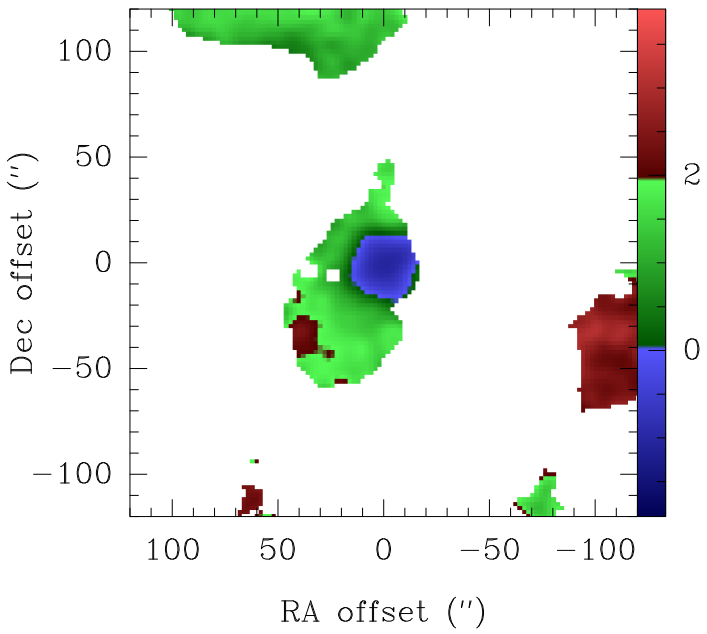

FIGURE 3.6: Spectral index map of and around MN101.

Adopting a standard [^{12}CO/H_2] = 10^{-4}, the total mass of molecular gas is 0.6$\pm$0.1 $M_\odot$ (0.5 $\pm$ 0.1 $M_\odot$ in the torus and 0.1 $M_\odot$ in the clump). For an inner radius of 15 arcsec on average ($\sim$ 0.18 pc at 2.5 kpc) and v_{exp} = 3 km s^{-1}, we obtain $t_{dyn} < 6 \times 10^4$ years and an average mass-loss rate of $\dot{M} = 0.8 - 1.2 \times 10^{-5}$ $M_\odot$ yr^{-1}. We find that,

if distances much larger than 2.5 kpc are considered, MN101 would rival η Car in luminosity, and would need to be a very efficient molecular factory to account for nebular masses of tens of $M_\odot$ (e.g., ~ 10 $M_\odot$ of molecular gas at d=10 kpc).

3.4.2 Continuum emission mechanisms

The exceptional sensitivity of the novel NIKA2 instrument allowed us to produce a spectral index map of the whole field of MN101, as displayed in Figure 3.6. We adopted the standard convention $S_\nu \propto \nu^\alpha$ for the spectral index, introduced in Section 2.2.2, and masked out those pixels with flux densities below 2σ. We identify multiple emission mechanisms at work, noting that the stellar source and the infrared bubble are detached from its environment, displaying mostly negative α values, in the range from –0.6 to 0, as expected for a stellar thermal wind superimposed to non-thermal processes.

Such a superposition is in excellent agreement with the spectral indices reported by Ingallinera et al. (2016) for the star (0.7) and the nebula (varying radially from -1.1 to -0.25), using higher-resolution VLA observations (see Figure 3.1. Indeed, NIKA2 resolution of 10-20 arcsec is not sufficient to separate the stellar contribution from the infrared nebula, but we can resort to the point-source flux density measured by Ingallinera et al. (2014), of 7.0 ± 0.2 mJy at 5 GHz, to estimate the current-day mass-loss rate following the prescription by Panagia & Felli (1975). From this method we obtain $(7.5\pm0.5)\times10^{-6}$ $M_\odot$ yr^{-1}, assuming a terminal wind velocity of $v_\infty = 100$ km s^{-1} and a plasma temperature of 10000 K, which are reasonable values for a typical LBV wind. The plateau that encloses the infrared bubble and the southern cloud shows an average α of 0.2, consistent with free-free emission found in dark clouds.

3.5 Concluding remarks

In Paper I, we identify a CO ring-like structure that encloses the infrared bubble of MN101, displaying morpho-kinematic features consistent with a slowly expanding torus. The average physical parameters of the gas, as estimated by means of LTE and non-LTE modelling of the observed transitions, are consistent with moderately dense ($n_{\rm H_2} \sim 10^3$ cm^{-3}) and relatively warm gas ($T_{\rm k} \sim 10 - 70$ K), which becomes slightly denser and warmer towards the NW clump. The [^{12}CO/^{13}CO] ratio measured in the structure lies in the range 5–7, well below typical ISM values. C^{18}O is not detected anywhere except in the contaminating cloud toward the SE, indicating a chemical differentiation. We propose a ^{13}CO overproduction due to the CNO cycle to explain the isotopic ratio observed in the ring. This implies that the structure is most likely composed by stellar ejecta from a past mass-loss episode. Adopting a distance of 2.5 kpc, we derive a total mass of molecular gas of 0.6 ± 0.1 $M_\odot$, corresponding to an average $\dot{M}$ of about 10^{-5} $M_\odot$ yr^{-1} for a steady ejection occurred 6×10^4 years ago. Such a $\dot{M}$ value is compatible with the LBV phase and only slightly higher than the current day mass-loss rate as estimated from literature radio continuum flux measurements. Using complementary continuum observations at 1 and 2 mm, in Paper II we disclose several emission mechanisms at work in the surroundings of MN101, including hints of non-thermal processes in the vicinity of the star, in agreement with previous literature results.

3.6 Bordiu et al., 2019 (Paper I)

Monthly Notices of the ROYAL ASTRONOMICAL SOCIETY

MNRAS **482,** 1651–1663 (2019) doi:10.1093/mnras/sty2726
Advance Access publication 2018 October 8

A slowly expanding torus associated with the candidate LBV MGE 042.0787+00.5084

Cristobal Bordiu,[1]★ J. Ricardo Rizzo[1]★ and Alessia Ritacco[2]
[1]*Centro de Astrobiología (INTA-CSIC), Ctra. M-108, km. 4, E-28850 Torrejón de Ardoz, Madrid, Spain*
[2]*Institut de Radioastronomie Millimétrique (IRAM), Av. Divina Pastora 7, Núcleo Central, E-18012 Granada, Spain Granada, Spain*

Accepted 2018 September 24. Received 2018 September 18; in original form 2018 August 5

ABSTRACT

The luminous blue variable (LBV) phase is a poorly understood stage in the evolution of high-mass stars, characterized by its brevity and instability. The surroundings of LBV stars are excellent test beds to study their dense stellar winds and eruptive mass-loss events. Aiming to improve our knowledge of the LBV phase, we observed the $J = 1 \rightarrow 0$ and $J = 2 \rightarrow 1$ lines of CO and ^{13}CO in a field of 1.5 × 1.5 arcmin around the recently identified candidate LBV MGE 042.0787+00.5084, using the Institut de Radioastronomie Millimétrique 30-m radio telescope. We report the first detection of molecular emission associated with this source, tracing a structure with an evident circumstellar distribution. The morphology and kinematics of the gas can be explained by an expanding torus, a structure that may have originated from stellar ejecta, or the action of stellar winds on to the parent molecular cloud. We derive the physical properties of the gas by means of local thermodynamic equilibrium (LTE) and non-LTE line modelling, obtaining densities of H_2 of the order of 10^3 cm^{-3} and kinetic temperatures below 100 K. In addition, we build a kinematic model to reproduce the structure and velocity field of the gas, which are in good agreement with the observations. We estimate a total molecular gas mass of 0.6 ± 0.1 M$_\odot$ and a dynamical age of 6×10^4 yr, leading to an average mass-loss rate of $0.8–1.2 \times 10^{-5}$ M$_\odot$ yr^{-1}.

Key words: stars: evolution – stars: massive – stars: mass-loss – ISM: clouds – ISM: kinematics and dynamics – ISM: molecules.

1 INTRODUCTION

High-mass stars strongly disturb the composition and structure of the interstellar medium (ISM) by delivering large amounts of thermal and mechanical energy into their surroundings.

Before exploding as core-collapse supernovae, high-mass stars evolve through a series of short-lived and violent phases (Langer et al. 1994). Among these transitional stages, the so-called luminous blue variable (LBV) phase is possibly the most puzzling due to its intrinsic instability. LBV stars are luminous and hot supergiants characterized by dense winds that sustain high mass-loss rates – sometimes reaching 10^{-3} M$_\odot$ yr^{-1}(van Boekel et al. 2003). This steady mass loss is occasionally accompanied by violent outbursts that eject the outer stellar layers into the ISM, like the eruptions of η Car in the 19th century (Davidson 1989). Consequently, most LBV stars are surrounded by expanding structures of dust and gas. These circumstellar structures typically have very different shapes, from simple spherical shells to more complex axisymmetric arrangements, including bipolar nebulae and rings (Marston & McCollum 2006). With characteristic times of 10^4 yr (Humphreys & Davidson 1994), the Galactic population of LBV stars is extremely scarce, with less than 20 confirmed members (Clark, Larionov & Arkharov 2005) and a few candidates that still require confirmation (Stringfellow et al. 2012). Circumstellar envelopes are also indirect probes of the existence of these sources, because they may contain information about past mass-loss events. (Mizuno et al. 2010; Gvaramadze et al. 2012).

LBV stars have been widely studied at optical and infrared wavelengths, with most of the research focusing on the determination of stellar parameters (temperatures, luminosities, metallicities, and variabilities) and, to a lesser extent, on the properties of the associated nebulae (neutral and ionized gas and warm dust; Umana et al. 2011; Ingallinera et al. 2014). However, most of the underlying physical processes during the LBV phase are far from being totally understood. Little is known about the mechanisms that drive its variability and violent outbursts, and its actual role in the late evolution of high-mass stars is unclear, with recent observations suggesting that LBV stars may be (under certain conditions) direct progenitors of Type II supernovae (Groh, Meynet & Ekström 2013). For these reasons, the current picture of the LBV phase is

★ E-mail: cbordiu@cab.inta-csic.es (CB); ricardo.rizzo@cab.inta-csic.es (JRR)

rather incomplete. As many LBVs are surrounded by complex and multiphase envelopes, targeting other components associated with these stars may provide valuable information to tackle some of these questions. In this regard, molecular gas is specially worthy of attention. This component has been historically overlooked, as molecules were thought to be rapidly destroyed by the strong ultraviolet (UV) radiation on the outskirts of LBV stars. Despite this, a series of pioneering studies has resulted in the detection of CO and NH_3 around a few LBVs. These detections prove that significant amounts of molecular gas can form and survive for long time-scales around sources of this type.

The best example is G79.29+0.46, an LBV nebula where Rizzo, Jiménez-Esteban & Ortiz (2008) reported nested shells of warm CO strikingly attached to the infrared nebula and tracing successive mass-loss events. In a further study, Rizzo et al. (2014) found several NH_3 warm clumps clearly associated with the star, proving that the chemistry in the environs of LBV stars is more complex than initially assumed. These results underlined the potential of dynamical studies of the molecular gas associated with LBV stars to achieve a complete vision of this elusive phase.

A particularly interesting but still unexplored case is that of MGE 042.0787+00.5084, a recently identified candidate LBV star. This source exhibits a nearly spherical circumstellar envelope with intense infrared emission, which was initially discovered in the *Spitzer* MIPSGAL 24-μm survey (Mizuno et al. 2010). The central star was later catalogued as a candidate LBV by means of near-infrared spectroscopy, which revealed strong hydrogen emission lines (including Pfund and Brackett series) and several metal lines (Mg II, Na II, Fe II) usually found in other LBV spectra (Flagey et al. 2014). On the other hand, recent 6-cm VLA observations (Ingallinera et al. 2016) unveiled a clumpy radio nebula strongly coupled to the infrared shell, with hints of a differentiated spectral index, as in other well-known LBV sources such as HR Car (Buemi et al. 2017).

In this paper we report the first detection of molecular material around MGE 042.0787+00.5084, using Institut de Radioastronomie Millimétrique (IRAM) 30-m observations of CO and ^{13}CO $J = 1 \rightarrow 0$ and $J = 2 \rightarrow 1$ lines. In Section 2 the observing set-up and procedures are detailed. In Section 3 we present the results of the observations. In Section 4 we estimate the physical parameters of the gas and provide an interpretation of the observed structure based on the derived mass-loss rate, which is compatible with the LBV nature of the object. We summarize our findings in Section 5.

2 OBSERVATIONS

We observed MGE 042.0787+00.5084 with the 30-m radio telescope of IRAM in Granada (Spain). Observations took place on the night of 2017 July 24, under good summer conditions (opacity ∼0.25, corresponding to 4.2 mm of precipitable water vapour at 225 GHz), with a total observing time of 3 h.

The telescope was configured to operate in dual-receiver mode to map the distribution of CO and ^{13}CO at 1.3 and 3 mm simultaneously, while covering other molecules of interest such as C^{18}O and C^{17}O. EMIR receivers E090 and E230 were used with two spectral set-ups: a first set-up addressing CO $J = 1 \rightarrow 0$, CO $J = 2 \rightarrow 1$, and ^{13}CO $J = 1 \rightarrow 0$ and a complementary set-up specifically targeting ^{13}CO $J = 2 \rightarrow 1$. The selected backend was the Fourier transform spectrometer (FTS), providing spectrometer, providing an instantaneous bandwidth of 4 GHz per polarization and a velocity resolution of 0.26 and 0.52 km s^{-1} at 1 and 3 mm, respectively.

On-the-fly mapping in zig-zag mode was used to make 1.5 × 1.5 arcmin maps around the source, using a position-switching strategy with a common reference for all subscans. Two orthogonal mapping directions were used for each set-up, with 21 parallel subscans per direction. The subscan length was set to 90 arcsec with a mapping speed of 3 arcsec s^{-1}, using a Nyquist-compliant spacing of 4.3 arcsec between subscans. The reference was located 10 arcmin away from the source to minimize background/foreground contamination from the Galactic plane. The map resolution corresponded to the half-power beamwidth of the telescope, which is ∼11 and ∼23 arcsec at 1 and 3 mm, respectively. In addition, a deep integration towards the star's position was done to search for other, less abundant molecules.

Table 1. Observational parameters.

Line	Freq. (GHz)	ΔV (km s^{-1})	HPBW[a] (arcsec)	rms (mK)
CO $J = 1 \rightarrow 0$	115.27	0.51	21.3	25
^{13}CO $J = 1 \rightarrow 0$	110.20	0.53	22.3	10
CO $J = 2 \rightarrow 1$	230.54	0.26	10.7	30
^{13}CO $J = 2 \rightarrow 1$	220.40	0.27	11.2	20

Note. [a]Half power beam width.

We used Saturn and the quasar 1749+096 for pointing correction, and G34.3+0.2 for line calibration. Pointing was checked regularly, while calibrations were run every 15 min and between consecutive maps. The pointing accuracy was always better than 5 arcsec.

A summary of the observational parameters for the target lines is provided in Table 1. Individual spectra were baseline-subtracted and combined to produce data cubes for each rotational transition. The data reduction and analysis were carried out with GILDAS, a software package especially tailored to deal with native 30-m data (Guilloteau & Lucas 2000). Hereafter in this work we adopt the following conventions: (1) Data is presented in main-beam temperature ($T_{\rm MB}$) scale unless specified otherwise. Conversion from antenna temperature ($T_{\rm A}^*$) is trivial via the relation $T_{\rm MB} = T_{\rm A}^*/\eta_{\rm eff}$, with

$$\eta_{\rm eff} = \frac{\eta_{\rm MB}}{\eta_{\rm l}} \approx 0.9 \exp - \left(\frac{\nu\,[\rm GHz]}{399.7} \right)^2 , \quad (1)$$

where $\eta_{\rm MB}$ and $\eta_{\rm l}$ denote the antenna main beam and forward efficiencies, respectively, expressed as a function of the frequency for the IRAM 30-m telescope (Sánchez Contreras et al. 2015). (2) Velocities are expressed with respect to the local standard of rest ($V_{\rm LSR}$). (3) Positions are given as offsets relative to the J2000 equatorial coordinates of the source, which are (RA, Dec.) = ($19^{\rm h}06^{\rm m}24\overset{\rm s}{.}57$, $+08^\circ22'01\overset{''}{.}9$). (4) Position angles are measured from north to east.

3 RESULTS

After a thorough search in the whole data cubes we found significant emission of CO and ^{13}CO at different velocities in the range from 10 to 80 km s^{-1}. Fig. 1 displays the spectra of the four transitions spatially averaged over the whole field. C^{18}O was detected only towards the south-east (SE) of the source, and C^{17}O was not detected at any position.

A detailed analysis of the spatial distribution of the emission reveals that, in the four CO and ^{13}CO lines, most of the velocity components are present over a significant part of the observed field, without a clear pattern with respect to the star; these components are presumably not related to the source, being most likely foreground/background contamination arising from molecular clouds

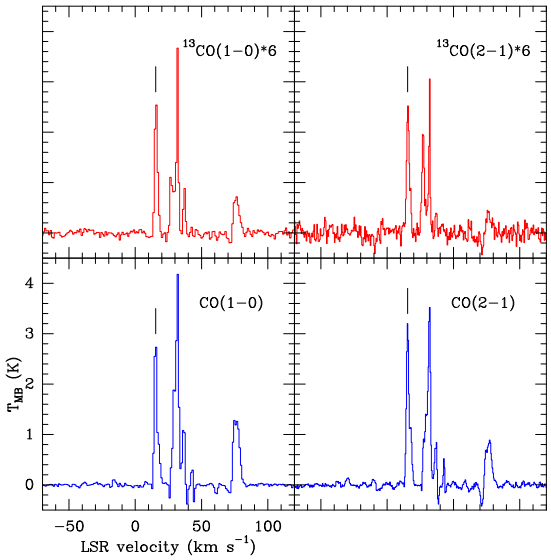

Figure 1. CO and ^{13}CO spatially averaged spectra towards MGE042.0787+00.5084. ^{13}CO spectra are scaled by a factor of 6 for easier comparison. Hanning smoothing has been applied to reduce the noise. The short vertical line on top of each spectra marks the component in the range (+13, +19) km s^{-1}.

in the line of sight. In contrast, the velocity component in the range (+13, +19) km s^{-1}, marked with vertical lines in the spectra, depicts a certain symmetry around the central star, in the form of a rather elongated ring-like structure. This component is represented as channel maps in Figs 2–5, in steps of ∼ 0.5 km s^{-1}. Several arcs more or less centred at the star position are noted; these arcs present different sizes at different velocities, moving from south-west (SW) to north-east (NE) as the velocity increases. At ∼15–15.5 km s^{-1} the emission is closed in elliptical features, especially noted in the CO $J = 2 \rightarrow 1$ line.

Fig. 6 shows the corresponding velocity-integrated intensity maps as contours superimposed on the 24-μm *Spitzer* MIPSGAL image of the infrared nebula (taken from Mizuno et al. 2010). These maps reveal a rather clumpy ring-like structure centred at the star position, displaying a remarkable elongation in the approximate south-east–north-west direction. By fitting an ellipse to the emission peaks, as shown in the figure, we derive an angular size of 35 × 21 arcsec with a position angle of 150°.

The structure is mostly unresolved, so we are not able to determine its actual thickness. Never the less, the 30-m angular resolution is sufficient to observe a certain degree of morphological differentiation, allowing us to identify a number of regions that might deserve further attention:

(i) the main ring-like feature, which completely surrounds the infrared nebula and accounts for most of the emission.
(ii) the inner cavity, a region in which molecular material is likely depleted. The extent of this cavity strikingly matches the infared nebula.
(iii) the partially isolated emission blob towards the north-west (NW; hereafter the north-western clump), projected ∼25 arcsec from the star. This region is particularly prominent in the $J = 2 \rightarrow 1$ images.
(iv) the SE region, from which arises the most intense and widespread emission.

This SE region, where the overall symmetry of the structure is lost, may be seriously contaminated by emission from a molecular cloud at a close V_{LSR}. Fig. 7 compares the spectra of ^{13}CO and C^{18}O $J = 1 \rightarrow 0$ averaged over three different parts of the map: the clump, the stellar position, and the SE region. C^{18}O is detected only in the latter, as a weak and narrow component in the velocity range (+25.6, +27.8) km s^{-1}. The non-detection of C^{18}O in other positions suggests the existence of a chemical differentiation, indicating that this widespread emission may be – at least partially – disaggregated from the main ring-like structure.

As shown in Fig. 8, a closer inspection of spectra in individual positions reveals that this structure is the blending of two different components at V_{LSR} = 15.4 and 17.8 km s^{-1}, depicted in dashed and solid contours, respectively. The component at 15.4 km s^{-1} is relatively ubiquitous and completely surrounds the source in all directions, but the component at 17.8 km s^{-1} is highly localized and only visible in the CO lines. It is prominent towards the east, with a peak temperature comparable to the other component, but almost non-existent in other positions (e.g. SW). Similarly, its motion with respect to the star is unclear. This makes it extremely difficult to confirm whether this component is related to the source in any way: It could be part of an interfering

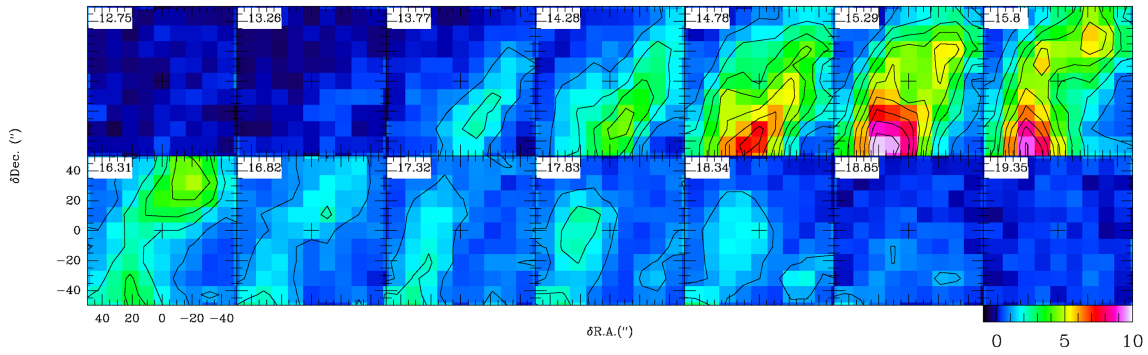

Figure 2. CO $J = 1 \rightarrow 0$ emission towards MGE 042.0787+00.5084 in the velocity range 12.75–19.35 km s^{-1}. The absolute V_{LSR} is shown in the top left corner of each panel. The colour scale represents T_{MB} in K. The contours start at 1 K with a spacing of 1 K. Crosses at (0,0) indicate the position of the star.

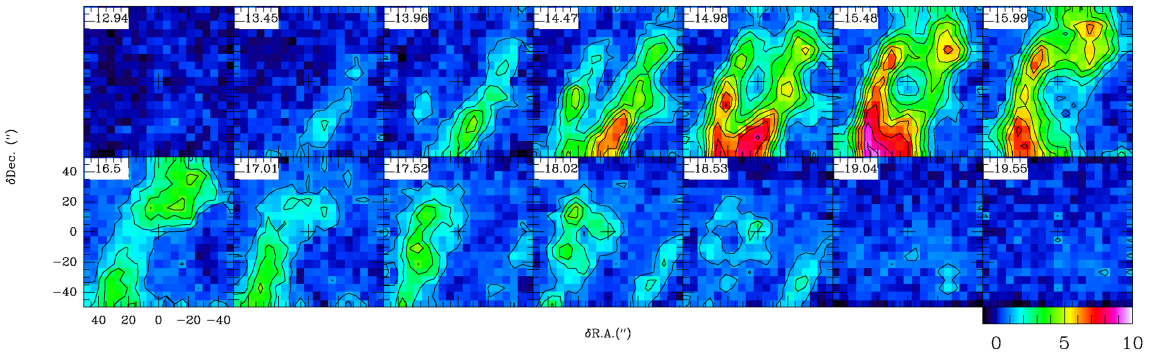

Figure 3. Same as Fig. 2 for CO $J = 2 \rightarrow 1$, with a channel binning of 2 (resolution ~ 0.5 km s^{-1}) for easier comparison. The contours start at 1 K with a spacing of 1 K.

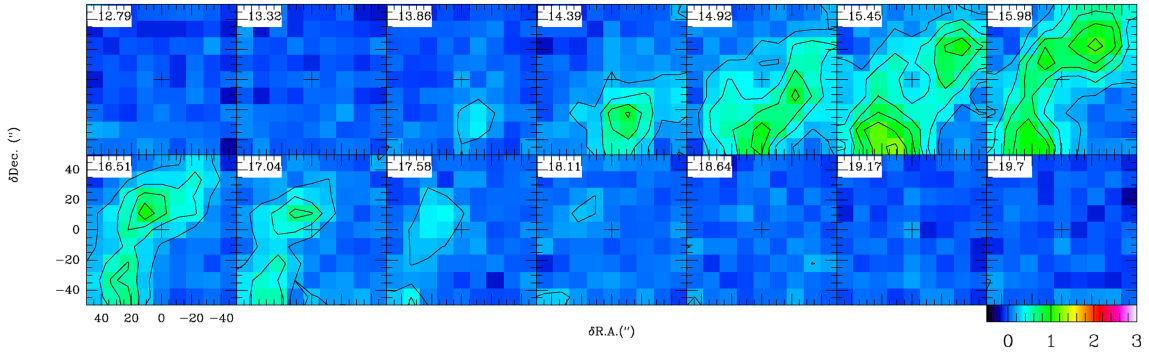

Figure 4. Same as Fig. 2 but for ^{13}CO $J = 1 \rightarrow 0$. The contours start at 100 mK with a spacing of 100 mK.

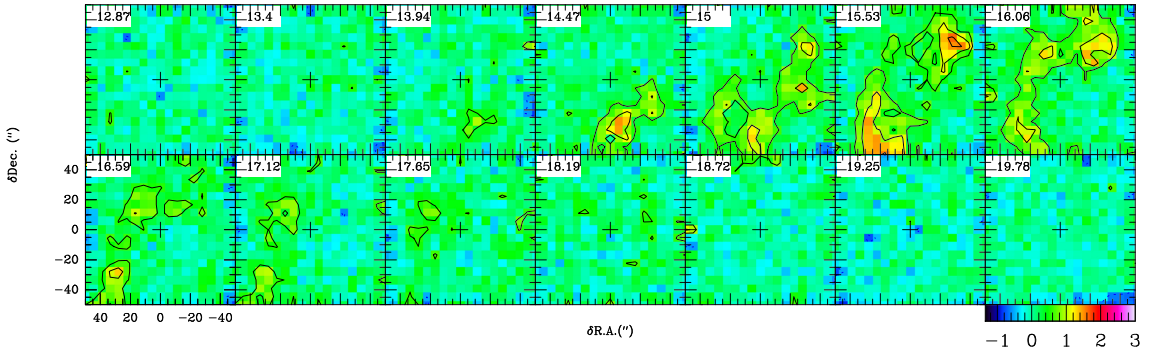

Figure 5. Same as Fig. 2 but for ^{13}CO $J = 2 \rightarrow 1$, with a channel binning of 2 (resolution ~ 0.5 km s^{-1}) for easier comparison. The contours start at 200 mK with a spacing of 200 mK.

cloud or a mere stratification of the main component. Regardless of its nature, the contribution of this component is negligible, as the overall emission is dominated by the component at 15.4 km s^{-1}. For this reason, we limit our analysis to the latter, adopting its central velocity as the systemic velocity of the structure.

For gaining a better understanding of the velocity structure of the CO and ^{13}CO emission, we studied the kinematics of the gas by means of position–velocity (PV) diagrams along the strips indicated with dashed lines in Fig. 6, which were selected according to the axes of the ellipse previously used for the fitting. The first slice goes from SE to NW (P.A. 150°), following the direction of maximum

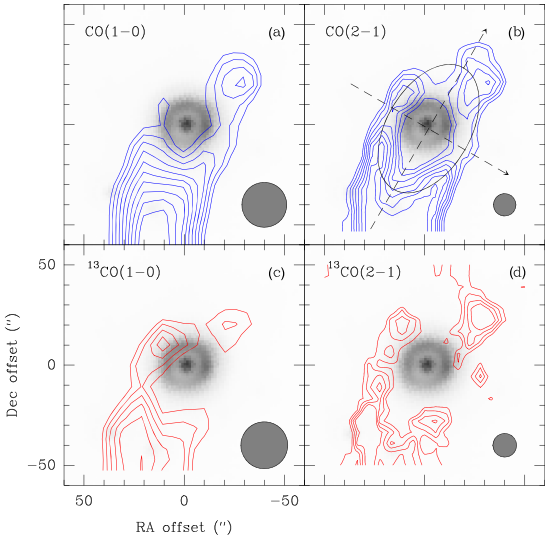

Figure 6. Velocity-integrated maps of CO and ^{13}CO towards MGE042.0787+00.5084 in the range (+13.4, +17.4) km s^{-1}, shown as contours, superimposed on the *Spitzer* MIPSGAL 24 μm image of the infrared nebula (Ingallinera et al. 2016). The contour starting values and steps are 6.5 and 0.6; 6.5 and 1.2; 1.35 and 0.15; and 1.5 and 0.25 K km s^{-1} for panels a, b, c, and d, respectively. The grey circle in the bottom right corner of each panel represents the beam size. Dashed lines in panel b indicate the cuts for the position–velocity diagrams used to interpret kinematic, and the ellipse used for the fitting is shown for reference.

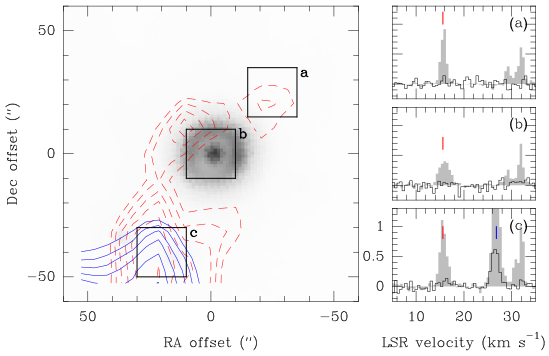

Figure 7. Overabundance of ^{13}CO. Left-hand panel: contour maps representing the emission of C^{18}O $J = 1 \rightarrow 0$ integrated in the velocity range (+25.6, +27.8) km s^{-1} (solid) and that of ^{13}CO $J = 1 \rightarrow 0$ integrated in the velocity range (+13.4, +17.4) km s^{-1} (dashed), superimposed on the *Spitzer* MIPSGAL 24 μm image of the infrared nebula in grey-scale. The contour starting values and steps are 0.4 and 0.1 and 1.35 and 0.15, respectively, in units of K km s^{-1}. The labelled squares represent regions of 20 × 20 arcsec where the spectra in the corresponding right-hand panels have been spatially averaged. Right-hand panels: averaged spectra of C^{18}O $J = 1 \rightarrow 0$ (black) and ^{13}CO $J = 1 \rightarrow 0$ (filled) over the region with the corresponding label. The former has been scaled by 2 for easier comparison. The velocity components represented by the contour maps are marked with vertical lines. Intensity scale is in units of K.

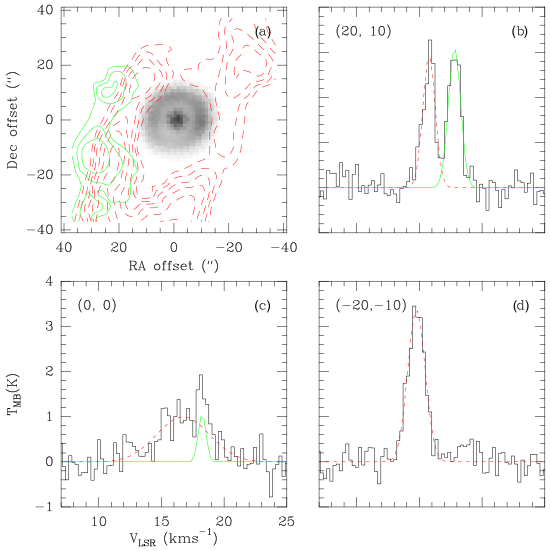

Figure 8. Hints of substructure in the CO gas: (a) the two velocity components as contours superimposed on the 24 μm image of the infrared nebula in grey-scale. In dashed contours, the component at $V_{\rm LSR} = 15.4$ km s^{-1}, with levels starting at 6.5 in steps of 1.2 K km s^{-1}; in solid contours, the component at $V_{\rm LSR} = 17.8$ km s^{-1}, with levels starting at 2.5 with steps of 0.6 K km s^{-1}. (b) Spectra at position (20, 10 arcsec). (c) Spectra at star's position (0, 0 arcsec). (d) Spectra at position (−20, −10 arcsec). A Gaussian fitting for each line is plotted.

elongation, and the second is orthogonal, from NW to SW (P.A. 60°). As seen in Fig. 9, we find emission highly concentrated in two isolated blobs either side of the star, each of them spanning for ∼ 2 km s^{-1}. The velocity difference between the blobs is small regardless of the direction of the cut, in the range 0.5–1.5 km s^{-1} from peak to peak.

4 DISCUSSION

4.1 Morphology and kinematics

Despite the contribution from the southern cloud, most of the emission arises from a circumstellar ring-like feature that encloses the infrared shell. The PV diagrams in Fig. 9 showed that material in the ring moves at different velocities either side of the exciting star, but a deeper analysis is required to disentangle the motion of the structure. We resorted to study the first-order moment of the emission, i.e. the intensity-weighted velocity distribution, presented in Fig. 10, which approximates the velocity field of the gas. The four CO and ^{13}CO lines share a common pattern, a smooth velocity gradient in the NE–SW direction that roughly splits the field across the semimajor axis of the structure. Therefore, the NE and SW regions show opposite motions, represented by two sets of contours in the maps: Gas in the NE moves away (redshifted emission) while gas in the SW moves towards the observer (blueshifted emission).

The spatial distribution of the emission can be explained by a torus seen at a certain angle, but the velocity gradient observed is compatible with a structure undergoing expansion or contraction. However, near-infrared spectroscopic observations by Flagey et al. (2014) proved that MGE 042.0787+00.5084 is a massive evolved

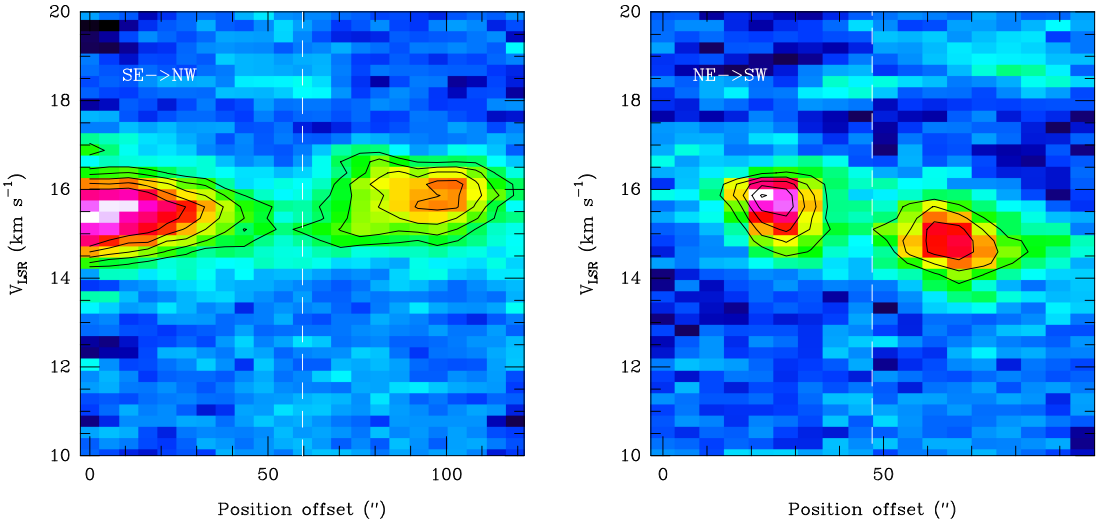

Figure 9. PV diagrams of the CO $J = 2 \rightarrow 1$ line in the slices defined in Fig. 6. The direction of the cut is indicated in the top left corner of each panel, and the vertical dashed line represents the position of the central star.

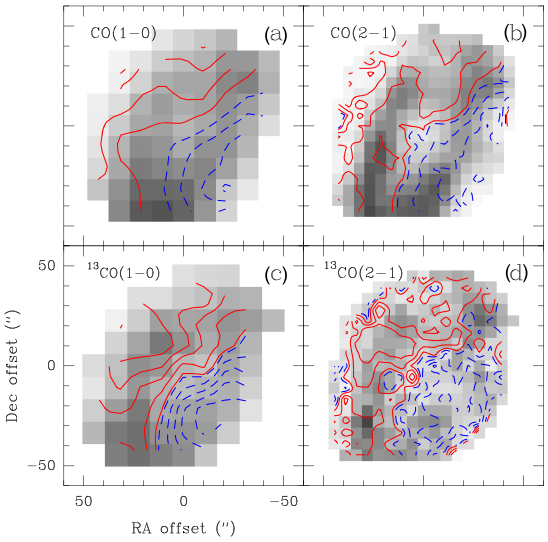

Figure 10. Intensity-weighted velocity maps of CO and ^{13}CO towards MGE042.0787+00.5084 shown as contours. The grey-scale represents the intensity of each transition at the original resolution, in units of K km s^{-1}. The dashed blue contours indicate $V_{LSR} < V_0$ and the solid red contours indicate$V_{LSR} > V_0$. Contour spacing is 0.15 and 0.25 K km s^{-1} for $J = 1 \rightarrow 0$ and $J = 2 \rightarrow 1$ lines, respectively. The borders of the maps have been masked out to minimize noise.

star, allowing us to confidently rule out the contraction scenario – i.e. material collapsing/accreting on to the star – and to therefore conclude that the gas is distributed in an expanding toroidal structure.

If the ring is expanding isotropically in a uniform medium, the observed elongation may be interpreted as a mere projection effect, which allows us to infer the inclination angle by fitting ellipses to the emission maxima as described in Section 3, and calculating the minor to major axial ratios. With this method we derive an inclination of 53 ± 6°. However, the overall morphology of the emission is heavily altered by the southern widespread component, and a local density gradient in the direction of the major axis may also contribute to the elongation, so we could be overestimating the inclination of the structure.

In this regard, we note similar velocity shifts in the two PV diagrams from Fig. 9, showing just a slightly larger difference in the NE–SW cut, which is likely more affected by projection according to the viewing geometry. This could be taken as an indicator of a low inclination. Therefore, we cannot merely rely on the ellipse fitting to constrain the inclination angle of the structure, and in Section 4.3.4 we consider a larger range of possible inclinations.

We can use the NE–SW cut to measure the projected expansion velocity as half the velocity difference between the emission blobs. We estimate a projected velocity of ∼1 km s^{-1}, which relates to the expansion velocity as

$$V_{\rm exp} = \frac{\Delta V}{2 \sin i}, \qquad (2)$$

where i is the inclination angle and ΔV the increment in velocity. Using the previously estimated inclination angle, we obtain $V_{\rm exp} =$ 1.2–1.4 km s^{-1}. This is an extremely low expansion velocity, an order of magnitude lower than those measured in other LBV sources (e.g. the main CO shell in G79.29+0.46 expands at 14 km s^{-1}; Rizzo et al. 2008), but it is important to bear in mind that this result is just a coarse lower limit, strongly affected by the inclination angle. Lower inclinations would be compatible with higher velocities.

4.2 Physical parameters of the gas

MGE 042.0787+00.5084 being a high-mass evolved star, mass-loss processes – both heavy steady winds and/or eruptive mass ejections – could have originated the structure seen in CO and ^{13}CO. The simultaneous observation of two rotational lines from

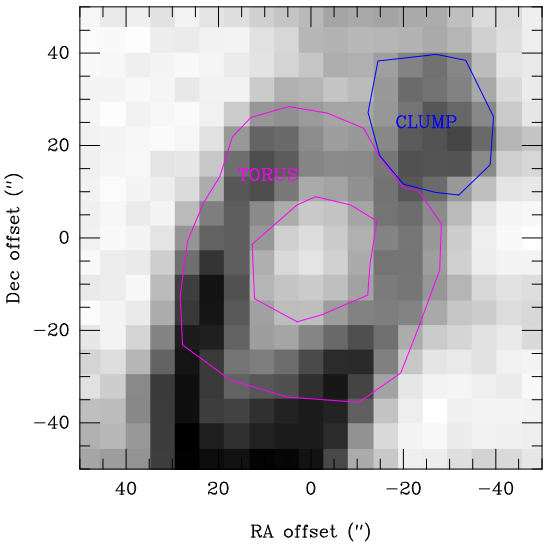

Figure 11. Regions in which physical parameters were derived independently: the north-western clump (blue) and the main torus (magenta). For reference, CO $J = 2 \rightarrow 1$ emission in the velocity range (+13.4, +17.4) km s^{-1} is shown in grey-scale.

two isotopologues allows us to derive some physical parameters of the gas.

To do so, we performed local thermodynamic equilibrium (LTE) and non-LTE analyses in two separate regions, to account for the spatial differentiation observed in the structure: the torus as a whole and the north-western clump. The two regions are depicted in Fig. 11. We excluded most of the the south-eastern region to minimize the contribution from the widespread emission.

4.2.1 LTE analysis

As a first approach we determined the global physical parameters of the gas in the LTE scenario, using ^{13}CO, the least intense and presumably least abundant observed species. By assuming optically thin emission, the column density in the lower level is given by

$$N_{\rm l} = 1.94 \times 10^3 \nu^2 \frac{g_{\rm l}}{g_{\rm u}} \frac{1}{A_{\rm ul}} \int T_{\rm MB} {\rm d}v, \quad (3)$$

where ν is the frequency of the line, $A_{\rm ul}$ is the spontaneous decay rate, $g_J = 2J + 1$ is the degeneracy of each rotational level, and the integral term depends on the excitation temperature $T_{\rm ex}$ through the relation $\int T_{\rm MB} {\rm d}v = T_{\rm ex} \int \tau {\rm d}v$, which is true in the optically thin regime (Wilson 2009). In LTE, levels are populated following a Boltzmann distribution described by a single $T_{\rm ex}$. In order to relate $N_{\rm l}$ to the total population of all energy levels in the molecule we use a rotational partition function $Q(T_{\rm ex})$ such that

$$N = 1.94 \times 10^3 \nu^2 \frac{g_{\rm l}}{g_{\rm u}} \frac{Q(T_{\rm ex})}{A_{\rm ul}} \exp\left(\frac{E_{\rm u}}{kT_{\rm ex}}\right) \int T_{\rm MB} {\rm d}v, \quad (4)$$

where $E_{\rm u}$ is the energy of the upper level and $T_{\rm ex}$ is the excitation temperature. The latter can be estimated from the $2 \rightarrow 1/1 \rightarrow 0$ line ratio by solving the relation

$$\frac{T_{\rm R}(21)}{T_{\rm R}(10)} = 4 \exp\left(-E_{21}/T_{\rm ex}\right), \quad (5)$$

Table 2. LTE column density estimates.

	$T_{\rm ex}$ (^{13}CO) (K)	N (^{13}CO) (10^{15} cm^{-2})	$T_{\rm ex}$ (CO) (K)	N (CO) (10^{15} cm^{-2})
Clump	11.2	1.0 (0.2)	11.6	6.1 (0.6)
Torus	9.8	1.0 (0.2)	12.1	6.1 (1.1)

with $T_{\rm R}$(ul) the peak temperature of the ul transition. The derived excitation temperatures, between 9 and 12 K, and column densities, all in the range of 10^{15} cm^{-2}, are summarized in Table 2. The column densities of each molecule do not vary significantly between the torus and the clump.

4.2.2 Non-LTE analysis

To study a more realistic scenario we ran simulations with the non-LTE excitation and radiative transfer code RADEX (van der Tak et al. 2007). RADEX uses the escape probability formulation with the large velocity gradient (LVG) approximation (Sobolev 1960) to constrain the excitation conditions of the gas according to the observed line intensities. We involved the four lines in the fitting, convolving the $2 \rightarrow 1$ maps to the $1 \rightarrow 0$ resolution to obtain true line ratios.

The calculations were made taking the CO and ^{13}CO collisional coefficients from the LAMDA database (Schöier et al. 2005), with a background temperature of 2.73 K. First, we ran RADEX for a range of kinetic temperatures ($T_{\rm k}$) from 10 to 250 K in steps of 10 K, solving the radiative transfer in a two-parameter space defined by $n({\rm H_2})$ – the H_2 volume density – and N (^{13}CO), with the aim of finding the best fit for the observed ^{13}CO $J = 1 \rightarrow 0$ intensities and $(2 \rightarrow 1)/(1 \rightarrow 0)$ ratios. Later we cross-checked the resulting $n_{\rm H_2}$ values with the CO line intensities and ratios in order to determine N (CO) and restrict the range of possible $T_{\rm k}$.

Simulation outcomes are compiled in Table 3 and some RADEX runs are presented in Fig. 12. We find ^{13}CO column densities in the range 1.0–1.3 $\times$ 10^{15} cm^{-2}, which only differ by 10–20 per cent from those of the LTE analysis. There is little variation between the column densities of the clump and those of the torus, with ^{13}CO opacities supporting the optically thin assumption. Similarly, the ^{13}CO and CO column densities are relatively insensitive to temperature, which is consistent with optically thin emission as well. Considering the uncertainties involved, N (CO) is only 5–7 times higher than N (^{13}CO), which indicates a surprisingly low isotopic ratio. The implications of this finding are discussed in Section 4.3.2.

The resulting gas densities are quite low, of a few 10^3 cm^{-3}, and we observe significant differences between the torus and the clump, with the latter being 1.5–2 times denser. These low densities are consistent with the non-detection of other high-density tracers, and somehow limit the range of possible kinetic temperatures, with solutions up to 70 K for the torus and 100 K for the clump. Above these values, $n_{\rm H_2}$ falls well below the critical density of the $1 \rightarrow 0$ transition.

In the case of CO we find higher τ values, suggesting that the observed intensities may be slightly affected by opacity, specially at low temperatures. In addition, we observe a significant dilution in the clump after convolution, which contrasts with the prominence of this region in the original maps. This may be related to a beam-filling issue, leading to a potential underestimation of the true densities. However, this effect is difficult to calibrate as the whole structure is unresolved. Interferometric observations would

Table 3. RADEX results.

T_K (K)	n (H_2) (10^3 cm^{-3})	N (^{13}CO) (10^{15} cm^{-2})	τ_{10}	τ_{21}	N (CO) (10^{15} cm^{-2})	τ_{10}	τ_{21}
			Clump				
10	7.2 (1.4)	1.2 (0.1)	0.05	0.11	8.3 (1.2)	0.35	0.7
30	1.5 (0.2)	1.0 (0.2)	0.02	0.09	7.1 (0.9)	0.12	0.51
50	1.0 (0.1)	1.0 (0.2)	0.01	0.09	6.8 (1.0)	0.09	0.49
70	0.8 (0.1)	1.0 (0.2)	0.01	0.08	6.8 (1.0)	0.08	0.49
			Torus				
10	4.1 (1.2)	1.3 (0.2)	0.06	0.14	7.6 (1.7)	0.39	0.71
30	1.0 (0.2)	1.2 (0.2)	0.04	0.12	6.2 (1.8)	0.19	0.56
50	0.7 (0.2)	1.1 (0.2)	0.03	0.12	6.2 (1.8)	0.18	0.56
70	0.5 (0.1)	1.1 (0.2)	0.03	0.12	6.2 (1.5)	0.17	0.55

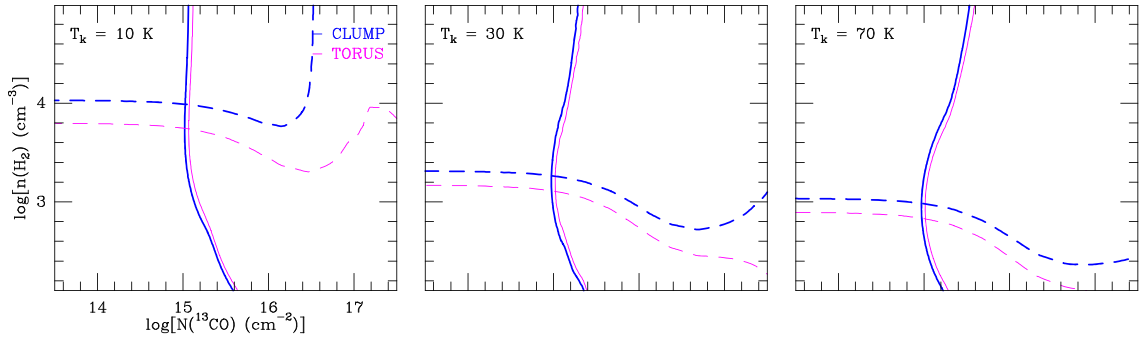

Figure 12. ^{13}CO RADEX fittings computed for $T_k = 10$ K (left), $T_k = 30$ K (centre), and $T_k = 70$ K (right), in the clump (thick blue line) and the torus (thin magenta line); see Fig. 11. Solid curves represent the observed ^{13}CO $J = 1 \rightarrow 0$ intensity, and dashed curves the ^{13}CO $(2 \rightarrow 1)/(1 \rightarrow 0)$ ratio. Intersections between two sets of contours indicate the most likely values of n (H_2) and N (^{13}CO).

reveal the actual angular extent of the structure, allowing for a more accurate estimation of its physical parameters.

4.3 Origin of the molecular gas

The morphology and kinematics of the structure raise the question of the origin of the gas. While tori are a quite unusual arrangement for circumstellar material around evolved high-mass stars, a few examples are found in the literature, such as the dusty torus around the LBV candidate HD168625 (O'Hara et al. 2003). There are two possible explanations for the formation of such a structure around an LBV star, namely (1) the observed molecular gas is stellar ejecta from a process of non-isotropic mass loss. In this scenario the observed CO and ^{13}CO formed when the stellar wind got colder and coagulated. (2) The molecular material is a relic of the molecular cloud where the star was born, accumulated and compressed by the steady action of a non-spherical wind from a previous stage.

The total mass of molecular gas present in the CO structure would shed some light on its origin, since very different orders of magnitude are expected in each scenario. This mass can be derived from the column density of H_2 via the relation

$$M_{\rm mol} = 2d^2 m_{\rm H} f_{\rm He} \int N({\rm H_2}) {\rm d}\Omega, \qquad (6)$$

where d is the distance to the object, $m_{\rm H}$ the mass of the hydrogen atom, $f_{\rm He} = 1.2$ is a correction factor to account for the hydrogen relative abundance, and the last term is the integral of the measured H_2 column density over the solid angle subtended by the source. Most of these factors are known or can be estimated with confidence, but the distance and the true H_2 column density are subject to a great uncertainty.

4.3.1 About the distance to MGE 042.0787+00.5084

There are no available estimates in the literature for the distance to MGE 042.0787+00.5084. By taking the systemic velocity of the structure of 15.4 km s^{-1}, we calculated two kinematic distances, namely 1.2 and 11.4 kpc. Details on how we determined these distances are provided in Appendix A. We can expect moderate deviations from Galactic rotation that would alter these estimates, but even departures of 20 km s^{-1} would increase the near distance just by a factor of ∼2, which is not critical for the subsequent interpretation.

Although the two distances are equally possible, we found a number of qualitative arguments that support the near distance: MGE 042.0787+00.5084 is by far the strongest object in the sample studied by Flagey et al. (2014), being remarkably bright in bands J, H, and K, and the symmetry and homogeneity of the nebula suggest a short age, which is more compatible with closer distances.

In order to narrow the range of possible distances, we explored the recently released data from the ESA's *Gaia* mission (*Gaia* DR2; Gaia Collaboration 2016; Gaia Collaboration 2018), finding

a match within 2 arcsec of the source position. This object (SourceID 4307460432455822976) has a parallax of $\pi = 0.05 \pm 0.2$ mas according to *Gaia*. With such a large uncertainty, distances in the range 4–20 kpc are possible within the error margin. Still, it is possible to deal with inaccurate parallax measurements by means of the Bayesian inference method described by Bailer-Jones et al. (2018), who applied this statistical approach on the whole DR2 catalogue to determine geometric distances according to the following probability density function:

$$P(r|\pi, \sigma_\pi, L_{\rm sph}) = r^2 \exp\left[-\frac{r}{L_{\rm sph}} - \frac{1}{2\sigma_\pi^2}\left(\pi - \pi_{\rm zp} - \frac{1}{r}\right)^2\right], \quad (7)$$

where π and σ_π are the parallax and its uncertainty, respectively, $\pi_{\rm zp}$ is the parallax zero-point, and $L_{\rm sph}$ is a prior that depends on the Galactic coordinates of the source.

This method has proven to be adequate for narrowing *Gaia* distances for other LBVs, reaching results in good agreement with literature values even when large uncertainties are involved (Smith et al. 2018). The inferred geometric distance for MGE 042.0787+00.5084 is thus $3.8^{+2.2}_{-1.3}$ kpc, but we must note that this result is based on a very inaccurate parallax and hence must be regarded with caution.

In the following we adopt a conservative distance of 2.5 kpc, as a compromise between the two approaches and taking into account possible departures from Galactic rotation. None the less, we admit that a larger distance is possible (e.g. 10 kpc). The implications of such a long distance on the global parameters of the structure are discussed in Section 4.4.

4.3.2 Isotopic ratios

Another essential factor when determining masses is X (^{13}CO), the ^{13}CO-to-H_2 relative abundance, which allows us to translate N (^{13}CO) into N (H_2). This parameter strongly depends on the ^{13}C abundance. We observe [^{12}CO/^{13}CO] line intensity ratios as low as 5–7 in large regions of the structure, as shown in the line ratio maps of the $1 \rightarrow 0$ and $2 \rightarrow 1$ transitions (Fig. 13). According to the LVG results, opacity by itself is not enough to explain an order of magnitude decrease in the [^{12}CO/^{13}CO] ratio with respect to the typical ISM values of 70–90 (Wilson & Matteucci 1992). This leaves just two possible explanations for such a low isotopic ratio: a ^{12}CO depletion or a ^{13}CO enhancement.

In the first scenario, chemical fractionation could account for the destruction of ^{12}CO. Similarly, ^{13}CO enhancement could be a direct consequence of stellar evolution. It is known whether the CNO cycle favours the production of ^{13}C in intermediate-mass stars (Berdyugina & Savanov 1994). The stellar mass range in which this overproduction takes place is not completely constrained, but some studies have measured low [^{12}CO/^{13}CO] ratios in a number of massive stars (e.g. α Ori; Lambert et al. 1984). If this process occurs in MGE 042.0787+00.5084 as well and the low [^{12}C/^{13}C] ratio is a result of the central star nucleosynthesis, it would be widespread in the surroundings, therefore indicating that a significant amount of molecular material is of stellar origin.

However, the non-detection of C^{18}O in the structure supports the ^{13}CO overproduction hypothesis. We detected this isotopologue in the south-eastern cloud, where abundances are close to the canonical values (e.g. [^{13}CO/C^{18}O] $\sim$ 5.5; see Fig. 7), but not in the structure, despite having CO and ^{13}CO intensities and rms comparable to those in the cloud. This may imply an excess of ^{13}CO. Never the less, other processes could be playing a role: High [^{13}CO/C^{18}O] ratios have been proposed as signposts of high-far-ultraviolet fields acting upon the outermost layers of molecular clouds (e.g. photon-dominated regions) and causing selective photodissociation of some isotopes (Shimajiri et al. 2014). In this case, this effect would explain the apparent absence of C^{18}O, but should only be noticeable locally, in the densest parts of the structure, particularly the north-western clump.

In the $2 \rightarrow 1$ map (panel b) we note a closed minimum towards the source. The spatial extent of this minimum is comparable to that of the beam, and the levels of CO and ^{13}CO in this region are above 5σ and 3σ, respectively. Therefore, this minimum is probably a meaningful feature.

Unfortunately, the angular resolution of the 30-m radio telescope does not allow us to study this feature in detail and discriminate between the two proposed scenarios. Interferometric observations would be valuable to assess whether the low isotopic ratio observed is the result of stellar evolution or a localized effect of the strong UV field of the star. Taking into account the strong uncertainty that affects the X (^{13}CO) factor, we use N (CO) to estimate the H_2 column density, adopting a canonical relative abundance of X (CO) $= 10^{-4}$.

4.3.3 Kinematic model

Using the global physical parameters as constraints, we developed a simple model to test the expanding-torus interpretation. The model aimed at reproducing the observed morphology and kinematics following a phenomenological approach. We used the pseudo-Monte Carlo non-LTE radiative transfer code LIME v1.8 (Brinch & Hogerheijde 2010). LIME simulates photon propagation through unstructured 3D Delaunay grids by applying the SimpleX algorithm (Ritzerveld & Icke 2006) and assuming ballistic transport. For a given molecule and transition LIME calculates level populations and generates synthetic spectral cubes, based on the LAMDA collisional rates. We processed these cubes with a custom PYTHON pipeline to simulate the observation with the IRAM 30-m telescope, obtaining maps directly comparable to the original data. We used the CO $J = 2 \rightarrow 1$ line because it provides the highest angular resolution and signal-to-noise ratio.

We modelled the structure as an expanding torus characterized by a set of geometrical and physical parameters. A complete list of the parameters is provided in Table 4 and the model is described in detail in Appendix B. The geometry is controlled by distance, inclination, and position angle. We defined r_0 as a scaling radius coincident with the inner edge of the torus to parametrize density and temperature. Density is described by a toroidal function where the parameter $\theta_{\rm H}$, the half-opening angle, determines the oblateness of the structure and the dimensionless parameters p and q dominate the steepness of the density gradient in the radial and angular directions. Since the torus is unresolved in the 30-m data we do not know its actual thickness, so we set some of these parameters manually for convenience. For the temperature profile we used a segmented function, which remains constant at a reference temperature in the cavity and behaves as a radial power law for $r > r_0$. Regarding the velocity field, we considered a purely radial expansion.

4.3.4 Model results

We adopted a distance of 2.5 kpc with a relative abundance X (CO) $= 10^{-4}$, as explained above. The free parameters of the model are the reference density ρ_0, related to n (H_2); the reference

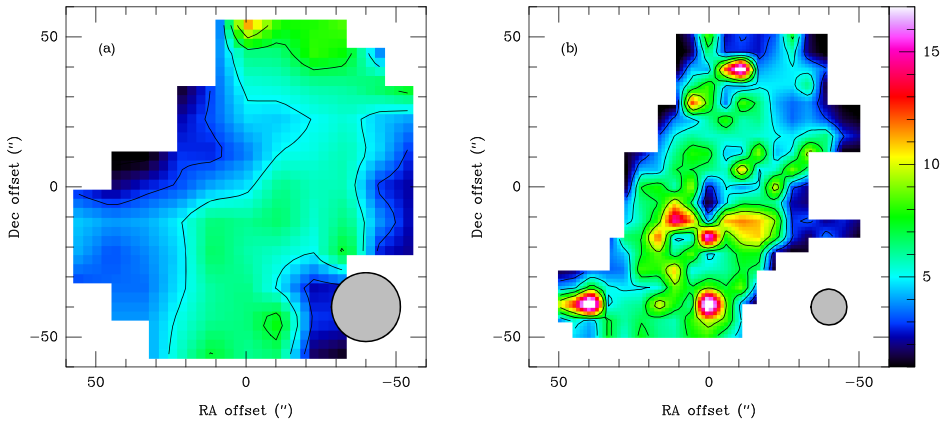

Figure 13. Isotopic ratio maps shown in colour scale: (a) the ^{12}CO/^{13}CO $J = 1 \rightarrow 0$ ratio and (b) the ^{12}CO/^{13}CO $J = 2 \rightarrow 1$ ratio. The colour scale is the same for the two maps, with contours at 1, 3, 5, and 7. In each map the two lines have been convolved to the same beam size, represented as a grey circle in the bottom right corner. Noisy pixels have been masked out and spatial smoothing has been applied to avoid artefacts.

Table 4. LIME model parametrization. Free parameters are expressed as a range.

Parameter	Meaning	Value	Unit
d	Distance	2.5	kpc
r_0	Inner radius	0.18	pc
p, q	Density steepness	2	–
γ	Temperature steepness	1.5	–
θ_H	Half-opening angle	15	deg
i	Inclination	15–45	deg
T_0	Temperature at r_0	10–80	K
ρ_0	Density at r_0	0.8–4 × 10^3	cm^{-3}
V_{exp}	Expansion velocity	1–5	km s^{-1}

Table 5. Best-fitting parameters for each LIME model.

Parameter	Model A ($i = 15°$)	B ($i = 30°$)	C ($i = 45°$)
ρ_0 (cm^{-3})	800	800	800
T_0 (K)	70	70	70
V_{exp} (km s^{-1})	3	1	1

temperature T_0, related to the kinetic temperature of the gas; the expansion velocity V_{exp}; and the inclination angle i. To account for the uncertainty in the determination of the inclination angle and the possibility of a nearly face-on structure discussed in Section 4.1, we built three types of models, A, B, and C, corresponding to inclinations of 15, 30, and 45°, respectively. We used reference temperatures in the range 10–70 K and densities of H_2 in the range 0.8–4 × 10^3 cm^{-3}, in agreement with the LVG results (see Table 3). We also let the expansion velocity vary from 1 to 5 km s^{-1} to cover possible scenarios where a low inclination somehow compensates for a higher velocity.

We explored the parameter space iteratively looking for the best fit in the velocity range (+13.4, +17.4) km s^{-1}, based on a channel-wise χ^2 criterion described in Appendix B. The best-fitting set of parameters for each kind of model is presented in Table 5 and a comparison of the main observables (line intensity maps, velocity fields, and position–velocity diagrams) is shown in Fig. 14. The three models show a preference towards warm, low-density solutions, as they reach the best fit for $\rho_0 = 0.8 \times 10^3$ cm^{-3} and $T_0 = 70$ K. It is important to note that these are reference values, so the average T_k and n (H_2) in the structure may be slightly lower. In any case, the best-fitting density is not particularly high, which could explain the non-detection of other less abundant molecules in the structure. Other denser and colder models fail to match the observed intensities, even by an order of magnitude.

Model A, which corresponds to an inclination of 15°, provides the best match, with a quite convincing reproduction of the morphology and kinematics of the gas. The expansion velocity of 3 km s^{-1} is ∼2 times higher than the prior estimates from the PV diagrams in Fig. 9, but still much lower than typical values. The integrated intensity map is slightly weaker than the data in most of the structure, but this difference is an expected side effect of the simpleness of our torus model and the uniformity of the density distribution. Never the less, model A is able to reproduce with high fidelity the observed velocity gradient everywhere but in the cavity, which in our model is highly depleted. Models B and C, corresponding to higher inclinations, fail to reproduce the observed morphology as the resulting structure is exceedingly elongated. Similarly, while the velocity gradient approaches that of model A, the velocity extent of the emission blobs in the PV diagrams is smaller than expected, of just 0.75–1 km s^{-1}, which means that the material in the line of sight is confined in a narrower velocity range.

4.4 Mass and mass loss

In view of these results, we conclude that the structure of molecular gas seen around MGE 042.0787+00.5084 is a low-density, nearly face-on torus that expands slowly. Adopting a conservative T_k of 50 K, we derive a total mass for the structure of 0.6 ± 0.1 $M_\odot$ (0.5 ± 0.1 $M_\odot$ in the torus and 0.1 $M_\odot$ in the clump). This mass is probably rather low to be the remnant of a molecular cloud piled up by the stellar wind, but it is compatible with masses of molecular gas found around other LBV stars (Rizzo et al. 2008).

Therefore, assuming all the gas formed from stellar ejecta, a crude estimate of the mass-loss rate of MGE 042.0787+00.5084 can be provided simply by calculating the dynamical age of the circumstellar structure. The torus deprojected radius is ∼15 arcsec

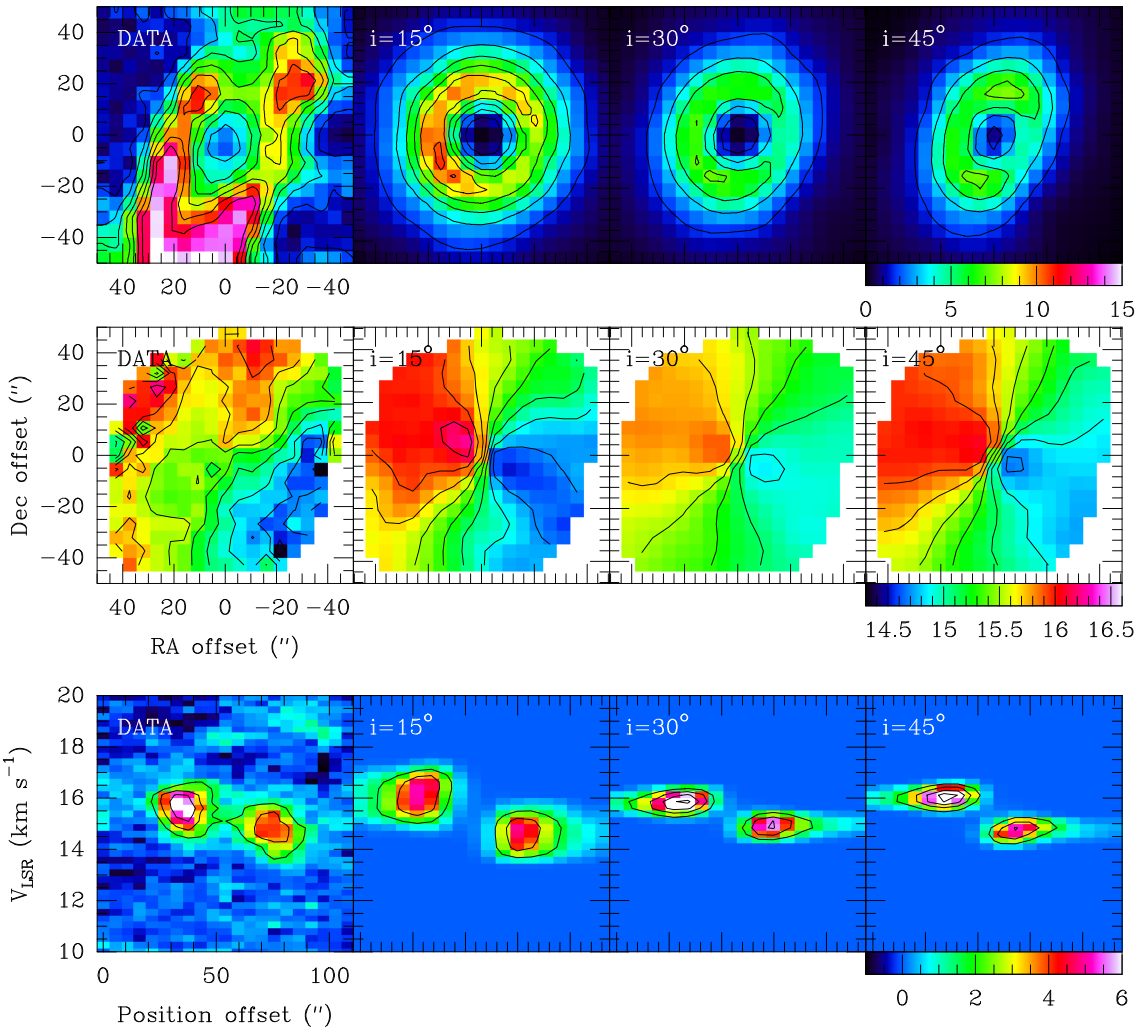

Figure 14. Comparison between data and best model for each inclination angle (see Table 5). Top row: CO $J = 2 \rightarrow 1$ integrated line intensity maps in the velocity range (+13.4, +17.4) km s^{-1}. Colour scale is in units of K km s^{-1}, with contours starting at 5σ with steps of 5σ. Middle row: intensity-weighted velocity maps in the same velocity range. Bottom row: position–velocity diagrams in the velocity range (+10, +20) km s^{-1} for a slice with a PA of 60°(see Fig. 6).

on average, which at 2.5 kpc translates into 0.18 pc. For $V_{\rm exp} = 3$ km s^{-1}, the dynamical age of the structure is

$$t_{\rm dyn} < \frac{R_{\rm inner}}{V_{\rm exp}} \sim 6 \times 10^4 \ {\rm yr}. \quad (8)$$

The LBV phase typically lasts for a few 10^4 yr, so this dynamical age is compatible with a structure formed during this period. However, the age derived by this method must be regarded as a coarse upper limit, as the expansion velocity of the gas could have been significantly higher in the past, implying a younger structure.

Never the less, this time-scale is useful to estimate the average mass-loss rate of the star during the LBV phase, yielding a value of $\dot{M} = 0.8$–1.2×10^{-5} M$_\odot$ yr^{-1}. This result is compatible with evolutionary models (Langer et al. 1994), lying in the lower end of the LBV spectrum, where stars exhibit high temperatures and moderate mass-loss rates (Lamers 1989).

Still, the mass-loss-rate estimate provided here must be interpreted carefully. It is a time average over a period of 6×10^4 yr, so the star could have experienced brief periods of severe mass loss in the past and we cannot use it to infer its current state. In addition, we only considered molecular gas in the calculation, which most likely is not the only contributor to the total mass. Other significant components (e.g. neutral and ionized gas) would increase the mass-loss rate but were not taken into account.

Finally, it is worth mentioning that the derived time-scale for the molecular gas structure also constrains the age of the inner nebula. While the torus is the result of steady stellar winds, the infrared nebula may trace a much more recent eruptive event. The possibility

of simultaneously observing two successive mass-loss events traced by different phenomena makes MGE 042.0787+00.5084 a very interesting target for further studies.

In our analysis we have adopted a conservative estimate of 2.5 kpc based on a series of reasonable assumptions from the scarce data available. We find that larger distances, in the range of 10 kpc or more, are still possible – according to *Gaia* parallaxes and admitting feasible departures from Galactic rotation – but are somehow less likely, as they lead to scenarios that are difficult to reconcile with the observations.

The size and age of the structure increase with d while its mass scales with d^2. Therefore, at 10 kpc the structure would be 2.4×10^5 yr old for $V_{\rm exp} = 3$ km s^{-1}, which places its origin in the main-sequence stage. The total mass of molecular gas in the torus would then be 9.6 ± 1.6 M$_\odot$. Groh et al. (2014) analysed the evolution of a non-rotating 60 M$_\odot$ star in terms of mass loss, finding that the mass lost during the 3 Myr prior to the LBV phase was less than 10 M$_\odot$ in total. Considering that molecular material represents just a fraction of the mass ejected, MGE 042.0787+00.5084 would need to rival the luminosity of η Car and should be an extremely efficient molecule producer in order to form such a massive structure. In addition, with the contribution of the inner nebula, the circumstellar material around this star would probably exceed the mass of any other known LBV nebula. On the other hand, the density of the gas is proportional to d^{-1}; as a consequence, at 10 kpc the gas would be diffuse, with an average n (H$_2$) of $\sim$80 cm^{-3}. Under these conditions, LTE modelling would require extremely high kinetic temperatures far from the star (above 400 K at 0.75 pc) to reproduce the observed CO line intensities.

These are only indirect arguments that do not allow us to rule out far distances but stress the need for an accurate distance determination, which would permit us to trace back the evolution and mass-loss record of this source.

5 CONCLUSIONS

We report the first detection of CO gas associated with the candidate LBV MGE 042.0787+00.5084 forming a circumstellar structure that encloses the infrared nebula. This detection was obtained by means of 1.3 and 3 mm observations in a region of 1.5×1.5 arcmin in the field of the source carried out with the IRAM 30-m telescope. After a detailed study of the morphology and kinematics of the structure, we estimate the global physical parameters of the gas by LTE and non-LTE modelling. Finally we provide an interpretation for the formation of the molecular gas that is consistent with two scenarios in the LBV phase. The key findings in this paper are the following:

(i) We found significant emission of CO and ^{13}CO $J = 1 \rightarrow 0$ and $J = 2 \rightarrow 1$ in the velocity range $(+13.4,\ +17.4)$ km s^{-1}, tracing a structure with a clear circumstellar distribution. We interpreted this structure as an expanding torus according to the observed morphology and kinematics.

(ii) We studied the physical conditions in two separate regions of the structure, namely the north-western clump and the main torus. We constrained the density, column density, and kinetic temperature under LTE and non-LTE assumptions, finding that the clump is denser than the main torus by a factor of 1.5–2 regardless of the temperature, with H$_2$ volume densities of a few 10^3 cm^{-3}. On the other hand, only kinetic temperatures in the range 10–70 K for the torus and 10–100 K for the clump are consistent with the observed line intensities and ratios.

(iii) The measured [^{12}CO/^{13}CO] ratio was rather low, in the range from 5 to 7 in most of the structure. This result was particularly intriguing as no C^{18}O was detected, except in the southern cloud. We proposed a ^{13}CO overproduction as an explanation for such an abnormal isotopic ratio, discussing the implications of this enhancement as a result of stellar evolution or selective photodissociation.

(iv) The formation of a toroidal structure around an LBV star can be explained by two scenarios: (1) molecular ejecta from the star via non-spherical mass loss or (2) compression of the parent molecular cloud due to the effects of the strong and steady stellar wind. The determination of the total amount of molecular material could pinpoint the most likely scenario, but the distance to the source is poorly constrained. By adopting $d = 2.5$ kpc, we derived a mass of molecular gas of 0.6 M$_\odot$, consistent with an average mass-loss rate of $0.8–1.2 \times 10^{-5}$ M$_\odot$ yr^{-1} during the LBV phase.

(v) We developed a simple kinematic model with the aim of reproducing the morphology and velocity fields of the structure. We studied the influence of density, temperature, inclination, and expansion velocity. The model with the lowest inclination ($i = 15^\circ$) and a rather low expansion velocity (3 km s^{-1}) provided the best fit, being able to accurately reproduce the observed velocity gradient in most of the structure, as proven by first-order moments and PV diagrams. This supports the interpretation of the structure as an expanding torus of CO with a nearly face-on viewing geometry.

The characterization of the molecular material associated with MGE 042.0787+00.5084 constitutes an excellent example of how studies of this kind provide useful information on the mass-loss processes during the LBV phase. This source has shown a great potential to learn about the interplay between evolved high-mass stars and the ISM, deserving follow-up studies to better constrain its physical parameters and evolutionary record. This can be achieved by means of interferometric observations and near-infrared high-resolution spectroscopy. Most importantly, this successful detection proves that the existence of molecular material in the vicinity of evolved massive stars is not an exceptional finding but likely a common feature, therefore laying the foundations for future studies involving similar sources and less abundant molecules.

ACKNOWLEDGEMENTS

This work is based on observations carried out under project number 043-17 with the IRAM 30-m telescope. IRAM is supported by INSU/CNRS (France), MPG (Germany), and IGN (Spain). We acknowledge the IRAM staff from Pico Veleta for the help provided during the observations. J.R.R. acknowledges the support from project ESP2015-65597-C4-1-R (MINECO/FEDER).

REFERENCES

Bailer-Jones C. A. L., Rybizki J., Fouesneau M., Mantelet G., Andrae R., 2018, AJ, 156, 58
Berdyugina S. V., Savanov I. S., 1994, Astron. Lett., 20, 639
Brinch C., Hogerheijde M. R., 2010, A&A, 523, A25
Buemi C. S. et al., 2017, MNRAS, 465, 4147
Clark J. S., Larionov V. M., Arkharov A., 2005, A&A, 435, 239
Davidson K., 1989, in Davidson K., Moffat A. F. J., Lamers H. J. G. L. M., eds, Astrophysics and Space Science Library, Vol. 157, IAU Colloq. 113: Physics of Luminous Blue Variables, Kluwer Academic Publishers, Val Morin, Canada, p. 101
Fich M., Blitz L., Stark A. A., 1989, ApJ, 342, 272
Flagey N., Noriega-Crespo A., Petric A., Geballe T. R., 2014, AJ, 148, 34
Gaia Collaboration, 2016, A&A, 595, A1

Gaia Collaboration, 2018, A&A, 616, A1
Groh J. H., Meynet G., Ekström S., 2013, A&A, 550, L7
Groh J. H., Meynet G., Ekström S., Georgy C., 2014, A&A, 564, A30
Guilloteau S., Lucas R., 2000, in Mangum J. G., Radford S. J. E., eds, ASP Conf. Ser. Vol. 217, Imaging at Radio through Submillimeter Wavelengths. Astron. Soc. Pac., San Francisco, p. 299
Gvaramadze V. V. et al., 2012, MNRAS, 421, 3325
Humphreys R. M., Davidson K., 1994, PASP, 106, 1025
Ingallinera A. et al., 2014, MNRAS, 437, 3626
Ingallinera A. et al., 2016, MNRAS, 463, 723
Lambert D. L., Brown J. A., Hinkle K. H., Johnson H. R., 1984, ApJ, 284, 223
Lamers H. J. G. L. M., 1989, in Davidson K., Moffat A. F. J., Lamers H. J. G. L. M., eds, Astrophysics and Space Science Library, Vol. 157, IAU Colloq. 113: Physics of Luminous Blue Variables, Kluwer Academic Publishers, Val Morin, Canada, p. 135
Langer N., Hamann W.-R., Lennon M., Najarro F., Pauldrach A. W. A., Puls J., 1994, A&A, 290, 819
Marston A. P., McCollum B., 2006, in Kraus M., Miroshnichenko A. S., eds, ASP Conf. Ser. Vol. 355, Stars with the B[e] Phenomenon. Astron. Soc. Pac., San Francisco, p. 189
Mizuno D. R. et al., 2010, AJ, 139, 1542
O'Hara T. B., Meixner M., Speck A. K., Ueta T., Bobrowsky M., 2003, ApJ, 598, 1255
Ossenkopf V., Henning T., 1994, A&A, 291, 943
Ritzerveld J., Icke V., 2006, Phys. Rev. E, 74, 026704
Rizzo J. R., Jiménez-Esteban F. M., Ortiz E., 2008, ApJ, 681, 355
Rizzo J. R., Palau A., Jiménez-Esteban F., Henkel C., 2014, A&A, 564, A21
Sánchez Contreras C. et al., 2015, A&A, 577, A52
Schöier F. L., van der Tak F. F. S., van Dishoeck E. F., Black J. H., 2005, A&A, 432, 369
Shimajiri Y. et al., 2014, A&A, 564, A68
Smith N., Aghakhanloo M., Murphy J. W., Stassun K. G., Drout M. R., Groh J. H., 2018, preprint (arXiv:1805.03298)
Sobolev V. V., 1960, Moving Envelopes of Stars. Harvard Univ. Press, Cambridge
Stringfellow G. S., Gvaramadze V. V., Beletsky Y., Kniazev A. Y., 2012, in Richards M. T., Hubeny I., eds, Proc. IAU Symp. 282, From Interacting Binaries to Exoplanets: Essential Modeling Tools. Cambridge Univ. Press, Cambridge, p. 267
Umana G., Buemi C. S., Trigilio C., Leto P., Hora J. L., Fazio G., 2011, Bull. Soc. R. Sci. Liege, 80, 335
van Boekel R. et al., 2003, A&A, 410, L37
van der Tak F. F. S., Black J. H., Schöier F. L., Jansen D. J., van Dishoeck E. F., 2007, A&A, 468, 627
Wilson T. L., Matteucci F., 1992, A&AR, 4, 1
Wilson T. L., 2009, preprint (arXiv:0903.0562)

APPENDIX A: COMPUTATION OF KINEMATIC DISTANCES

Assuming MGE 042.0787+00.5084 is in circular rotation around the Galactic Centre, its angular velocity is given by

$$\omega = \frac{V_{\rm LSR}}{R_0 \sin l \cos b} + \omega_0, \tag{A1}$$

where l and b denote the Galactic longitude and latitude of the source and R_0 and ω_0 are the galactocentric distance and angular velocity of the Sun, respectively. Considering the fit for the rotation curve of the Milky Way provided by Fich, Blitz & Stark (1989), the galactocentric radius of an object with angular velocity ω is

$$R = \frac{1.00746 R_0}{\frac{\omega}{\omega_0} + 0.017112}. \tag{A2}$$

This galactocentric radius R relates to the distance through the expression

$$R = (R_0^2 + d^2 - 2R_0 d \cos l)^{1/2}, \tag{A3}$$

which is a regular second-degree equation and thus admits two possible solutions. Taking the canonical values for the local Galactic constants $R_0 = 8.5$ kpc and $\Theta_0 = 220$ km s^{-1}, we obtain a galactocentric radius of $R = 7.63$ kpc for MGE 042.0787+00.5084, which corresponds with $d_{\rm near} = 1.2$ kpc and $d_{\rm far} = 11.4$ kpc.

APPENDIX B: LIME MODEL

The model is an ideal, axisymmetric torus defined in a cylindrical coordinate system (r, ϕ, z). The geometry of the model is defined by three parameters: distance, position angle, and inclination angle of the structure with respect to the line of sight.

We used ortho- and para-H_2 as the main collision partners for photon propagation, with an ortho–para ratio of 3, and grains covered by thin ice mantles for dust opacity (Ossenkopf & Henning 1994). A CO relative abundance of $X_{\rm CO} = 10^{-4}$ was used. No magnetic field was included in the model.

The model assumes gas and dust are thermally coupled, following the same torus-like density distribution, such that

$$\rho(r, z) = \begin{cases} \rho_0 \left(\frac{r}{r_0}\right)^{-p} \exp\left[-q|\cos\theta|\right] & \text{if } r \geq r_0, \theta \leq \theta_{\rm H} \\ \delta\rho_0 & \text{otherwise,} \end{cases}$$

where r_0 is a scaling radius equal to the inner radius of the torus, ρ_0 is a reference density value, p and q are dimensionless parameters that determine the radial and angular density gradients, respectively, and $\theta_{\rm H}$ is the half-opening angle of the torus. To model the inner cavity we added a depletion factor $\delta = 10^{-5}$ that weights the reference density when $r \leq r_0$. Accordingly, points with $\theta \geq \theta_{\rm H}$ (i.e. outside the torus) are similarly depleted.

We modelled the temperature profile with a simple radial power law controlled by the dimensionless parameter γ,

$$T(r) = T_0 \left(\frac{r}{r_0}\right)^{\gamma} \tag{B2}$$

for $r \geq r_0$, remaining constant at the reference temperature T_0 within the cavity, which is consistent with the absence of material to absorb radiation.

Regarding the torus kinematics, we adopted a velocity field consistent with a structure expanding at a constant rate, as discussed in Section 4.1. Consequently the velocity vector is completely radial in the model space, with $|\vec{v}| = V_{\rm exp}$.

To measure the goodness of the fitting we used a channel-wise χ^2 criterion in the velocity range of interest ($+13.4$, $+17.4$ km s^{-1}), defined as

$$\chi^2 = \sum_j \frac{\left(T_j^{\rm model} - T_j^{\rm data}\right)^2}{\sigma^2}, \tag{B3}$$

where $T^{\rm model}$ and $T^{\rm data}$ are the main-beam temperature per pixel for the model and data, respectively, σ is the data rms scaling factor, and j denotes the velocity channel. By doing so we account for the morphology and velocity extent of the emission simultaneously.

This paper has been typeset from a TEX/LATEX file prepared by the author.

3.7 Rizzo et al., 2020 (Paper II)

EPJ Web of Conferences **228**, 00023 (2020) https://doi.org/10.1051/epjconf/202022800023
mm Universe @ NIKA2

NIKA2 observations around LBV stars

Emission from stars and circumstellar material

J. Ricardo Rizzo[1,3,*], *Alessia* Ritacco[2], and *Cristobal* Bordiu[1]

[1]Centro de Astrobiología (CSIC-INTA), Ctra. M-108, km. 4, E-28850 Torrejón de Ardoz, Madrid, Spain
[2]Institut de Radioastronomie Milimétrique (IRAM), E-18012 Granada, Spain
[3]ISDEFE, Beatriz de Bobadilla 3, E-28040 Madrid, Spain

Abstract. Luminous Blue Variable (LBV) stars are evolved massive objects, previous to core-collapse supernova. LBVs are characterized by photometric and spectroscopic variability, produced by strong and dense winds, mass-loss events and very intense UV radiation. LBVs strongly disturb their surroundings by heating and shocking, and produce important amounts of dust. The study of the circumstellar material is therefore crucial to understand how these massive stars evolve, and also to characterize their effects onto the interstellar medium. The versatility of NIKA2 is a key in providing simultaneous observations of both the stellar continuum and the extended, circumstellar contribution. The NIKA2 frequencies (150 and 260 GHz) are in the range where thermal dust and free-free emission compete, and hence NIKA2 has the capacity to provide key information about the spatial distribution of circumstellar ionized gas, warm dust and nearby dark clouds; non-thermal emission is also possible even at these high frequencies. We show the results of the first NIKA2 survey towards five LBVs. We detected emission from four stars, three of them immersed in tenuous circumstellar material. The spectral indices show a complex distribution and allowed us to separate and characterize different components. We also found nearby dark clouds, with spectral indices typical of thermal emission from dust. Spectral indices of the detected stars are negative and hard to be explained only by free-free processes. In one of the sources, G79.29+0.46, we also found a strong correlation of the 1mm and 2mm continuum emission with respect to nested molecular shells at ≈1 pc from the LBV. The spectral index in this region clearly separates four components: the LBV star, a bubble characterized by free-free emission, and a shell interacting with a nearby infrared dark cloud.

1 Background

Luminous Blue Variable (LBV) stars are among the most massive objects, previous to core-collapse supernova (SN). The evolutive path around this short-lived stage (some 10^4 yr) is not totally well settled yet, being considered previous to Wolf-Rayet [1] and also direct precursors of SN [2]. These stars develop strong and dense winds (up to 10^{-4} $M_\odot$), and are among the most intense sources, with luminosities up to several 10^5 $L_\odot$. LBVs are close to the

*e-mail: ricardo.rizzo@cab.inta-csic.es

EPJ Web of Conferences **228**, 00023 (2020) https://doi.org/10.1051/epjconf/202022800023
mm Universe @ NIKA2

Humphreys-Davidson limit [3] and experience several dynamical instabilities which, at the end, result in violent outbursts of several solar masses.

The environs of LBVs are then heavily affected by copious UV radiation and the mass-loss events. Almost all LBVs are surrounded by IR nebulae, composed by a rich mixture of dust and CNO-processed neutral and ionized gas [4–6]. This circumstellar material (CSM) is therefore the consequence of ionization, shocks, dust formation and a presumably complex chemistry. The knowledge and characterization of the CSM linked to LBVs is therefore crucial not only to learn about the chemical and dynamical evolution of the Galaxy, but also to understand the physical processes which drive the massive star evolution.

Important efforts have been made in the study of the molecular structures around LBVs. The best studied object is probably G79.29+0.46, where we discovered a number of concentric, shocked shells associated with mass-loss events developed in the last 10^3 – 10^4 yr [7–10]. In MGE042.0787+00.5084 (hereafter MGE042), we also found a molecular torus in slow expansion, with similar dynamical ages [11]. Recently, η Carina was also the subject of molecular studies, where molecular material connected to the Homunculus and a more recent outburst were discovered [12–16].

Dust structures and the ionized and molecular gas around these hot stars may extend up $\approx$ 1 pc from them. At the distances of galactic LBVs, these circumstellar features span angular sizes typically between 20" and 2′. The large field of view of NIKA2 (6.′5) permits efficient and simultaneous observations of the stellar objects, their CSM and also the extended emission arising from nearby clouds [17]. The observations are made in two key bands, where both thermal dust and free-free emission of gas can compete.

NIKA2 even has potential to detect non-thermal (synchrotron) emission from this kind of sources. Although non-thermal emission has been traditionally studied in the radio (cm-wavelengths) regime [18], it has been detected in several other massive stars, such as O-type and Wolf-Rayet [19]. This emission is often associated to colliding winds in binaries, where electrons are shocked, accelerated to relativistic velocities and later coupled to an existent magnetic field [20]. The same physical processes may account in LBV stars, and the possibility of this mechanism should not be easily discarded.

In this paper we report the first results and preliminary analysis of an observational campaign in four fields around five confirmed or candidate LBVs.

2 Observations

The observations were made at the IRAM 30m radio telescope, during the first open pool session of NIKA2 [17] which has been carried out in October 2017, during three consecutive evenings. Four fields have been observed, enclosing 5 LBVs. All the observations were performed in day time, with typical precipitable water vapour of 2mm, opacity $\tau \approx 0.2$ measured at 225 GHz by the taumeter of the 30m telescope and stable weather conditions.

A summary of the observations is presented in Table 1. For each field, number of scans, integration time, typical elevations and *rms* are shown. Atmospheric opacity corrections are applied to the observed scans by using the NIKA2 skydip procedure described in [17]. This procedure uses NIKA2 itself as taumeter providing an opacity correction per observing scan. For all the scans, the opacities estimated varies between 0.17 and 0.24 for the 150 GHz band, and between 0.30 and 0.39 for the 260 GHz band.

The maps were obtained by using NIKA2 IDL pipeline developed by the NIKA2 collaboration. In particular, we used an iterative method to subtract the correlated noise common to all the pixels of the arrays of NIKA2. At each iteration we combine all the maps for the different objects and we estimate the final averaged map. At the first iteration we subtract the noise estimated using all those pixels which are off-source, i.e. they detect the signal from the

EPJ Web of Conferences **228**, 00023 (2020) https://doi.org/10.1051/epjconf/202022800023
mm Universe @ NIKA2

Table 1. Summary of observations

Source	scans	$t_{\rm int}$ hr	elv °	$\sigma_{\rm 1mm}$ mJy/beam	$\sigma_{\rm 2mm}$ mJy/beam
G79.29+0.46	12	1.1	68	5.2	1.3
MGE042	60	2.0	56	1.6	0.5
HD168625(*)	24	1.0	36	2.1	0.6
MGE027(**)	30	0.9	48	2.7	0.8

(*) HD168607 included in the same field of HD168625
(**) MGE027 stands for MGE027.3839-00.3031 [5]

background which is a combination of atmospheric signal, electronic noise, cryogenic noise etc. Performing the difference between two consecutive maps we obtain the noise map that we subtract to the next iteration. At each iteration the signal to noise ratio increases, leading to a gaussian noise which is consistent with a white noise.

On-the-fly maps have been performed in different directions to overcome any striping effect that could appear along the scan direction. Combining the maps with different directions of scan we average this kind of effect and ease the offline data analysis processing.

3 Results

After combining individual scans and removing the background, we smoothed all images to a common angular resolution of 20". This resolution was chosen as a compromise to improve the signal-to-noise ratio without sacrificing too much the level of detail in the maps, and to avoid excessive dilution of the stellar sources. The final images are sketched in Fig. 1. The emission at both bands arises not only from the stars, but also from some circumstellar material and ambient clouds. The white contour is at approximately 5-sigma level, so all the visible features are significant.

The G79.29+0.46 field is dominated by bright and intense emission running from south-east to west. This emission corresponds to an infrared dark cloud (IRDC) linked to DR15, which is known to host active star formation [21], probably induced by the close LBV [9, 10]. The star is detected at both bands, more clearly at 2mm. A shell structure of $\approx$ 100" in radius is also noted, especially at the 2mm band. The NIKA2 shell is clearly correlated with an infrared shell already reported [8]. This shell is also bounded by two concentric CO shells related to past mass-loss events [7].

In the MGE042 field we also note a rather extended molecular cloud to the north, not clearly associated with the star. The LBV and a compact cloud $\approx$ 30" to the south-east are also clearly identified. It is noteworthy that the star is relatively more intense at 2mm, while the compact cloud looks the opposite. The compact cloud is spatially almost coincident to the densest part of the expanding CO torus [11].

The LBVs HD 168625 and HD 168607 are surrounded by extended features without a clear morphological association. Contrarily to the previous two cases, part of this extended emission is brighter at 2mm. HD168625 seems also immersed within a low-level emission plateau, which is angularly correlated with a bright infrared nebula [4].

The LBV star MGE027 is definitively not detected at the NIKA2 frequencies. Its field is dominated by extended, filamentary, and clumpy material.

The Fig. 2 shows a closer view of the four fields in both bands, in order to disclose the presence of any extended, circumstellar emission around the LBVs. Cyan circles have widths of 20" (the angular resolution after smoothing) and are centred on the stars. The contours are

EPJ Web of Conferences **228**, 00023 (2020) https://doi.org/10.1051/epjconf/202022800023
mm Universe @ NIKA2

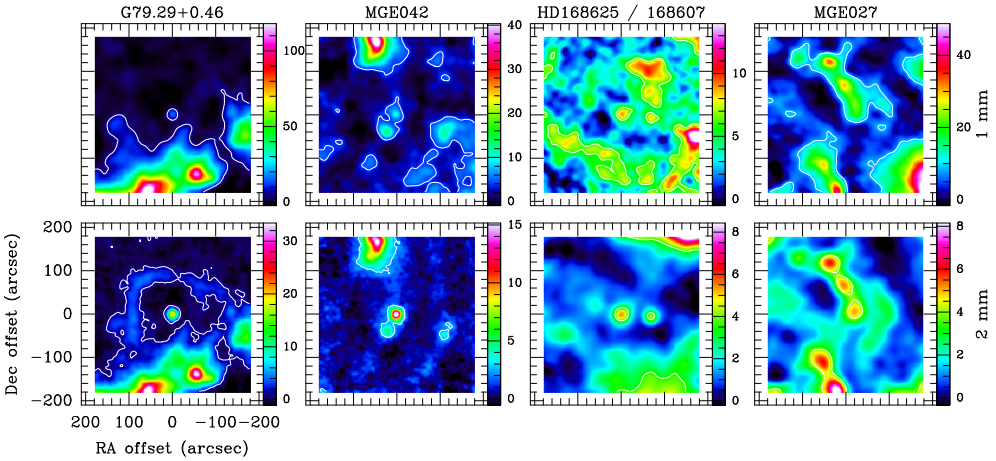

Figure 1. Final images in the four fields observed, smoothed to a HPBW of 20". Top row contains the images at 260 GHz, while the bottom row depict those images at 150 GHz. Sources are indicated in the upper parts of the 260 GHz images. Colorbars are also depicted at the right of each image, in mJy. A diversity of features are seen, including the LBV stars themselves, but also some CSM and even Galactic dark clouds. White contours are at approximately 5-sigma level.

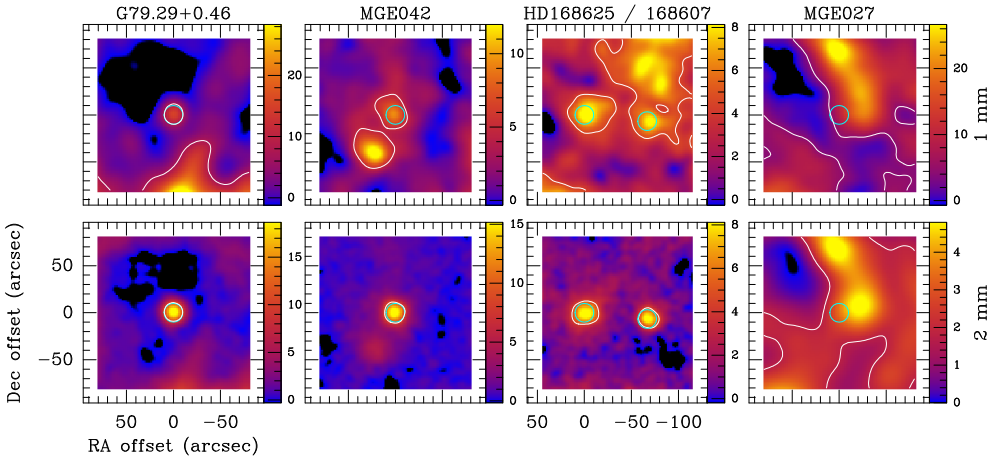

Figure 2. Details around the LBV stars, with colorbars in mJy at the right. Cyan circles indicate the HPBW of the images and are centred at the star positions. White contours correspond to half the flux density at the star position. Note a different range in right ascension for the third field from left, where HD 168625 is in (0", 0") and HD 168607 is ≈ 70" west.

half of the peak fluxes on each star. In G79.29+0.46, we see that the contour matches the circle almost perfectly, indicating that this emission arises only from the star and not from possible circumstellar gas or dust. In MGE042, the point source emission arises only at 2mm. The compact cloud at south east is notoriously more intense at 1mm. Both MGE042 and the close compact cloud are immersed within a tenuous plateau, which is more evident at 1mm band. HD 168625 displays some extended emission in both bands, while HD 168607 depicts point source emission only at 2mm.

EPJ Web of Conferences **228**, 00023 (2020) https://doi.org/10.1051/epjconf/202022800023
mm Universe @ NIKA2

The Table 2 sketches a quick glance of the features identified. We distinguish five different components or sources of emission: (1) the LBV star; (2) some circumstellar material; (3) more extended emission where the stars are embedded; (4) star-centred shell-like structure; and (5) clouds without a clear morphological relationship to the LBVs. The circumstellar emission appears very close to the stars, while the extended emission (or "plateau") is detached from the star emission. There are therefore complex and varied scenarios towards different LBVs, possibly with different composition and excitation mechanisms.

Table 2. Morphology of the components

Field	Star		CSM		Plateau		Shell		Cloud	
	1mm	2mm	1mm	2mm	1mm	2mm	1mm	2mm	1mm	2mm
G79.29+0.46	✔	✔	✘	✘	✘	✘	?	✔	✔	✔
MGE042	✔	✔	✔	✘	✔	✔	✘	✘	✔	✔
HD168625	✔	✔	✔	✔	✔	✔	✘	✘	✔	✔
HD168607	✔	✔	?	✘	✔	✔	✘	✘	✔	✔
MGE027	✘	✘	✘	✘	✘	✘	✘	✘	✔	✔

✔: detected. ✘: not detected. **?**: doubtful.

4 About the emission mechanisms

NIKA2 frequencies are especially suitable to gather first estimates about the excitation mechanisms of the detected material. Thermal dust is usually relevant at mid-infrared, and steeply decreases when increasing the wavelength. Free-free emission normally from ionized hot gas slightly increases with decreasing frequencies. Depending on the specific physical conditions, both mechanisms may be significant at wavelengths of a few mm.

As we see in the previous section, LBVs are mm-wavelengths continuum sources. Their ejecta are mainly made of ionized atomic gas. When this hot gas moves away from the star it progressively forms molecules, which later may form copious amounts of dust at certain distance. Therefore, we expect important contribution from both free-free gas emission and thermal dust [22, 23].

The existence of non-thermal emission, often found in Wolf-Rayet and other massive stars, should not be discarded. The non-thermal emission may have its origin in different processes, such as the shocks of colliding winds in binary systems or the relativistic particle acceleration due to magnetic fields [18]. The relative contribution of non-thermal emission at mm-wavelengths is, however, hard to estimate [24].

We can make some guesses about the relative importance of thermal dust, free-free gas and non-thermal processes by computing the spectral index α, defined as

$$S_\nu \propto \nu^\alpha \tag{1}$$

where S_ν is the flux density at the frequency ν. For a spherical expanding HII region we expect $-0.1 < \alpha < 1.5$ ([25] and references therein), while roughly $\alpha = 0.6$ is expected for an evolved stellar wind [26], and $\alpha > 0.6$ if the wind is radiatively shocked [27]. We expect $\alpha = 2$ for ideal thermal black body emission, and $\alpha = (2+\beta)$ for a black body modified by the frequency-dependent dust emissivity; β is the dust emissivity index, and takes typical values between 1 and 2.7 ([28] and references therein).

We computed α in the four fields only for those pixels with flux densities above 2-sigma. The result is shown in Fig. 3. The colour scale runs from -1 to 4 in the four panels; blue

EPJ Web of Conferences **228**, 00023 (2020) https://doi.org/10.1051/epjconf/202022800023
mm Universe @ NIKA2

tones run approximately from −1 to 0.6, green tones from 0.6 to 2.3, and dark red tones from 2.3 to 4.

These first results are striking. The spectral indices computed between the two NIKA2 frequencies outstandingly show three separate components, presumably related to different physical conditions or excitation processes.

The stellar sources are clearly detached from their surroundings, as we can see in the cases of MGE042, HD 168625 and HD 168607; those stars and G79.29+0.46 have the lowest α, with values well below those corresponding to pure Bremsstrahlung. Such highly negative values of the spectral indices are indicative of a significant contribution of non-thermal processes.

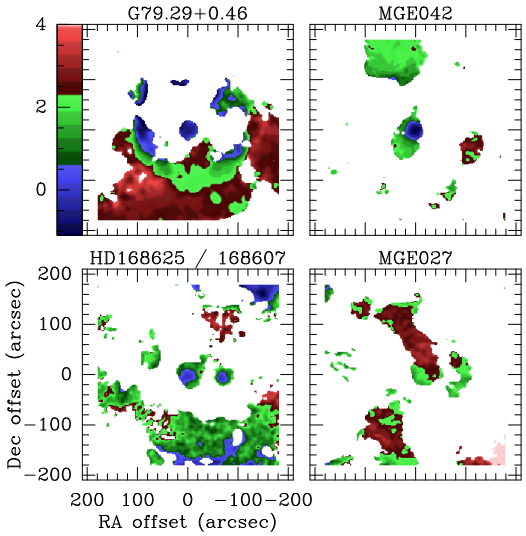

Figure 3. Spectral indices of and around the LBV stars observed. The same range is depicted in the four fields.

In G79.29+0.46, the bubble enshrouded by the infrared/mm-continuum and CO shells [7, 8] becomes evident, with values of α typical of free-free emission. It is noteworthy the layered structure seen around the (100”, −20”) position, where it is clearly noted the bubble in blue, the shell affected by a mass-loss process in red and the unaffected IRDC in red. The lowest values of α are consistent with non-thermal emission probably produced by the shocks already discovered [9, 10]. On the other hand, most of the IRDC (related to DR15) depicts values of α compatible with a cold cloud [28].

The CSM and the plateau identified in MGE042 and HD 168625/HD 168607 fields are mostly free-free. In addition, some of these components have values of α compatible with dark clouds.

The MGE027 field is dominated by values of α which are indicative of dark clouds, although with “skins” of lower spectral indices (note that this skin is almost absent in the IRDC of the G79.29+0.4 field). This behaviour may indicate that the dark clouds are immersed in a tenuous ambient partly affected by free-free radiation. The non-detection of the star in this case is indeed puzzling.

EPJ Web of Conferences **228**, 00023 (2020) https://doi.org/10.1051/epjconf/202022800023
mm Universe @ NIKA2

5 Concluding remarks

NIKA2 has opened a new road to explore the physical processes associated with the massive star evolution, improving our knowledge of the LBVs themselves and their CSM.

We report the detection of mm-continuum emission in four out of five of the observed LBVs. In addition, some circumstellar material, a shell, and surrounding clouds have also been detected.

First estimates of the spectral indices allowed us to disentangle the nature of the different components. The lowest values of α are found towards the stars and are hardly explained by free-free emission only. We propose that there is some non-thermal contribution to the total flux measured, especially at 2mm. MGE042, HD 168625, and HD 168607 are immersed within material having values of α typical of free-free emission. G79.29+0.46 is completely isolated; it is surrounded by a shell of free-free emission, which is clearly interacting with a nearby IRDC. Contrarily, the field of MGE027 is dominated by a cloud apparently driven by thermal dust emission, probably surrounded by tenuous gas.

The results gathered by these observations are relevant, but the whole work is far from being concluded. In some cases (such as G79.29+0.46 at 1mm or HD 168625 at 2mm) more observations are needed to improve the signal-to-noise ratio. The sample may be enlarged to more LBVs or candidates. Thorough modelling of the thermal and non-thermal processes in each particular case would be made and later analysed. Better angular resolution would be necessary to disclose material close to the star, presumably related to recent ejecta. Finally, the polarimetric capabilities of NIKA2 would be useful to perform polarimetry studies in these scenarios.

We would like to thank the IRAM staff for their professional support during the campaigns. The NIKA dilution cryostat has been designed and built at the Institut Néel. We acknowledge the crucial contribution of the Cryogenics Group, and in particular Gregory Garde, Henri Rodenas, Jean Paul Leggeri, and Philippe Camus. This work has been partially funded by the Foundation Nanoscience Grenoble and the LabEx FOCUS ANR-11-LABX-0013. This work is supported by the French National Research Agency under the contracts "MKIDS" and "NIKA" and in the framework of the "Investissements d'avenir" program (ANR-15-IDEX-02). This work has benefited from the support of the European Research Council Advanced Grant ORISTARS under the European Union's Seventh Framework Programme (Grant Agreement no. 291294). J.R.R. acknowledges support from Spanish grants ESP2015-65597-C4-1-R (MINECO/FEDER, UE) and ESP2017-86582-C4-1-R (AEI/FEDER, UE). A.R. acknowledges support from Spanish grant AYA2015-66211-C2-2 (MINECO/FEDER, UE).

References

[1] J. H. Groh, G. Meynet, S. Ekström, & C. Georgy, A&A **564**, A30 (2014)
[2] J. H. Groh, G. Meynet, & S. Ekström, A&A **550**, L7 (2013)
[3] W. Glatzel, & M. Kiriakidis, MNRAS **263**, 375 (1993)
[4] T. B. O'Hara, M. Meixner, A. K. Speck, T. Ueta, & M. Bobrowsky, ApJ **598**, 1255 (2003)
[5] D. R. Mizuno, K. E. Kraemer, N. Flagey, et al., AJ **139**, 1542 (2010) D. R.
[6] C. S. Buemi, C. Trigilio, P. Leto, et al., MNRAS **465**, 4147 (2017)
[7] J. R. Rizzo, F. M. Jiménez-Esteban, & E. Ortiz, ApJ **681**, 355 (2008)
[8] F. M. Jiménez-Esteban, J. R. Rizzo, & A. Palau, ApJ **713**, 429 (2010)
[9] J. R. Rizzo, A. Palau, F. Jiménez-Esteban, & C. Henkel, A&A **564**, A21 (2014)

EPJ Web of Conferences **228**, 00023 (2020) https://doi.org/10.1051/epjconf/202022800023
mm Universe @ NIKA2

[10] A. Palau, J. R. Rizzo, J. M. Girart, & C. Henkel, ApJL **784**, L21 (2014)
[11] C. Bordiu, J. R. Rizzo, & A. Ritacco, MNRAS **482**, 1651 (2019)
[12] L. Loinard, K. M. Menten, R. Güsten, L. A. Zapata, & L. F. Rodríguez, ApJL **749**, L4 (2012)
[13] L. Loinard, T. Kamiński, P. Serra, et al., ApJ **833**, 48 (2016)
[14] P. W. Morris, T. R. Gull, D. J. Hillier, et al., ApJ **842**, 79 (2017)
[15] N. Smith, A. Ginsburg, & J. Bally, MNRAS **474**, 4988 (2018)
[16] C. Bordiu, & J. R. Rizzo, MNRAS **490**, 1570 (2019)
[17] R. Adam, A. Adane, P. A. R. Ade, et al., A&A **609**, A115 (2018)
[18] M. De Becker, A&ARev **14**, 171 (2007)
[19] R. Blomme, Bulletin de la Societe Royale des Sciences de Liege **80**, 67 (2011)
[20] J. Sanchez-Bermudez, A. Alberdi, R. Schödel, et al., A&A **624**, A55 (2019)
[21] S. Rivera-Gálvez, C. G. Román-Zúñiga, E. Jiménez-Bailón, et al., AJ **150**, 191 (2015)
[22] C. Agliozzo, A. Noriega-Crespo, G. Umana, et al., MNRAS **440**, 1391 (2014)
[23] C. Agliozzo, A. Mehner, N. M. Phillips, et al., A&A **626**, A126 (2019)
[24] R. Blomme, D. M. Fenech, R. K. Prinja, J. M. Pittard, & J. C. Morford, A&A **608**, A69 (2017)
[25] A. R. Tieftrunk, R. A. Gaume, M. J. Claussen, T. L. Wilson, & K. J. Johnston, A&A **318**, 931 (1997)
[26] A. E. Wright, & M. J. Barlow, MNRAS **170**, 41 (1975)
[27] G. Montes, R. F. González, J. Cantó, M. A. Pérez-Torres, & A. Alberdi, A&A **531**, A52 (2011)
[28] S. Schnee, M. Enoch, A. Noriega-Crespo, et al., ApJ **708**, 127 (2010)

CHAPTER 4
A MOLECULAR RING IN AG CAR

In this chapter, we present a detailed study of the luminous blue variable AG Car and its circumstellar environment, combining APEX and ALMA observations of continuum and CO with ancillary archival data. We report the detection of a molecular ring-like structure, rather uncorrelated with the ionised nebula, that surrounds the star near its equatorial plane. We analyse its physical properties and propose several alternative formation scenarios, namely the accumulation of swept-up interstellar material by the stellar wind, a past non-conservative mass transfer event in a binary or a merger, and an equatorial mass-loss event induced by rotation. The content of this chapter has been published in Paper III.

4.1 Source details

AG Car is a canonical member of the LBV class. Located on the far side of the Carina arm (Humphreys et al., 1989) at a distance of 6±1 kpc (recently revised down to $4.7^{+1.2}_{-0.8}$ kpc, Smith et al. 2019), it stands out as one of the most luminous stars in the galaxy (1.5×10^6 $L_\odot$, Groh et al. 2011), and exhibits a remarkable spectrophotometric variability of up to 2 visual magnitudes, governed by decade-long S Dor cycles (Humphreys & Davidson, 1994; Stahl et al., 2001; Sterken, 2003).

Its circumstellar environment has been the target of multiple observations since the discovery of its ring nebula by Thackeray (1950). The structure, slightly elongated in the NW-SE direction, has a size of 30×40 arcsec, and expands at 70 km s^{-1} (Nota et al., 1992), being most likely associated with an eruptive mass-loss event occurred $\sim 10^4$ years ago (Vamvatira-Nakou et al., 2015). The dust and ionised gas content of the nebula have been thoroughly studied by Voors et al. (2000) and Vamvatira-Nakou et al. (2015) in the optical and infrared domains, who estimated a total nebular mass of around ~ 15 $M_\odot$. The star and the nebula have been detected also at cm-wavelengths with the Australia Telescope Compact Array (ATCA; Duncan & White 2002), showing strong hints of non-thermal processes currently at work ($\alpha = -0.1$).

Interestingly, Nota et al. (2002) reported a tentative detection of CO emission related to the star. Using the now decommissioned Swedish-ESO Submillimetre telescope (SEST), they coarsely mapped the distribution of CO $J = 1 \rightarrow 0$ and $J = 2 \rightarrow 1$ around AG Car, with a beam of 45 and 23 arcsec respectively, revealing a crowded

spectrum with multiple overlapping velocity components. Despite the moderate angular resolution achieved, a detailed kinematic analysis of the observed components led the authors to propose that a broad emission feature detected around 26.5 km s^{-1} was likely associated with the star, either forming an expanding envelope or a disk of about ~ 3 M$_{\odot}$. While this promising result was never confirmed by follow-up observations, it clearly suggested that the environs of AG Carina contains key information about the recent mass-loss processes, beyond what is traced by ionised gas and dust. The existence of a molecular phase in this source is certainly worth to be confirmed and explored in more detail.

4.2 Observations

AG Car was observed in two separate campaigns, using the Atacama Pathfinder Experiment (APEX) telescope and the Atacama Large Millimetre/Submillimetre Array (ALMA), located at Llano de Chajnantor (Chile). First, single-dish APEX observations were carried out in September 2014, as part of the project E-094-0598A (PI: G. Umana), targeting the CO $J = 3 \rightarrow 2$ transition. An OTF map of 100×100 arcsec around AG Car was performed under average weather conditions, 1–2 mm of precipitable water vapour (pwv), with a primary beam size of 19.2 arcsec and an effective velocity resolution of 0.08 km s^{-1} at the observing frequency.

Follow-up interferometric observations with ALMA were performed in October 2019, using the 7m and Total Power arrays (i.e., the Atacama Compact Array, or ACA), under good (pwv $\sim$ 1.25 mm) and excellent (pwv $\sim$ 0.25 mm) weather conditions, respectively. This run was framed in the project 2019.1.01056.S (P.I: L. Cerrigone). The spectral setup involved two windows targeting the lines CO $J = 2 \rightarrow 1$ and ^{13}CO $J = 2 \rightarrow 1$, plus additional spectral windows for continuum. The correlator was set to maximise the velocity coverage in the spectral line windows, obtaining a moderate velocity resolution of ~ 1.3 km s^{-1}. The beams of the interferometric and single-dish datasets were $\sim$7 and 28.5 arcsec, respectively. The two datasets were combined using the feathering procedure to recover all spatial scales with a 99.7% accuracy.

4.3 Summary of results

APEX and ALMA spectra confirm that the field toward AG Car is crowded by multiple velocity components of CO and ^{13}CO overlapping in the approximated velocity range $(0, +50)$ km s^{-1} (see Figure 4.1, right panel), in agreement with the literature spectra by Nota et al. (2002). After a close inspection of the data, we found that most of the components in the APEX CO $J = 3 \rightarrow 2$ spectra present a relatively ubiquitous spatial distribution and thus can be interpreted in terms of foreground and background contamination. However, a weak component at $\sim$32.5 km s^{-1}, marginally detected in the literature, displays a roughly bipolar morphology with respect to AG Car, as shown in the integrated intensity map of Figure 4.1.

ACA CO and ^{13}CO $J = 2 \rightarrow 1$ spectra, on the other hand, provide a three-fold angular resolution improvement over APEX data, and filter out most of the emission in the range v <30 km s^{-1}. Conversely, in the range $(+30, +40)$ km s^{-1} –roughly

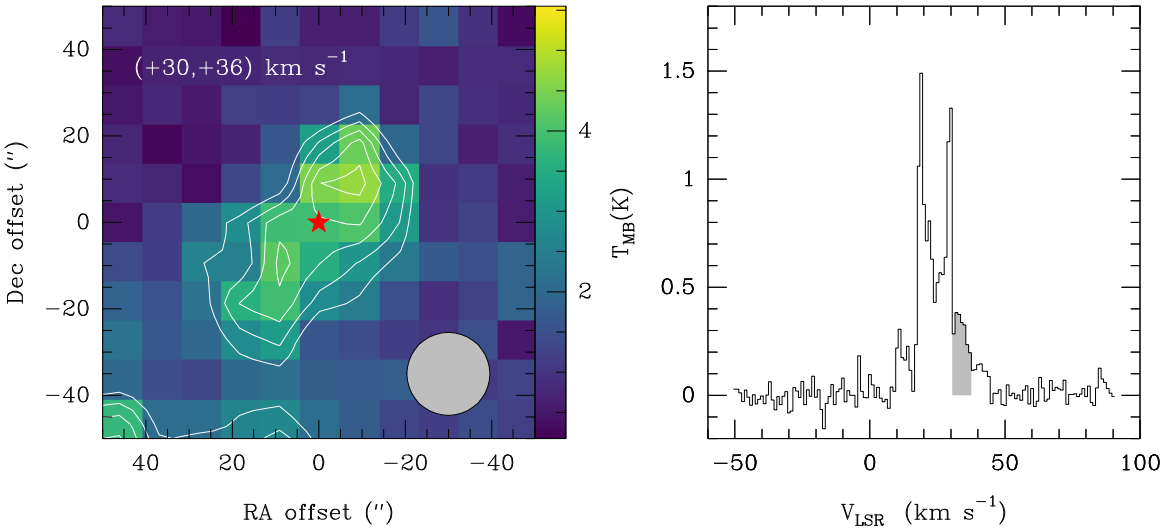

FIGURE 4.1: APEX velocity-integrated map of the CO $J = 3 \rightarrow 2$ transition towards AG Car, in the range (+30, +36) km s^{-1}, as highlighted in the spectra of the right panel. Contours starting at 2.5 K km s^{-1}, in steps of 1.1 K km s^{-1}. The position of the star is indicated by the red marker. The grey filled circle represents the APEX beam size.

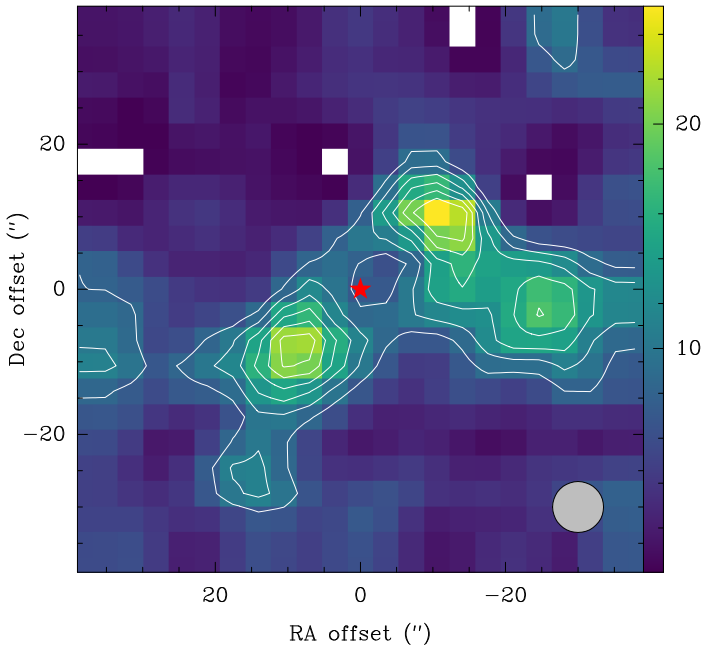

FIGURE 4.2: ACA velocity-integrated map of the CO $J = 2 \rightarrow 1$ transition toward AG Car. Contours starting at 8 K km s^{-1}, in steps of 2.5 K km s^{-1}. The position of the star is indicated by the red marker. The grey filled circle represents the ACA synthesized beam size.

matching the velocities of the bipolar component– a significant fraction of the flux is preserved (see Figure 2 in Paper III), suggesting a likely compact emission. Indeed,

the integrated intensity map over this range reveals an elliptical ring-like structure centred at 32.5 km s^{-1} that completely encloses the star, as seen in Figure 4.2. The structure extends roughly from 29 to 36 km s^{-1} and has an approximate angular size of 35 × 15 arcsec, with a position angle of 135°. It is dominated by two bright lobes at $(+10'', -10'')$ and $(-10'', +10'')$, connected by fainter arcs. A clump located at $(-25'', -5'')$ partially disrupts the ring on the west side.

Regarding the continuum emission, the ACA map at 225 GHz, shown in Figure 4.3, depicts a central point-like source surrounded by a ionised detached shell, resembling the ATCA continuum at 5.5 and 8.5 GHz (Duncan & White, 2002). We measure a flux density of 30.2 ± 2.2 mJy in the point source, and an integrated nebular flux of 40 ± 15 mJy.

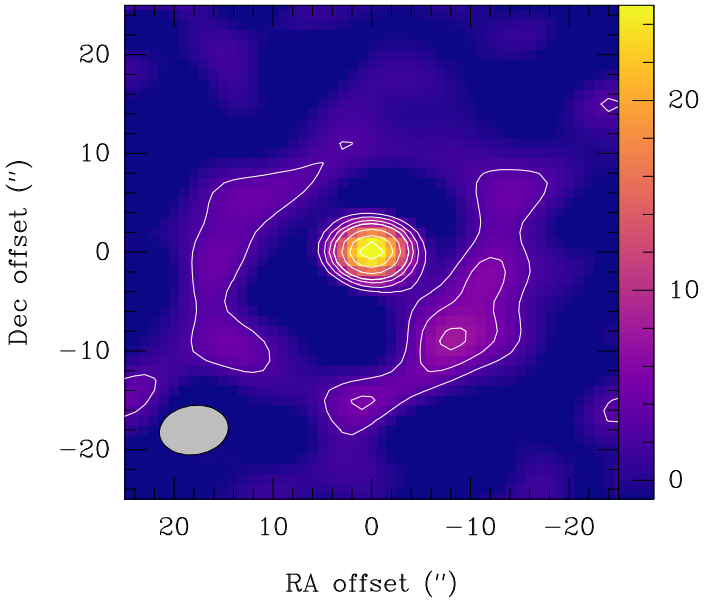

FIGURE 4.3: ACA continuum emission toward AG Car at 225 GHz. Contours starting at 2.5 mJy beam^{-1}, in steps of 2.5 mJy beam^{-1}. The grey filled ellipse represents the ACA synthesized beam.

4.4 Analysis and interpretation

The detection of a molecular ring-like structure surrounding AG Car adds a new piece to the complex circumstellar environment of this LBV star. To clarify the origin of the ring, we studied the properties of the gas in the context of the evolutionary history of AG Car. First, we carried out a detailed analysis of gas morphology and kinematics. We analysed gas dynamics employing channel maps (see Figure 5 in Paper III), identifying a clear velocity gradient along the major and minor axes of the structure, consistent with an outward radial motion. Considering the ellipse axis ratio and the location of the brightness peaks, we interpreted the structure as a circumstellar ring or torus seen nearly edge-on, with an inclination of 68 ± 3 degrees and a slow expansion velocity of $v_{\rm exp} = 3.5 \pm 0.5$ km s^{-1}.

To obtain insights on the excitation conditions of the gas, we computed the CO $(3 \rightarrow 2)/(2 \rightarrow 1)$ and $[^{12}CO/^{13}CO]$ line ratios from the single-dish data (APEX and Total Power) and used them to estimate the average physical parameters of the structure under non-LTE conditions. To do so, we created a grid of `RADEX` models and looked for the best fit to the observed ratios using a χ^2 criterion, as described in Chapter 2. The best-fitting model corresponds to $N(\mathrm{CO}) = 2.4 \times 10^{16}$ cm^{-2}, $T_\mathrm{k} = 50$ K and $n(\mathrm{H_2}) = 1.3 \times 10^3$ cm^{-3}, and moderately thick opacity (τ=0.8–1.2). These must be regarded only as average first estimates, i.e, higher-resolution observations could reveal more compact regions within the ring with higher densities and temperatures. In contrast, when applying the same fitting procedure to the other contaminating components in the field, we were unable to constrain the density and temperature properly, but systematically obtained order-of-magnitude lower column densities and optically thin solutions ($\tau \ll 1$).

Finally, to better disclose the velocity field of the gas, we created a kinematic model. Using the 3D radiative transfer code `LIME`, we built a simple ring model, following the same approach as for [GKF2010] MN101 in Paper I (see Chapter 3). We took the average density and temperature derived with `RADEX` as inputs and explored the influence of different velocity fields in the resulting channel maps. Four models were tested: a purely rotating ring with a constant rotation velocity $v_\phi = 1$ km s^{-1}, a purely expanding ring with $v_\mathrm{exp} = 3.5$ km s^{-1}, an expanding disk with a small differential rotation component, and an expanding ring with turbulent deviations of up to 0.25 km s^{-1}. The last two models (i.e., the expanding-rotating and the expanding-turbulent ring) reproduce satisfactorily most of the observed morpho-kinematic features, as well as the integrated and peak intensities of the CO $J = 2 \rightarrow 1$ map with an accuracy of $\sim$90% (see Figs. 11 and 12 in Paper III).

4.4.1 The continuum emission of AG Car

AG Car was observed with the ATCA telescope between 1994 and 1996, as part of the campaign C312, with the goal of disclosing the continuum emission of a number of LBV stars (Duncan & White, 2002). We have reprocessed the archival data at 5.5 and 8.8 GHz, with an angular resolution of $\sim$1 arcsec, to compare the relative brightness distribution with the new ACA map at 225 GHz. Figure 4.4 shows the two ATCA maps depicting a very similar morphology: a point-like source surrounded by a detached nebula, slightly elongated in the SE-NW direction. Duncan & White (2002) report a slightly negative spectral index of $\alpha = -0.1$ for both components, following the convention defined in Chapter 2.

In the low frequency regime, nebular emission clearly dominates over the central point source. Strikingly, our ACA data shows the opposite behaviour, with the most intense emission arising from the star, and a much shallower nebular component (see Figure 4.3). Besides, the point source flux density of ACA, 30.2 ± 2.2 mJy, is remarkably above the value predicted by the ATCA spectral index –which would be around 0.9 mJy. Such a discrepancy may obey to different reasons: AG Car could be highly variable in the radio, pretty much as it behaves in the optical; a new thermal component could be contributing to the emission at mm wavelengths, e.g., thermal dust; or both mechanisms could be acting simultaneously. Either way, if we combine the high and low-frequency fluxes to compute a more robust spectral index –ignoring

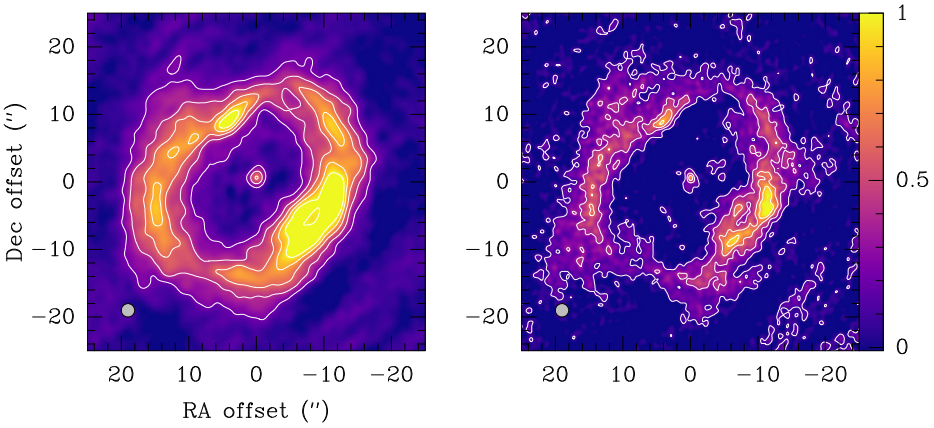

FIGURE 4.4: ATCA continuum emission toward AG Car at 5.5 GHz (left) and 8.8 GHz (right), from project C312 (reprocessed). Contours starting at 0.5 and 0.1 mJy beam^{-1}, in steps of 0.5 and 0.25 mJy beam^{-1}, respectively. The grey filled ellipse represents the ACA synthesized beam.

the temporal difference between measurements, of about 25 years–, we obtain $\alpha \sim 0.8$. This value is perfectly compatible with a thermal stellar wind, typical of LBV stars.

The nebular flux of ACA, on the other hand, is slightly lower than predicted from the literature spectral indices. In this case, the disagreement is easily explained by the fact that the largest angular scale of ACA at 225 GHz is about $\sim 1/3$ of that of ATCA at 5.5 GHz, which implies that a large fraction of the extended flux of the nebula is missed.

4.4.2 On the possible origin of the molecular ring

The molecular ring enclosing AG Car is affected by the star, presenting slightly different physical conditions from other surrounding gas clouds. We propose three scenarios that can account for the formation of such a structure, discussed in detail in Section 4.3 of Paper III. In the first, simplest scenario, the ring would be swept up pre-existing gas, either interstellar material or a remnant of the parent molecular cloud, that has survived the erosion by the strong UV fields and steady stellar winds of AG Car.

An alternative explanation is that the ring was formed through binary interaction, either from a non-conservative mass transfer episode in a close binary system or as a by-product of a complete stellar merger. Both processes could result in an equatorial density enhancement, slowly expanding outwards. In this regard, the possibility of AG Car belonging to a multiple system has been recently reinvigorated. Mahy et al. (2021), by means of interferometric observations with the Very Large Telescope (VLT), have reported a 7σ detection of a stellar companion, with a position angle of $\sim 100°$. This value is in good agreement with the position angle derived for the CO ring (135°), implying that the latter would lie close to the orbital plane of the binary system. Still, formation due to a merger event in the past cannot be completely ruled out. Indeed, a merger in a hierarchical triple system has been recently proposed as the detonator of η Car's Great Eruption in the 19th century (Portegies Zwart & van

den Heuvel, 2016; Smith et al., 2018a). The possible occurrence of a similar event in AG Car is thought-provoking and needs to be further investigated.

Finally, an equatorially enhanced mass-loss event would also explain the formation of a molecular ring from a single-star perspective. This event would be triggered by a rotationally induced bi-stability jump, as proposed for very luminous, fast-rotating stars (e.g., Maeder & Desjacques 2001). It is known that AG Car is a fast-rotator at least in its hottest state (Groh et al., 2006), and the molecular ring ($i \sim 70°$) is also close to the equatorial plane of the star ($i \sim 90°$, Groh et al. 2009a). Moreover, the presence of aspherical, bipolar features in the main nebula, including a helical dusty jet perpendicular to the molecular ring (see Figure 9 in Paper III), seem to support this hypothesis.

Under the assumption that the molecular gas formed in situ in an episode of equatorial mass loss, we reconstructed the mass loss history of AG Car incorporating this new piece of evidence. The dynamical age of the ring, taking $v_{\rm exp} = 3.5$ km s^{-1} as a lower limit, would be $t_{\rm dyn} < 10^5$ years. By invoking the standard wind interaction model, it is possible to explain the shaping of the CSM around AG Car qualitatively: first, the star may have suffered a slow equatorial mass-loss outflow triggered by rotation, which swept the surrounding ISM; this wind eventually got colder, coagulated and formed molecules. Then, a more violent isotropic outburst occurred, getting pinched by the previous dense wind at equatorial latitudes and expanding more freely toward the poles, giving rise to the slightly bipolar morphology observed at infrared and radio wavelengths. This scenario is consistent with the dynamical timescale derived from the infrared (Vamvatira-Nakou et al., 2015).

We thus reviewed the mass budget and mass loss rates in the literature, taking into account this new molecular component. We determined a total mass of molecular gas of 2.7 ± 0.9 M$_\odot$ for a standard [CO/H$_2$] abundance of 10^{-4}. The total circumstellar mass adds up to 9.3 ± 2.8 M$_\odot$ considering the mass of ionised gas estimated by Vamvatira-Nakou et al. (2015) (6.6 ± 1.9 M$_\odot$), or to 5.9 ± 2.8 M$_\odot$, if we derive the ionised mass independently using the ACA continuum. Either way, we conclude that molecular gas represents *at least* a 30% of the total circumstellar mass of AG Car. This result underlines the need for a proper characterization of the molecular component in the CSM of LBV stars.

At this point, it is also interesting to estimate the net linear momentum of this circumstellar material. Assuming an isotropic expansion at a constant velocity of $v_{\rm main} = 70$ km s^{-1} for the main nebula (Nota et al., 1992), and radial expansion at $v_{\rm ring} = 3.5$ km s^{-1} for the molecular ring, the linear momentum of the gas p (in module) can be written as:

$$p = M_{\rm main} v_{\rm main} + M_{\rm ring} v_{\rm ring} \tag{4.1}$$

obtaining 9.4×10^{35} kg m s^{-1}. The total kinetic energy is $E_{\rm k} = 3 \times 10^{47}$ ergs, of which only 0.1% ($\sim 10^{43}$ erg) corresponds to the ring, strongly suggesting that it originated in a much less energetic event than the main nebula. Indeed, the total kinetic energy of the CSM of AG Car falls several orders of magnitude short when compared to the Homunculus Nebula of η Car, even for the most conservative estimates of mass and expansion velocity ($\sim 10^{50}$ erg, Smith 2013). This discrepancy somewhat weakens the stellar merger hypothesis.

We can likewise estimate the mechanical luminosity of AG Car, given by:

$$L_{\rm mech} = \frac{1}{2}\dot{M}v_{\infty}^{2} \tag{4.2}$$

where $\dot{M}$ is the mass-loss rate and v_{∞} the terminal wind velocity. Taking $\dot{M} = 1\times10^{-5}$ $M_{\odot}$ yr^{-1} and $v_{\infty} = 200$ km s^{-1} as representative values for AG Car in its current steady state (e.g., Groh et al. 2009b), we obtain $L_{\rm mech} \sim 10^{35}$ erg s^{-1}. The kinetic energy of the molecular ring is hence equivalent to the accumulated mechanical output of the star in ~ 3 years.

Finally, we used the 225 GHz continuum flux density of the stellar point source to provide a new, independent estimate of the current day mass-loss rate of AG Car. Following the empirical formula by Panagia & Felli (1975) as introduced in Chapter 2, and adopting average wind parameters Groh et al. 2009b, we obtain $(1.55\pm0.21)\times10^{-5}$ $M_{\odot}$ yr^{-1}, in excellent agreement with previous literature values derived by other means.

4.5 Concluding remarks

In Paper III, we combined new APEX and ALMA observations to confirm the existence of a molecular structure in the surroundings of AG Car, as hypothesised by Nota et al. (2002). From the analysis of multi-transition CO spectra and continuum data, we conclude that AG Car is surrounded by a slowly expanding ($v_{exp} = 3.5$ km s^{-1}), warm ($T_k \sim 50$ K) and moderately dense ($n(H_2) \sim 10^3$ cm^{-3}) molecular ring, aligned with the equatorial plane of the star. At least three evolutionary scenarios can account for the formation of the structure: (i) the accumulation of pre-existing material by the action of the stellar wind; (ii) a non-conservative mass transfer episode or a merger in a close binary system; (iii) an equatorially enhanced mass loss episode. Considering the evidence available, we regard the last scenario as the most plausible at the moment, but the recent discovery of a possible stellar companion underlines the need to further explore the binary formation mechanisms. The mass of molecular gas is 2.7 ± 0.9 $M_{\odot}$. Putting together a global view of the mass-loss record of AG Car, and assuming that the molecular gas formed in situ, the molecular phase represents at least a 30% of the total mass ejected by AG Car.

4.6 Bordiu et al., 2021 (Paper III)

Monthly Notices of the ROYAL ASTRONOMICAL SOCIETY

MNRAS **500,** 5500–5514 (2021) doi:10.1093/mnras/staa3606
Advance Access publication 2020 November 20

A warm molecular ring in AG Car: composing the mass-loss puzzle

C. Bordiu [1,2★] F. Bufano,[1] L. Cerrigone,[3] G. Umana,[1] J. R. Rizzo,[2,4] C. S. Buemi,[1] P. Leto [1] F. Cavallaro [1,5] A. Ingallinera [1] S. Loru,[1] C. Trigilio[1] and S. Riggi[1]

[1]*INAF-Osservatorio Astrofisico di Catania, Via Santa Sofia 78, I-95123 Catania, Italy*
[2]*Centro de Astrobiología (INTA-CSIC), Ctra. M-108, km. 4, Torrejón de Ardoz, E-28850 Madrid, Spain*
[3]*Joint ALMA Observatory, Alonso de Córdova 3107, Vitacura, 7630000, Santiago, Chile*
[4]*ISDEFE, Beatriz de Bobadilla 3, E-28040 Madrid, Spain*
[5]*Department of Astronomy, The Inter-University Institute for Data Intensive Astronomy (IDIA), University of Cape Town, Private Bag X3, Rondebosch, 7701, South Africa*

Accepted 2020 November 13. Received 2020 November 6; in original form 2020 September 8

ABSTRACT

We present APEX observations of CO $J = 3 \rightarrow 2$ and ALMA observations of CO $J = 2 \rightarrow 1$, ^{13}CO $J = 2 \rightarrow 1$, and continuum towards the Galactic luminous blue variable AG Car. These new observations reveal the presence of a ring-like molecular structure surrounding the star. Morphology and kinematics of the gas are consistent with a slowly expanding torus located near the equatorial plane of AG Car. Using non-LTE line modelling, we derived the physical parameters of the gas, which is warm ($\sim$50 K) and moderately dense ($\sim 10^3$ cm^{-3}). The total mass of molecular gas in the ring is 2.7 ± 0.9 M$_\odot$. We analysed the radio continuum map, which depicts a point-like source surrounded by a shallow nebula. From the flux of the point-like source, we derived a current mass-loss rate of $\dot{M} = (1.55 \pm 0.21) \times 10^{-5}$ M$_\odot$ yr^{-1}. Finally, to better understand the complex circumstellar environment of AG Car, we put the newly detected ring in relation to the main nebula of dust and ionized gas. We discuss possible formation scenarios for the ring, namely, the accumulation of interstellar material due to the action of the stellar wind, the remnant of a close binary interaction or merger, and an equatorially enhanced mass-loss episode. If molecular gas formed *in situ* as a result of a mass eruption, it would account for at least a 30 per cent of the total mass ejected by AG Car. This detection adds a new piece to the puzzle of the complex mass-loss history of AG Car, providing new clues about the interplay between LBV stars and their surroundings.

Key words: stars: evolution – stars: individual: AG Carina – stars: massive – stars: mass-loss – ISM: abundances – ISM: molecules.

1 INTRODUCTION

Over the course of their lifetime, massive stars have a great impact in the chemistry, structure, and dynamics of the interstellar medium (ISM). This impact intensifies as they enter the luminous blue variable (LBV) phase, a brief ($\sim 10^4$ yr) and unstable post-main-sequence stage, in which massive stars exhibit the highest mass-loss rates (up to 10^{-3} M$_\odot$ yr^{-1}). Such a copious mass-loss occurs by virtue of dense and steady stellar winds and, sporadically, violent outbursts like the Great Eruption of η Car in the 19th century. The interaction between this mass-loss, interstellar material, and different wind regimes shapes the closest circumstellar environment, leading to the formation of large multiphase nebulae.

Nebulae around LBV stars (LBVNs) therefore emerge as valuable laboratories to understand the feedback mechanisms between the parent stars and their environment. The multiwavelength study of this circumstellar material is a crucial tool to trace back the mass-loss record of these sources throughout their different evolutionary phases (e.g. Umana et al. 2005, 2009, 2010; Agliozzo et al. 2014; Cerrigone et al. 2014; Buemi et al. 2017). However, most of the research so far has focused on the dust and ionized gas content of LBVNs, paying little attention to the missing piece of the picture: the molecular gas.

In recent years, carbon monoxide and a handful of other simple molecular species have been detected in the surroundings of several candidate and confirmed LBVs, such as G79.29+0.46 (Rizzo, Jiménez-Esteban & Ortiz 2008, Rizzo et al. 2014), [GKF2010] MN101 (=MGE 042.0787+00.5084, Bordiu, Rizzo & Ritacco 2019), and the well-known η Car (Smith & Davidson 2001; Loinard et al. 2012; Loinard et al. 2016; Smith; Ginsburg & Bally 2018a; Bordiu & Rizzo 2019; Gull et al. 2020; Morris et al. 2020). All these successful detections demonstrate that, provided the adequate physical conditions, conspicuous amounts of molecular gas can arise and survive for some time in the hostile outskirts of these stars. By analysing the emission at mm- and sub-mm wavelengths from rotational transitions of CO and other species, one can obtain valuable kinematic information that allows for precisely reconstructing previous mass-loss events and place constraints on the timescales of the observed structures. Therefore, the very existence of these molecules opens a complementary window to learn about the mass-loss phenomena in these hot, massive stars, beyond what is

★ E-mail: cristobal.bordiu@inaf.it

CHAPTER 5

THE PECULIAR INNER EJECTA OF η CARINA

In this chapter, we describe the results of our research on the LBV star η Carina. We present ALMA interferometric observations at a resolution better than 0.2 arcsec, mapping the distribution of CO, HCN, $H^{13}CN$ and HCO^+ in the Homunculus Nebula. We report the discovery of new molecular ejecta very close to the star, likely associated with the eruption that took place in the 1890s. This work has been published in Paper IV.

5.1 Source details

η Carina is a very massive binary system in which the primary source, η Car A, is a bona fide LBV star with a current mass of $\sim$100 $M_\odot$, and its companion, η Car B, is a hotter, less massive star of about 30–40 $M_\odot$ (Mehner et al., 2010), with spectroscopic signatures only found in late-O and WR stars (Iping et al., 2005). The system is very eccentric ($e = 0.9$), with a well-determined orbital period of 5.54 years and a minimum separation at periastron of 1.54 A.U (Damineli, 1996).

η Car A (hereafter η Car) is an outstanding and peculiar member of the LBV family and one of the most luminous sources in the Milky Way ($>5 \times 10^6$ $L_\odot$, Davidson & Humphreys 1997) –indeed the brightest object at mid-infrared wavelengths (Smith, 2012)–. It has been exhaustively studied ever since it underwent a prodigious outburst around 1843, that was nicknamed the Great Eruption. This event, which constitutes the archetypal LBV giant mass eruption, expelled more than 20 $M_\odot$ of gas and dust in a very short time (Gomez et al., 2010), irrigating the surroundings of η Car with CNO-enriched matter and giving birth to the prominent Homunculus Nebula (Gaviola 1950, Davidson & Humphreys 1997). The Homunculus is a bipolar nebula with a current size of 16×10 arcsec (Allen & Hillier, 1993), expanding at $\sim$650 km s^{-1} (Davidson & Humphreys, 1997). It is surrounded by the so-called outer ejecta, fast moving material with velocities of several $\sim$1000s km s^{-1} (Smith, 2008) and a diffuse halo of X-ray emission, of roughly 40×70 arcsec (Seward et al., 2001). A few years after the Great Eruption, around the 1890s, η Car suffered a second, lesser outburst, which produced a similar but much smaller inner structure, commonly referred to as the Little Homunculus, almost mimicking a matryoshka doll (Ishibashi et al., 2003).

The innermost region of the Homunculus, i.e., the central arcseconds around η Car, is an extremely hostile environment, exposed to strong FUV/X-ray fields and periodical shocks, modulated by the 5.54-year orbital period of the binary system (Pittard & Corcoran, 2002; Corcoran et al., 2017). The two stars are so close that their winds interact in intricate manners, producing complex wind structures that accumulate with every new orbit. Okazaki et al. (2008) and Gull et al. (2009, 2016) characterised the fossil wind structures in detail, identifying distinctive knots, shells and arc-like features traced by forbidden lines of Fe and N, and proposed an interaction scenario in which a low-density cavity, approximately pointing to apastron, is carved out when the hot and fast wind of η Car B disrupts the slower and much denser primary wind. This region represents a large reservoir of ionised gas, as suggested by the detection of multiple radio recombination lines and strong thermal continuum emission (Abraham et al., 2014)

η Car harbours the largest molecular inventory among the LBV class. Detection of H_2, distributed all over the surface of the lobes of the Homunculus, was accomplished by Smith & Davidson (2001). Later, Smith et al. (2006) tentatively detected NH_3 toward the inner region of the nebula[1]. The first thorough molecular survey of η Car was carried out by Loinard et al. (2012) with the APEX single-dish telescope. They reported the detection of six species, namely CO, CN, HCN, HNC, HCO^+ and N_2H^+, and two isotopologues, ^{13}CO and $H^{13}CN$. However, the moderate angular resolution of the observations prevented a proper study of the spatial distribution of these molecules. Some years later, Loinard et al. (2016) coarsely mapped the distribution of HCN with ATCA, achieving a resolution of 5 arcsec, and concluded that the molecular reservoir was located in the central few arcseconds of the Homunculus. Recently, ALMA observations at 1 arcsec resolution by Smith et al. (2018b) revealed the existence of an expanding torus of CO in the waist of the Homunculus, i.e., nearly coincident with the equatorial plane of η Car. The gas in the torus is expanding at $\sim$100 km s^{-1}, and its kinematic age is consistent with an ejection date around the 1840s, probably linked to the Great Eruption. This result implies that substantial amounts of molecular gas can form out of stellar ejecta in very short time scales ($\sim$ 200 years), even in such a harsh environment. η Car becomes a rare laboratory where we can learn about the fast formation pathways of molecular gas under the most extreme conditions.

5.2 Archival data

In this work, we analysed public Atacama Large Millimetre-Submillimetre Array (ALMA) Band 7 archival observations of η Car and its surroundings, corresponding to project 2016.1.00585.S (P.I: G. Pech-Castillo). The source was observed for 668 s on 2016 October 24, under excellent weather conditions –0.57 mm of precipitable water vapour–. A total of 41 12-m antennas were used, providing an excellent uv-coverage and a maximum baseline of 1.8 km, resulting in a synthesised beam of 0.17×0.13 arcsec. The correlator was set to simultaneously observe four spectral windows corresponding to the rotational lines CO $J = 3 \rightarrow 2$, $H^{13}CN$ $J = 4 \rightarrow 3$,

[1]Loinard et al. (2016) claims that this detection is a misidentification of the H81β RRL

HCN $J = 4 \rightarrow 3$ and HCO^+ $J = 4 \rightarrow 3$. The resulting data products include four spectral cubes and a continuum map.

5.3 Summary of results

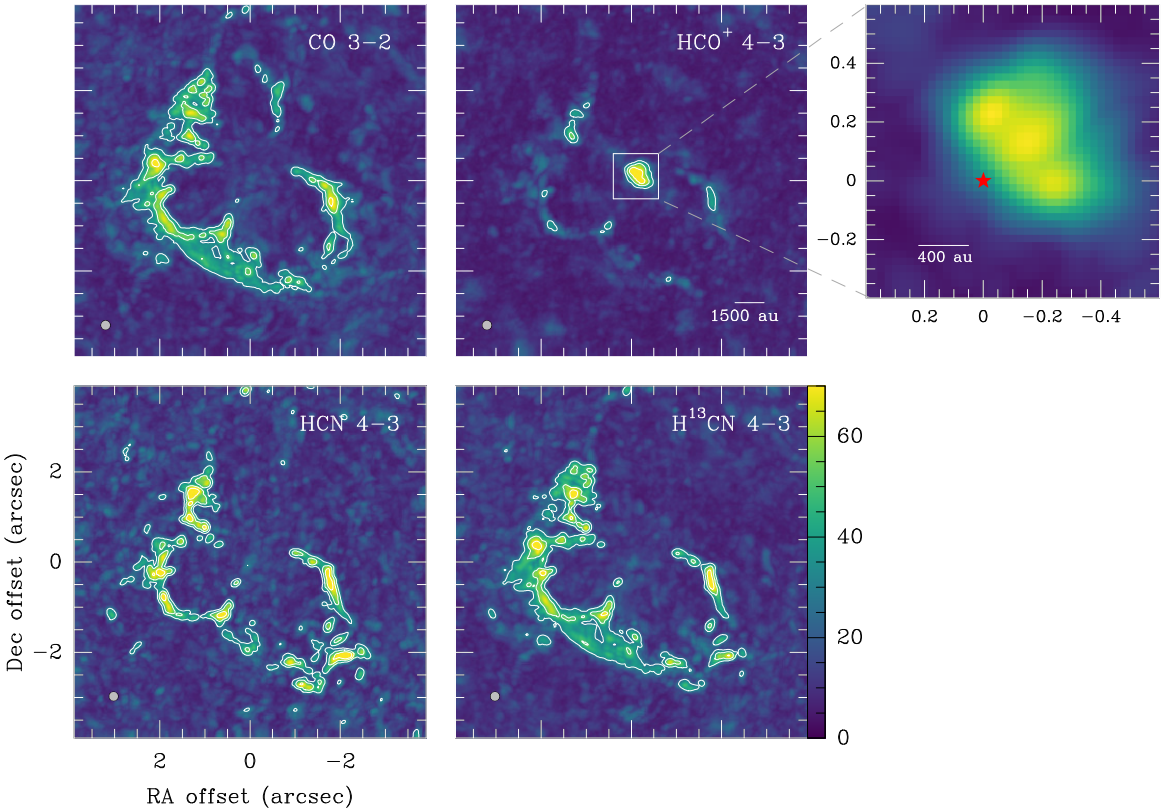

FIGURE 5.1: Peak-intensity maps of the observed species in the field of η Car, as indicated in the top right corner. Contours at 30, 50 and 70 K. The inset shows a close-in view of the HCO^+ emission in the innermost region, with the position of η Car indicated by the red marker.

Emission from CO, HCN, $H^{13}CN$, and HCO^+ is detected arising from multiple independent components towards η Car, in the approximate velocity range $(-100, +100)$ km s^{-1}. Integrating the emission over this range, all the molecules trace a clumpy C-shaped structure surrounding the star, as shown in Figure 5.1. This structure corresponds to the equatorial torus described by Smith et al. (2018b) from CO $J = 2 \rightarrow 1$ observations, also related to the dusty "Butterfly nebula" described by (Chesneau et al., 2005). A second structure, smaller and located closer to the star (<1000 au), slightly to the NW, is only visible in the HCO^+ map. The structure is elongated, with an approximate size of 0.6×0.4 arcsec, and bright, with a peak intensity of 77.5 ± 6.8 K. We nicknamed this structure "the Peanut" for its peculiar morphology (see the inset in Figure 5.1).

Radio continuum emission is only detected above 5σ in the inner arcsec of the Homunculus. It is composed of a point-like source, presumably related to the η Car system, and an extended emission matching the distribution of HCO^+, as portrayed

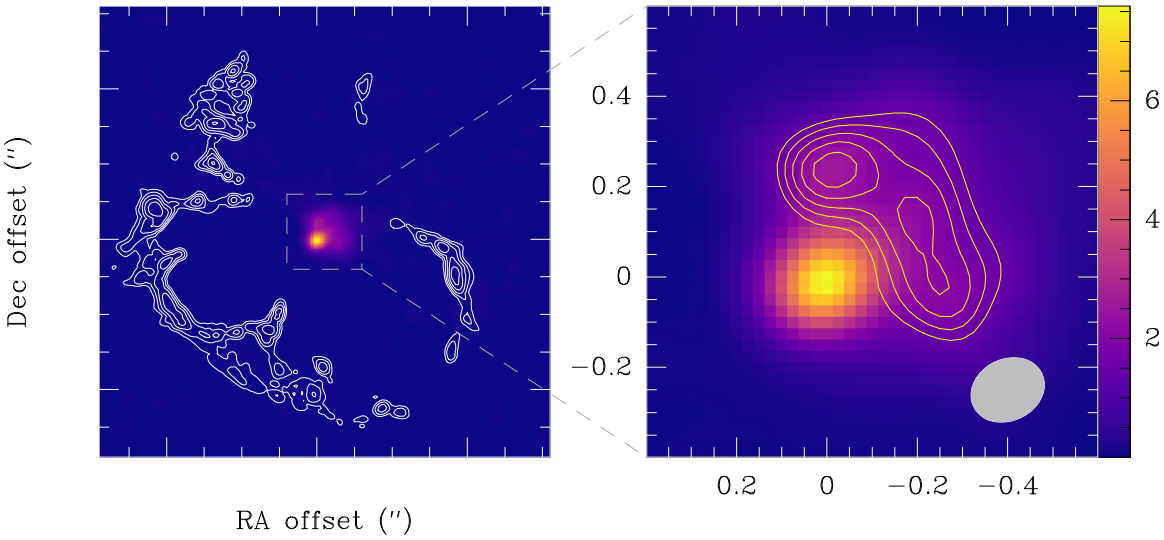

FIGURE 5.2: Continuum emission toward η Car. Left: Overall continuum emission in the field of η Car in colour scale, with the CO contours from Figure 5.1 shown as reference. Right: Close-in view of the continuum emission in the innermost region, composed by a point-like source and an extended component. Contours from 1.4 to 2.2 Jy beam^{-1} after point-source subtraction. The grey filled ellipse represents the ALMA beam size.

in Figure 5.2. The continuum point-like source has a deconvolved size of 0.11 × 0.11 arcsec, with a peak intensity of 6.41±0.02 Jy beam^{-1}. On the other hand, the extended component has an integrated flux density of 17.4±1.1 Jy.

Finally, a number of absorption components of CO, HCN and H^{13}CN are detected toward the continuum-emitting region (see Figure 2 in Paper IV). The CO absorption is narrow, with a FWHM of 0.6 km s^{-1} and a central velocity of −9 km s^{-1}. Conversely, the HCN and H^{13}CN absorptions are broader, with FWHMs of ∼ 12 km s^{-1} and central velocities of −60 km s^{-1}, and appear only toward the point source.

5.4 Analysis and interpretation

We thoroughly analysed the morpho-kinematic features and physical conditions of the detected emission, to properly relate the molecular gas and previously known structures, and link its formation and survival with the complex evolutionary record of η Car.

First, we carried out a detailed analysis of the HCO$^+$ emission from the Peanut. Inspection of the spatial distribution of HCO$^+$ indicates a possible relation with the Weigelt blobs, a group of ionised clumps of ejecta probably expelled in the 1890s eruption, that are moving at nearly −40 km s^{-1} close to the orbital plane of the binary system (Weigelt & Ebersberger, 1986). This somehow suggests that the molecular gas arises from the same ejecta. However, analysis of the molecular gas kinematics (see Figures 3 and 4 in Paper IV) reveals an incompatible velocity gradient toward positive velocities. The channel maps of HCO$^+$ in the range (−80, +80) km s^{-1} show a complex succession of arc-like features evolving from SE to NW that seem to

surround the position of the Weigelt blobs. We propose a very simple conical model able to reconcile the motion of the Weigelt blobs with the velocity field of the HCO^+ gas. This model, displayed in Figure 5.3, is in excellent agreement with previous simulations of the colliding wind region of η Car, predicted to have a roughly conical structure with the opening toward apastron (e.g., Okazaki et al. 2008; Gull et al. 2009).

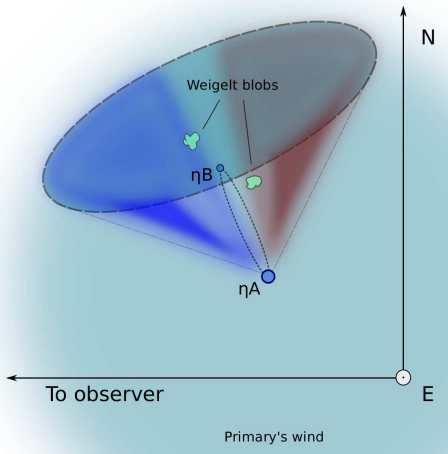

FIGURE 5.3: Proposed model for the viewing geometry of the HCO^+ emission in the innermost region of the Homunculus. The blue and red colours indicate the motion of the gas relative to the observer. The primary wind sphere, the shock cone, the Weigelt blobs and the orbital plane are arbitrarily scaled.

The presence of HCO^+ in such a harsh region is challenging, so we assessed its survivability close to η Car. The innermost region of the Homunculus nebula is exposed to strong FUV fields modulated by the orbital cycle of the binary, that should quickly photodissociate molecules. Still, we note that: (i) HCO^+ is particularly immune to FUV photons (e.g., Koch et al. 1995) and that (ii) previously reported ionised structures in the innermost region of the Homunculus, traced by [FeII] and [FeIII] (e.g., Gull et al. 2016) may provide sufficient shielding to ensure the survival of significant amounts of molecules, as noted by Morris et al. (2017).

The detection of several absorptions of CO, HCN and $H^{13}CN$ toward the core of the Homunculus constitutes another puzzling feature of η Car. As shown in Figure 5.4, the CO absorption is spatially extended, being particularly deep toward the continuum point source, with a shallower component spreading over the continuum-emitting region to the NW. The absorption is extremely narrow (FWHM ~ 0.5 km s^{-1}), with a rest velocity of ~ -9 km s^{-1}, that we associate with an intervening cloud at some point along the line of sight. Interestingly, Damineli et al. (2019, 2021) provided evidence in favour of the existence of a "natural coronagraph", a dusty cloud partially

blocking our view of η Car. The slow dissipation of such a cloud would be responsible for the secular brightening of η Car –as opposed to the Homunculus Nebula, whose brightness remains almost constant through the years. A possible relation between the CO absorption and this structure is worth to be explored in further works (e.g., by evaluating if the absorption changes due to the alleged dissipation of the cloud).

Contrarily, the HCN and $H^{13}CN$ absorptions are considerably broader (FWHM $\sim$ 12 km s^{-1}), compact and almost –but not perfectly– coincident with the point-like source. We interpret these absorptions as hot bullets expelled by the star, with a relative velocity of -40 km s^{-1}(comparable to that of the Weigelt blobs). We also identify the vibrationally excited ($v_2 = 1$) counterparts of the HCN and $H^{13}CN$ lines at the same velocity, excited by the strong infrared photons emitted by η Car (see Figure 5.4). In the third panel, corresponding to the vibrationally excited component, a second clump, totally isolated from other structures, is seen in emission toward the SE. All these features provide evidence of other bullets ejected from the star.

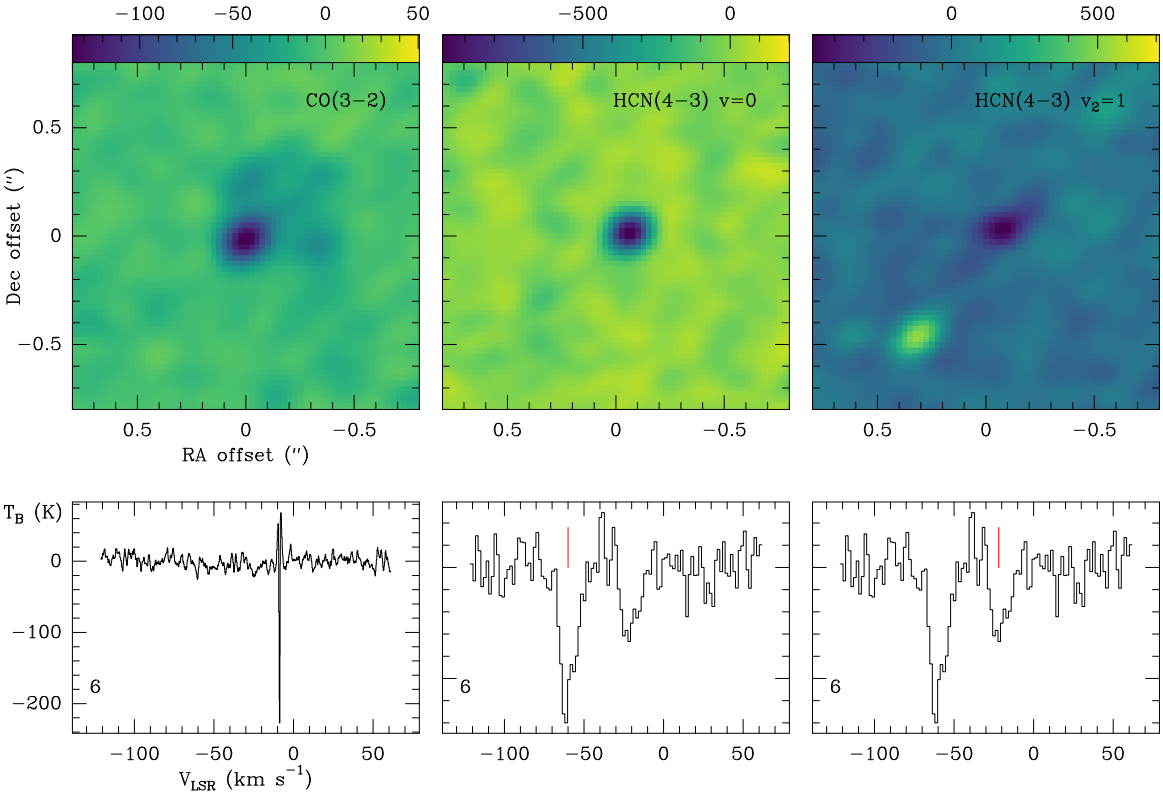

FIGURE 5.4: Line absorptions of CO $J = 3 \rightarrow 2$, HCN $J = 4 \rightarrow 3$, $v = 0$ and HCN $J = 4 \rightarrow 3$, $v_2 = 1$ toward η Car. Top: integrated intensity maps of the absorptions. Note the different distribution of CO, extending toward the NW. Bottom: spectra of the transitions indicated in the top panels, averaged in a region of 0.1 arcsec around the continuum point source. Red markers identify the HCN $v = 0$ and $v_1 = 2$ transitions in the corresponding panels.

To better understand the origin of all these features, we studied the molecular abundances in the torus, the Peanut and the bullets. At different positions in the torus (see Figure 8 in Paper IV), we obtain CO column densities of the order of 10^{18} cm^{-2}, compatible with those reported by Morris et al. (2017) from high-J CO

observations of the Homunculus Nebula. We measure [HCN/CO] ratios of $\sim 10^{-3}$, in line with previous evidence of strong N-enrichment in η Car. In the bullet, the HCN and $H^{13}CN$ column densities are remarkably similar, of 0.6×10^{15} and 0.7×10^{15} cm^{-2} respectively, resulting in a low [HCN/H^{13}CN] ratio close to ∼1. This points to a very low [C^{12}/C^{13}] proportion, which, as discussed in Chapter 3, is the typical footprint of heavily processed ejecta, due to the favoured production of ^{13}C as a by-product of the CNO cycle (Berdyugina & Savanov, 1994).

From previous literature estimates of the molecular gas mass in the equator of the Homunculus (e.g., Smith et al., 2018c), we inferred a CO under abundance factor of 8–40 with respect to standard ISM values, in line with previous claims by Morris et al. (2017). Finally, using HCO^+ as a proxy, we derived a parameterised expression of the mass of molecular gas in the Peanut, of $(0.8 \pm 0.3) \times \frac{X_{HCO^+}}{10^{-8}}$ M$_\odot$. This is useful to constrain the possible range of masses. For [HCO^+/H_2] ratios of 10^{-9} and 10^{-8}, typical of ultracompact HII regions and young stellar objects, respectively (Liszt, 2007; Hogerheijde et al., 1997), we obtain masses in the range 0.1–1 M$_\odot$. These masses are similar to the estimates for the 1890s eruption by Ishibashi et al. (2003), who established an upper limit of 1 M$_\odot$ of ionized gas and 0.01 M$_\odot$ of dust. Our result hence supports that molecular gas traces a significant, non-negligible fraction of the total ejected mass, as occurs in other objects like AG Car (see Chapter 4).

5.4.1 On the puzzling chemistry of the Peanut

The Peanut exhibits a truly intriguing chemistry, since HCO^+ is the only molecule observed in this region. While the non-detection of HCN and its isotopologues can be easily explained by invoking an aggressive photochemistry, the detection of significant amounts of HCO^+ apparently in the absence of CO –which indeed does not obey to sensitivity issues– is extremely hard to explain. The dominant formation and destruction routes of HCO^+ in the ISM (proton-transfer and dissociative recombination reactions, respectively) involve CO at some point, as elaborated in Section 5.3 of Paper IV. Therefore, this seeming chemical imbalance highlights the need for exploring alternative formation pathways and developing new chemical models, able to reproduce the formation and destruction of molecules in extreme environments and short timescales.

The innermost region of η Car is characterised by intense emission from multiple radio recombination lines, that arise from highly ionised material (Abraham et al., 2014). Indeed, recent ALMA observations with very high angular resolution of the H30α and He30α lines have disclosed a compact core (the binary system) and several unresolved knots extending to the NW and more or less coincident with the HCO^+ emission (Abraham et al., 2020). The authors, in view of the harsh conditions of the region and the difficulty to explain the survival of molecular material so close to η Car, have proposed that the HCO^+ detection may be instead a misidentification of the H40δ line. Considering the similar rest frequencies (356.734 and 356.658 GHz, respectively) and the large velocity dispersion and clumpy nature of the gas towards this region, we acknowledge this possibility. Further high-resolution observations of the core of the Homunculus, involving other transitions and tracers, will be required to settle this matter.

5.5 Concluding remarks

In Paper IV, we report ALMA observations of the innermost region of the Homunculus Nebula, with an unprecedented resolution better than 0.2 arcsec. We identify the HCN, $H^{13}CN$ and HCO^+ counterpart of the CO torus reported by Smith et al. (2018b), resolving its clumpy structure for the first time. Besides, we report the detection of a new structure closer to η Car, toward the NW, only visible in HCO^+ and continuum. After studying its morpho-kinematic features, we interpret the structure as a conical ejecta from the 1890s lesser eruption, moving outwards within the cavity carved by the wind-wind interactions of the binary.

We also detected absorption lines of CO, HCN, and $H^{13}CN$ toward the continuum-emitting region. The CO absorption is most likely produced by an intervening dusty cloud that partially blocks our vision of the Homunculus, while the HCN and $H^{13}CN$ absorptions, with a more compact morphology, correspond to several hot bullets of ejecta expelled by the star.

Finally, by studying the molecular abundances in each region, we found strong hints of N-enrichment in the torus and bullets, as well as a notable CO under abundance, consistent with the massive evolved nature of η Car, and a puzzling chemistry toward the Peanut, where considerable amounts of HCO^+ are observed together with a striking lack of CO.

5.6 Bordiu & Rizzo, 2019 (Paper IV)

Monthly Notices of the ROYAL ASTRONOMICAL SOCIETY

MNRAS **490,** 1570–1580 (2019) doi:10.1093/mnras/stz2621
Advance Access publication 2019 September 19

The peculiar chemistry of the inner ejecta of Eta Carina

Cristobal Bordiu [1]★ and J. Ricardo Rizzo[1,2]★

[1]*Centro de Astrobiología (INTA-CSIC), Ctra. M-108, km. 4, E-28850 Torrejón de Ardoz, Madrid, Spain*
[2]*ISDEFE, Beatriz de Bobadilla, 3, E-28040 Madrid, Spain*

Accepted 2019 September 12. Received 2019 September 12; in original form 2019 March 27

ABSTRACT

We investigated continuum and molecular line emission of four species (CO, HCN, $H^{13}CN$, and HCO^+) at 0.8 mm in the inner region around η Car, using ALMA archival observations at a resolution better than 0.2 arcsec. We report the discovery of an asymmetric extended structure north-west of the star, independent from the continuum point source. The structure is only traced by continuum and HCO^+, and not detected in the other lines. Kinematics of this structure reveal that the HCO^+ gas likely arises from ejecta expelled in the 1890s eruption. The ejecta is propagating outwards within the cavity produced by the current wind–wind interaction of η Car A and its companion. Chemical analysis of the ejecta reveals an apparent lack of CO and nitrogen-bearing species. We explore possible explanations for this peculiar chemistry, that differentiates this structure from the ejecta of the Great Eruption, rich in HCN and $H^{13}CN$. We also report an absorption component near the continuum point source, only traced by HCN and $H^{13}CN$ in their vibrational-ground and vibrationally excited states. This absorbing gas is attributed to a hot bullet of N-enriched material expelled at a projected velocity of 40 km s^{-1}.

Key words: stars: evolution – stars: individual: η Carina – stars: massive – stars: mass-loss – ISM: abundances – ISM: molecules.

1 INTRODUCTION

Luminous blue variables (LBVs) are evolved massive stars characterized by remarkable spectrophotometric variability and heavy mass loss in the form of dense and steady winds and occasional eruptions. LBVs shed out large amounts of dust and CNO-enriched material into their surroundings. The shocks and strong FUV fields produced by LBVs represent a continuous energy input to the stellar neighbourhood, eventually altering its structure and composition.

η Car is the archetypal member of the LBV family, and one of the most luminous sources in the Galaxy (5×10^6 $L_\odot$). It is a very eccentric binary system composed by an LBV star (η Car A) of 100 $M_\odot$ and a hotter, less massive companion (η Car B) of about 30–40 $M_\odot$ (Hillier et al. 2001; Mehner et al. 2010). η Car is located at 2350 ± 50 pc in the Carina arm (Smith 2006), with an LSR velocity of −19.7 km s^{-1} (Smith 2004). Its peculiarity, brightness, and closeness represent a unique chance to witness the last breaths of a high-mass star. Consequently, η Car and its surroundings have been exhaustively observed during the last decades, becoming one of the best-studied objects in the Galaxy (e.g. Davidson et al. 1995; Smith et al. 2003b; Smith 2008).

★ E-mail: cbordiu@cab.inta-csic.es (CB); ricardo.rizzo@cab.inta-csic.es (JRR)

η Car underwent a devastating outburst in the 1840s, an event nicknamed the Great Eruption that expelled more than 40 $M_\odot$ of processed material (Gomez et al. 2010; Morris et al. 2017), forming the bipolar Homunculus Nebula (Davidson 1989). This outburst was followed by a second, lesser eruption in the 1890s that gave birth to a smaller structure known as the Little Homunculus (Ishibashi et al. 2003). Around the 1940s, a third abrupt rise in the light curve of η Car happened, followed by a continuous luminosity increase which persists until the present days (Fernández-Lajús et al. 2009). This peculiar behaviour of the light curve has been explained as caused by the dissipation of obscuring debris in the line of sight (Damineli et al. 2019).

The innermost region of η Car is a hostile environment, subject to strong FUV/X-ray fields (Pittard & Corcoran 2002; Corcoran et al. 2017; Hamaguchi et al. 2018) and periodical shocks governed by the 5.54-yr orbital cycle of the binary (Damineli et al. 2000). In particular, Okazaki et al. (2008), Gull et al. (2009), Teodoro et al. (2013), and Gull et al. (2016) studied the complex wind–wind interactions of η Car A and its companion, revealing multiple structures surrounding the binary. These structures, detected in forbidden emission lines of Fe and N, allowed constraints to the orbital geometry of the system and the properties of the stellar winds.

Gull et al. (2016) depicts a very complex scenario in which a number of substructures coexist at different velocity regimes and evolve throughout the orbital cycle depending on the ionization

state: (1) a low-density cavity is carved out when the hot and fast wind of η Car B disrupts the slower and denser primary wind. This structure may be linked to the multiple hydrogen radio recombination lines (RRLs) that were detected towards the NW quadrant of η Car (Duncan & White 2003; Abraham, Falceta-Gonçalves & Beaklini 2014), which possibly arise from the ionized gas within the cavity; (2) multiple arc-like structures, visible in [Fe II] and [Fe III], trace expanding fossil shells of compressed, high-density primary wind that pile up with each 5.54-yr cycle. These structures are formed due to the passage of η Car B through the massive primary wind during periastron, when the two stars get as close as 1.5 au. The shells are particularly prominent in the far side of η Car. Fainter [Fe II] arcs and clumps, likely the remnants of even older cycles, are still visible at larger distances from the star, moving at velocities comparable to the terminal velocity of the primary wind, of 420 km s^{-1} (Groh et al. 2012); and (3) slowly moving clumps of debris from the 19th century events dominate the emission in the near side of η Car, propagating in the direction of apastron. This matter includes the Weigelt blobs and their associated extended structures, visible at infrared wavelengths (Chesneau et al. 2005).

The Weigelt blobs are close-in ejecta located at 0.1–0.3 arcsec of the star, moving at −40 km s^{-1} near the orbital plane (Weigelt & Ebersberger 1986). These clumps are partially ionized and exhibit rapidly varying spectral features modulated by the orbital cycle (Hartman et al. 2005; Johansson, Hartman & Letokhov 2006). The ejection of the blobs took place at some point between 1880 and 1930 (Weigelt & Kraus 2012). Gull et al. (2016) argues that the Weigelt blobs are just the ionized surfaces of a larger neutral structure, like 'blisters' in the skin of a cloud of dust and gas, exposed to mid/far-ultraviolet (MUV/FUV) radiation from the stars. Therefore, the slowly moving material that propagates within the wind-blown cavity was most likely expelled during the 1890s eruption.

A significant fraction of the (sub-)millimetre continuum flux from η Car corresponds to free–free radiation, whereas thermal dust dominates the infrared continuum (Cox et al. 1995). A detailed study of the dust content of the Homunculus combining legacy ISO data with *Herschel* observations allowed Morris et al. (2017) to identify a primary source of thermal radiation in the central 5 × 7 arcsec around η Car. In addition, a separate feature at 350 μm that exhibited a certain level of variability was detected. This second feature was consistent with a compact source of 2 arcsec, being also tentatively linked to the free–free emitting region reported by Abraham et al. (2014).

Molecular spectroscopy, in combination with the resolving power of interferometry, could provide a complementary point of view of the complex central region of η Car. The study of the formation and survival of molecules and the evolution of its relative abundances is key to understand the physical and chemical processes involved in such a harsh environment. Pioneering research by Rizzo, Martín-Pintado & Henkel (2001), Rizzo, Martín-Pintado & Desmurs (2003b), and Rizzo, Jiménez-Esteban & Ortiz (2008) demonstrated the potential of molecular gas associated with evolved massive stars as a tool to understand their evolution and mass-loss history. Molecular hydrogen around η Car was first detected by Smith (2002), distributed over the surface of the Homunculus. Later, Smith et al. (2006) reported a tentative detection of NH_3 towards the inner region of the nebula – although Loinard et al. (2016) claims this detection as arising from the H81β RRL at 23.861 GHz. Loinard et al. (2012) carried out the first molecular survey with APEX, reporting the detection of eight species – including CO and four N-bearing molecules such as CN, HCN, and HNC. Recently, ALMA observations with a resolution of about 1 arcsec (Smith, Ginsburg & Bally 2018) revealed an expanding torus of CO in the waist of the Homunculus. A similar structure has been already discovered around the LBV object MN101 (MGE042.0787 + 00.5084), possibly in a more advanced stage (Bordiu, Rizzo & Ritacco 2019).

In this work, we present ALMA archival observations of CO, HCO^+, HCN, and $H^{13}CN$ towards η Car with an unprecedented resolution better than 0.2 arcsec. We analyse the spatial distribution and kinematics of the emission in the innermost region of the Homunculus, also providing hints on its chemistry and linking the observed features to the violent history of η Car.

2 DATA AND OVERALL RESULTS

We make use of ALMA band 7 archival observations from project 2016.1.00585.S (P.I: G. Pech-Castillo). The source was observed on 2016 October 24 under excellent weather conditions, 0.57 mm of precipitable water vapour, with an integration time of 668 s. A total of 41 12-m antennas were used, providing a maximum baseline of 1.8 km. Quasars J1107–4449, J1047–6217, and J0538–4405 were used for flux, phase, and bandpass calibration, respectively. The correlator was set to observe four simultaneous spectral windows of 1 GHz each, targeting the rotational lines of CO $J = 3 \rightarrow 2$ (345.795989 GHz), $H^{13}CN$ $J = 4 \rightarrow 3$ (345.339769 GHz), HCN $J = 4 \rightarrow 3$ (354.505475 GHz), and HCO^+ $J = 4 \rightarrow 3$ (356.734223 GHz). Visibilities were reduced following the standard ALMA pipeline with CASA v.4.7.0 r38335. The resulting QA2 products included four spectral cubes and a continuum map, with a characteristic beam of 0.17 × 0.13 arcsec (P.A. −60°). The phase centre is shifted by (−0.″1, +0.″15) with respect to the continuum peak, presumably the star.

We adopt the following conventions: (1) intensities are given in a brightness temperature scale (T_b). The conversion from flux density to T_b is made through the expression

$$T_b = 1.22 \times 10^6 \frac{S_\nu}{\nu^2 \theta_{maj} \theta_{min}} \quad (1)$$

with T_b in K, S_ν in Jy beam^{-1}, ν the frequency in GHz and θ_{maj} and θ_{min} the major and minor beam sizes in arcsec; (2) positions are offsets relative to the J2000 coordinates of the source;[1] and (3) velocities are expressed in the local standard of rest frame (LSR).

Fig. 1 presents the peak-intensity maps of CO, HCN, $H^{13}CN$, and HCO^+ in a region of 8 × 8 arcsec around the star. In CO, HCN, and $H^{13}CN$ we distinguish a clumpy C-shaped structure that surrounds the binary at an average radius of 2 arcsec – about 4700 au. This structure corresponds to the disrupted torus described by Smith et al. (2018) from CO $J = 2 \rightarrow 1$ observations, who dated it back to the Great Eruption. The torus traces the bright rims of the so-called 'butterfly nebula', a region of efficient dust formation surrounding η Car, clearly visible in mid-IR images (Chesneau et al. 2005). The clumpiness of the gas in the torus translates into multiple velocity components in the range (−100, +100) km s^{-1}.

Contrary to CO, HCN, and $H^{13}CN$, which display a remarkably similar spatial distribution, HCO^+ tells a very different story. The torus is still visible as faint spots, but the most intense emission, with a peak intensity of 77.5 ± 6.8 K, arises from a slightly elongated region very close to the star, roughly 0.6 × 0.4 arcsec. Hereafter,

[1] $\alpha = 10^h45^m03^s.5362$, $\delta = -59°41'04''.0534$ (J2000) (Gaia Collaboration 2018).

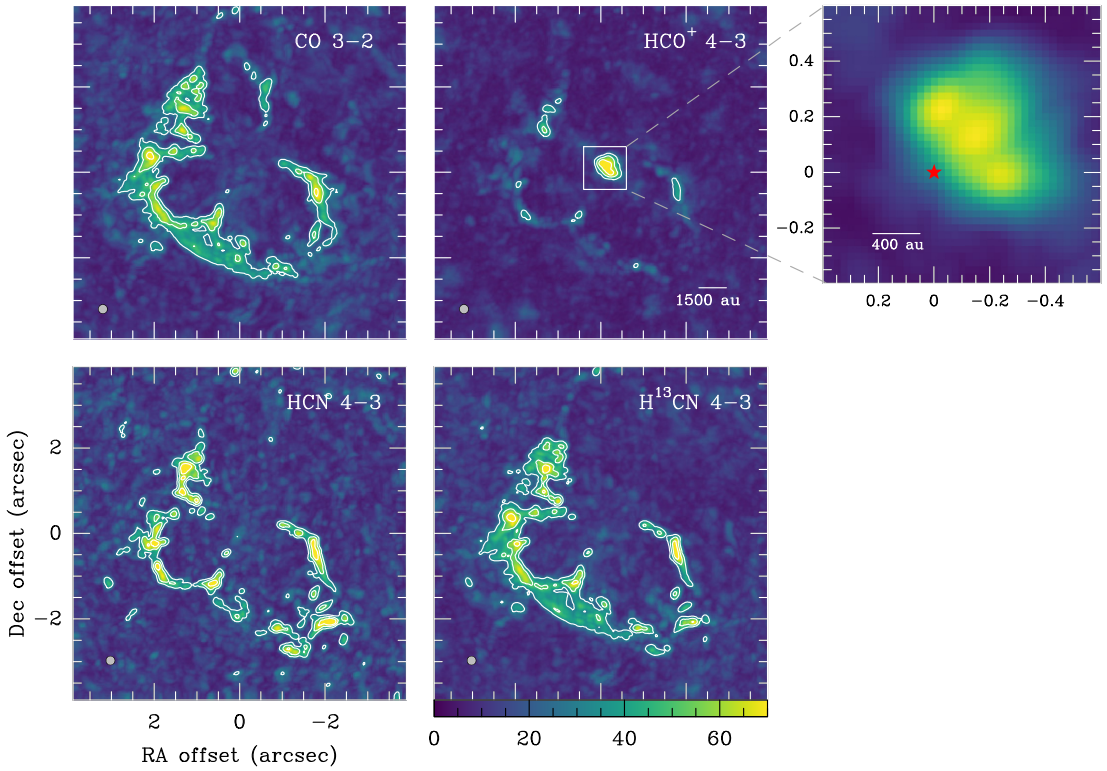

Figure 1. Peak-intensity maps of CO $J = 3 \rightarrow 2$, HCN $J = 4 \rightarrow 3$, $H^{13}CN$ $J = 4 \rightarrow 3$, and HCO^+ $J = 4 \rightarrow 3$ in colour scale. Spectral lines are indicated in the top right corner. Contours are 30, 50, and 70 K. A close-in view of the central HCO^+ emission (the Peanut) is shown in the inset, with the position of η Car indicated by the red marker. Beam width is shown in the bottom left corner of each panel.

we refer to this structure as 'the Peanut' due to its particular shape (see inset).

Continuum emission is only detected at a significant level (5σ) in the inner 0.6 arcsec, as shown in Fig. 2. It depicts a point-like source – presumably related to η Car – and an extended component matching the Peanut. We attempted to isolate the point source emission by fitting it to a single 2D Gaussian. Surprisingly, the point source has an extension slightly larger than the beam, with a deconvolved size of 0.11×0.11 arcsec (i.e. 260 au). This unresolved region is fairly smaller than the estimates by Abraham et al. (2014) for the hydrogen RRL emitting region. The contours in Fig. 2 show the extended component isolated from the point source. The peak intensity of the point source is 6.41 ± 0.02 Jy beam^{-1}, while the integrated fluxes of the point-like and extended sources are 13.1 ± 0.5 and 17.4 ± 1.1 Jy, respectively. This flux is remarkably below those quoted by Abraham et al. (2014) at 225.4 and 291.2 GHz, even when adding up the point source and the extended component (30.5 Jy). This is particularly surprising as observations were gathered close to apastron, when flux is expected to be maximum (White et al. 2005). However, we note that these fluxes correspond to apertures of about 1 arcsec^2. We do not observe significant emission at this scale, but integrating a circular area of this size yields a flux of 38.9 ± 0.6 Jy, which is in very good agreement with previous results. This reveals the existence of a low-intensity plateau at the noise level that surrounds the resolved structures.

The right-hand panels of Fig. 2 also show the discovery of CO, HCN, and $H^{13}CN$ absorbing the continuum. The CO absorption is projected on to the whole continuum-emitting region, with a central velocity of -9 km s^{-1} and a width of 0.6 km s^{-1}. The absorptions of HCN and $H^{13}CN$ are notoriously different: they are point-like, located very close to the star and centred at -60 km s^{-1}, with widths of 12 km s^{-1}. Strikingly, we also detected the $v_2 = 1$ lines of HCN and $H^{13}CN$, as shown in the figure. We analyse the distribution and excitation of these lines in Section 4.

3 THE PEANUT

The Peanut is the most prominent emission feature in the central region. It is located to the NW of η Car, at a projected distance of just 0.1–0.2 arcsec (<1000 au) from the star position. Its projected major axis is aligned in the NE–SW direction (see Fig. 1). To the best of our knowledge, this is the very first direct detection of this structure beyond infrared; but considering the size uncertainty, it may well be related to the free–free emitting source inferred by Morris et al. (2017). The Peanut is significantly closer to η Car and smaller than the torus; therefore, it is presumably a younger structure. In principle, its location and shape are consistent with ejecta expelled in an asymmetric – or 'one-sided'– mass ejection. The occurrence of such events in η Car was first studied by Kiminki, Reiter & Smith (2016), and later proposed by Smith et al. (2018) as a possible explanation for the gap in the CO torus.

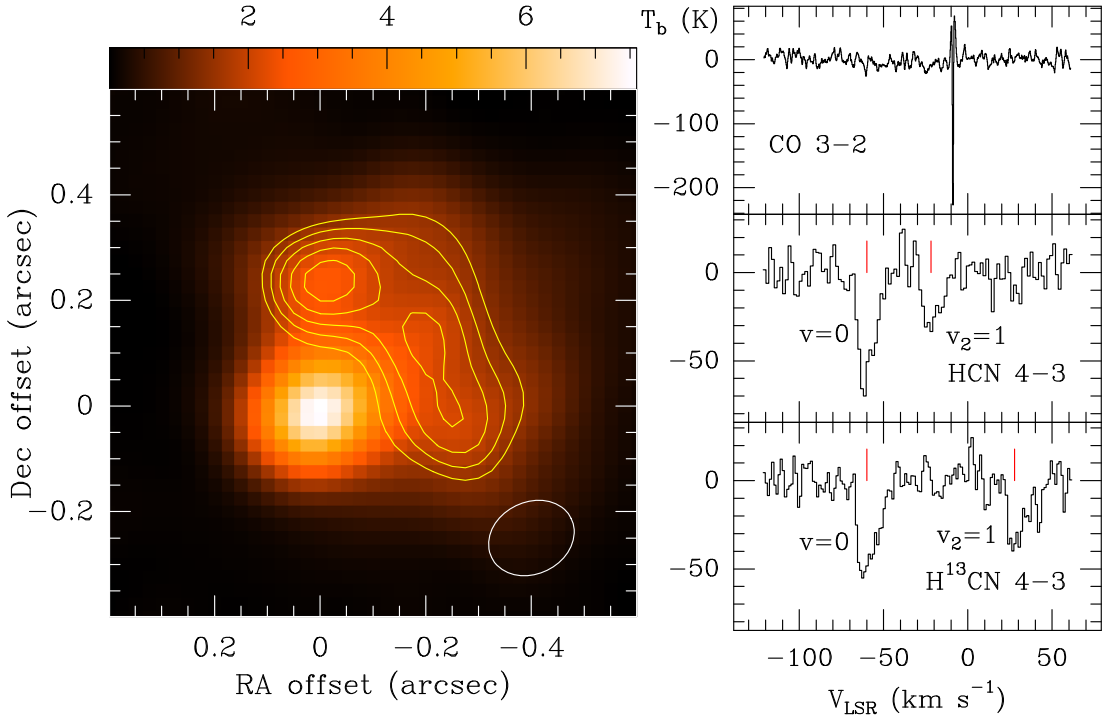

Figure 2. Continuum emission and line absorptions at 345.8 GHz. The continuum image (left, colour scale) is composed by a point-like source and an extended source coincident with the Peanut. Contours are 1.4, 1.6, 1.8, 2.0, and 2.2 Jy beam^{-1}, and correspond to the resultant image after a point source subtraction. Half power beamwidth is indicated by the white ellipse at the lower right corner. Spectra depicted in the right panels are from an average of 0.1 arcsec around the point source. The CO line is at −9 km s^{-1}, while the HCN and H^{13}CN lines appear at −60 km s^{-1} (red vertical marker).

The Peanut is only visible in HCO^+ and continuum, without any hints of the other observed molecules. Due to its proximity to η Car, it may be directly exposed to intense UV radiation. The survival of dust and molecules at such a short distance of the star requires an efficient shielding mechanism. The wind fossil structures accumulated during multiple cycles could protect the central region as discussed by Morris et al. (2017). In this regard, the Peanut strikingly resembles the 'hook' structure detected towards the NW of η Car in forbidden emission lines of [Fe II] and [Fe III] (see fig. 2 in Gull et al. 2016). The hook exhibits significant changes during the 5.54-yr cycle, depending on the ionization state: it is visible in [Fe II] across the whole orbit, but fades away in [Fe III] during periastron passage, when most of the FUV radiation of η Car B is blocked by the primary wind. Provided that the molecular and ionized phases are co-spatial to some extent, then the Peanut is – at least partially – shielded by this intervening hook, the irradiation of the molecular gas is presumably dominated by MUV photons. However, we must note that survival of HCO^+ might not be strongly affected by the ionization state or the shielding efficiency, since this molecule is almost transparent to UV radiation (Koch, van Hemert & van Dishoeck 1995; van Dishoeck, Jonkheid & van Hemert 2006; Walsh et al. 2012). This point is further discussed in Section 5.

We clearly identify three maxima across the Peanut, as seen in the HCO^+ peak intensity map. Two of these maxima are nearly coincident with the brightest peaks in the hook. Indeed, Gull et al. (2016) reports that these peaks correspond to the position of Weigelt blobs C and D. This could imply that the Peanut and the blobs are also related, hence confirming a common origin in the eruptive events of the 19th century. We note, though, that the Peanut is slightly closer – in terms of projected distance – to η Car than the hook and the blobs (shifted towards the SE by about 0.1–0.15 arcsec from peak to peak). This probably indicates that the molecular and ionized gas phases are not totally coupled, as we should expect a spatial transition from ionized to molecular gas (e.g. [Fe III] → [Fe II] → HCO^+) in the direction of the FUV field.

3.1 Kinematics of the Peanut

Analysis of the kinematics of HCO^+ could help to understand the origin of this structure and its complex geometry. We found serious discrepancies between the motion of the Peanut and the Weigelt blobs and their associated structures. First, HCO^+ is mostly confined to the velocity range (−100, +100) km s^{-1}, with the most intense emission arising from −20 to +70 km s^{-1}. Conversely, the hook is completely blueshifted with respect to the systemic velocity of η Car (−19.7 km s^{-1}), extending from −72 to −32 km s^{-1}.[2] Therefore, the HCO^+ emission that lies in the velocity range of the hook is almost marginal. As this velocity mismatch suggests, a significant part of the molecular gas might be directly exposed to the FUV field of η Car B.

[2]The range reported in Gull et al. (2016) is from −60 to −20 km s^{-1}. For η Car, $V_{LSR} = V_{Hel} - 12$ km s^{-1} (Smith 2004).

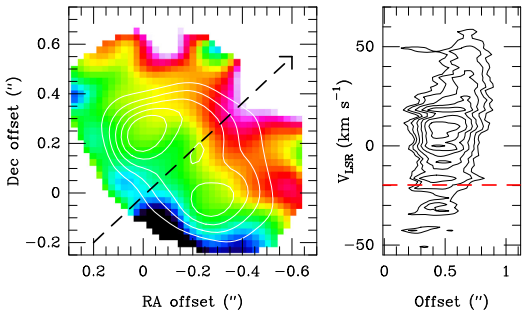

Figure 3. Velocity field of the HCO^+ gas. Left-hand panel: First-order moment map of HCO^+ (colour scale), with the integrated intensity superimposed as white contours. Right-hand panel: Position–velocity cut in the direction indicated by the black dashed line in the left-hand panel. Contours start at 5σ with steps of 3σ. The red dashed line represents the systemic velocity of η Car.

Secondly, it is accepted that Weigelt blobs C and D are moving close to the system's orbital plane, which is almost coincident with the Homunculus mid-plane (Davidson & Humphreys 1997). We find this motion to be also incompatible with the kinematics of the HCO^+: the gas presents a clear gradient from the SE (negative velocities) to the NW (positive velocities), with most of the emission at positive velocities – and therefore redshifted with respect to the systemic velocity of η Car (see Fig. 3). This velocity distribution, that in principle is consistent with an asymmetric eruptive event like the 1890s outburst, does not match the motion pattern of the Weigelt blobs in the most accepted orbital geometry (e.g. Okazaki et al. 2008; Teodoro et al. 2016), where periastron occurs on the far side of η Car A and apastron on the near side. If the Weigelt blobs are escaping from the star towards the NW (i.e. towards apastron) and close to the orbital plane, they are necessarily blueshifted, approaching the observer. Contrarily, the HCO^+ gas in this direction is mostly receding.

In order to solve this puzzle, a more detailed analysis of the kinematics of the Peanut is required. Fig. 4 presents intensity maps of HCO^+ integrated in velocity bins of 20 km s^{-1} over the range $(-80, +80)$ km s^{-1}. Note that contours are relative to the maximum level of each map to emphasize the peaks. We identify a set of features evolving from SE to NW as we advance towards positive velocities. The most intense emission is concentrated in an irregular bar-like feature in the range $(-20, +40)$ km s^{-1}, but two fainter substructures are particularly noteworthy: the two patchy arcs that are clearly visible in the velocity ranges $(-60, -40)$ and $(+40, +60)$ km s^{-1}. They are almost symmetrically located with respect to the bulk emission: the blueshifted arc opening towards the NW and the redshifted towards the SE. When taken together, the arcs describe an ellipsoid of 0.6×0.4 arcsec with a position angle of 30° east of north, as seen in Fig. 5.

All these features may be explained by a clumpy, roughly conical structure of ejecta from the 1890s outburst. This 'cone', with its opening towards apastron, is expanding within the wind-blown cavity described by the colliding wind models proposed by Okazaki et al. (2008), Gull et al. (2009), and Madura et al. (2013) and briefly discussed in Section 1. In this scenario, the Weigelt blobs would be just UV-illuminated surfaces in this larger structure. Matter within the cavity would be highly ionized during most of the orbital cycle, producing continuum thermal emission (Abraham et al. 2014). The cone would be periodically disrupted as the dense primary wind (slow, but still five times faster than the ejecta) flows past during each periastron. Part of the ejecta may be also driven towards the inner walls of the cavity, creating a high-density layer where HCO^+ may also arise.

To put all the pieces together we present a simple sketch model in Fig. 6. The proposed orientation of the cone explains the observed velocity pattern of HCO^+: the SE side of the cone moves towards the observer (the blueshifted arc) while the NW side moves away (the redshifted arc). The 'tangent' parts of the cone (towards NE and SW) would move almost in the plane of the sky, explaining the emission peaks that appear near 0 km s^{-1}. These peaks may be caused by an accumulation of material in the line of sight towards these regions. The bulk of the bar would correspond to the densest parts of the structure. This interpretation is able to reconcile the HCO^+ gas with the motion of the Weigelt blobs and the ionized Fe structures. Fig. 5 shows the position of blobs C and D with respect to the arcs and the bar. The arcs approximately enclose the blobs, which also supports the idea that these structures are moving outwards within the cavity created by the colliding winds. The apparent spatial correlation with the HCO^+ peaks is then a mere projection effect. The blobs may be actually closer to the apex of the cone and thus directly exposed to a more intense FUV field.

Finally, it is important to note that kinematics of the molecular gas also provide valuable 3D information about the eruption. The location of the Peanut with respect to the star plus the lack of a counterpart for the slowly moving material in the far side of η Car are important evidences that support the asymmetric outburst hypothesis. But most importantly, the remarkable radial velocity dispersion of the HCO^+ gas with respect to η Car (of about 80–100 km s^{-1}) may also indicate a latitudinal distribution in the ejecta – in contrast to the equatorial nature of the Weigelt blobs.

It is important to keep in mind, though, that here we are working at scales comparable to the beam size. To understand gas motions in such small regions and refine the interpretations provided in this work, observations at higher angular resolution are essential. These would provide key insights about the formation and dynamics of molecular gas, its interplay with the ionized and neutral phases, and (especially) its dependency on the orbital phase.

4 LINE ABSORPTIONS

In this section, we present a more detailed description of the absorbing gas, whose overall distribution is depicted in Fig. 7. The three top panels show the distribution in a 4×4 arcsec field in false colour; the bottom panels show a zoom in the inner arcsec, with the line absorption as contours superimposed to the continuum. The figure does not include the distribution of the absorbing $H^{13}CN$, which is basically identical to the main isotopologue at both vibrational levels ($v = 0$ and $v_2 = 1$).

Absorbing CO distribution mimics the whole continuum emission, including both the hot star and Peanut. It is probably a foreground interstellar cloud located somewhere in the foreground of η Car. Its velocity (−9 km s^{-1}) lies halfway between the corresponding velocities of a local cloud (0 km s^{-1}) and the Carina arm (−20/−25 km s^{-1}); its line width (0.6 km s^{-1}) is typically found in cold clouds. Nevertheless, this cloud may be related to the dissipating dusty clump proposed by Damineli et al. (2019) to explain the brightening of the central source, that would act as a 'natural coronograph'.

Contrarily, HCN and $H^{13}CN$ absorptions are concentrated in a very compact and unresolved region. Its centre is close, but not

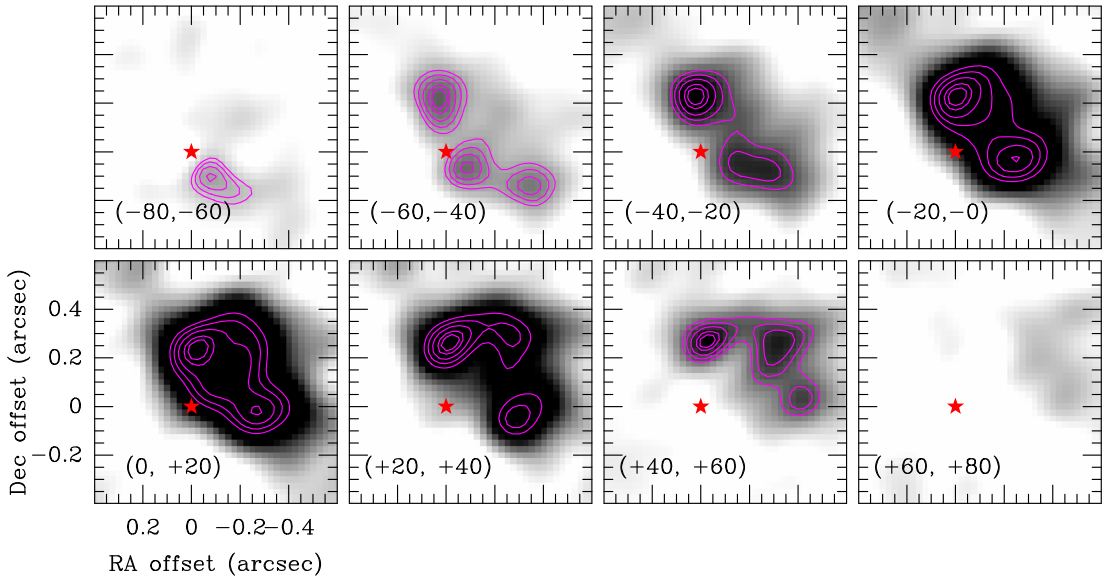

Figure 4. Velocity-integrated intensity maps of HCO^+ in colour scale, integrated in bins of 20 km s^{-1} from −80 to + 80 km s^{-1}. All the maps have the same intensity scale. Contours at 60, 70, 80, 90, and 95 per cent of the peak intensity of each map. The integration range is shown in the bottom left corner of each panel, and the position of η Car is indicated by the red marker.

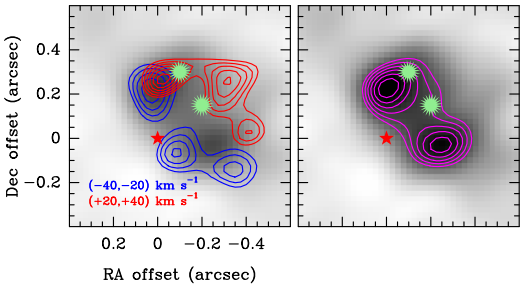

Figure 5. Relative position of the Weigelt blobs with respect to the most prominent features of HCO^+. Left-hand panel: Integrated line intensity of HCO^+ from −40 to −20 (blue) and from +20 to + 40 (red) km s^{-1}, as contours, superimposed to the integrated intensity in the range (−20, 0) km s^{-1} in colour scale. Right-hand panel: Integrated line intensity of HCO^+ from −20 (systemic velocity) to 0 km s^{-1}, as contours and colour scale. The position of η Car and Weigelt blobs C and D (taken from Gull et al. 2016) is indicated by the red and green markers, respectively.

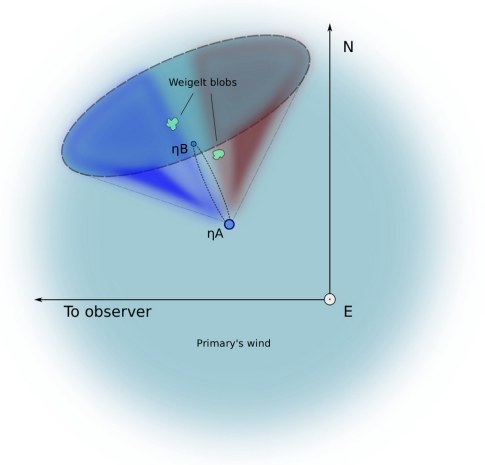

Figure 6. Sketch of the viewing geometry of the HCO^+ emission. The colours indicate the motion of the gas relative to the observer. The primary wind sphere, the shock cone, the Weigelt blobs and the orbital plane are arbitrarily scaled for illustration purposes.

coincident with the hot star. The projected distance to the star is around 0.08 arcsec (180 au), which is smaller than the angular resolution but clearly significant after looking the CO absorption at the very centre of the point source. Velocity (−60 km s^{-1}) and line widths (10–12 km s^{-1}) are similar to those measured in emission in the torus and the Peanut. All these observational findings are consistent with a bullet-like cloud being expelled from η Car at a projected velocity of 40 km s^{-1}. It is finally noteworthy the lack of emission or absorption of the other molecules, which indicates that this hot bullet is likely very N-enriched.

The $H^{13}CN$ and HCN lines have similar intensities. This translates, as we develop in Section 5, to a very low $^{12}C/^{13}C$ ratio. However, the most striking result is the detection of the vibrationally excited lines with intensities slightly below half of those corresponding to the $v = 0$ lines. HCN and $H^{13}CN$ $v_2 = 1$ excited states correspond to a double degenerate bending mode with an energy of 729.7 cm^{-1} (≈1050 K). It is virtually impossible to populate such energy level exclusively by collisions, and the most probable mechanism is the infrared radiative pumping by the absorption of photons at ≈14μm (Bruderer, Harsono & van Dishoeck 2015). The

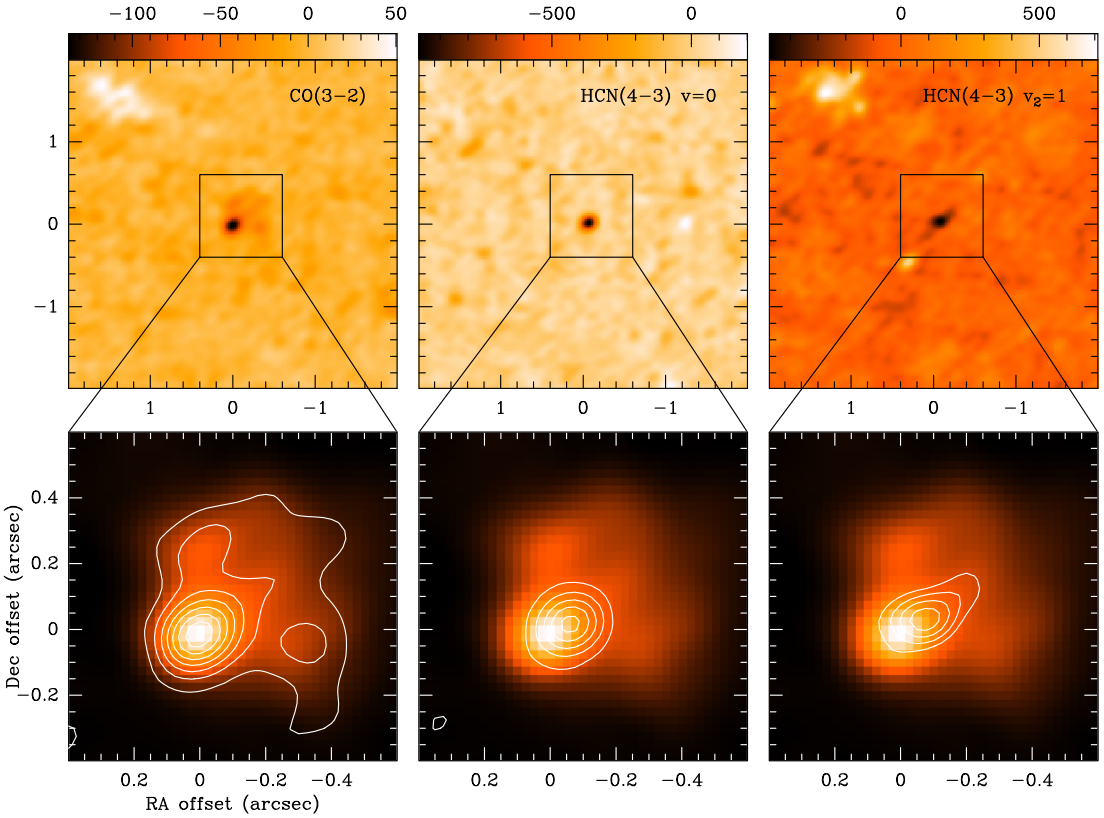

Figure 7. Spatial distribution of the absorptions towards η Car. Top panels: Intensity maps of CO, HCN $v = 0$, and HCN $v_2 = 1$ in colour scale, integrated in the velocity range $(-67, -49)$ km s^{-1} for a region of 4×4 arcsec. Note that the emission in the top left corner of the CO and HCN $v_2 = 1$ panels corresponds to CO and HCN $v = 0$ emission arising from the torus. Bottom panels: Close-in view of the central arcsec for the corresponding lines in the top panels. Integrated intensity as white contours, superimposed to the continuum emission in colour scale.

strong infrared continuum of Eta Carina ensures the availability of huge amounts of photons for such pumping.

These and other vibrationally excited lines with comparable energy levels have been observed in other astrophysical environments, such as carbon stars (Izumiura et al. 1987; Bieging 2001), hot cores (Esplugues et al. 2013; Pagani et al. 2017), or ultraluminous infrared galaxies (Imanishi & Nakanishi 2013; Imanishi, Nakanishi & Izumi 2016). In all those cases, however, the intensity of the vibrationally excited lines remains as a small fraction of the ground level lines. Therefore, the bullet is being shocked and accelerated by a copious amount of infrared photons, in a particularly harsh environment.

5 COLUMN DENSITIES AND RELATIVE ABUNDANCES

5.1 Column densities

We estimated the column densities of the observed species in different positions, as depicted in Fig. 8: the torus – positions A and B – the clump at $(0.''4, -0.''65)$ – position C – the Peanut and the absorbing bullet. For the emission lines we assumed that the gas is in local thermodynamic equilibrium (LTE), the emission is optically thin and that radiative excitation dominates over collisions due to the strong radiation field of η Car. If gas and dust are thermally coupled, gas temperature may be approximated by the dust temperature. We took the equation by Smith et al. (2003a):

$$T_{\rm dust}({\rm K}) \approx 13100 \times D({\rm au})^{-\frac{1}{2}}, \quad (2)$$

where $T_{\rm dust}$ is the blackbody equilibrium temperature of a dust grain at a distance D of the source. Translating angular separation into real distances is almost immediate for the torus after correcting for the inclination (the polar axis of the Homunculus is tilted by 49°; Smith 2006). We derive temperatures ranging from 170 to 190 K. For the Peanut, on the contrary, obtaining a proper distance estimate is not straightforward. We note that the maximum at $(0'', 0.''25)$ corresponds to emission present across the whole velocity range (see Fig. 4). This allows us to approximate the real distance by the projected distance. The resulting temperature, of about 500 K, is an upper limit, as we are considering the material that is closest to the star.

For the absorbing bullet, we fully solved the transfer equation with LTE as the only assumption. Considering the proximity to η Car, we cannot neglect the excitation term like in the case of absorptions of cold clouds (Liszt & Lucas 2001; Ando et al. 2016; Liszt & Gerin 2018). The continuum and excitation temperatures result to be 3390 and 500 K, respectively. The four lines are optically

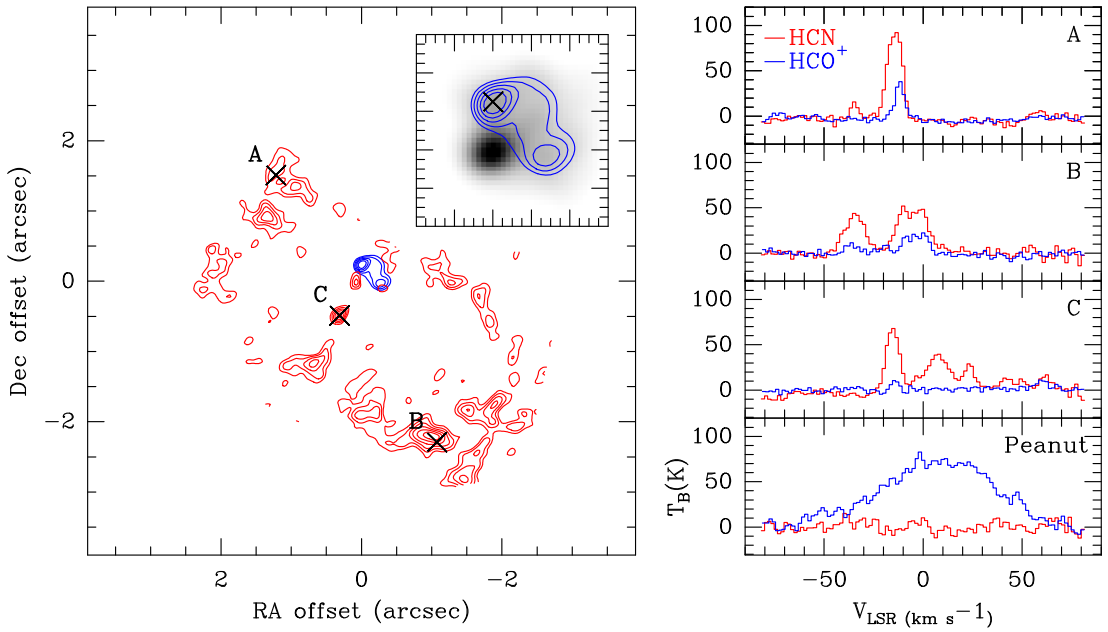

Figure 8. Hints of chemical differentiation in the innermost region of the Homunculus. Left-hand panel: Line intensity maps of HCO^+ (blue) and HCN (red) in the velocity range (–100, + 80) km s^{-1}. The inset shows a close-in view of the Peanut, superimposed to the continuum image (gray scale). Black crosses indicate the positions of the spectra shown to the right. Right-hand panel: HCO^+ (blue) and HCN (red) spatially averaged spectra in the corresponding positions of the left panel.

thin, with opacities from 0.01 to 0.025. Table 1 summarizes the resulting column densities and the most relevant abundance ratios. We note that our column densities are consistently lower than those reported by Loinard et al. (2012) by a factor of 3–5. While this may obey to beam filling issues, our estimates are more in line with the column densities derived by Morris et al. (2017) from large beam CO $J = 5 \rightarrow 4$ to $9 \rightarrow 8$ observations of the Homunculus.

5.2 Abundances in the torus

Some molecular abundances vary drastically among different positions. The torus presents $[HCO^+]/[CO]$ ratios of 10^{-4}, comparable to those measured around other massive evolved stars, like the Wolf–Rayet nebula NGC 2359 (Rizzo, Martín-Pintado & Desmurs 2003a). Similar ratios are also found in the Orion Bar photodissociation region (Young Owl et al. 2000) and some molecular clouds, such as TMC-1 (Pratap et al. 1997).

On the contrary, we found significantly altered [HCN]/[CO] relative abundances, with values of a few 10^{-3}. These are almost 100 times larger than the ratios measured in TMC-1 and NGC 2359 and just slightly above those of the Orion Bar PDR, but still much lower than in environments where the grain chemistry dominates (Shalabiea & Greenberg 1996). The highest ratios are measured towards the clump and the absorbing bullet, which suggests that these two features may be of similar nature. Interestingly, the $[H^{13}CN]/[CO]$ ratio reaches comparable values in all the studied positions.

These high relative abundances of nitrogen-bearing molecules with respect to CO are a typical hint of N-rich gas. The N-enrichment of the Homunculus is a widely studied topic: by means of UV and optical spectroscopy, Davidson et al. (1986) demonstrated a N-enrichment factor of 10 with respect to solar abundances; Dufour et al. (1997) and Verner, Bruhweiler & Gull (2005) found evidence of heavy C and O depletion, a sign of intensive CNO processing. Still, we are not in a position to report N-enrichment in absolute terms as we lack information about H_2 in these specific regions (just overall estimates for the Homunculus). But regardless of the absolute N abundance, the $[HCN]/[H^{13}CN]$ ratio is a good proxy to confirm that the torus is made of CNO-processed matter (since ^{13}C is another intermediate product of the CNO cycle). In every position, we measure $[HCN]/[H^{13}CN]$ ratios close to unity. This value is exceptional and holds for the vibrationally excited lines as well. It indicates an extremely low $[^{12}C]/[^{13}C]$ isotopic ratio, even for a massive star (typically in the range 3–10; e.g. Lambert et al. 1984, Bordiu et al. 2019).

5.3 Hints of chemical differentiation

The situation in the Peanut is completely different, as Fig. 1 suggested. Towards this region, none of the molecules except HCO^+ is detected. Therefore, we constrained the column densities of CO, HCN, and $H^{13}CN$ taking the 3σ level as the line intensity upper limit. In this case, this approach tends to favour these column densities since the maps are noisier towards the continuum emitting region, but we still obtain limits notably below the values measured in the torus. On the other hand, the column density of HCO^+ is remarkably enhanced, reaching 10^{16} cm^{-2}. Consequently, the $[HCO^+]/[CO]$ and $[HCO^+]/[HCN]$ ratios increase by a factor of up to 125.

The non-detection of CO, HCN, and $H^{13}CN$ in the Peanut implies that the gas in this region is chemically different from the ejecta of

Table 1. Column densities and abundance ratios of CO, HCN, $H^{13}CN$, and HCO^+ in the regions depicted in Fig. 2.

Pos.	T (K)	V_{lo}, V_{up} (km s^{-1})	N(CO) (10^{18} cm^{-2})	N(HCN) (10^{15} cm^{-2})	N($H^{13}CN$) (10^{15} cm^{-2})	N(HCO^+) (10^{14} cm^{-2})	$\frac{[HCO^+]}{[CO]}$ (10^{-4})	$\frac{[HCN]}{[CO]}$ (10^{-3})	$\frac{[HCO^+]}{[HCN]}$	$\frac{[HCN]}{[H^{13}CN]}$
Tor. A	190	(−35, + 0)	0.73 ± 0.01	1.13 ± 0.08	1.14 ± 0.04	1.48 ± 0.14	2.0	1.6	0.13	0.99
Tor. B	170	(−90, + 20)	1.23 ± 0.03	1.72 ± 0.14	1.82 ± 0.10	4.24 ± 0.75	3.5	1.4	0.25	0.94
Tor. C	350	(−20, + 70)	0.68 ± 0.07	3.54 ± 0.11	2.68 ± 0.10	<4.6	<6.8	5.2	<0.12	1.32
Peanut	500	(−66, + 81)	<0.56	<0.81	<0.87	141.6 ± 4.4	>250	–	>18	–
Absorp	500	(−67, −49)	<0.28	0.62 ± 0.06	0.70 ± 0.05	<3.4	–	>2.2	<0.55	0.89

Note. In position Absorp, N(HCN) and N($H^{13}CN$) consider the vibrational-ground ($v = 0$) and vibrationally excited ($v_2 = 1$) states.

the Great Eruption – i.e. the torus. Indeed, Chesneau et al. (2005) compared the composition of the dust in the Weigelt region and other parts of the butterfly nebula, finding significant differences. Since the ejecta from the 1840s and 1890s eruptions are likely similar in terms of initial CNO abundances, the observed differences may obey to the extreme physical conditions to which the Peanut is exposed.

In dense clouds, one of the principal formation routes of gas-phase HCN is

$$CH_2 + N \rightarrow HCN + H \quad (3)$$

a neutral–neutral reaction much slower than the ion-molecule reaction that produces HCO^+ (Boger & Sternberg 2005). While reaction rates may explain the dominance of HCO^+ in the Peanut, by no means it is enough to explain the apparent lack of N-bearing species. Provided that N is abundant to a certain degree – as expected in CNO-processed material – the non-detection of neither HCN nor $H^{13}CN$ may be the consequence of an aggressive photochemistry. We know that the structures traced by [Fe II] and [Fe III] protect – at least partially – the Peanut, blocking the most energetic FUV radiation. Because of that, the Peanut is primarily exposed to a substantial flux of MUV photons with wavelengths larger than 1800 Å. HCO^+ formation and destruction does not directly involve any photochemical route, so this molecule is relatively immune to these photons. On the other hand, HCN is rapidly photodissociated through

$$HCN + \nu \rightarrow CN + H \quad (4)$$

producing CN, which in turn is less vulnerable to photodissociation (requiring photons with $\lambda < 1100$ Å; van Dishoeck et al. 2006). If photodissociation is the prevailing destruction mechanism of HCN and $H^{13}CN$ in the Peanut, CN should be abundant in this region. In fact, CN was already detected towards η Car in single-dish observations by Loinard et al. (2012), but higher angular resolution is needed to confirm its origin.

Still, the non-detection of CO is challenging and hard to explain, especially when taking into account the high column density of HCO^+. The dominant formation pathway of HCO^+ in the ISM is the proton transfer reaction

$$H_3^+ + CO \rightarrow HCO^+ + H_2 \quad (5)$$

(e.g. Illies, Jarrold & Bowers 1982; Liszt, Lucas & Black 2004), which requires a substantial amount of CO to be efficient. Likewise, HCO^+ is mainly destroyed by dissociative recombination through

$$HCO^+ + e^- \rightarrow CO + H \quad (6)$$

as long as the electron density is high enough (Yan et al. 2000). This reaction should increase the total CO abundance. The detection of hydrogen RRL emission towards the Peanut somehow supports this mechanism, as the resulting H atoms would be quickly ionized. For that reason, the apparent lack of CO in the Peanut is particularly shocking. However, alternative formation routes of HCO^+ that do not require CO cannot be ruled out. Then CO may be simply forming at a much slower rate than HCO^+, which would explain its non-detection considering the short time-scales involved (100 yr). In any case, the development of new chemical models is key to understand the chemical evolution of the inner ejecta of η Car.

5.4 Mass estimates

Determining the masses of the observed molecular structures is not straightforward, since all the abundances refer to CO. It is then fundamental to know the true $[CO]/[H_2]$ ratio to translate these results into masses. Ferland et al. (2005) and Smith et al. (2006) provided an average H_2 column density through the walls of the Homunculus of around 10^{22} cm^{-2}. Loinard et al. (2012) adopted this value to derive a relative abundance of CO of 2.2×10^{-4} for the whole Homunculus.

In principle, we could use this CO abundance, but it may lead to unreliable results, as we are dealing with resolved, clumpy structures, for which the actual H_2 column density may be higher. For the torus, a standard $[CO]/[H_2]$ abundance of 10^{-4} yields a mass of 0.07 ± 0.02 M$_\odot$. This value seems exceedingly low considering that around 10–20 per cent of the Homunculus mass may reside in its equatorial plane (Smith et al. 2003a). Smith et al. (2018) constrained the mass of the torus to 0.2–1 M$_\odot$ exploring a range of possible abundances. In view of our results, we conclude that CO should be underabundant by a factor of 8–40 in order to be compatible with such mass range. This agrees, again, with the results by Morris et al. (2017), who reports $[CO]/[H_2]$ abundances 10–20 times below cosmic levels.

In the Peanut, the usual approach of determining the H_2 mass from CO is not possible due to the non-detection of the latter. HCO^+ is the only available H_2 tracer, but its relative abundance is also uncertain. HCO^+ is found in many astrophysical environments, with abundances ranging from 10^{-7} to 10^{-10} (see e.g. Bergin & Langer 1997; Gibb & Little 2000; Tafoya et al. 2007). Thus, we could express the mass of the Peanut as a function of the HCO^+ abundance, X_{HCO^+}, by taking a reference value of 10^{-8} (typically measured in oxygen-rich envelopes; Pulliam, Edwards & Ziurys 2011):

$$M = (0.8 \pm 0.3) \times \frac{X_{HCO^+}}{10^{-8}}\ M_\odot. \quad (7)$$

Even adopting conservative abundances, such as the value proposed by Loinard et al. (2012) of 5.7×10^{-8}, this expression yields masses at least comparable to the mass of ionized gas ejected during the 1890s eruption, which according to Ishibashi et al. (2003) lies in the range 0.1–1 M$_\odot$. None the less, we note that all these estimates must be regarded with caution.

6 CONCLUDING REMARKS

We analysed ALMA archival observations of continuum, CO, HCN, $H^{13}CN$, and HCO^+ of the inner 8 arcsec of the Homunculus around η Car. The unprecedented resolution of these data allowed us to discover some key ingredients related to the recent mass-loss history of the source and provide complementary insights into the complex wind–wind interactions. The key findings in this work are summarized below:

(i) We reported the detection of the HCN, $H^{13}CN$, and HCO^+ counterparts of the equatorial torus around η Car described by Smith et al. (2018) from CO $J = 2 \rightarrow 1$ observations. In addition, the CO $J = 3 \rightarrow 2$ map presented here improves resolution by a factor of 5, confirming the clumpy nature of this structure.

(ii) We reported the detection of an extended, asymmetric structure in the inner arcsec, the Peanut, located NW of the star and only visible in continuum and HCO^+.

(iii) We studied the morphology and kinematics of the Peanut in the context of previously known fossil wind structures and ejecta from the 19th century eruptions. We found several velocity features that allowed us to identify the Peanut as a roughly conical structure of ejecta expanding outwards within the cavity blown-out by the current wind interactions. The ejecta, rich in dust and gas, encompasses the Weigelt blobs, which may be partially ionized surfaces of the structure, exposed to intense MUV/FUV fields. This scenario is consistent with the current knowledge of the inner ejecta of η Car and existing SPH models.

(iv) We found a strong absorption feature almost coincident with the star, only visible in HCN and $H^{13}CN$. We also stress the detection of the corresponding vibrationally excited states of these lines, with unusually high relative intensities. The high temperatures required to excite these states prove that the absorbing gas is close to the photosphere rather than part of a foreground cloud (i.e. the obscuring debris proposed by Damineli et al. 2019 to explain the light curve.)

(v) We analysed the chemistry of the torus and the Peanut, finding remarkably different molecular abundances. We also compared the results with other astrophysical environments. The abundance of N-bearing species with respect to CO and the extremely low [HCN]/[$H^{13}CN$] ratios measured in the torus are consistent with CNO processed matter. Contrarily, the Peanut is very bright in HCO^+ but it is not detected in any of the other lines. The non-detection of CO, the most ubiquitous molecule after H_2, is exceptionally intriguing, as it is generally involved in the formation and destruction of HCO^+.

All of these findings uncover a complex and challenging scenario. The Peanut is an environment subject to violent changes, where very energetic processes act upon the products of the CNO cycle in very short time-scales. Under these extreme conditions, the constituents of molecular gas are exposed to intense UV fields and may have no time to reach chemical equilibrium. This would explain the non-detection of HCN and $H^{13}CN$ towards this region. However, if further surveys confirm that the Peanut is indeed deficient in N-bearing species, other alternative scenarios may come into play: for instance, the Peanut may be ejecta from η Car B.

Molecular spectroscopy has proven to be a valuable tool, providing a new, complementary approach to the physics, chemistry, and evolution of η Car and its surroundings. Monitoring of the chemical evolution of the Peanut, together with a revision of stellar evolution models, is of paramount importance to explain the measured abundances. Moreover, observations at different orbital phases will be key to understand the dynamical evolution and excitation mechanisms of the observed ejecta structures. Finally, extending the observations to other molecules and transitions with the highest resolution possible will allow to constrain the physical conditions of the gas and complete the chemical puzzle of η Car.

ACKNOWLEDGEMENTS

We thank the anonymous referee for the insightful comments provided. This paper makes use of the following ALMA data: ADS/JAO.ALMA#2016.1.00585.S. ALMA is a partnership of ESO (representing its member states), NSF (USA) and NINS (Japan), together with NRC (Canada), MOST and ASIAA (Taiwan), and KASI (Republic of Korea), in cooperation with the Republic of Chile. The Joint ALMA Observatory is operated by ESO, AUI/NRAO and NAOJ. JRR acknowledges the support from Spanish Ministerio de Economía y Competitividad under grant ESP2015-65597-C4-1-R (MINECO/FEDER, UE) and Spanish Agencia Estatal de Investigación under grant ESP2017-86582-C4-1-R (AEI/FEDER, UE).

REFERENCES

Abraham Z., Falceta-Gonçalves D., Beaklini P. P. B., 2014, ApJ, 791, 95
Ando R., Kohno K., Tamura Y., Izumi T., Umehata H., Nagai H., 2016, PASJ, 68, 6
Bergin E. A., Langer W. D., 1997, ApJ, 486, 316
Bieging J. H., 2001, ApJ, 549, L125
Boger G. I., Sternberg A., 2005, ApJ, 632, 302
Bordiu C., Rizzo J. R., Ritacco A., 2019, MNRAS, 482, 1651
Bruderer S., Harsono D., van Dishoeck E. F., 2015, A&A, 575, A94
Chesneau O. et al., 2005, A&A, 435, 1043
Corcoran M. F. et al., 2017, ApJ, 838, 45
Cox P., Mezger P. G., Sievers A., Najarro F., Bronfman L., Kreysa E., Haslam G., 1995, A&A, 297, 168
Damineli A., Kaufer A., Wolf B., Stahl O., Lopes D. F., de Araújo F. X., 2000, ApJ, 528, L101
Damineli A. et al., 2019, MNRAS, 484, 1325
Davidson K., 1989, in Davidson K., Moffat A. F. J., Lamers H. J. G. L. M., eds, Physics of Luminous Blue Variables. Kluwer, Dordrecht, p. 101
Davidson K., Humphreys R. M., 1997, ARA&A, 35, 1
Davidson K., Dufour R. J., Walborn N. R., Gull T. R., 1986, ApJ, 305, 867
Davidson K., Ebbets D., Weigelt G., Humphreys R. M., Hajian A. R., Walborn N. R., Rosa M., 1995, AJ, 109, 1784
Dufour R. J., Glover T. W., Hester J. J., Curie D. G., van Orsow D., Walter D. K., 1997, in Nota A., Lamers H., eds, ASP Conf. Ser. Vol. 120, Luminous Blue Variables: Massive Stars in Transition. Astron. Soc. Pac., San Francisco, p. 255
Duncan R. A., White S. M., 2003, MNRAS, 338, 425
Esplugues G. B. et al., 2013, A&A, 559, A51
Ferland G. J., Abel N., Davidson K., Smith N., 2005, in Humphreys R., Stanek K., eds, ASP Conf. Ser. Vol. 332, The Fate of the Most Massive Stars. Astron. Soc. Pac., San Francisco, p. 298
Fernández-Lajús E. et al., 2009, A&A, 493, 1093
Gaia Collaboration, 2018, A&A, 616, A1
Gibb A. G., Little L. T., 2000, MNRAS, 313, 663
Gomez H. L., Vlahakis C., Stretch C. M., Dunne L., Eales S. A., Beelen A., Gomez E. L., Edmunds M. G., 2010, MNRAS, 401, L48
Groh J. H., Hillier D. J., Madura T. I., Weigelt G., 2012, MNRAS, 423, 1623
Gull T. R. et al., 2009, MNRAS, 396, 1308
Gull T. R. et al., 2016, MNRAS, 462, 3196
Hamaguchi K. et al., 2018, Nature Astron., 2, 731
Hartman H., Damineli A., Johansson S., Letokhov V. S., 2005, A&A, 436, 945
Hillier D. J., Davidson K., Ishibashi K., Gull T., 2001, ApJ, 553, 837
Illies A. J., Jarrold M. F., Bowers M. T., 1982, Chem. Phys., 65, 19
Imanishi M., Nakanishi K., 2013, AJ, 146, 91

Imanishi M., Nakanishi K., Izumi T., 2016, ApJ, 825, 44
Ishibashi K. et al., 2003, AJ, 125, 3222
Izumiura H., Ukita N., Kawabe R., Kaifu N., Tsuji T., Unno W., Koyama K., 1987, ApJ, 323, L81
Johansson S., Hartman H., Letokhov V. S., 2006, A&A, 452, 253
Kiminki M. M., Reiter M., Smith N., 2016, MNRAS, 463, 845
Koch A., van Hemert M. C., van Dishoeck E. F., 1995, J. Chem. Phys., 103, 7006
Lambert D. L., Brown J. A., Hinkle K. H., Johnson H. R., 1984, ApJ, 284, 223
Liszt H., Gerin M., 2018, A&A, 610, A49
Liszt H., Lucas R., 2001, A&A, 370, 576
Liszt H., Lucas R., Black J. H., 2004, A&A, 428, 117
Loinard L., Menten K. M., Güsten R., Zapata L. A., Rodríguez L. F., 2012, ApJ, 749, L4
Loinard L., Kamiński T., Serra P., Menten K. M., Zapata L. A., Rodríguez L. F., 2016, ApJ, 833, 48
Madura T. I. et al., 2013, MNRAS, 436, 3820
Mehner A., Davidson K., Ferland G. J., Humphreys R. M., 2010, ApJ, 710, 729
Morris P. W., Gull T. R., Hillier D. J., Barlow M. J., Royer P., Nielsen K., Black J., Swinyard B., 2017, ApJ, 842, 79
Okazaki A. T., Owocki S. P., Russell C. M. P., Corcoran M. F., 2008, MNRAS, 388, L39
Pagani L., Favre C., Goldsmith P. F., Bergin E. A., Snell R., Melnick G., 2017, A&A, 604, A32
Pittard J. M., Corcoran M. F., 2002, A&A, 383, 636
Pratap P., Dickens J. E., Snell R. L., Miralles M. P., Bergin E. A., Irvine W. M., Schloerb F. P., 1997, ApJ, 486, 862
Pulliam R. L., Edwards J. L., Ziurys L. M., 2011, ApJ, 743, 36
Rizzo J. R., Martín-Pintado J., Henkel C., 2001, ApJ, 553, L181
Rizzo J. R., Martín-Pintado J., Desmurs J.-F., 2003a, in van der Hucht K., Herrero A., Esteban C., eds, Proc. IAU Symp. 212, A Massive Star Odyssey: From Main Sequence to Supernova. Lanzarote, Spain, p. 742
Rizzo J. R., Martín-Pintado J., Desmurs J.-F., 2003b, A&A, 411, 465
Rizzo J. R., Jiménez-Esteban F. M., Ortiz E., 2008, ApJ, 681, 355
Shalabiea O. M., Greenberg J. M., 1996, A&A, 307, 52
Smith N., 2002, MNRAS, 337, 1252
Smith N., 2004, MNRAS, 351, L15
Smith N., 2006, ApJ, 644, 1151
Smith N., 2008, Nature, 455, 201
Smith N., Gehrz R. D., Hinz P. M., Hoffmann W. F., Hora J. L., Mamajek E. E., Meyer M. R., 2003a, AJ, 125, 1458
Smith N., Davidson K., Gull T. R., Ishibashi K., Hillier D. J., 2003b, ApJ, 586, 432
Smith N., Brooks K. J., Koribalski B. S., Bally J., 2006, ApJ, 645, L41
Smith N., Ginsburg A., Bally J., 2018, MNRAS, 474, 4988
Tafoya D. et al., 2007, AJ, 133, 364
Teodoro M., Madura T. I., Gull T. R., Corcoran M. F., Hamaguchi K., 2013, ApJ, 773, L16
Teodoro M. et al., 2016, ApJ, 819, 131
van Dishoeck E. F., Jonkheid B., van Hemert M. C., 2006, Faraday Discuss., 133, 231
Verner E., Bruhweiler F., Gull T., 2005, ApJ, 624, 973
Walsh C., Nomura H., Millar T. J., Aikawa Y., 2012, ApJ, 747, 114
Weigelt G., Ebersberger J., 1986, A&A, 163, L5
Weigelt G., Kraus S., 2012, in Davidson K., Humphreys R. M., eds, Astrophysics and Space Science Library Vol. 384, Eta Carinae and the Supernova Impostors. Springer-Verlag, Berlin, p. 129
White S. M., Duncan R. A., Chapman J. M., Koribalski B., 2005, in Humphreys R., Stanek K., eds, ASP Conf. Ser. Vol. 332, The Fate of the Most Massive Stars. Astron. Soc. Pac., San Francisco, p. 129
Yan M., Dalgarno A., Klemperer W., Miller A. E. S., 2000, MNRAS, 313, L17
Young Owl R. C., Meixner M. M., Wolfire M., Tielens A. G. G. M., Tauber J., 2000, ApJ, 540, 886

This paper has been typeset from a TEX/LATEX file prepared by the author.

CHAPTER 6
RESULTS IN OTHER SOURCES

This chapter describes preliminary and partially unpublished results from spectral line and continuum observations of six additional LBV sources, namely G79.29+0.46, HD168625, HD168607, [GKF2010] MN87, [GKF2010] MN48, and AFGL2298. The continuum results, regarding G79.29+0.46, HD168625, HD168607 and [GKF2010] MN87, have been published in Paper II. Despite some findings presented in this chapter are not conclusive, they constitute a significant part of the observational efforts done in the course of this thesis. These partial results are thus interesting in their own right, contribute to a more comprehensive view of the LBV mass-loss phenomena, and provide support for further observations.

6.1 G79.29+0.46

G79.29+0.46 is a galactic LBV candidate immersed in the complex Cygnus X region, at a distance of 1.7 kpc (Schneider et al., 2006). It constitutes a canonical case of study of molecular chemistry around LBV sources. G79.29+0.46 is surrounded by two nearly spherical nested shells of dust, formed as a result of several mass eruptions in the past. These structures, clearly visible at mid-infrared wavelengths (Jiménez-Esteban et al., 2010), exhibit a molecular counterpart of warm and dense CO (e.g., Rizzo et al., 2008), whose velocity profiles reveal low-velocity shocks due to changes in the stellar wind regime, as well as hints of dynamical interaction with the neighbouring infrared dark cloud (IRDC) G79.3+0.3 (Redman et al., 2003), linked to DR15 (Figure 6.1). An NH_3 ring, plus several hot clumps, have also been reported toward the shell. The gas phase abundances measured, unexpectedly high in the presence of strong UV fields, can be interpreted as a signpost of active shock-induced chemistry: the low-velocity shocks triggered by the stellar wind would be releasing ammonia from dust grains (Rizzo et al., 2014). As of today, G79.29+0.46 is the only LBV-like object, along with η Car, where ammonia has been reported.

The radio continuum emission properties of G79.29+0.46 were investigated by Higgs et al. (1994) and Umana et al. (2011) in the 1–10 GHz regime. The latter observations, obtained with the EVLA (expanded Very Large Array) at an angular resolution comparable to the *Spitzer* infrared images, allowed for tracing the distribution of ionised gas, revealing that only the innermost dusty shell is ionised. From

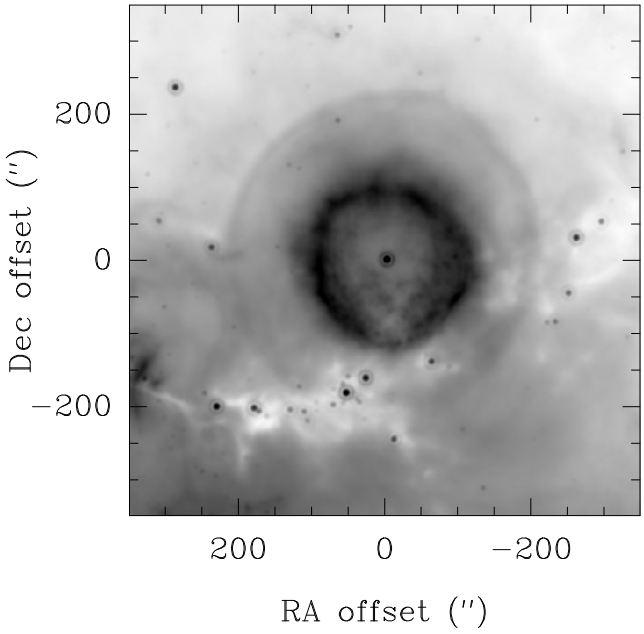

FIGURE 6.1: *Spitzer* MIPS 24 μm image of G79.29+0.46 and its surroundings. The cloud crossing the field from the south is the IRDC G79.3+0.3.

the flux density of the central object, the authors estimated a current-day mass loss rate $\dot{M} = 5 \times 10^{-7}$ M$_\odot$ yr^{-1}, one order of magnitude below the mass-loss rates derived for other LBVs.

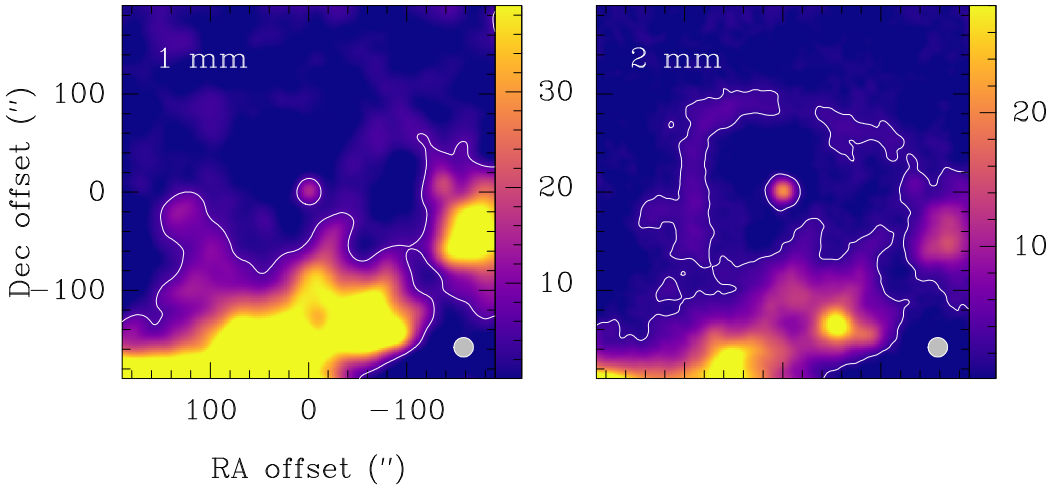

FIGURE 6.2: NIKA2 continuum maps at 1 and 2 mm of the field around G79.29+0.46, convolved to a common angular resolution of 20 arcsec for easier comparison. Intensity scale in mJy beam^{-1}, with contours depicting the half-power level of the point-like source, 5.3 and 2 mJy beam^{-1}, respectively.

However, little is known about the continuum emission at mm wavelengths. For that reason, we observed the source with the NIKA2 instrument at the IRAM 30m telescope, under project P044-17 (P.I: J. R. Rizzo). The source was observed for a

total of 1.1 hours in October 2017, achieving a rms of 5.2 and 1.3 mJy beam^{-1} at 1 and 2 mm respectively, under excellent weather conditions.

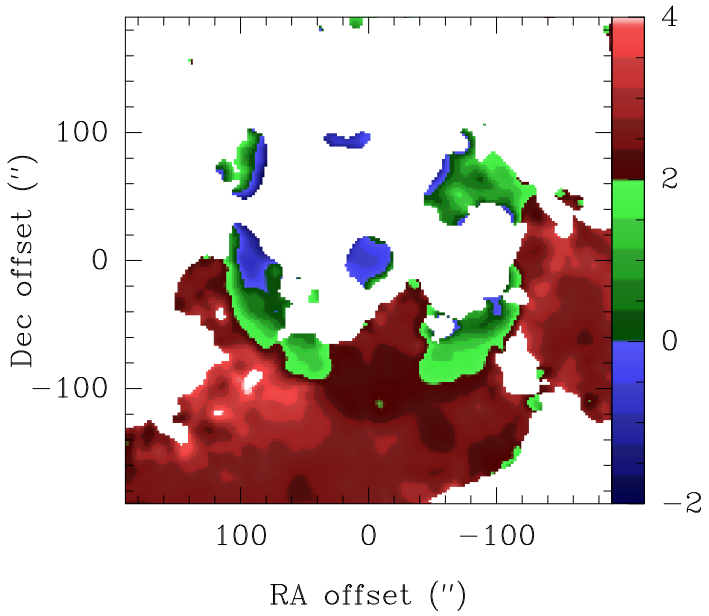

FIGURE 6.3: Spectral index map of and around G79.29+0.46.

Figure 6.2 shows the 1 and 2 mm NIKA2 maps in a 400×400 arcsec field centred on G79.29+0.46 and smoothed to a common beam of 20 arcsec. In both maps, the most intense feature is an *arm* extending from SE to W, corresponding to the neighbouring IRDC. The central star is detected at the two frequencies, completely detached from its surroundings. A shallow shell-like structure is also detected in the two maps, being more prominent at 2 mm, where non-thermal emission dominates. It has a radius of ∼100 arcsec, nearly coincident with the innermost infrared shell.

To unveil the physical mechanisms responsible for the observed emission, we computed the spectral index map, as defined in Chapter 2, considering only those pixels with flux densities above 2σ. The resulting map, presented in Figure 6.3, is striking, clearly displaying three separate components coexisting in the field of G79.29+0.46. The stellar position presents a negative spectral index, with a beam averaged value of ~ -0.3. This contrasts with the positive spectral index of 1.39 ± 0.14 between 5 and 8.4 GHz, derived from higher-resolution VLA observations by Higgs et al. (1994). We note that the source is far from being resolved by the NIKA2 beam, thus measuring a negative α value may suggest a significant contribution by a non-thermal component in the vicinity of the star. Such a component, only noted at higher frequencies, would be "masking" the expected thermal stellar wind ($\alpha \sim 0.6$). Conversely, in the shell, we measure thermal values as expected for free-free emission; whereas in the IRDC, we observe the highest values of α, typical of a cold interstellar cloud. However, the most outstanding feature is the stratification observed towards the position $(+100'', -20'')$, a transition from the quiescent IRDC, characterised by positive, thermal α values, to likely shocked material within the nebula, displaying a negative, likely non-thermal spectral index (Palau et al., 2014).

6.2 [GKF2010] MN87

[GKF2010] MN87 (=MGE G027.3839-00.3031, hereafter MN87) is a peculiar ring-like infrared bubble first identified in the MIPSGAL legacy survey as a possible LBV candidate by Gvaramadze et al. (2010), who also reported a faint radio counterpart at 20 cm from the MAGPIS survey. The infrared 24 μm image of MN87 depicts a nearly circular ring of about $\sim$1 arcmin in diameter, characterised by a strikingly asymmetric brightness distribution, with the most intense emission arising from the southeastern side, and a faint central source. VLA continuum observations at 5 GHz revealed an apparently unrelated radio morphology, consisting of a central point source surrounded by clumpy, limb-brightened circumstellar nebulae with a remarkable bipolarity along the EW axis (Ingallinera et al. 2016, see Figure. 6.4). The spectral index of the central source was found to be compatible with a stellar wind, although loosely constrained due to large uncertainties ($\alpha = 0.9 \pm 1.0$). Near-infrared spectroscopy with VLT/SINFONI confirmed that the central source is a massive star with strong H, He and metal emission lines, reassuring its classification as a candidate LBV (Silva et al., 2017).

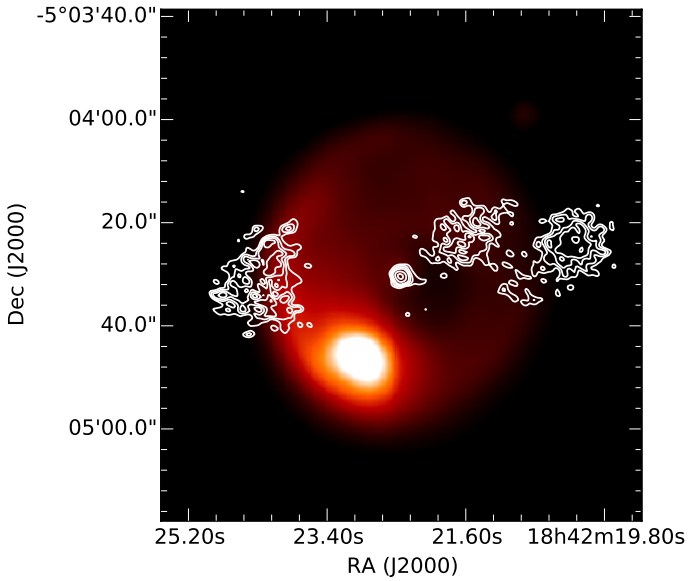

FIGURE 6.4: VLA 6-cm continuum emission as contours, superimposed to the MIPSGAL 24 μm image of MN87 (Credits: Ingallinera et al. 2016).

MN87 was observed along with MN101 (see Chapter 3) as part of the programs P043-17 and P044-17 at the IRAM 30m radio telescope in Pico Veleta (Granada, Spain), to map the distribution of molecular gas in the outskirts of the star and study its mm-wavelength continuum emission. Spectroscopic observations targeting CO, ^{13}CO and C^{18}O took place in July 2017, under good summer conditions (4 mm of precipitable water vapour). NIKA2 continuum observations were taken during the pool session in October 2017, for a total integration time of 0.9 hours distributed in 30 scans.

Careful inspection of the spectra toward MN87 reveals no significant emission unambiguously associated with the infrared nebula, with the notable exception of a cavity of roughly 80×20 arcsec surrounding the star in the velocity range $(+67.3, +69.9)$ km s^{-1}, as depicted in Figure 6.5. This cavity exhibits an irregular morphology: it is slightly off-centre from the position of the star, and elongated in the SE-NW direction, approximately perpendicular to the galactic plane. These features may be easily explained by pressure and density gradients in the ISM.

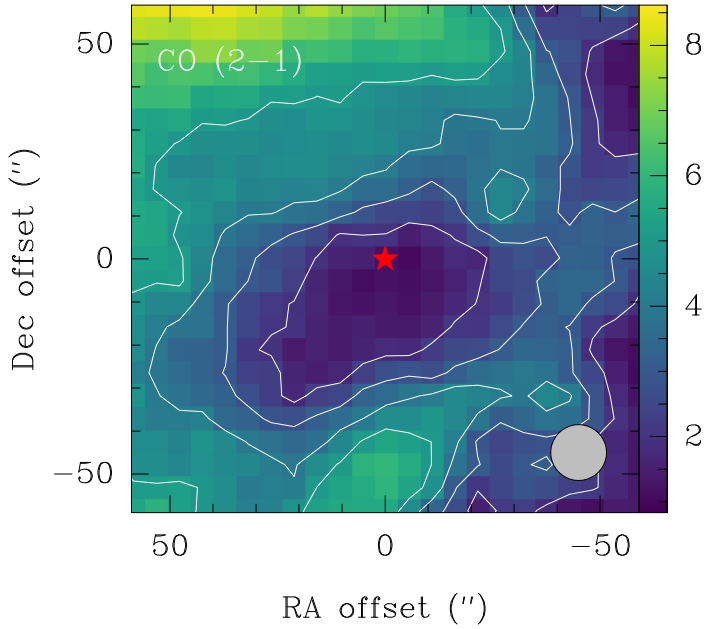

FIGURE 6.5: Velocity-integrated map of CO $J = 2 \rightarrow 1$ in the range $(+67.3, +69.9)$ km s^{-1} in colour scale and contours. Contours start at 1 K km s^{-1}, in steps of 1 K km s^{-1}. The position of the star is indicated by the red marker. The grey filled circle in the bottom right corner represents the IRAM 30m beam size.

This molecular cavity may well be part of a wind-blown bubble carved by the main sequence stellar wind of MN87, similar to the large scale structures observed in G24.73+0.69 (Petriella et al., 2012) and G26.47+0.02 (Paron et al., 2012). We can make some basic calculations to assess this possibility. The distance to MN87 is unknown, but a geometric distance can be derived from Gaia data, applying the Bayesian method described by Bailer-Jones et al. (2018). The resulting most likely distance is $d = 3.8$ kpc, with uncertainties in the range 2–6 kpc. Such values are consistent with the kinematic distance derived from the systemic velocity of the structure. The size of the cavity would then equal to 1.5×0.4 pc at $d = 3.8$ kpc. This is a somewhat modest size compared to the typical dimensions of main sequence wind-blown bubbles, usually spanning up to 30 pc (Garcia-Segura et al., 1996b). Still, we note that the limited map coverage may be preventing us from seeing the entire bubble, which may be considerably larger.

It is possible to roughly estimate the amount of gas swept-up by the stellar wind. Assuming that the cavity is an ellipsoid, with a size along the line of sight equal to that of the minor axis, its volume would be ~ 0.13 pc^3. For an average ISM density of 1 cm^{-3} ($\sim 10^{-24}$ g cm^{-3}), the evacuated mass would be just 0.002 M$_\odot$. We may

consider that the natal molecular cloud where the star formed would have a fairly higher density, perhaps as high as ∼1000 cm^{-3}, in which case the evacuated mass would be around 2 M$_\odot$. As an alternative approach, we can estimate the "missing mass" from the integrated intensity map, presuming that the cavity would be initially filled with an amount of material comparable to that of the surroundings, thus having a similar integrated intensity. For an excitation temperature of 20 K and under LTE conditions, the resulting missing mass is ∼ 0.15 M$_\odot$, an intermediate value quite in agreement with the previous ones.

In any case, these estimates do not allow for reliably confirming or rejecting the wind-blown bubble hypothesis. Follow-up observations of a larger area around the source will be useful to better constrain the dimensions of the cavity, its nature and its relation to the source.

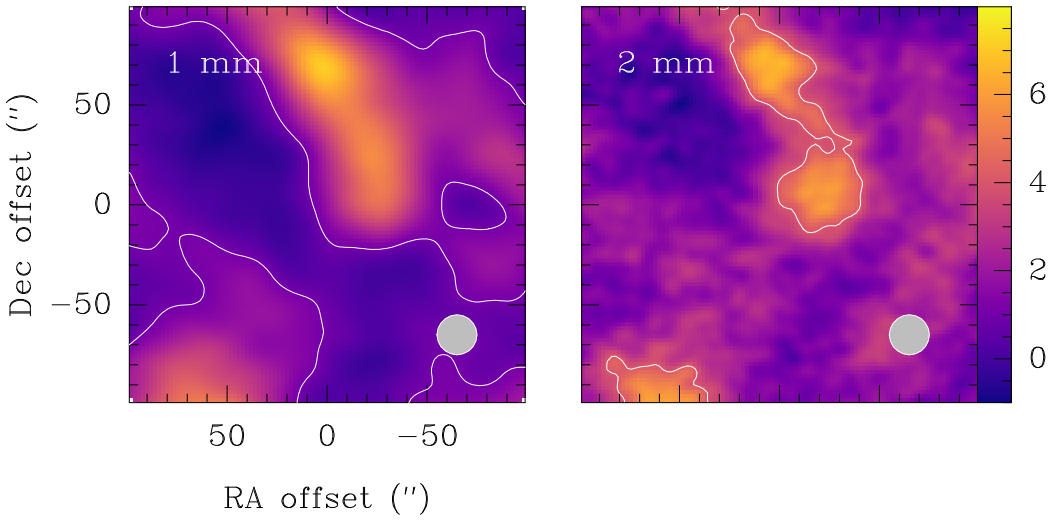

FIGURE 6.6: NIKA2 continuum maps at 1 and 2 mm of the field around MN87. The two maps have been convolved to a common angular resolution of 20 arcsec for easier comparison and have the same colour scale. The white contour represents the 5σ level, of 5 and 4 mJy beam^{-1}, respectively.

Regarding the continuum, the NIKA2 results are equally surprising, as neither the star nor the nebula are detected. The entire field, as displayed in Figure 6.6, is dominated by extended, filamentary emission extending from the SE and NE. The spectral index map is mostly positive, consistent with thermal dust emission from interstellar clouds, possibly immersed in a tenuous ionised gas. This supports the idea that the region has been mostly evacuated, although the non-detection of the star is particularly puzzling, considering its positive spectral index at cm wavelengths (Ingallinera et al., 2016).

6.3 HD168625 and HD168607

HD168625 (=IRAS 18148-1623) is a B2–B8 LBV candidate (Hutsemekers et al., 1994) located at $d = 2.8$ kpc (Pasquali et al., 2002) which shows no remarkable spectrophotometric variability. However, this object is particularly interesting due to its extremely complex circumstellar morphology, which consists of a central, compact dusty torus of 10×13 arcsec (Nota et al., 1996), and a more diffuse, perpendicular and slightly bipolar nebula with two plane parallel polar rings (Smith, 2007a), of roughly 16×24 arcsec. Overall, these nebular structures around HD168625 closely resemble the circumstellar ejecta of SN1987A, making of HD168625 a promising analogue to shed new light onto the hypothesis of LBV stars as direct progenitors of core-collapse supernovae (see Chapter 1). Indeed, the possible relationship between LBV stars with ring-like structures and SN1987A is a hot topic with important implications for stellar evolution, and therefore is thoroughly discussed in Chapter 7. Umana et al. (2010) reported clumpy radio continuum emission arising from the central torus and the point source, as well as spectral features attributable to PAHs, possibly tracing a PDR in the ionised nebula.

HD168607 is a confirmed LBV star (Chentsov, 1980) that lies about ∼1' westward of HD168625. No circumstellar material has been detected around it so far (Hutsemekers et al., 1994). There are claims that the two stars are physically close, not only in projection (e.g., Chentsov & Gorda 2004), thus belonging to the Ser OB1 association, which would imply a shorter distance. However, such a relationship is still dubious and needs to be confirmed. Figure 6.7 shows the IRAC 8 μm image of the two stars.

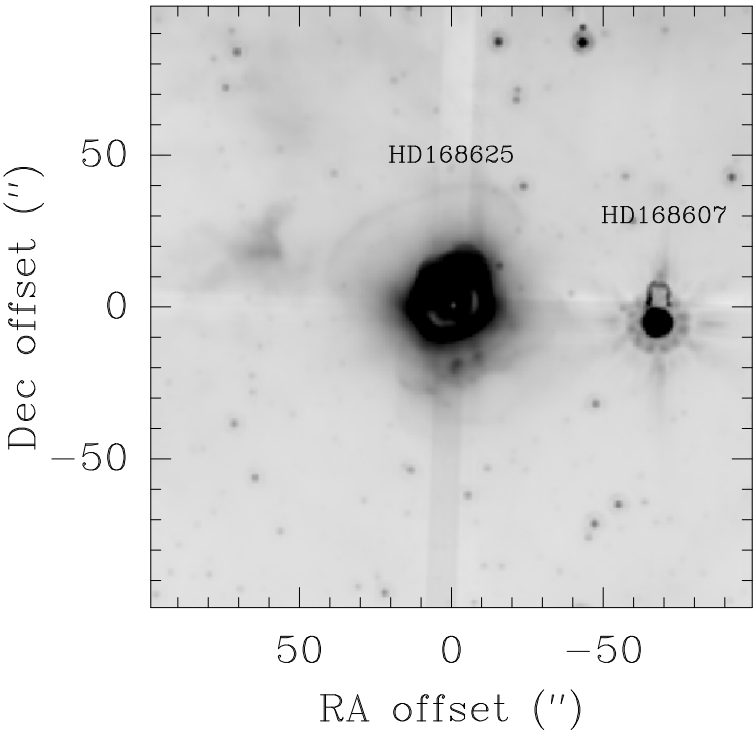

FIGURE 6.7: IRAC 8 μm image of the field of HD168625 and HD168607.

The nebular material around HD168625, due to its striking likeness to that of SN1987A, is an excellent laboratory to investigate the conditions of pre-SN CSM. Aiming at exploring the possible existence of molecular material in the outskirts of HD168625 and learning about its continuum emission mechanisms at mm wavelengths, we observed the source in two consecutive campaigns at the IRAM 30m telescope: first, with the NIKA2 instrument, under project P044-17 (P.I: J. R. Rizzo) in October 2017; and later, in a dedicated molecular spectroscopy project, with code P053-18 (P.I: C. Bordiu), in September 2018. In both cases, we took advantage of the closeness to HD168607, observing a broad field that included the other LBV as a secondary target.

Figure 6.8 presents the CO $J = 2 \rightarrow 1$ spectra toward HD168625 and HD168607, averaged in a region of 15 arcsec in radius around each star. The spectra reveal a crowded field, with multiple overlapping velocity components of very different widths, and some reference problems, as suggested by the strong negative features between $(+50, +70)$ km s^{-1}. Many of the components are visible, at different intensity levels, in the two spectra, clearly indicating a rather ubiquitous (interstellar) nature. According to Pittard & Corcoran (2002), HD168625 has a LSR velocity of 25.5 km s^{-1}. No component centred at this velocity is detected in the spectra, but closer inspection of the spatial distribution of the emission allows us to identify a series of clumps surrounding the nebula. Most of these clumps are part of widespread features that appear throughout the whole field. This heavy contamination makes it extremely difficult to establish a clear connection between the clumps and the star.

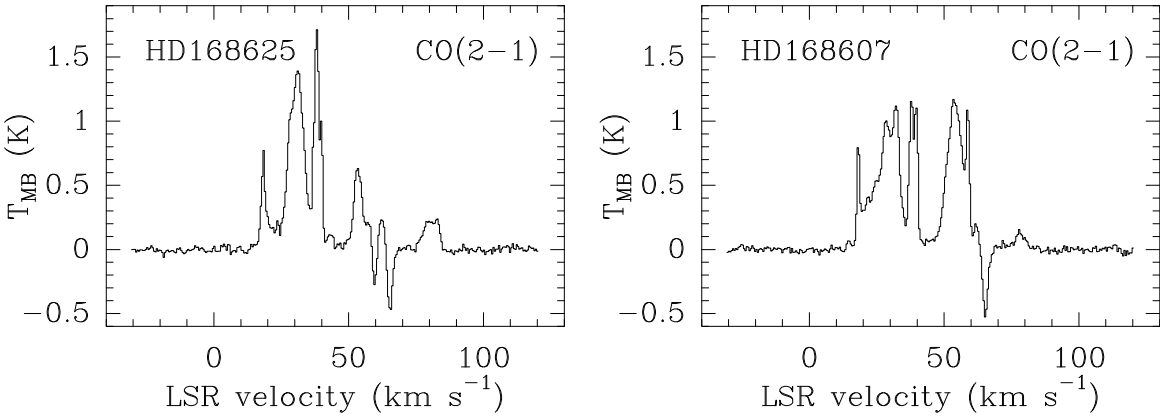

FIGURE 6.8: CO $J = 2 \rightarrow 1$ spectra toward HD168625 (left) and HD168607 (right), averaged in a region of 15 arcsec in radius centred in the corresponding stellar positions.

Nevertheless, we note the presence of a promising feature in the approximate velocity range $(+17, +19)$ km s^{-1}, visible both in CO and ^{13}CO. Figure 6.9, left panel, shows the integrated intensity map of CO $J = 2 \rightarrow 1$ over this range. The field appears mostly evacuated, except for two clumps, remarkably symmetric with respect to HD168625. The clumps embrace the infrared nebula on the EW direction, at an angular separation of ∼20 arcsec, corresponding to a physical distance of ∼0.3 pc. The eastern clump is brighter and slightly more extended than the one in the West.

Both clumps have almost the same velocity, blueshifted by ∼8–9 km s^{-1} from the systemic velocity of HD168625. We unsuccessfully searched for a redshifted counterpart in the opposite velocity range, which is heavily contaminated. Figure 6.9, right

panel, shows a position velocity cut along the two clumps, roughly in the EW direction. No kinematic pattern is evident, but the clumps seem surprisingly isolated in velocity, without any other nearby emission in at least ±20 km s^{-1}.

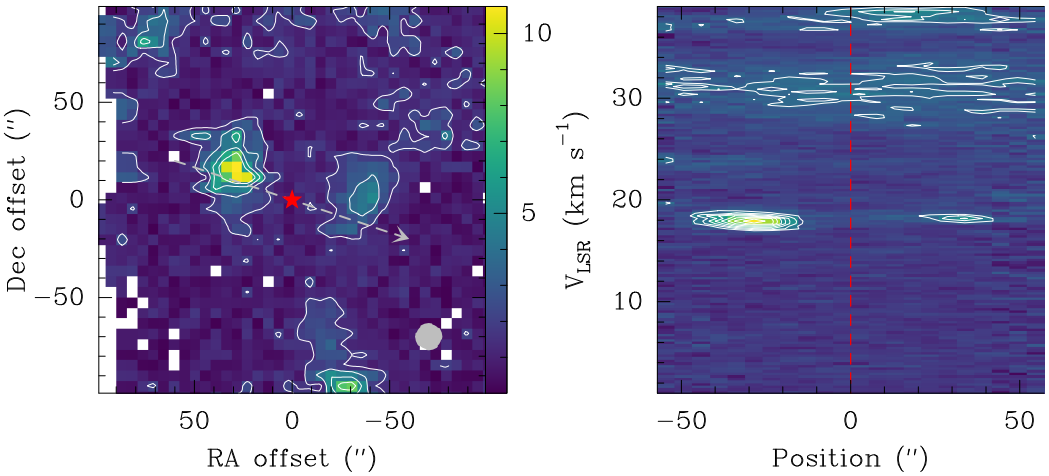

FIGURE 6.9: CO $J = 2 \rightarrow 1$ emission towards HD168625. Left: velocity-integrated map of CO $J = 2 \rightarrow 1$ towards HD168625, in the range $(+17, +19)$ km s^{-1}. Contours starting at 1.75 K km s^{-1}, in steps of 0.75 K km s^{-1}. The position of the star is indicated by the red marker. The grey filled circle in the bottom right corner represents the IRAM 30m beam size. Right: position-velocity diagram in the direction indicated by the grey arrow on the left panel. The position of the star is indicated by the red vertical line.

To constrain the origin of these clumps, we can make a crude estimate of their mass from the velocity-integrated intensity. Table 6.1 summarizes the column densities and masses derived by assuming LTE conditions and an excitation temperature of 20 K. The CO column densities, of 10^{15} cm^{-2}, are similar to those found in other LBVs, but the corresponding mass is just $\sim$0.05 M$_\odot$, a surprisingly low value compared to the structures around AG Car and [GKF2010] MN101.

Position	W (σW) [K km s^{-1}]	N(CO) [cm^{-2}]	Mass [M$_\odot$]
clump E	6.3 (0.9)	1.8 (0.3) $\times 10^{15}$	0.038 (0.006)
clump W	3.9 (0.9)	1.1 (0.3) $\times 10^{15}$	0.011 (0.004)

TABLE 6.1: Mass estimates for the CO clumps of HD168625.

With the information at hand, it is not possible to provide a reliable interpretation of these features: they could just be two unrelated clumps aligned by chance, some fragments of the parent molecular cloud that have survived shielded by the dusty torus, or even a bipolar outflow. However, the discovery of compact emission features in the vicinity of HD168625 is encouraging in its own right, and underlines the need for follow-up interferometric observations that preserve only the small scale emission. On the contrary, the lack of significant features toward HD168607 is consistent with

previous negative detections of associated circumstellar material (Hutsemekers et al., 1994).

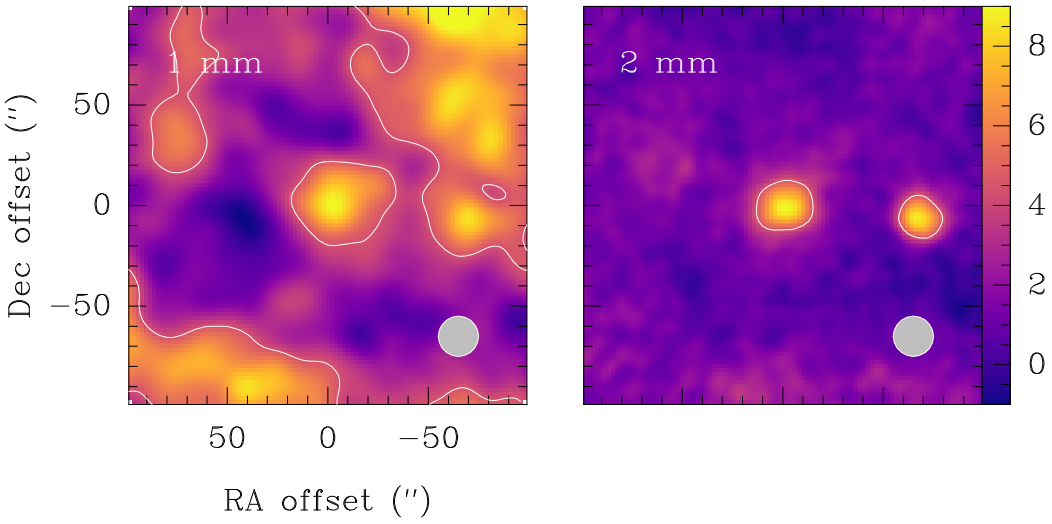

FIGURE 6.10: NIKA2 continuum maps at 1 and 2 mm of the field around HD168625 and HD168607 (to the west). The two maps have been convolved to a common angular resolution of 20 arcsec for easier comparison and have the same colour scale. The white contours depict the half-power level measured at the position of HD168625, 4.4 and 4.5 mJy beam^{-1}, respectively.

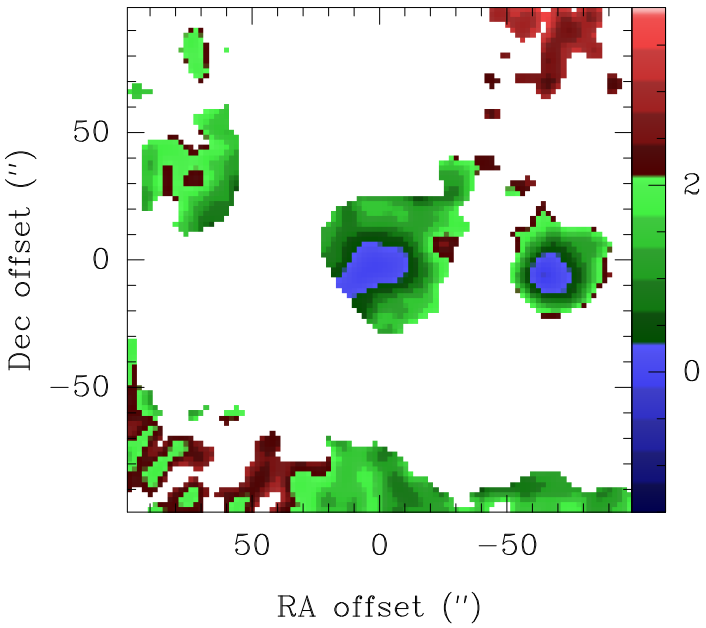

FIGURE 6.11: Spectral index map of HD168625 and HD168607.

Interestingly, both HD168625 and HD168607 are detected at 1 and 2 mm in the NIKA2 maps, as shown in Figure 6.10. The whole field is contaminated by extended emission toward the SE and NW, bright at 1 mm. HD168625 is embedded in a shallow plateau, whose angular extent is compatible with the size of the infrared nebula seen

at 8 μm. The plateau is less pronounced at 2 mm, where the two sources appear isolated from their surroundings.

The spectral index map, as in the case of G79.29+0.46, allows us to discriminate the stars from their circumstellar environment. The stars exhibit the lowest α in the field, with beam-averaged values of $\sim$0.1 and $\sim$0.2 for HD168625 and HD168607, respectively. These values are below, but still compatible with, the stellar thermal wind expected in LBV stars, characterised by $\alpha \approx 0.6$. However, the sources are not resolved by the NIKA2 beam, so the low α can also be explained by an overlapping non-thermal component acting close to the stars. In this sense, it should be noted the recent detection of stellar companions for both LBV sources by means of optical interferometry (Mahy et al., 2021), which somehow supports the occurrence of non-thermal processes due to binary interactions, e.g., wind-wind collisions. On the other hand, most of the surrounding medium presents significantly higher spectral indices: the plateau in which the sources are immersed has values of 0.6–1.2, compatible with thermal emission from cold clouds, whereas at the edges of the field we find the highest α values, possibly tracing warm dust.

6.4 [GKF2010] MN48

[GKF2010] MN48 (=MGE G340.0297-00.5840, hereafter MN48) was identified as a bright infrared bubble in archival *Spitzer* MIPSGAL imagery (Gvaramadze et al., 2010). Spectrophotometric follow up of the central source revealed significant brightness variations of >1 mag, leading to its recent classification as a bona fide galactic LBV (Kniazev et al., 2016). MN48 constitutes an excellent analogue of the LBV candidate G79.29+0.46, mimicking its main morphological features. It is surrounded by a nearly spherical dusty shell of a radius of $\sim$ 1.5 arcmin, mainly visible between 22 and 24 μm. The brightness of the shell increases toward its western side, which is interpreted as a clear signpost of interaction with the nearby HII region IRAS 16455-4531, located less than 5 arcmin to the west. In some aspects, this scenario resembles the proposed interaction between G79.29+0.46 and the IRDC G79.3+0.3 (e.g., Rizzo et al., 2014).

Intending to investigate if the physical conditions in the outskirts of MN48 are adequate for molecules and if molecular counterparts of dusty infrared shells represent a common feature of LBV stars, we observed MN48 in a dedicated program (E-0103.D-0778A-2019, P.I: C. Bordiu) at the APEX telescope in Llano de Chajnantor (Chile). Observations, conducted between May 10 and Sep 04, 2019, combined two strategies: (1) an on-the-fly map of 360×360 arcsec around the star, to map the distribution of CO and its isotopologues ^{13}CO and C^{18}O; and (2) deep integrations at positions $(0'', 0'')$, $(-65'', 70'')$ and $(-80'', -60'')$, corresponding to the star, the NW and the SW edges of the shell, respectively. For the deep integrations, two additional spectral setups were used, to explore the possible chemical complexity of the environment, targeting CN, HCN, HNC and HCO$^+$ among other tracers. Total observing time amounted to 21.6 h, with precipitable water vapour varying from 0.7 to 2.4 mm between the different observing sessions. The average rms per frequency channel in the final spectra was about 20 mK.

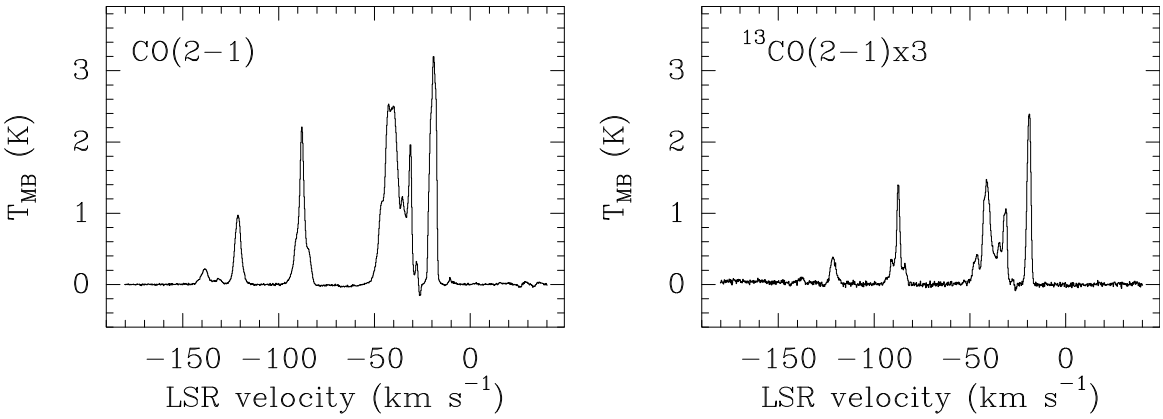

FIGURE 6.12: CO and ^{13}CO $J = 2 \rightarrow 1$ spectra toward MN48, averaged in a region of radius ∼90 arcsec centred in star. The ^{13}CO spectra has been scaled by a factor of 3.

Figure 6.12 shows averaged spectra of CO and ^{13}CO within a radius of 90 arcsec around MN48, corresponding to the extent of the infrared nebula. The spectrum is populated by multiple components at negative velocities, extending approximately from −150 to −10 km s^{-1} and detected in the two transitions. Kniazev et al. (2016)

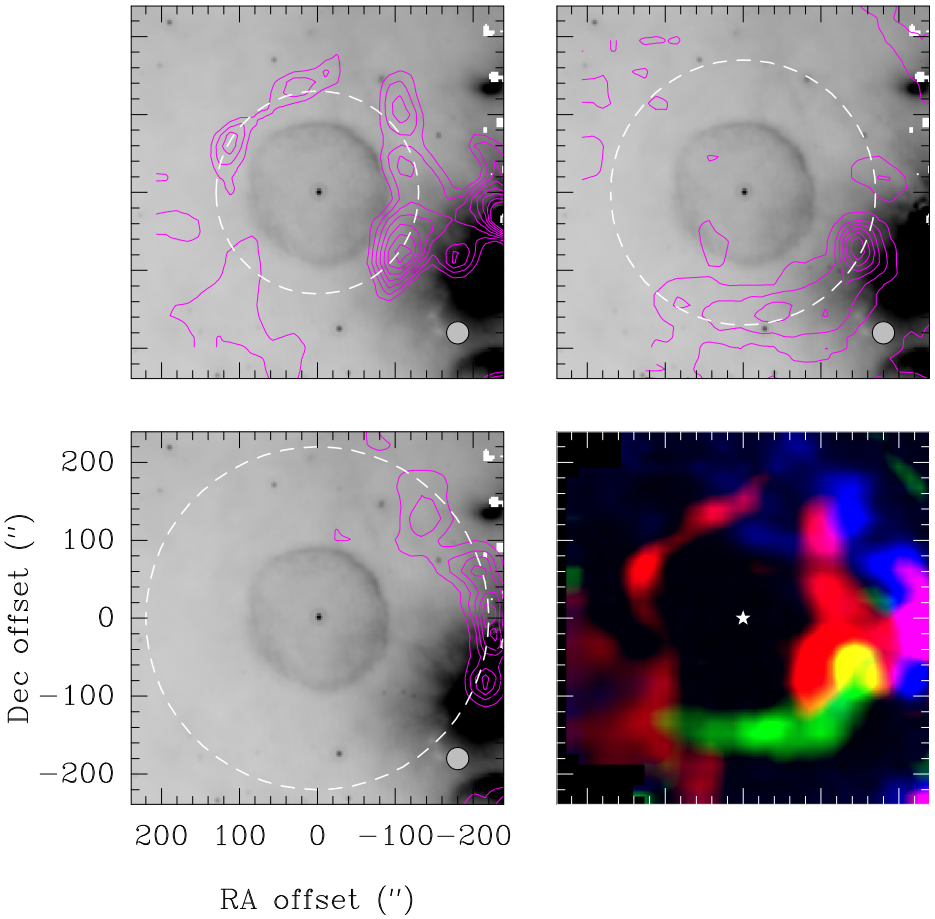

FIGURE 6.13: CO $J = 2 \rightarrow 1$ velocity-integrated maps of the inner, middle and outer shells around MN48, as contours (starting at 1.5 K km s^{-1}, in steps of 1.5 K km s^{-1}), superimposed to the MIPS 24 μm image of the field. The grey filled circle in the bottom right corner represents the APEX beam size at the observing frequency. Bottom right: RGB composition of the three shells. The white marker indicates the star position.

reports a systemic heliocentric velocity of -37 km s^{-1} from measurements of the [FeII]λ7155 line, corresponding to -28.5 km s^{-1} LSR. This velocity falls within the most contaminated spectral range, where multiple components overlap. After a detailed inspection of the spatial distribution of the emission, we found no evident features near the systemic velocity.

However, at other velocity ranges we identify a series of concentric shell-like structures that partially enclose the infrared nebula, as depicted in Figure 6.13. The most prominent one is the innermost shell, which lies in the approximate range $(-91, -87)$ km s^{-1}. The gas traces a clumpy and incomplete ring of $\sim$ 130 arcsec, with an opening towards the North. Its brightness distribution closely follows that of the infrared nebula, with the most intense emission arising from the southwestern side, where the alleged interaction with the nearby HII region occurs. The second, intermediate shell appears at -10 km s^{-1}, being an arc of radius $\sim$170 arcsec that loosely embraces the innermost shell towards the southwest. Finally, the third, outer arc, arises at positive velocities ($\sim$ +20km s^{-1}), toward the western edge of the map. An RGB composite

Shell	W (σW) [K km s^{-1}]	N(CO) [cm^{-2}]	Mass [M$_\odot$]	Radius [pc]	v_r [km s^{-1}]
inner	14.7 (0.6)	4.2 (0.2) $\times 10^{15}$	9.9 (0.5)	3.2	$\sim$60
middle	2.6 (0.2)	7.5 (0.4) $\times 10^{14}$	1.4 (0.1)	4.1	$\sim$20
outer	4.4 (0.1)	1.3 (0.1) $\times 10^{15}$	1.5 (0.1)	5.3	$\sim$50

TABLE 6.2: Mass, size and projected expansion velocity (v_r) of the shells of [GKF2010] MN48.

image of the three shells is shown in Figure 6.13 to highlight the layered structure of the emission. No other molecules have been detected toward the star or the shells.

MN48 is most likely located at $d = 5$ kpc (Kniazev et al., 2016). Such a distance implies that the arc-like structures are considerably large, with radii of 3.2, 4.1 and 5.3 pc respectively. One possible explanation is that they trace ISM material, that has been accumulated and compressed by the variable stellar wind of MN48. An alternative scenario is that the molecules have formed *in situ*, as a result of one or more mass eruptions, once the ejecta cooled off. The mass contained in the shells could be a discriminating factor, so we used the average integrated intensity of the shells to crudely estimate their masses, considering an excitation temperature of 20 K and assuming LTE conditions. The resulting CO column densities and masses are compiled in Table 6.2. The innermost shell is by far the most massive, with $\sim$10 M$_\odot$, comparable to the mass of the shell of G79.29+0.46 (Rizzo et al., 2008). The middle and outer shells, on the other hand, have similar but smaller masses, of $\sim$1.5 M$_\odot$ each. In view of the size of these shells, the molecular gas lies sufficiently far away from the star to be reasonably protected from the stellar UV field. Therefore, the progressive accumulation of several solar masses over relatively long time-scales is perfectly possible.

Another crucial point to disclose the origin of these shells is gas kinematics. At this point, we must consider two hypotheses: either the shells originated independently, in successive events, or they belong to the same physical structure, i.e., they are "slices" of a spherical shell. Under the first hypothesis, we can assume that we are observing the shells at their maximum extent. Therefore, we can estimate their dynamic age, t_dyn as R/v_r, with $v_\mathrm{r} = |v_\mathrm{sys} - v_\mathrm{shell}|$ the projected expansion velocity (see Table 6.2). We thus obtain dynamic ages of 5×10^4, 2×10^5 and 1×10^5 years for the inner, middle and outer arcs, respectively. These quantities are clearly inconsistent from a kinematic perspective: the outer shell, which is on the edge of the map, cannot be simultaneously younger and more extended than the middle one. For that reason, we consider that the outer arc is not a genuine shell fragment, but an unrelated feature, possibly associated with the nearby HII region. Observations of a larger field of view could help to confirm this point. The timescale for the inner shell is barely compatible with the LBV phase, while the middle shell is likely tracing an older, pre-LBV event.

On the contrary, determining the dynamical age if we assume that the shells belong to the same structure requires a different approach. Figure 6.14 shows a model of the viewing geometry of the arcs as "slices" of a single shell. The outer arc is not included due to the inconsistency of its projected velocity, as discussed before. If the inner and middle arcs originated in the same event, and the event was isotropic, their t_dyn should

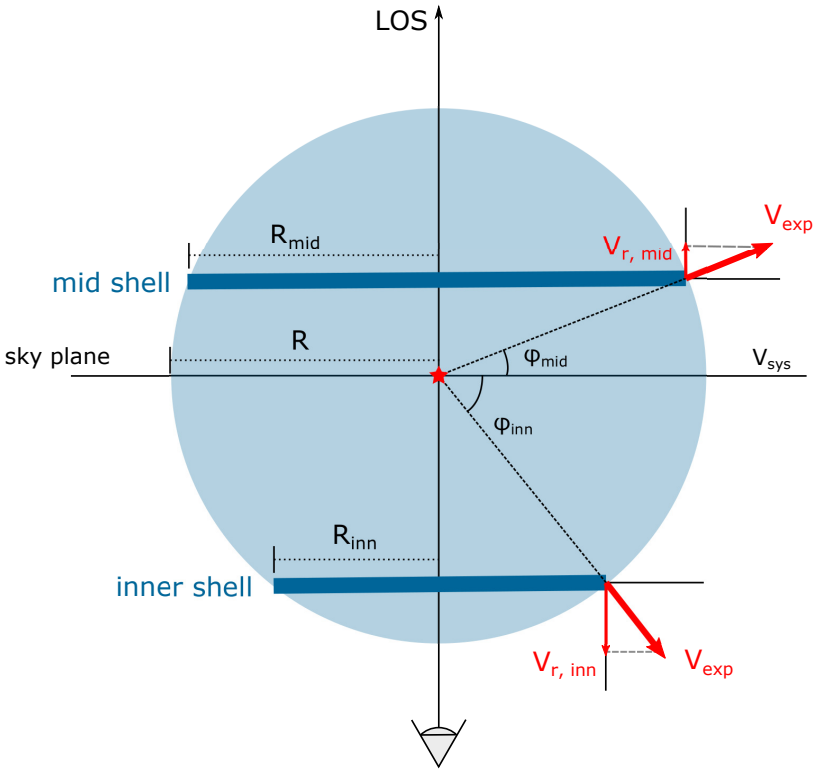

FIGURE 6.14: Single-shell model of MN48, view from the top, depicting the inner and middle molecular shells at arbitrary angles $\phi_{\rm inn}, \phi_{\rm mid}$ with respect to the plane of the sky.

be the same. Therefore, the angles of these arcs with respect to the "largest slice" –or, equivalently, the plane of sky, which corresponds to the reference velocity $v_{\rm LSR}$ =28.5 km s^{-1}–, namely $\phi_{\rm inn}$ and $\phi_{\rm mid}$, must satisfy the condition $|\phi_{\rm inn}| > |\phi_{\rm mid}|$ (because the inner shell is smaller). The two angles can be related through the trigonometric equation:

$$\frac{R_{\rm inn}}{v_{\rm r,inn}} \tan\phi_{\rm inn} = \frac{R_{\rm mid}}{v_{\rm r,mid}} \tan\phi_{\rm mid} \tag{6.1}$$

where $R_{\rm inn}$, $R_{\rm mid}$, $v_{\rm r,inn}$, $v_{\rm r,mid}$ are the radius and projected expansion velocity of the inner and middle shells, respectively (see Table 6.2). The general solution to this equation takes the form $\phi_{\rm mid} = \tan^{-1}\left(\frac{\tan\phi_{\rm inn}}{4}\right)$. $\phi_{\rm inn}$ cannot be neither 0° nor 90°, so constraining the solutions to the interval (20°,70°), we obtain $\phi_{\rm mid} \in (5°, 35°)$. We can further constrain the solution imposing an additional condition, relating the radius of the inner and middle arcs to the actual shell radius R, i.e., the radius of the largest slice:

$$R\cos\phi_{\rm mid} - R\cos\phi_{\rm inn} = 40 \tag{6.2}$$

where 40 is the difference in arcsec between the inner and middle arcs. We ignore the value of R, but it must fulfil $R \geq R_{\rm mid}$. For a reference value of $R = 200$ arcsec, we obtain a valid solution with $\phi_{\rm inner} = 39°$ and $\phi_{\rm inner} = 12°$, corresponding to a dynamical age of 4×10^4 years, still in agreement with the typical timescales of the LBV phase.

Furthermore, the innermost shell provides solid evidence of the ongoing interaction between MN48 and IRAS 16455-4531, as proposed by Kniazev et al. (2016). Figure 6.15 shows a position-velocity cut passing through the innermost shell peaks, roughly in the NE-SW direction. In the SW region, a sudden velocity broadening occurs when crossing the shell, at $\sim$ 150 arcsec from the star position, going from -87 to -94 km s^{-1}(see right panel in Figure 6.15). This feature might constitute a dynamical indicator of a low-velocity shock, with a projected velocity of $\sim$7 km s^{-1}, analogue of the shocks observed in the CO shell of G79.29+0.46 (Rizzo et al., 2008). Interestingly, a comparable jump or velocity broadening is observed at the same exact position around -40 km s^{-1}, this time spanning $\sim$10 km s^{-1}. This second broadening may indicate that the star affects the gas also in this velocity range, which is not too far from the systemic velocity.

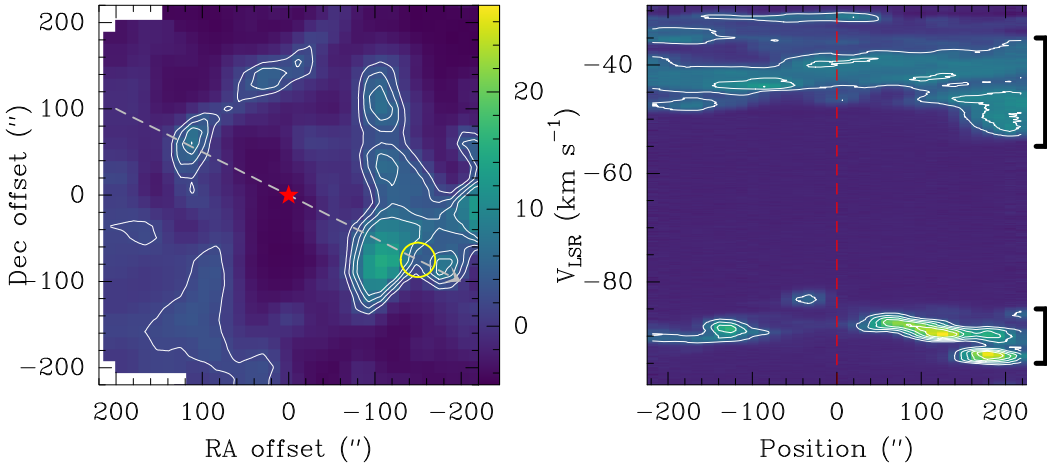

FIGURE 6.15: Left: integrated intensity map of CO $J = 2 \rightarrow 1$ toward MN48, in the velocity range corresponding to the innermost shell, $(-91, -87)$ km s^{-1}. Contours are the same as in Figure 6.13. The red marker indicates the position of the star, and the yellow circle the approximate location of the velocity jumps. Right: position-velocity cut along the direction indicated by the dashed arrow in the left panel. The red dashed line indicates the position of the star, and the black brackets indicate the velocity jumps or broadenings, starting $\sim$ 140 arcsec from the star.

All these hints make of MN48 a promising source, displaying morpho-kinematic features that suggest an active mass-loss record beyond what is inferred from the infrared shell. Follow-up observations, including mm continuum, will provide a more complete view of the dominant processes in the surroundings of this LBV star, shedding new light on the interaction between the star and the nearby HII region, and disclosing the true nature of the molecular shells.

6.5 AFGL2298

AFGL2298 (=IRAS 18576+0341) is a B0-B0.5 supergiant and confirmed LBV (Clark et al., 2003) surrounded by a dusty circumstellar nebula of roughly spherical shape, especially bright at mid-infrared wavelengths. The nebula has an inner radius of about 0.12 pc at a distance of 10 kpc, with an inferred kinematic age of 1.2×10^4 assuming an expansion velocity of ∼50 km s^{-1} (Ueta et al., 2001). At cm wavelengths, the nebula appears structured and highly asymmetric, with most of the emission concentrated to the NE, perhaps indicating enhanced photoionization from an external source or ongoing mechanical interaction with surrounding matter (Umana et al., 2005). From the flux of the central source, a current day mass-loss rate of 3.7×10^{-5} M$_\odot$ yr^{-1} was derived.

We included AFGL2298 as a target of the program P043-17 at the IRAM 30m radio telescope, with the aim of searching for molecular emission associated with the nebula. We used the same observing strategies and setups as for [GKF2010] MN101 and [GKF2010] MN87, combining on-the-fly maps with on-off pointings. Observations took place in July 2017, under good summer conditions (precipitable water vapour of 4 mm).

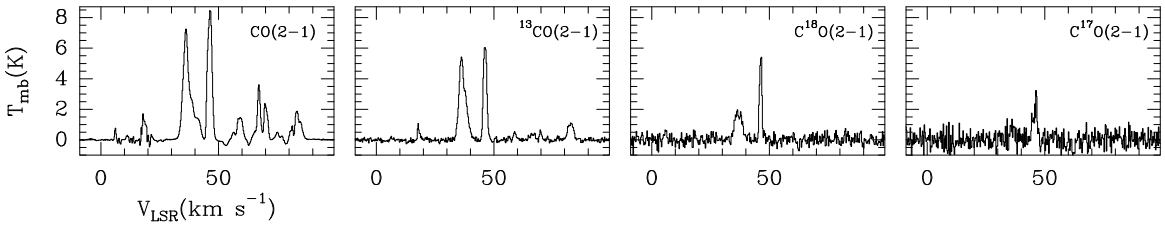

FIGURE 6.16: On-off spectra of the $J = 2 \rightarrow 1$ transitions of CO and its isotopologues toward AFGL2298. The spectra of ^{13}CO, C^{18}O and C^{17}O have been scaled by a factor of 2, 6 and 10, respectively.

The spectra towards AFGL2298 shows multiple velocity components of CO, ^{13}CO C^{18}O and C^{17}O in the range (0, +100) km s^{-1}, as shown in Figure 6.16. The spatial distribution of the emission traces several clumps across the observed field, most of them showing no clear association with the star nor the nebula. However, the velocity component at ∼46 km s^{-1} is especially noteworthy, as it always peaks towards the stellar position in all the four species, suggesting some kind of connection with AFGL2298. In the case of CO, this emission peak cannot be entirely dissociated from other neighbouring clumps or clouds, but the emission from the other isotopologues is relatively isolated in this range –in fact, C^{17}O is only clearly detected at 46 km s^{-1}–. Figure 6.17 shows the integrated intensity maps of the $J = 1 \rightarrow 0$ and $J = 2 \rightarrow 1$ transitions of C^{17}O and C^{18}O, in the velocity range (+45, +48) km s^{-1}. The four lines show a comparable spatial distribution, with C^{18}O being more extended. Despite the moderate angular resolution, the overall distribution of the molecular emission follows the approximate direction where the infrared nebula is brighter in the VLT/VISIR PAH2 filters (Umana et al., 2010), reinforcing the idea of the star actively affecting the surrounding gas.

This hypothesis is further supported by the detection of several other molecules near ∼ 46 km s^{-1}. These include N-bearing compounds, such as CN, HCN, HNC,

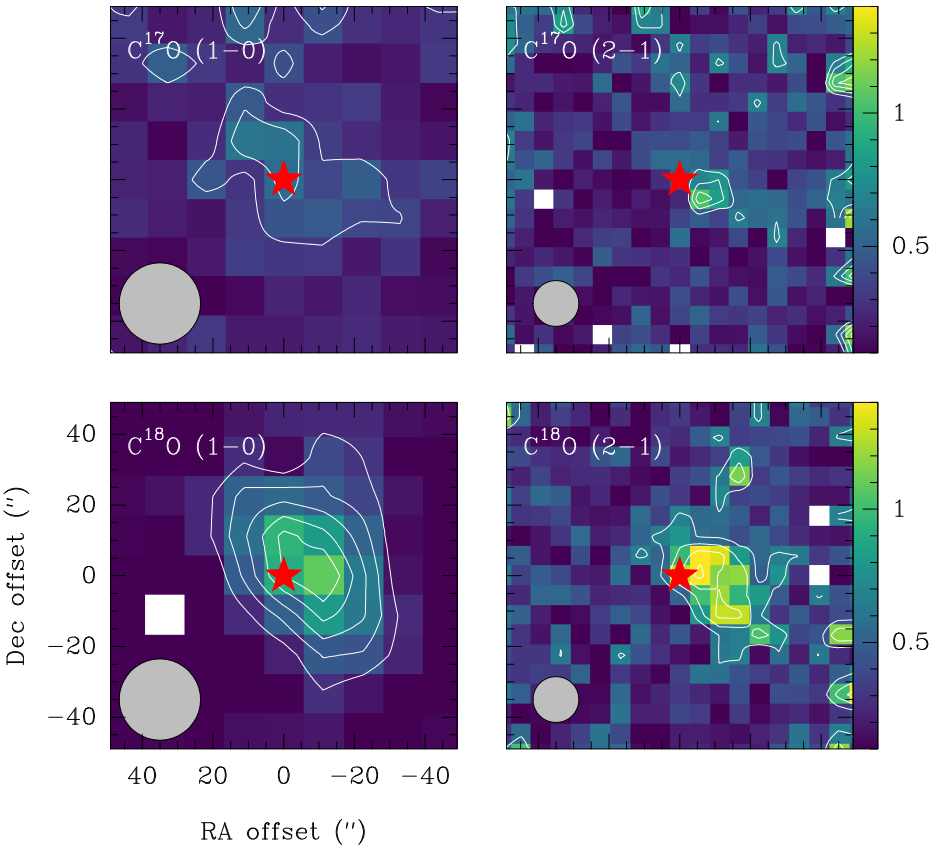

FIGURE 6.17: Integrated intensity maps of the $J = 1 \rightarrow 0$ and $J = 2 \rightarrow 1$ transitions of $C^{17}O$ and $C^{18}O$ toward AFGL2298, integrated in the velocity range $(+45, +48)$ km s^{-1}. Contours starting at 0.3 K km s^{-1}, in steps of 0.3 K km s^{-1}. The intensity scale of $C^{17}O$ $J = 1 \rightarrow 0$ is 1/3 of the others. The red marker indicates the position of the star. The grey filled circle in the bottom right corner represents the IRAM 30m beam size.

also found in the N-rich ejecta of η Car, as well as reactive species like the radical C_2H and the ions HCO^+ and N_2H^+ (see Figure 6.18). All these molecules present two non-overlapping velocity components –some of them have hyperfine structure–, at 36 and 46 km s^{-1}, respectively. The former is coincident with the velocity range dominated by ambient clouds, whereas the one at 46 km s^{-1} peaks toward AFGL2298 without exception. In some cases, such as HCO^+, the emission is even spatially isolated from other emitting clumps in the field, such as occurs with $C^{17}O$ and $C^{18}O$.

These detections can be explained in terms of two alternative scenarios: either the gas arises from a molecular cloud in the line of sight, that is being affected by the stellar winds or UV fields of AGL2298, or the molecules have formed in situ as a result of an eruptive event, as in the case of η Car and other LBV sources.

With the data available, it is not possible to disclose the actual origin of the gas. Most of the lines are weak, barely reaching a 2.5σ threshold, which complicates the study of their spatial distribution – as they are only detected in the deep on-off integrations but not in the on-the-fly maps. Besides, in most cases it is impossible to separate the emission toward the star from other contaminating components in the

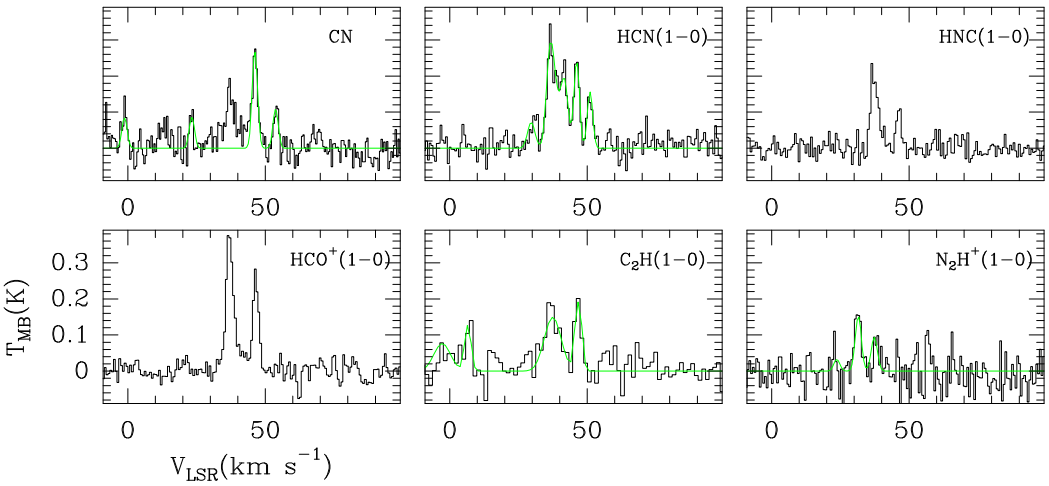

FIGURE 6.18: On-off spectra of CN (113.490 GHz), HCN $J = 1 \rightarrow 0$, HNC $J = 1 \rightarrow 0$, HCO^+ $J = 1 \rightarrow 0$, C_2H $J = 3/2 \rightarrow 1/2$ and N_2H^+ $J = 1 \rightarrow 0$ toward AFGL2298. A fit of the hyperfine structure of the 46 km s^{-1} component of CN, HCN, C_2H and N_2H^+ is superimposed in green. The spectra of CN, C_2H and N_2H^+ have been scaled by a factor of 2.

field, hampering a reliable estimate of the physical parameters of the gas. This fact, together with the small angular size of the infrared nebula (< 10 arcsec), underlines the need for interferometry. Follow-up observations will greatly contribute to elucidate the actual origin of the gas, allowing for a more accurate study of excitation conditions of the nebula and filtering most of the extended emission. Still, an in-depth analysis of the achieved detections will be presented in a forthcoming paper (Rizzo et al., *in prep*), that will explore the similarity of AFGL2298 and η Car, in terms of molecular complexity.

CHAPTER 7

OVERALL DISCUSSION, KEY INSIGHTS AND IMPLICATIONS

The existence of molecular gas structures in the outskirts of LBV stars has far-reaching implications for the current understanding of these challenging objects. Our work has significantly increased the number of sources with confirmed structures, shedding new light on their formation mechanisms and putting them in the broader context of stellar evolution. Molecular spectroscopy, in combination with millimetre continuum observations of the stars and the surrounding dust and ionised gas, allows for a precise characterisation of the circumstellar environment of these sources, raising new questions about their evolution and mass-loss history. In this chapter, we present a cohesive discussion integrating the main results of the previous chapters, highlighting their potential impact and laying the groundwork for further research.

7.1 Outlook

In the preceding chapters, we have presented a comprehensive survey of molecular gas toward a sample of bona fide and candidate LBV stars, in conjunction with a detailed study of their mm-continuum emission. The results confirm the unambiguous detection of conspicuous amounts of molecular gas associated with [GKF2010] MN101 and AG Car, as well as the discovery of a new molecular structure in the innermost region of the Homunculus Nebula, most likely associated with the lesser eruption of η Car circa 1890. In addition, a handful of other sources also show hints of associated circumstellar molecular material, even though some of these detections are non-conclusive, thus requiring follow-up observations.

Table 7.1 summarises the current state-of-the-art of molecular spectroscopy studies toward LBV stars, highlighting the contribution of this thesis. Taken altogether, these detections demonstrate that the formation and long-term survival of considerable amounts of molecular gas in the outskirts of these sources is the norm rather than the exception, contrary to the assumption that molecules were promptly destroyed by the strong radiative fields. However, some interesting questions arise about the origins of this gas and its physical and chemical properties.

Source	Species	Association	Distribution	Mass ($M_\odot$)	Origin	Comments
HD168625*	**CO**, **^{13}CO**	Loose	Roughly bipolar structure	∼0.05	uncertain	Crowded field, association unclear.
G24.73+0.69[(1)]	^{13}CO	Loose	Large fragmented shell	∼1000	wind-blown, compressed ISM	
G26.47+0.02*[(2)]	^{13}CO	Loose	Large fragmented shell	∼125	wind-blown, compressed ISM	
AFGL2298	**CO**, **^{13}CO**, **C^{18}O**, **C$_2$H**, **CN**, **HCN**, **HNC**, **HCO$^+$**	Loose	Clumps peaking toward the star	–	uncertain	Single component at 46 km s^{-1} in all lines.
MN101*	**CO**, **^{13}CO**	Clear	Equatorial torus	0.6 (0.1)	mass-loss event	Mass estimate uncertain due to poorly constrained distance.
G79.29+0.46*[(3,4)]	CO, ^{13}CO, NH_3, C_3H_2	Clear	Compact fragmented shell (CO), hot clumps (NH_3)	∼13	wind-blown, compressed ISM (mostly shell), mass-loss event (clumps)	The molecular shell tightly encloses the IR nebula and presents shock signatures toward the SW.
η **Car**[(5,6,7)]	H_2, **CO**, ^{13}CO, **HCO$^+$**, **HCN**, CN, and other C-, N- and O-bearing species[†]	Clear	Equatorial torus (all), inner cloud (HCO$^+$), Homunculus caps and walls (H_2)	0.2–5	mass-loss event	Mass estimates uncertain due to poorly constrained [CO/H_2].
AG Car	**CO**, **^{13}CO**	Clear	Equatorial torus	2.7 (0.9)	mass-loss event or binary interaction remnant	
MN48	**CO**, **^{13}CO**	Likely	Compact fragmented shell	∼10	wind-blown, compressed ISM	The molecular shell tightly encloses the IR nebula and presents shock signatures.

TABLE 7.1: Molecular gas associated with candidate and bona fide LBV stars, ordered in ascending galactic longitude. The * symbol denotes candidate LBVs. Sources and species studied in this thesis are displayed in boldface. References: [(1)]Petriella et al., 2012, [(2)]Paron et al., 2012, [(3)]Rizzo et al., 2008, [(4)]Rizzo et al., 2014, [(5)]Smith & Davidson, 2001, [(6)]Loinard et al., 2012, [(7)]Gull et al., 2020. [†]For a comprehensive list of molecules, see Tables 2 and 3 in Gull et al., 2020.

7.2 Molecular gas as a mass-loss tracer

As explained in Section 2.4, to establish a causal relationship between the gas and the stars is not always possible. We can only rely on a series of loose morphological, kinematic and chemical criteria to tentatively discriminate between two general scenarios: pre-existing gas –e.g., fragments of a parent molecular cloud, surviving throughout the life of the star, or shells of interstellar gas accelerated and compressed by stellar winds– or molecular gas of stellar origin –e.g., formed in situ after a mass eruption–.

The case of the LBV G24.73+0.69 (Petriella et al., 2012) and the candidate G26.47+0.02 (Paron et al., 2012) are representative of the first scenario. The environment of these two sources was investigated using ^{13}CO $J = 1 \rightarrow 0$ data from the Galactic Ring Survey (Jackson et al., 2006). Several large scale features were detected, fragmented shells partially bounding the infrared nebulae. However, these features extended well beyond the immediate surroundings of the star (see Figure 2 in Petriella et al. 2012 or Figure 3 in Paron et al. 2012), being sometimes connected to larger clouds. Moreover, the limited angular resolution of 46 arcsec prevented a detailed morphological study of small-scale features. Considering the evidence available, these fragmented shells likely reflect the action of the Main Sequence stellar winds, that blown cavities in the ISM, piling up and compressing molecular material at the edges. Indeed, the detected structures display kinematic signatures that strongly suggest a dynamical interaction between the stars and the molecular gas. Studies like these are therefore relevant to constrain the stellar wind properties and its impact on the stellar neighbourhood.

Conversely, we find η Car as a prime example of the role of molecular gas as a mass-loss tracer. Two decades ago, some dynamical models of the Great Eruption proposed a pre-existing massive disk, that would have shaped the material expelled during the outburst into the current Homunculus Nebula, pinching the ejecta as it expanded. Such a disk would correspond to the dusty equatorial torus reported by Morris et al. (1999). However, the recent detection of a molecular counterpart of the torus, with a kinematic age of 170±15 years (Smith et al., 2018b), indicates that this structure was most likely another product of the Great Eruption, being roughly as old as the Homunculus. This ability to place tight time constraints on the circumstellar material around LBV stars underlines the value of molecular spectroscopy as a powerful complementary tool to study the mass-loss history of these stars. Also, the abundances present in the torus (Paper IV) are typical of very processed material, where molecules have formed in less than 200 years, which is a very narrow time-scale in the context of stellar evolution. The mass of molecular material measured in the equator of the Homunculus is only loosely constrained due to uncertainties in the determination of [CO/H_2] ratio, but Smith et al. (2018b) provides a range from 0.2 to 5 $M_\odot$. Interestingly, this range does not differ too much from other sources where the surrounding molecular material can be totally or partially attributed to mass loss events, as in the case of G79.29+0.46 (∼13 $M_\odot$), AG Car (∼3 $M_\odot$) or MN101 (∼0.6 $M_\odot$). On the contrary, in sources where the surrounding gas comes most likely from swept-up pre-existing ISM matter, such as G24.73+0.69 or G26.47+0.02, the masses are found to be at least two orders of magnitude higher. This remarkable difference –well beyond uncertainties associated with observations, interpretation or modelling– establishes an additional ad hoc criterion to tell apart stellar ejecta from ISM material.

The molecular ejecta structures presented in this thesis thus unveil a *missing circumstellar mass component*, not detected at optical and infrared wavelengths and therefore previously neglected. In most cases, the contribution of molecular gas to the total budget of circumstellar mass is comparable to other nebular components: in G79.29+0.46, the main infrared shell has a mass of ∼14 $M_\odot$ (Waters et al., 1996), so molecular gas accounts for ∼50% of the ejecta. Similarly, the molecular ring of AG Car traces at least a ∼30% of the total nebular mass (Paper III). Finally, in η Car we find that molecular gas in the equator of the Homunculus Nebula may constitute up to a 25% of the mass expelled in the Great Eruption, whereas the inner Peanut could account for up to a 50% of the matter shed in the 1890 outburst (Paper IV). These figures underline the need for a careful review of the mass-loss budgets of LBV stars, which have been probably underestimated in most cases. Such a revision may have a profound impact on stellar evolution models, for which accurate mass loss rate estimates are crucial to reproduce the evolutionary track of the most massive stars.

7.3 One ring to explain them all?

Although η Car has been long regarded as an archetypal member of the LBV class, the extensive observation and increasing understanding of this source are pointing out some outstanding peculiarities: its mass, its complex nebular structure, its chemistry and variability find no match among the galactic population of LBV stars and candidates. The same holds from the point of view of molecular spectroscopy. The disrupted torus in the waist of the Homunculus has been mapped in four different species, namely CO (Smith et al., 2018b), HCN, $H^{13}CN$ and HCO^+ (Paper IV). At the moment of writing these lines, Gull et al. (2020) have published a thorough investigation using *Herschel* data in which they report the first detection of a handful of new species toward the Homunculus Nebula. These include C- and O-bearing molecules such as CH, CH^+, and OH, and new N-bearing species like NH_2 and NH_3 (hence confirming the tentative detection of this molecule by Smith et al., 2006). Despite the coarse spatial resolution of 10–30 arcsec, the velocity profile of the lines strongly suggest that most of these molecules arise from the equatorial torus. These results reaffirm that η Car is, by far, the LBV star with the largest and richest molecular inventory.

Apart from η Car, we have found other two LBV sources that host ring-like equatorial structures traced by molecular gas: AG Car and the candidate MN101. It is thus of key importance to compare their morphology, kinematics, and physical properties. The torus around AG Car bears some striking resemblance to that of MN101: as we have seen in Chapters 3 and 4, the two structures have comparable dynamic timescales of less than 10^5 years; sizes of a few tenths of pc; are warm (∼ 50 K) and relatively diffuse (∼10^3 cm^{-3}) on average; and, most importantly, expand quite slowly, at less than 5 km s^{-1}. On the other hand, the torus of η Car, a considerably younger structure, is more compact (∼4700 au in radius), warmer (∼200 K, Paper IV, Gull et al. 2020), denser (∼10^8 cm^{-3}, Gull et al. 2020) and expands much faster (∼123 km s^{-1}, Smith et al. 2018b). These differences become even more notorious if we look at the structures from an energetic point of view. Table 7.2 summarizes the expansion velocity ($v_{\rm exp}$), mass (M), kinetic energy ($E_{\rm kin} = \frac{1}{2}Mv_{\rm exp}^2$) and linear momentum ($P = Mv_{\rm exp}$) of the rings around η Car, AG Car and MN101. It also includes

Source	$M_{\rm ring}$ ($M_\odot$)	$v_{\rm exp}$ (km s^{-1})	$E_{\rm kin}$ (10^{45} erg)	P ($M_\odot$ km s^{-1})	$\dot{P}_{\rm wind}$ ($M_\odot$ km s^{-1} yr^{-1})	$L_{\rm mech}$ ($L_\odot$)
η Car	[0.2–5]	123	[30–750]	[24.6–615]	0.4	14450
AG Car	2.7 (0.9)	3.5	0.3 (0.1)	9.5 (3.2)	0.006	98.3
MN 101	0.6 (0.1)	3	0.05 (0.01)	1.8 (0.3)	0.001	8.2

TABLE 7.2: Parameters of the molecular equatorial rings and the stellar wind. $\dot{P}_{\rm wind}$ and $L_{\rm mech}$ computed from wind parameters taken from Gull et al. (2016) and Groh et al. (2011) for η Car and AG Car, respectively, and assumed to be standard values of $\dot{M}$= 10^{-5} $M_\odot$ yr^{-1} and v_∞ = 100 km s^{-1} for MN101.

the momentum rate ($\dot{P} = \dot{M} v_\infty$) of the stellar wind and the mechanical luminosity of the star ($L_{\rm mech} = \frac{1}{2}\dot{M} v_\infty^2$).

The rings of AG Car and MN101 are not too different in terms of kinetic energy and momentum. However, both fall several orders of magnitude short when compared to η Car's equatorial torus, even for the most conservative molecular mass estimate of 0.2 $M_\odot$ (Smith et al., 2018b). The kinetic energy conveyed in this expanding ring, $\sim 10^{47}$ erg, is similar to the total kinetic energy deposited in the *entire* RSG phase of a 35 $M_\odot$ star, i.e., during a period of several 10^5 years (Garcia-Segura et al., 1996b,a). This gives an idea of the violent nature of the event that produced the ring. Still, if we consider the whole Homunculus, the equatorial ring only accounts for 0.1 % of the total kinetic energy of the Great Eruption (Smith, 2013). The same holds for AG Car, as seen in Chapter 4.

In view of these estimates, it is reasonable to consider whether we are just witnessing successive snapshots of the same type object as it evolves. In other words, whether the structures around AG Car and MN101 are simply the ageing relatives of the torus of η Car, as we suggested in Paper III. Under this perspective, these rings were in the past more similar to what we observe today in η Car. The gradual expansion of the ejecta into the ISM over a few 10^4 years would explain the decrease in density; the increasing distance to the central star would account for the colder temperature; and finally, the –current– low expansion velocity would be a consequence of sustained friction with the surrounding ISM matter, slowly transferring the kinetic energy to the ambient material.

Such an appealing hypothesis is consistent with the available observational evidence, but we are still missing some crucial pieces of information: which is the terminal state of these structures? Are there more examples of similar, slowly expanding equatorial structures around evolved massive stars? Do these structures leave a trace after the star goes supernova? Luckily, the CSM of SN1987A provides a promising answer to these questions. Located at 51.4±1.2 kpc in the Large Magellanic Cloud (Panagia, 1999), SN1987A is surrounded by close-in ejecta expanding at ∼1000 km s^{-1}, plus an equatorial ring of dust and gas of ∼0.3 pc and two fainter, and somewhat larger polar rings, resulting in its characteristic hourglass shape (Burrows et al., 1995; McCray & Fransson, 2016).

This triple ring system, a fossil from the late evolutionary stages of the progenitor star Sk −69 202, was only discovered *after* the supernova event, due to the sudden

ionisation caused by the UV flash (Wampler & Richichi, 1989). Interestingly, the gas in the equatorial ring exhibits some physical conditions resembling those in the oldest LBV toroids, such as a low density (a few 10^3 cm^{-3}) and a nitrogen enhancement consistent with CNO-processing (Lundqvist & Fransson, 1996). Still, the most striking feature of the equatorial ring is its remarkably slow expansion velocity, of just 8.3 km s^{-1} (Meaburn et al. 1995, Smith 2007a), a value in the order of magnitude of the rings surrounding AG Car and MN101. The corresponding kinematic age, of $\sim$2.2$\times$10^4 years, is also in excellent agreement. One could therefore consider these molecular structures as close analogues of the equatorial ring of SN1987A, at least from a morpho-kinematic perspective. The triple ring system of SN1987A finds another –almost perfect– sibling in the dusty CSM of the galactic LBV candidate HD168625 (see Chapter 6, Figure 6.9). Smith (2007a) found that the equatorial ring around this star is somewhat younger ($\sim$4000 years) and expands slightly faster ($\sim$20 km s^{-1}) than its counterpart in SN1987A. These values lie conveniently halfway between the extreme conditions of the torus of η Car and the more quiescent rings around AG Car and MN101, thus filling the two-order-of-magnitude gap in our proposed sequence and completing a self-consistent evolutionary portrait of these puzzling circumstellar structures, provided that all of them share a common origin. Figure 7.1 shows the correlation between the size and kinematic age of these rings. A linear fit to the data (R^2 = 0.67) provides a slope of $\sim$ 3 km s^{-1}, that would represent the average expansion velocity of the rings, well below that of typical LBV nebulae of $\sim$ 20–100 km s^{-1} (Weis, 2012).

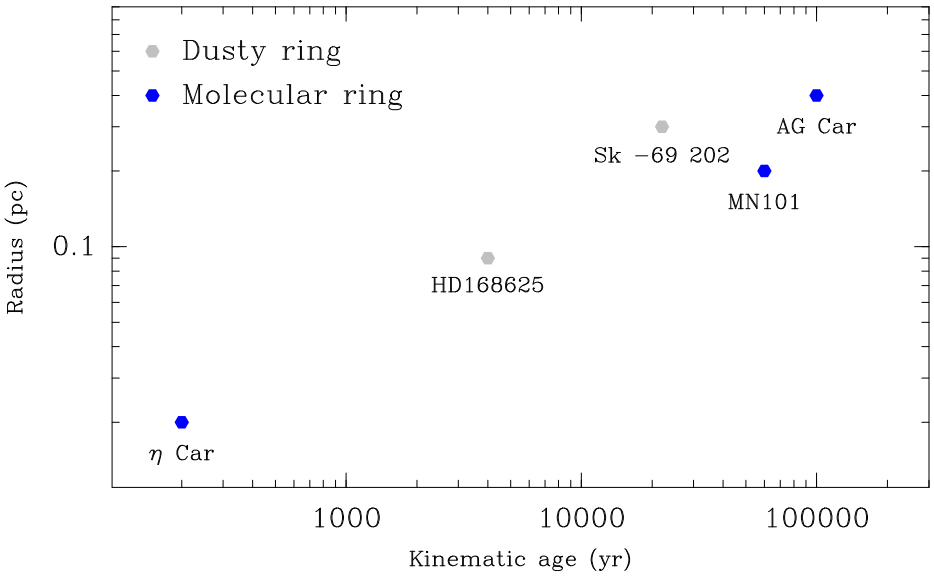

FIGURE 7.1: Physical radius in pc as a function of the kinematic age for the equatorial rings around η Car, HD168625, MN101, AG Car and Sk -69 2020 (progenitor of SN1987A). Blue and grey dots represent molecular and dusty rings, respectively. Kinematic ages are upper limits assuming a constant expansion velocity.

However, we must note two potential weaknesses of this otherwise convincing line of reasoning: the apparent lack of molecules in the ring of SN1987A, and the nature of its progenitor star, Sk −69 202. Recent ALMA observations of SN1987A (Abellán

et al., 2017; Cigan et al., 2019) have revealed clumps of molecular gas in the innermost ejecta, but not in the equatorial ring. Even so, this is not necessarily in contradiction with the proposed scenario. The ring is bright up to X-ray wavelengths (e.g., Ng et al. 2009), displaying a radio spectral index $\alpha = -0.70 \pm 0.06$, typical of synchrotron (Cigan et al., 2019). This radiation, whose brightness is increasing with time, is likely caused by the violent blast wave of the supernova interacting and propagating through the ring. It is known that shocks faster than 50 km s^{-1} destroy molecules (Hollenbach & McKee, 1980), and shock velocities of several ∼1000s km s^{-1} have been estimated for SN1987A (e.g., Zhekov et al. 2005). Under these extreme conditions, the destruction of any molecular material existing in the ring is more than likely. In fact, some authors propose that the whole equatorial ring will be completely wiped out by ∼2025 (Fransson et al., 2015). Regarding the nature of Sk −69 202, it is widely accepted that it was a blue supergiant, with an initial mass around ∼20 $M_\odot$ (Walborn et al., 1987). Still, it is important to remark that the LBV status is, as noted in Chapter 1, a phenomenological classification, and as such, the distinction between classical blue supergiants and LBVs is sometimes blurry. The lower mass limit of the LBV class is only loosely constrained, with some models predicting LBVs in the 20 $M_\odot$ range as direct SN progenitors (Groh et al., 2013b). The possibility of Sk −69 202 having experienced a brief LBV-like episode is therefore worth considering, as comprehensively discussed by Smith (2007a).

To be confirmed, the proposed evolutionary sequence connecting η Car, HD168625, AG Car, MN101 and Sk −69 202/SN1987 through their equatorial structures will need additional observations and modelling work. These first results encourage the search for molecules in other potential analogues. The formation of slow structures of molecular gas at equatorial latitudes might not be an isolated phenomenon associated only with the LBV class, but a common feature of different types of evolved massive stars. The detection of CO in circumstellar detached rings around some B[e]SG stars (e.g., Muratore et al. 2015) may support this hypothesis. Sher 25 and SBW1, galactic blue supergiants that also exhibit circumstellar rings (Smith, 2007b), are appropriate targets to explore this hypothesis. The impact of this research extends beyond the late stages of stellar evolution: a proper characterisation of potential SN progenitors and their surrounding CSM is essential to understand the shaping of the eventual supernova remnants (Chiotellis et al., 2021).

7.4 Shaping of circumstellar molecular structures

LBV nebulae come in different shapes, owing to the different processes involved in their formation, such as mass-loss episodes and wind-wind interactions: roughly ∼ 40% of them are spherical, ∼ 10% irregular and about 50% display some degree of bipolarity (Weis 2011, Weis 2012). On the contrary, in view of Table 7.1, molecular gas associated with LBV stars seems to arrange preferentially as shells (e.g., G79.29+0.46 or MN48) or equatorial rings (η Car, AG Car and MN101), not necessarily following the distribution of other nebular components.

Molecular shells are inextricably associated with infrared shells of dust and ionised gas, even in those cases in which the molecular gas is most likely swept-up material. The dusty shells originate from the dense, inhomogeneous isotropic winds of the central star, generally as a result of an abrupt change in the wind regime (e.g., a mass

eruption). At a certain distance from the star, the winds get sufficiently cold as to form dust grains, and, eventually, molecules that end up creating an outer layer that wraps the inner shell.

However, the mechanism that leads to the slowly expanding equatorial rings remains to be fully elucidated. In Paper III we explored the possible origin of the ring around AG Car, mainly focusing on two scenarios that can be generalised to explain the ring-like structures around other LBV sources: an equatorially-enhanced mass-loss episode, or a binary interaction remnant.

The first scenario sits on top of the traditional view of LBV stars in the frame of single-star evolution. Rotation has a profound impact on stellar hydrostatic stability (Maeder & Meynet, 2000), playing a pivotal role in structuring the mass-loss from massive stars, i.e., in determining the wind density distribution (Owocki, 2008). The Eddington limit (Eddington, 1926) represents the maximum theoretical luminosity of a star such that hydrostatic equilibrium is preserved, i.e., radiation pressure (pushing outwards) is compensated by self-gravity (pulling inwards). Formally, it is defined as $L_{\rm Edd} = 4\pi cGM/k_e$, with M the stellar mass and k_e the electron scattering opacity. For a star of luminosity L, it is possible to define the Eddington factor Γ as:

$$\Gamma = \frac{L}{L_{\rm Edd}} = \frac{k_e L}{4\pi cGM} \tag{7.1}$$

so that the star will become unstable if $\Gamma > 1$. When a star rotates, though, centrifugal acceleration –which has a latitudinal dependence, being stronger near the equator and almost negligible near the poles– alters the equilibrium, making it necessary to introduce an additional stability criterion. Without diving into the details (see, for instance, Langer 1997), one can define the critical rotation for a star of mass M and radius R as:

$$v_{\rm crit} = \sqrt{\frac{GM}{R}(1-\Gamma)} \tag{7.2}$$

Analogously to the Γ factor, the Ω factor for a star rotating at $v_{\rm rot}$ is:

$$\Omega = \frac{v_{\rm rot}}{v_{\rm crit}} \tag{7.3}$$

so the star will become unstable if $\Omega > 1$, starting to eject matter. It is important to notice that the Γ and Ω criteria are not independent. For very luminous stars close to the Eddington limit, $\Gamma \to 1$, and thus, from Equation 7.2, $v_{\rm crit} \to 0$. In other words, more luminous stars have lower critical velocities, meaning that they do not have to rotate extremely fast to reach the break-up. Formally, for stars with $\Gamma = 1$, the *escape velocity* of a particle on the stellar surface is zero.

The net effect of rotation, by virtue of von Zeipel's theorem, is a decrease in effective gravity $g_{\rm eff}$ toward the equator and the subsequent decrease in $T_{\rm eff}$. Such changes may heavily disrupt the stellar wind properties: the study of the winds of the LBV star P Cyg by Pauldrach & Puls (1990) revealed the so-called bi-stability jump, an abrupt discontinuity in the mass flux and terminal wind velocity that occurs when $g_{\rm eff}$ (or, equivalently, $T_{\rm eff}$) falls below a certain threshold. In rotating stars, we can expect a similar discontinuity to occur near the equator due to the latitudinal temperature/density gradient, resulting in slower and denser winds, and thereby enhancing

the equatorial mass flux. A rotationally-induced bi-stability jump has been tentatively proposed as the origin of the disks and rings around B[e] supergiants (Lamers et al., 1995; Lamers & Pauldrach, 1991; Curé et al., 2005; Pelupessy et al., 2000). Likewise, this mechanism could be responsible for the observed asymmetries of LBV winds and the shedding of substantial amounts of mass near the equatorial plane. In consequence, the denser and slower equatorial winds generated by fast rotating LBVs would be more prone to form molecules, producing the expanding molecular rings observed around η Car[1], AG Car or MN101.

Nevertheless, this rotationally induced mechanism requires that these stars rotate at a significant fraction of their break-up velocity, i.e., $v_{\rm rot} \rightarrow v_{\rm crit}$. Groh et al. (2009a) proposed that all LBVs displaying strong variability (S Dor cycles) are fast rotators, whereas quiescent LBVs like P Cyg or HD168625 are not. This is certainly the case for AG Car (Groh et al., 2011, 2009b), which rotates at an 86% of its critical velocity, making the bi-stability hypothesis quite reasonable. Further support to this idea comes from observational evidence of a two-component wind (Leitherer et al., 1994). Considering the noteworthy similarities of the molecular rings of AG Car and MN101, the natural question that arises is, *is MN101 also a fast rotator?* To answer this question, we gathered near-infrared, mid-resolution spectroscopic observations in bands J, H and K with the GTC in the Canary Islands (project GTC114-19A, P.I: C. Bordiu). The data corresponding to this project, partially reduced, is presented in Annex A. P Cygni profiles from wind lines dominate the spectra, although several photospheric lines could be identified, such as the SiII line at 1.69 μm. However, the limited spectral resolution, in combination with a non-negligible contribution from atmospheric macro turbulence, yields degenerate solutions for the fitting, hampering a reliable determination of the rotation velocity.

The rotationally induced bi-stability jump mechanism discussed here emerges as a plausible hypothesis to explain the density contrasts found in the winds of many LBV stars and the formation of slow equatorial structures. Fast rotation could even influence the evolutionary track of the stars, as proposed by Groh et al. (2009a), who suggest that fast-rotating LBVs could prematurely explode as SN due to their inability to lose angular momentum. However, a larger sample of objects must be explored to confirm the validity of these ideas. In this sense, we note that finding LBV objects with equatorial rings that are not fast rotators, like HD168625 (Mahy et al., 2016), is not necessarily a problem: not much is known about the driving factors of S Dor variability, and its relationship with fast rotation is not well understood nor totally confirmed. Moreover, magnetic braking could account for nowadays quiescent stars that were fast-rotators at the moment of ejecting their circumstellar structures, as discussed by Gvaramadze et al. (2015).

The second scenario involves the formation of equatorial structures around LBVs due to interaction with a binary companion. In the intermediate-mass regime, binary interactions certainly outperform single star scenarios in explaining many observational features of planetary nebulae, including slow equatorial toroids, as investigated by Livio (1997) and Soker (1998). Strikingly, these toroids are usually molecule-rich, accounting, together with the polar jets, for most of the molecular emission toward

[1]The polar winds of η Car reach 600 km s^{-1}, much faster than the expansion velocity of the equatorial torus (Smith et al., 2003)

these sources (Kastner et al., 1996). Binarity is hence becoming a preferential argument to explain some of the phenomenology associated with the LBV class, following two main "schools of thought". The first one, based on the apparent isolation of many LBVs, proposes that they are massive "blue stragglers", somewhat rejuvenated mass gainers that, by means of binary mass transfer, got enriched, spun up and eventually expelled from their original cluster by their companion's supernova explosion (e.g., Smith & Tombleson 2015). In the second one (e.g., Justham et al. 2014; Aghakhanloo et al. 2017), LBVs are regarded as binary merger remnants. Some authors even relate the entire "giant LBV outburst" phenomenon to close binary interactions (Kashi, 2010; Kashi & Soker, 2010). These ideas find strong observational support in the recent results by Mahy et al. (2021), who surveyed a large sample of Galactic LBV-like objects, finding a binary fraction between 62 and 78 % – derived from spectroscopy and optical interferometry, respectively.

We discussed the feasibility of all these scenarios in Paper III. Non-conservative mass transfer episodes in a close binary system may produce equatorial density enhancements or outflows, either by means of common envelope ejection or mass leakages through the outer Lagrange point. This idea is far from being new, as it has been suggested before to account for other massive stars harbouring rings, including B and B[e] supergiants (see, for instance, Gvaramadze et al. 2015; Smith et al. 2007a, 2011), but our results represent a prime chance to link molecular formation and binarity. A more extreme but equally exciting possibility is a complete binary merger. In principle, the merger scenario is particularly convenient as it allows us to circumvent the lack of observational evidence for current-day binarity in some of the sources with rings, such as MN101. In a merger event, equatorial density enhancements are also expected due to the absorption by the common envelope of most of the orbital angular momentum, spinning up and becoming oblate. This transient process may end up with the merger product –in this case, an LBV– surrounded by an expanding ring of debris.

The Great Eruption might indeed represent the ultimate evidence in favour of the merger scenario. Recent observations and modelling work strongly suggest that η Car was perhaps an unstable triple-star system in origin, that underwent a violent merger episode around 1840, of which the current day LBV η Car A would be the product (Portegies Zwart & van den Heuvel, 2016; Smith et al., 2018a; Hirai et al., 2021). Last but not least, it is worth noting that Morris & Podsiadlowski (2007) proposed a merger model to explain the ring system around SN1987A, once again strengthening the possible connection between these objects. In their model, however, the equatorial ring was caused by the merger product releasing an angular momentum excess through a dense equatorial outflow. This model highlights another important property of binary interactions: the transference of significant amounts of angular momentum to the mass gainer (or merger product), that usually becomes a fast rotator. We should then regard binarity and fast rotation as complementary rather than antagonistic scenarios.

7.5 Molecular complexity around LBV stars

Molecular formation is only possible under quite specific physical conditions: it requires relatively high density, moderate temperatures and efficient protection against

UV photons. Such conditions are easily met, for instance, in the circumstellar envelopes (CSEs) around intermediate-mass AGB stars. These CSEs, typically rich in carbon and oxygen, exhibit a rich molecular complexity: currently, more than 70 species have been found in AGB CSEs, including organic and inorganic molecules and also radicals (e.g., Velilla Prieto et al. 2015; Sánchez Contreras et al. 2015; García-Hernández & Manchado 2016). In comparison, the environments of LBV stars seem barren. The strong stellar winds and intense UV fields of these stars render their surroundings a much less favourable place for molecules. As shown throughout this thesis and summarised in Table 7.1, finding CO associated with LBV nebulae is not unlikely: its critical density is somewhat low, and as long as sufficient shielding is provided, significant amounts can form and survive. Still, the search for other tracers was not as fruitful. In most of the sources where we did detect associated CO structures, no other species apart from ^{13}CO were found. This scarcity is not surprising considering the low H_2 densities measured, of a few 10^3 cm^{-3}. On the other hand, G79.29+0.46, AFGL2298 and η Car stand out as notable exceptions, depicting a more complicated chemical scenario in which different physical processes are involved in the production and destruction of multiple species.

In G79.29+0.46, the detection of several clumps of NH_3 (Rizzo et al., 2014), a molecule rapidly destroyed by UV photons, is a strong signature of shock-induced chemistry: NH_3 is most likely locked up in dust grains, being eventually released back to gas phase due to the passage of low-velocity shocks, as the ones reported by Rizzo et al. (2008). To a lesser extent, the detection of the more resistant C_3H_2 and its layered distribution with respect to NH_3 supports the existence of a PDR bounding the ionised nebula (Palau et al., 2014). These findings demonstrate a sustained mechanical and radiative interaction between the parent star and the surrounding material.

Likewise, AFGL2298 represents a promising chance to learn about molecular complexity in the surroundings of LBV stars. The velocity component detected at 46 km s^{-1}, clearly visible in all the observed species, always peaks toward the star, strongly suggesting that AFGL2298 takes active part in the excitation of the gas. Still, the heavy contamination by ambient clouds in the field, in addition to the moderate resolution of our data, hamper a reliable interpretation: the detected component could be part of nearby cloud, illuminated by the star, or genuine stellar ejecta embedded in a larger cloud at a similar systemic velocity. While an analysis of the general physical properties of the gas will be presented in a future paper (Rizzo et al., *in prep*), together with a thorough discussion of the possible scenarios, interferometric observations will play a fundamental role in disclosing the relationship between the star and the gas, allowing for drawing solid conclusions from a chemical point of view.

In η Car and the Homunculus Nebula, the chemical panorama becomes even more intricate, deserving a separate discussion. In their recent far-infrared/sub-mm survey, Gull et al. (2020) reported dozens of atomic and molecular lines, extending the inventory of molecules with new C-, O- and N-bearing species, and unveiling a chemical environment of fascinating complexity. Looking at the distribution and kinematics of the detected atomic and molecular species, they pinpoint several regions of interest in the surroundings of η Car, namely: (1) the outer ejecta, composed of fast-moving clumps at velocities exceeding 1000 km s^{-1}(e.g., Smith 2008), visible in [NII]; (2) the polar lobes, where NH and several forbidden lines arise (e.g., [CII], [FeII], [OII] and [OIII]); (3) the equatorial torus, which constitutes the main reservoir of molecular gas,

harbouring most of the C- and N- bearing species; and (4) the innermost central region, where radio recombination lines (Abraham et al., 2014) and some molecules have been detected, including hot HCN bullets, HCO^+ (Paper IV) and CH_3OH, (Morris et al., 2020). In this compact region, less than 1000 au away from the stars, material expelled in the lesser outburst that followed the Great Eruption in the 1890s is expanding away from η Car at $\sim$100 km s^{-1}, including the famous ionised structures known as the Weigelt blobs (Weigelt & Ebersberger, 1986), that move at velocities comparable to the HCN bullets.

As thoroughly discussed in Chapter 5, this central region, the core of the Homunculus Nebula, is subject to the most extreme conditions: very high temperatures, fluctuating MUV/FUV fluxes and periodical shocks modulated by the 5.54-yr orbital period of the binary. Our detection of HCO^+ –and no other molecules– towards the extended continuum emitting region (nicknamed "the Peanut") is a puzzling result, not easily explained by standard chemical chains. In this regard, Abraham et al. (2020) have recently published a detailed study of radio recombination lines in the Homunculus, suggesting that the detected HCO^+ may indeed be a misidentification of the H40δ recombination line, which lies close in frequency. Considering the prominent emission of radio recombination lines in the region, and the large velocity dispersion of the gas –with multiple blended components spanning the approximate range $(-100, +100)$ km s^{-1}–, we acknowledge that the H40δ line may account for a significant fraction of the detected emission. Line identification in this turbulent region is indeed tricky (see, e.g., the discussion about NH_3 and H81β in Loinard et al. 2016), but a number of qualitative arguments may support the existence of a certain amount of HCO^+ close to the central stars. First, we know that the ejecta of η Car is prone to form this molecule, unambiguously detected in the equatorial torus (Paper IV, Gull et al. 2020). Second, the ionization state of the Peanut changes drastically during the binary orbital cycle, greatly reducing the radiation field. Finally, the layered [FeII] wind-wind structures reported by Gull et al. (2016) could perfectly protect a molecular reservoir, as first proposed by Morris et al. (2017).

In any case, the survival of HCO^+ so close to the binary is a stimulating possibility, and invites us to review its main formation pathways. In the ISM, the main formation route for HCO^+ involves CO through the proton transfer reaction:

$$H_3^+ + CO \rightarrow HCO^+ + H_2 \tag{7.4}$$

This route cannot be the primary source of HCO^+ in the Peanut, since it would require substantial amounts of CO, which would have been otherwise observed. We must then resort to other chemical networks to explain our findings. Providing a solution to the complex chemistry of the Peanut is beyond the scope of this thesis –additional observations and chemical modelling will undoubtedly be necessary for that–. However, it is convenient to outline here some alternative ideas.

The recent detection of H_2O, OH and CH^+ towards the inner region of the Homunculus (Morris et al. 2020, Gull et al. 2020) might provide new clues about the mechanisms at work. The authors propose that gas-phase oxygen forms OH by collision with vibrationally-excited molecular hydrogen (H_2^*), such that:

$$O + H_2^* \rightarrow OH + H \tag{7.5}$$

and then, OH produces water through:

$$OH + H_2^* \rightarrow H_2O + H \tag{7.6}$$

One could argue that CH^+, a highly reactive radical, could be part of an analogous reaction to form HCO^+. Gas-phase oxygen would produce CO^+:

$$CH^+ + O \rightarrow CO^+ + H \tag{7.7}$$

and finally,

$$CO^+ + H_2 \rightarrow HCO^+ + H \tag{7.8}$$

This route is particularly favoured in environments of active photochemistry and high temperatures (Hasegawa et al., 2000). An even faster and more efficient route, with a reaction rate of 3×10^{-9} s^{-1}, comparable to that of the main formation pathway, would directly involve H_2O, so that:

$$CH^+ + H_2O \rightarrow HCO^+ + H_2 \tag{7.9}$$

These are alternative mechanisms that could explain the presence of HCO^+ while circumventing the lack of CO in the core of η Car. Another key issue is the survival and destruction of HCO^+. HCO^+ is known to be resistant against UV photons; it only has a single photo-dissociative state with a very small cross-section at around 11.5 eV (Koch et al., 1995). As a consequence, HCO^+ is relatively immune to the strong radiation fields of η Car, having one of the lowest photodissociation rates, of about $\sim 5 \times 10^{-12}$ s^{-1}, corresponding to an average lifetime of ∼6000 years (Heays et al., 2017). However, this does not mean that HCO^+ cannot be affected by UV radiation: it is, *indirectly*, if it resides in a highly ionised environment: HCO^+ is mostly destroyed by dissociative recombination with free electrons:

$$HCO^+ + e^- \rightarrow CO + H \tag{7.10}$$

which are particularly abundant in these hot regions. The recombination rate of HCO^+ is $\sim 3 \times 10^{-7}$ cm^3 s^{-1} at the temperatures expected for the Peanut (Amano, 1990). The electron densities of a few 10^7 cm^{-3} predicted by Abraham et al. (2020) in the core region would imply almost instantaneous destruction of HCO^+, if the molecules and the ionised gas were co-spatial. But, again, this reaction produces CO, that we do not observe. Two explanations are possible at this point: either HCO^+ is being destroyed by another mechanism; or it is not being destroyed *at all* (or, at least, at an appreciable rate). The latter could be the case if the molecules and the ionised gas were distributed in a layered, PDR-like structure. This would be quite consistent with our morphological model of a conical cavity filled by most of the ionised gas (including the Weigelt blobs) with the HCO^+ tracing only the outer walls (see Figure 5.3 in Chapter 5).

It is important to bear in mind that, considering the short timescales involved, the fresh ejecta that constitutes the Peanut is far from reaching chemical equilibrium, meaning that we are perhaps witnessing a transient situation. To settle the question about the existence of HCO^+ further observations will be required, at a higher angular

resolution and involving other transitions, and possibly other tracers not likely to be confused with recombination lines.

The chemistry around η Car is definitely a hot topic in molecular astrophysics, drawing much attention in recent times. That such a molecular "blossoming" has occurred in less than 200 years indicates that molecules *find a way* even under the most hostile conditions. Understanding how molecular gas forms and survives in the outskirts of evolved massive stars is thus capital to our understanding of the enrichment in the early Universe, and η Car, thanks to its proximity and its outstanding characteristics, is the best possible laboratory to test our ideas.

7.6 Non-thermal emission and LBV binarity

Millimetre continuum observations complement molecular spectroscopy in the study of LBVs because they have the potential to provide additional information about the stars and the dominant physical processes in their surroundings. In particular, the results from our NIKA2 campaign could help understand how the observed molecular structures form and evolve.

Four of the five sources surveyed with NIKA2 at 1 and 2 mm, namely G79.29+0.46, HD168625, HD168607 and MN101, display nearly flat or even negative spectral indices, in any case below the typical $\alpha = 0.6$ expected for a thermal stellar wind. We note that the sources are not resolved by the NIKA beam, meaning that what we measure is a composite spectral index, i.e., the sum of multiple contributions arising from the stellar photosphere and beyond. The low values observed may be interpreted as a strong signature of a non-thermal component close to the star, e.g., synchrotron radiation. Still, variability is a characteristic feature of these sources, and the spectral indices are surely affected by it.

As seen in Section 2.1, synchrotron radiation is produced when a population of relativistic electrons moves throughout a magnetic field. It has been proposed that early-type massive stars, owing to their intense magnetic fields and strong stellar winds, could generate this kind of non-thermal radiation if they are members of a binary system (Usov, 1992; Eichler & Usov, 1993). The collisions expected in the wind interaction region would produce strong shocks, accelerating electrons to the required velocities. A fair number of O and WR colliding-wind binaries are known to be non-thermal emitters (De Becker, 2007). Could this also be the case for some LBV stars? In addition to the sources studied in this thesis, we find in the literature a few other examples of LBV stars and candidates displaying hints of non-thermal emission: G26.47+0.02 (Paron et al., 2012), HR Car (Buemi et al., 2017) and η Car (Farnier et al., 2011), all of them confirmed or candidate binaries.

Focusing on the sources with equatorial rings, we find that, apart from MN101 and HD168625, AG Car also displays a slightly negative spectral index of $\alpha = -0.1$ at cm-wavelengths (Duncan & White, 2002). Interestingly, AG Car and HD168625 –along with MWC314, the Pistol Star and a handful of other LBV sources– have been recently confirmed as binaries by means of optical interferometry (Mahy et al., 2021). A possible correlation among non-thermal emission, binarity and equatorial rings could help to understand the origin of these structures, as discussed in Section 7.4, especially if MN101 turns out to be a binary as well.

On the other hand, we also find non-thermal signatures in G79.29+0.46, which is not a binary and whose CSM displays a shell-like morphology, without any noticeable departure from spherical symmetry. However, single stars could theoretically produce synchrotron radiation through wind-embedded shocks with high compression factors (White, 1985; Puls, 2011). The detection of shocked CO by Rizzo et al. (2008) might support this scenario, although we note that the CO shocks are found on the shell, at a relatively large distance from the central source.

The NIKA2 results, taken as a whole, underline the need to investigate even further the possible connection between equatorial structures around LBVs and the binary nature (either current or past) of the parent stars. New models are required to address how binary interactions or mergers influence the shaping of the CSM. Some work is being carried out in this respect (e.g., Hirai et al. 2020), but there is still a long way to go until we fully understand the processes that lead to the observed morphologies.

CHAPTER 8
CONCLUSIONS AND FUTURE WORK

This thesis contributes to expanding the current understanding of the LBV phase, its associated phenomena and its role in massive star evolution, providing novel insights from the combined perspective of molecular spectroscopy and millimetre continuum and helping to answer some long-standing questions regarding these intriguing objects. In this last chapter, we briefly review the key points of this work, providing a unified picture of the results achieved, and introducing potential topics to be explored in follow-up studies.

8.1 Summary and conclusions

In this thesis, we have presented and analysed spectroscopic and continuum observations at millimetre wavelengths of a selected sample of bona fide and candidate LBV stars. The aim of this work was two-fold: to detect and characterise the molecular gas unambiguously associated with these stars, and to disclose the dominant radiation mechanisms in the mm band. The results obtained, presented in the preceding chapters, are summarised below:

i) In Paper I, we achieved the first detection of molecular gas associated with the candidate LBV [GKF2010] MN101. Observations with the IRAM-30m telescope unveiled a slowly expanding torus-like structure of CO enclosing the infrared bubble. Radiative transfer modelling suggests that the torus is made, on average, of warm ($\lesssim 100$ K) and not very dense ($\sim 10^3$ cm^{-3}) gas, with a total mass of ~ 0.6 M$_\odot$–although some hotter, unresolved clumps with higher densities are possible. Its kinematic age, according to the low expansion velocity of the gas ($\lesssim$5 km s^{-1}), is of a few 10^4 years at most, consistent with the typical time-scales of the LBV phase.

ii) Combining APEX single-dish and ALMA interferometric data, in Paper III we imaged for the first time a molecular ring-like structure surrounding the canonical LBV AG Car, confirming previous results in the literature that suggested the presence of molecular gas around this source. We explored the physical properties of this ring, finding a striking resemblance to the torus of [GKF2010]

MN101 in terms of average density ($\sim 10^3$ cm^{-3}), temperature (~ 50 K), mass (~ 2.7 M$_\odot$) and kinematic age ($< 10^5$ years). We discussed in detail different mechanisms that could possibly account for the formation of such a structure.

iii) In Paper IV, we analysed ALMA archival observations of η Car, revealing the HCO^+, HCN and $H^{13}CN$ counterpart of the dusty equatorial torus and disclosing a previously unknown molecular structure traced only by HCO^+ and continuum in the innermost region of the Homunculus, less than 1000 au from the binary and most likely associated with the lesser eruption in the 1890s. This detection, particularly challenging in the absence of CO, implies that the molecular chemistry in the close vicinity of active LBV stars is more rich and complex than previously assumed.

iv) We conducted a survey with the IRAM 30m NIKA2 instrument to explore the mm-continuum emission of a sample of LBV stars, namely G79.29+0.46, HD168625, HD168607, [GKF2010] MN101 and [GKF2010] MN87. As reported in Paper II, we were able to identify different emission mechanisms at work in the surroundings of these sources, mostly thermal emission from warm dust and ionized gas. Interestingly, we also found strong hints of a non-thermal contribution in the immediate vicinity of four of the five surveyed stars.

These results have doubled the number of known molecular structures related to LBV stars, highlighting previously unknown aspects of the LBV phenomenology. The analysis and interpretation of these results, together with ongoing work on other observed sources, lead us to the following key findings:

i) Survival of molecular gas in the hostile outskirts of luminous blue variables and, perhaps more generally, evolved massive stars, seems to be far more common than previously believed, as long as high enough densities and sufficient shielding from UV radiation is provided.

ii) If molecular gas forms in situ as a result of mass-loss, either by steady stellar winds sweeping the stellar surroundings or sporadic LBV outbursts, it may represent a significant fraction of the total mass lost, up to 50% in some cases. In view of this figure, it is clear that a proper quantitative characterisation of the sometimes neglected molecular component is crucial for massive star evolution models, especially sensitive to $\dot{M}$.

iii) Molecular gas around LBV stars appears to arrange preferentially as shells or equatorial toroids. The formation of the latter is especially puzzling as it requires significant wind density enhancements near the stellar equator. These structures can be explained invoking either single or binary star scenarios: (1) in the single-star frame, a bi-stability jump induced by rotation could produce equatorial outflows, as in B/B[e] SGs. The fact that many LBVs are nearly critical rotators supports this scenario; (2) in the binary case, a mass-transfer episode or a complete merger could lead to the formation of equatorial rings. The observations of these mechanisms at work in other mass regimes and abundant modelling work seem to back this hypothesis.

iv) Regardless of their origin, the similarity of the torus-like structures around η Car, AG Car, and [GKF2010] MN101, in combination with their dynamic timescales, suggest some kind of evolutionary connection. If we assume that these rings have a common nature, i.e, they are formed by the same physical process, we could be witnessing snapshots of the same type of structure at different evolutionary stages. This hypothesis is worth to be studied in the future.

v) The interaction between supernova shockwaves and the pre-existing circumstellar material has effects not well determined on the light curve and the shaping and properties of the subsequent remnants, like SN1987A. Therefore, there is a clear need for an accurate characterisation of the CSM around LBVs and other potential supernova progenitors.

vi) The presence of a non-thermal contribution in the mm-wavelength continuum emission of many LBVs which have been recently confirmed as binaries, could imply that binarity is a typical treat in this class of objects. Still, other potential factors must be considered, such as strong magnetic fields and wind shocks.

8.2 Current work and future perspectives

The work presented in this thesis will be hopefully taken as a reference in future studies of molecular gas associated with LBV stars. However, many aspects regarding the survival of molecules in extreme environments, the shaping mechanisms of LBV nebulae, and even the very nature of the LBV class remain open. Below, we introduce a number of possible actions to address these topics.

Molecular rings: extending the sample

The evolved molecular rings around AG Car and [GKF2010] MN101 indeed represent a new type of structure, worth to be explored in more detail. It is thus exciting to look for analogous rings in other LBV stars, that could help us build a more comprehensive view of these structures and better constrain their formation mechanisms. A combination of single-dish observations plus moderate resolution interferometry, as done with AG Car, has proven to be a suitable and efficient approach for this kind of studies. Rather than a blind search, it is convenient to follow the trail of potential fast-rotators and binaries, specifically looking for: (1) LBV stars (confirmed and candidates) whose CSM displays significant departures of spherical symmetry and (2) active LBVs currently undergoing S Dor variability. Objects like HR Car and Wray 15-751 are ideal candidates. Moreover, it is reasonable to think that the phenomenology that leads to these equatorial structures is not restricted to the LBV class, but is common to more types of evolved massive stars (see, e.g., the case of Sk -69 202 / SN1987A). To further explore this idea, ringed blue supergiants like Sher 25 or SWB1 should be also investigated.

Chemical complexity studies

As discussed in Chapter 7, the molecular chemistry in the outskirts of LBV stars is generally less rich than, for instance, in AGB CSEs, with the notable exception of η

Car. In this sense, the promising detections in AFGL2298, that will be thoroughly reported in a forthcoming paper (Rizzo et al., *in prep.*), unveil an intriguing molecular panorama, perhaps rivalling the complexity of the Homunculus Nebula.

Nevertheless, after achieving the first detection of CO in a handful of new sources, we could follow the successful example of G79.29+0.46 and explore the radiative and mechanical interactions between the stars and the gas by looking for specific tracers. Taking into account the noteworthy similarities between G79.29+0.46 and [GKF2010] MN48, looking for ammonia in the outskirts of the latter could be a good starting point.

η Car, a treasure to be explored

Our detection of HCO^+ and several HCN bullets in the innermost ejecta of η Car almost begs for further observations, even more when taking into account the recent discovery of other molecules arising from this region by Gull et al. (2020). To disclose the peculiar chemistry at work in the core of the Homunculus Nebula, we should (1) observe other transitions of HCO^+ to confirm its existence and constrain its physical properties, (2) sample the chemical networks involved in the formation of this radical, (3) develop and test 'ad hoc' chemical models able to deal with extreme conditions (shocks, UV radiation) in extremely short chemical time-scales ($\sim$ 100 years).

The role of metallicity

In this work, we focused exclusively on Galactic LBVs, therefore not considering another crucial aspect that heavily influences stellar evolution and mass loss: metallicity. Metallicity could indeed have an impact on our proposed relation between the rings of some Galactic LBVs and the pre-existing CSM of SN1987A in the Large Magellanic Cloud (LMC), with about a half of the solar metallicity. In this sense, there is evidence that LBVs in the LMC have systematically larger nebulae and slower winds (see, for instance, Weis 2012). While this may partially obey to a selection effect, differences in the wind density and the density or pressure gradients of the surrounding ISM are also to be considered. Most likely, any molecular structures around these sources will also be affected, presenting different kinematics. The detected LBV nebulae in the LMC have angular sizes of a few arcsec and are thus accessible to interferometers like ATCA and ALMA. Indeed, some continuum studies of a handful of extragalactic LBVs have been carried out (Agliozzo et al., 2012). Complementing these works with molecular gas observations is, therefore, a realistic, achievable goal, that could provide valuable information about CSM kinematics, constraining ejection time-scales and possibly bringing new light to the alleged connection between SN1987A and its Galactic twins.

Continuum studies beyond the LBV phase

ASKAP[1] and MeerKAT[2], precursors of the Square Kilometre Array (SKA), are revolutionising all-sky continuum surveys. Reaching unprecedented levels of sensitivity, angular resolution and *uv*-coverage, these new surveys are opening a new window for

[1] https://www.atnf.csiro.au/projects/askap/index.html
[2] https://www.sarao.ac.za/science/meerkat/about-meerkat/

Galactic science, allowing for the simultaneous study of entire populations of radio emitting sources, such as HII regions, luminous blue variables, Wolf-Rayet stars, planetary nebulae and supernova remnants. These sources span the entire stellar lifecycle, from star formation to the late evolutionary stages, and thus unveil the "big picture" of massive star evolution from the continuum perspective.

APPENDIX A
NEAR-INFRARED SPECTROSCOPY OF MN101

In this appendix, preliminary, mid-resolution J, H, and K band spectra of MN101 are presented, along with a brief discussion on the possible fast-rotating nature of the star.

A.1 Data description and line identification

Mid-resolution ($R = 4000 - 5000$) near-infrared J, H, and K spectra of [GKF2010] MN101 were obtained using the GTC EMIR Multi-Object-Spectrograph. The observations, corresponding to project GTC114-19A were conducted in May 2019 under good weather conditions. Fig. A.1 shows the preliminary spectra after telluric subtraction and wavelength calibration, in arbitrary intensity units.

All spectra are clearly dominated by wind emission lines with pronounced P Cygni profiles. Overall features are essentially the same as reported by Flagey et al. (2014) from lower resolution TripleSpec data: strong hydrogen lines corresponding to the Pfund and Brackett series, weak He lines in absorption and several metal lines characteristic of LBV spectra, such as the strong FeII lines at 1.69 and 2.09 μm or the MgII lines at 2.138 and 2.144 μm.

A.2 Could MN101 be a fast rotator?

We investigated the possibility of MN101 being a fast rotator. Generally, the projected rotation velocity, $v \sin i$ is best determined measuring the broadening of genuinely photospheric metal lines, free of blends (Simón-Díaz et al., 2006). Therefore, we took the SiII line at 1.6906 μm as a reference.

First, considering a pure rotational profile, we constrained the value of $v \sin i$ with the Fourier Transform method (e.g., Carroll 1933; Dravins et al. 1990), obtaining a value of $v \sin i \sim 37$ km s^{-1}. While there are a lot of uncertainties about MN101, including its exact distance, luminosity and mass, the orientation of its rotation axis can be confidently established from the inclination of the CO torus reported in Paper I. The best-fitting model of the torus has an inclination of $i = 15°$. Adopting a conservative range of (15°–30°), the corresponding deprojected rotation velocities would be somewhere between 70 and 143 km s^{-1}. The latter is a certainly high value for

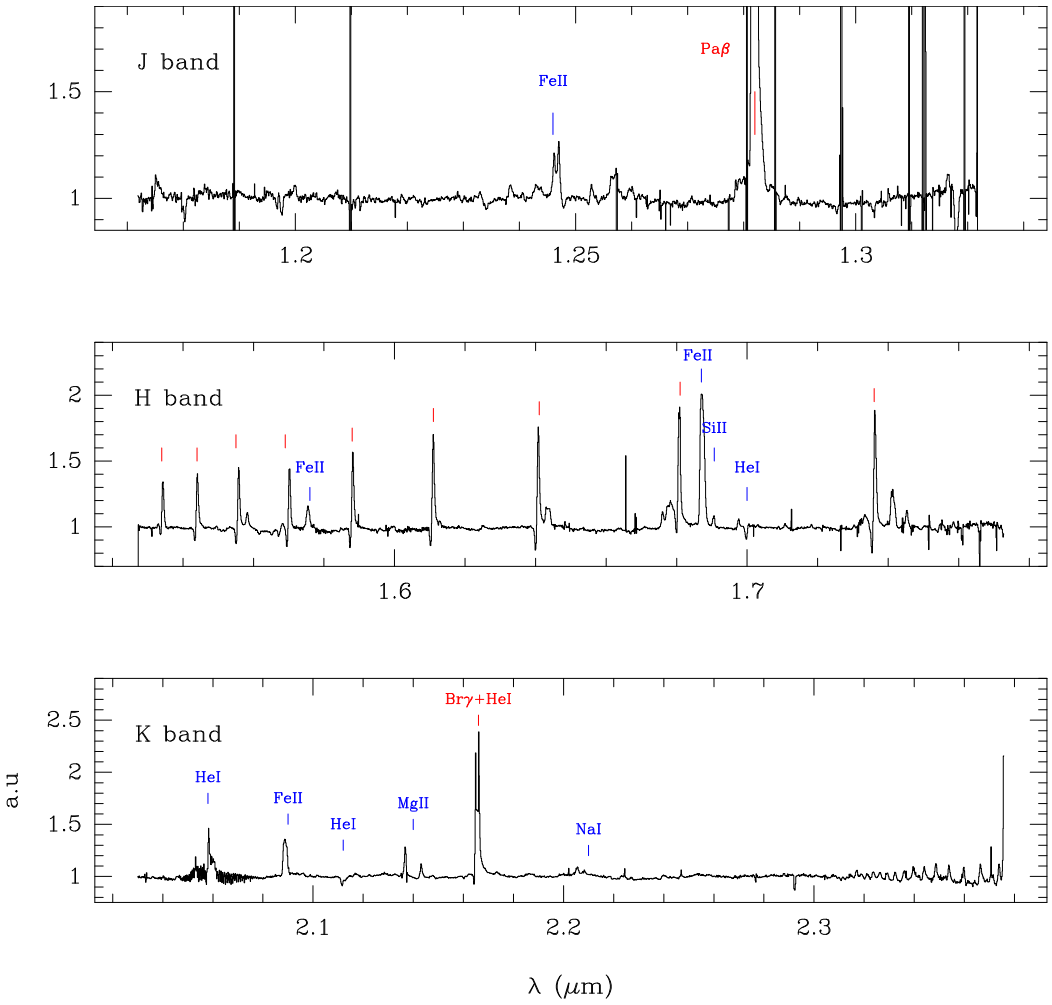

FIGURE A.1: J, H and K band spectra of MN101, in arbitrary intensity units. Main H lines indicated with red markers, He and metal lines indicated with blue markers.

a star likely close to the Eddington luminosity limit, to the point that it could be considered a fast-rotator.

However, we note that for massive early-type stars, atmospheric macro turbulence plays a crucial role in the line broadening, comparable to that of rotation. For that reason, we used the `iacob_broad` procedure [1] to simulate the broadening of a model line profile, taking into account both rotation and radial-tangential macro turbulence. We explored a grid of models with different combinations of $v \sin i$ and $\Theta_{\rm RT}$, evaluating the goodness of fit with respect to the SiII line using a χ^2 approach. We found that rotation alone is unable to reproduce the observed line profile. Moreover, due to the limited resolution of our spectra ($\Delta\lambda \sim 1.7$ angstrom) the solutions are degenerate, obtaining equally good fits for ($v \sin i = 37$ km s^{-1}, $\Theta_R T = 70.3$ km s^{-1}) and ($v \sin i = 50$ km s^{-1}, $\Theta_R T = 61.1$ km s^{-1}). The conclusion is that the current spectroscopic data does not allow us to confirm whether MN101 is a fast rotator or not.

[1] http://research.iac.es/proyecto/iacob/pages/en/useful-tools.php

APPENDIX B

LIST OF PUBLICATIONS AND PERSONAL CONTRIBUTION

Here I list all the published works related to this thesis and thoroughly describe my contribution to each of them.

B.1 Refereed publications

1. "A slowly expanding torus associated with the candidate LBV MGE 042.0787+00.5084"
(Paper I)
Bordiu, C., Rizzo, J. R., and Ritacco, A.
Monthly Notices of the Royal Astronomical Society, Volume 482, Issue 2, pp. 1651-1663 (2019)

2. "NIKA2 observations around LBV stars: emission from stars and circumstellar material"
(Paper II)
Rizzo, J. R., Ritacco, A., and **Bordiu, C.**
European Physical Journal Web of Conferences, Volume 2028, 00023 (2020)

3. "A warm molecular ring around AG Car: completing the mass-loss puzzle"
(Paper III)
Bordiu, C., Bufano, F., Cerrigone, L., Umana, G., Rizzo, J. R., Buemi, C. S., Leto, P., Cavallaro, F., Ingallinera, A., Loru, S., Trigilio, C., and Riggi, S.
Monthly Notices of the Royal Astronomical Society, Volume 500, Issue 4, pp. 5500-5514 (2021)

4. "The peculiar chemistry of the inner ejecta of η Car"
(Paper IV)
Bordiu, C., Rizzo, J. R.
Monthly Notices of the Royal Astronomical Society, Volume 490, Issue 2, pp. 1570-1580 (2019)

B.2 Conference contributions

1. "Tracing back the mass-loss history of MGE042.0787+00.5084"
   Bordiu, C., Rizzo, J. R., and Ritacco, A.
   Poster contribution presented at *XIII Reunión de la Sociedad Española de Astronomía*, July 2018, Salamanca (Spain)

2. "ALMA spectroscopy toward recent ejecta in η Car"
   Rizzo, J. R. and **Bordiu, C.**
   Poster contribution presented at *ALMA2019: Science Results and Cross-Facility Synergies*, October 2019, Cagliari (Italy)

3. "NIKA2 observations around LBV stars: emission from stars and circumstellar material"
   Rizzo, J. R., Ritacco, A., and **Bordiu, C.**
   Oral contribution presented at *Observing the millimeter Universe with the NIKA2 camera* conference, June 2019, Grenoble (France)

4. "A molecular window to the past - mass loss archaeology of very massive stars"
   Bordiu, C., and Rizzo, J. R., and Bufano, F.
   Oral contribution presented at *European Astronomy Society Annual Meeting 2020*, June 2020 (virtual)

B.3 Personal contribution

I participated in five observing programs directly related to this Ph.D. thesis, leading four of them (projects P043-17, P053-18, GTC114-19A, E-0103.D-0778A-2019) and obtaining ∼80 hours of observing time in a number of top tier facilities, such as the IRAM 30m telescope and the GTC. My contribution to these projects involved scientific target selection, proposal writing, setup configuration and, for projects P043-17 and P053-18, in situ observation as visiting astronomer.

The first pillar paper of this thesis, Bordiu et al. (2019), is based on data from project P043-17, which I reduced, analysed and interpreted under the supervision of Dr. Ricardo Rizzo. For these tasks, I developed my own `GILDAS` and Python scripts, and I built the `RADEX` and `LIME` models used to interpret the data. Preliminary results of this work were presented as a poster at the *XIII Reunión Científica de la Sociedad Española de Astronomía*, where I also gave a short pitch.

The second pillar paper, Bordiu & Rizzo (2019), is entirely based on ALMA band 6 observations, found when searching the archive for useful ancillary data for future proposals. As in the previous work, I developed the necessary scripts to analyse and interpret the data, under supervision of my advisor, using `GILDAS` and `CASA` packages. This publication led to a press release by the Centro de Astrobiología[1], with media repercussion. A poster showcasing the results of this work was presented by Dr. Ricardo Rizzo at the *ALMA 2019: Science Results and Cross-Facility Synergies* conference in Cagliari (Italy).

[1] https://www.cab.inta-csic.es/es/noticias/417/descubiertas-dos-nuevas-estructuras-moleculares-asociadas-a-la-ultima-erupcion-de-eta-carina

As regards the publication Rizzo et al. (2020), I actively participated in the proposal preparation (P044-17) and paper writing. This work was presented by Dr. J. R. Rizzo at the *Observing the millimetre Universe with the NIKA2 camera* conference in Grenoble.

Between November 2019 and January 2020, I did a three-month stay at the Radio Astronomy Group of the Osservatorio Astronomico di Catania (INAF). The goal of the stay were to acquire experience in proposal preparation, data reduction and analysis of radio continuum observations of the Galactic Plane, given the vast expertise of the Group with this type of data. In addition, I had the opportunity to analyse archival molecular spectroscopy observations performed by the Group with APEX and ALMA, which led to the third pillar paper, Bordiu et al. (2021).

In the course of this thesis, I attended several workshops, seminars and conferences. I presented a summary of my work in a talk at the European Astronomy Society Meeting 2020, entitled *A molecular window to the past – mass-loss archaeology of evolved massive stars*. Currently, as a member of the Radio Astronomy Group of the Osservatorio Astrofisico di Catania, I am involved in the analysis of SKA precursor data, including ASKAP and MeerKAT, exploring ways to apply machine learning procedures to source extraction, characterization and classification in all-sky radio continuum surveys, with a particular emphasis on supernova remnants. In parallel, I continue my research on formation and destruction pathways of molecular gas around evolved massive stars, following the lines exposed in Chapter 8.

BIBLIOGRAPHY

Heger, A., Woosley, S. E., Fryer, C. L., & Langer, N. (2003). Massive Star Evolution Through the Ages (W. Hillebrandt & B. Leibundgut, Eds.). In W. Hillebrandt & B. Leibundgut (Eds.), *From twilight to highlight: The physics of supernovae*. https://doi.org/10.1007/10828549_1

Poelarends, A. J. T., Herwig, F., Langer, N., & Heger, A. (2008). The Supernova Channel of Super-AGB Stars., *675*(1), arXiv 0705.4643, 614–625. https://doi.org/10.1086/520872

Bethe, H. A., & Critchfield, C. L. (1938). The Formation of Deuterons by Proton Combination. *Physical Review*, *54*(4), 248–254. https://doi.org/10.1103/PhysRev.54.248

von Weizsacker, C. F. (1937). Uber elementumwandlungen im innern der sterne. *I (On.*

Bethe, H. A. (1939). Energy Production in Stars. *Physical Review*, *55*(5), 434–456. https://doi.org/10.1103/PhysRev.55.434

Iben, J., Icko. (1967). Stellar Evolution Within and off the Main Sequence., *5*, 571. https://doi.org/10.1146/annurev.aa.05.090167.003035

Mac Low, M.-M., Balsara, D. S., Kim, J., & de Avillez, M. A. (2005). The Distribution of Pressures in a Supernova-driven Interstellar Medium. I. Magnetized Medium., *626*(2), arXiv astro-ph/0410734, 864–876. https://doi.org/10.1086/430122

Bresolin, F., Crowther, P. A., & Puls, J. (2008). Massive Stars as Cosmic Engines, In *Massive stars as cosmic engines*.

Langer, N. (2012). Presupernova Evolution of Massive Single and Binary Stars., *50*arXiv 1206.5443, 107–164. https://doi.org/10.1146/annurev-astro-081811-125534

Vink, J. S., Brott, I., Gräfener, G., Langer, N., de Koter, A., & Lennon, D. J. (2010). The nature of B supergiants: clues from a steep drop in rotation rates at 22 000 K. The possibility of Bi-stability braking., *512*arXiv 1003.1280, L7. https://doi.org/10.1051/0004-6361/201014205

Meynet, G., & Maeder, A. (2000). Stellar evolution with rotation. V. Changes in all the outputs of massive star models., *361*arXiv astro-ph/0006404, 101–120.

Brott, I., de Mink, S. E., Cantiello, M., Langer, N., de Koter, A., Evans, C. J., Hunter, I., Trundle, C., & Vink, J. S. (2011). Rotating massive main-sequence stars.

I. Grids of evolutionary models and isochrones., *530*arXiv 1102.0530, A115. https://doi.org/10.1051/0004-6361/201016113

Yusof, N., Hirschi, R., Meynet, G., Crowther, P. A., Ekström, S., Frischknecht, U., Georgy, C., Abu Kassim, H., & Schnurr, O. (2013). Evolution and fate of very massive stars., *433*(2), arXiv 1305.2099, 1114–1132. https://doi.org/10.1093/mnras/stt794

Köhler, K., Langer, N., de Koter, A., de Mink, S. E., Crowther, P. A., Evans, C. J., Gräfener, G., Sana, H., Sanyal, D., Schneider, F. R. N., & Vink, J. S. (2015). The evolution of rotating very massive stars with LMC composition., *573*arXiv 1501.03794, A71. https://doi.org/10.1051/0004-6361/201424356

Vink, J. S. (2011). The theory of stellar winds., *336*(1), arXiv 1112.0952, 163–167. https://doi.org/10.1007/s10509-011-0636-7

Vink, J. S., Muijres, L. E., Anthonisse, B., de Koter, A., Gräfener, G., & Langer, N. (2011). Wind modelling of very massive stars up to 300 solar masses., *531*arXiv 1105.0556, A132. https://doi.org/10.1051/0004-6361/201116614

Maeder, A. (1983). Evolution of chemical abundances in massive stars. I. OB stars, Hubble-Sandage variables and Wolf-Rayet stars. Changes at stellar surfaces and galactic enrichment by stellar winds., *120*, 113–129.

Chiosi, C., & Maeder, A. (1986). The evolution of massive stars with mass loss., *24*, 329–375. https://doi.org/10.1146/annurev.aa.24.090186.001553

Maeder, A., & Meynet, G. (1987). Grids of evolutionary models of massive stars with mass loss and overshooting - Properties of Wolf-Rayet stars sensitive to overshooting., *182*, 243–263.

Lamers, H. J. G. L. M., & Leitherer, C. (1993). What are the Mass-Loss Rates of O Stars?, *412*, 771. https://doi.org/10.1086/172960

Herrero, A., Kudritzki, R. P., Vilchez, J. M., Kunze, D., Butler, K., & Haser, S. (1992). The mass and helium discrepancy in massive young stars. In U. Heber & C. S. Jeffery (Eds.), *The atmospheres of early-type stars* (p. 21). https://doi.org/10.1007/3-540-55256-1_269

Langer, N., Hamann, W. R., Lennon, M., Najarro, F., Pauldrach, A. W. A., & Puls, J. (1994). Towards an understanding of very massive stars. A new evolutionary scenario relating O stars, LBVs and Wolf-Rayet stars., *290*, 819–833.

Maeder, A. (1995). Population I Stellar Structure and Evolution: facing the lingering difficulties to make a step forward. In R. S. Stobie & P. A. Whitelock (Eds.), *Iau colloq. 155: Astrophysical applications of stellar pulsation* (p. 1).

Venn, K. A. (1995). CNO Abundances and the Evolutionary Status of Galactic, A-Type Supergiants., *449*, 839. https://doi.org/10.1086/176102

Venn, K. A., Lambert, D. L., & Lemke, M. (1996). The abundance of boron in evolved A- and B-type stars., *307*arXiv astro-ph/9508001, 849–859.

Langer, N., & Maeder, A. (1995). The problem of the blue-to-red supergiant ratio in galaxies., *295*, 685.

Langer, N. (1991). Wolf-Rayet stars of type WN/WC and mixing processes during core helium burning of massive stars?, *248*, 531.

Meynet, G., & Maeder, A. (1997). Stellar evolution with rotation. I. The computational method and the inhibiting effect of the μ-gradient., *321*, 465–476.

Maeder, A. (1997). Stellar evolution with rotation. II. A new approach for shear mixing., *321*, 134–144.

Maeder, A., & Zahn, J.-P. (1998). Stellar evolution with rotation. III. Meridional circulation with MU -gradients and non-stationarity., *334*, 1000–1006.

Smartt, S. J. (2009). Progenitors of Core-Collapse Supernovae., *47*(1), arXiv 0908.0700, 63–106. https://doi.org/10.1146/annurev-astro-082708-101737

Kotak, R., & Vink, J. S. (2006). Luminous blue variables as the progenitors of supernovae with quasi-periodic radio modulations., *460*(2), arXiv astro-ph/0610095, L5–L8. https://doi.org/10.1051/0004-6361:20065800

Smith, N. (2007b). Galactic Twins of the Nebula Around SN 1987A: Hints that LBVs may be supernova progenitors (S. Immler, K. Weiler, & R. McCray, Eds.). In S. Immler, K. Weiler, & R. McCray (Eds.), *Supernova 1987a: 20 years after: Supernovae and gamma-ray bursters*. https://doi.org/10.1063/1.3682897

Gal-Yam, A., & Leonard, D. C. (2009). A massive hypergiant star as the progenitor of the supernova SN 2005gl., *458*(7240), 865–867. https://doi.org/10.1038/nature07934

Maeder, A., & Meynet, G. (2008). Mass Loss and the Evolution of Massive Stars (A. de Koter, L. J. Smith, & L. B. F. M. Waters, Eds.). In A. de Koter, L. J. Smith, & L. B. F. M. Waters (Eds.), *Mass loss from stars and the evolution of stellar clusters*.

Ekström, S., Georgy, C., Eggenberger, P., Meynet, G., Mowlavi, N., Wyttenbach, A., Granada, A., Decressin, T., Hirschi, R., Frischknecht, U., Charbonnel, C., & Maeder, A. (2012). Grids of stellar models with rotation. I. Models from 0.8 to 120 M at solar metallicity (Z = 0.014)., *537*arXiv 1110.5049, A146. https://doi.org/10.1051/0004-6361/201117751

Georgy, C., Ekström, S., Meynet, G., Massey, P., Levesque, E. M., Hirschi, R., Eggenberger, P., & Maeder, A. (2012). Grids of stellar models with rotation. II. WR populations and supernovae/GRB progenitors at Z = 0.014., *542*arXiv 1203.5243, A29. https://doi.org/10.1051/0004-6361/201118340

Groh, J. H., Meynet, G., & Ekström, S. (2013a). Massive star evolution: luminous blue variables as unexpected supernova progenitors., *550*arXiv 1301.1519, L7. https://doi.org/10.1051/0004-6361/201220741

Walmswell, J. J., & Eldridge, J. J. (2012). Circumstellar dust as a solution to the red supergiant supernova progenitor problem., *419*(3), arXiv 1109.4637, 2054–2062. https://doi.org/10.1111/j.1365-2966.2011.19860.x

Meynet, G., Ekstrom, S., Maeder, A., Eggenberger, P., Saio, H., Chomienne, V., & Haemmerlé, L. (2013). Models of Rotating Massive Stars: Impacts of Various Prescriptions. In M. Goupil, K. Belkacem, C. Neiner, F. Lignières, & J. J. Green (Eds.), *Lecture notes in physics, berlin springer verlag* (p. 3). https://doi.org/10.1007/978-3-642-33380-4_1

Stothers, R. B., & Chin, C.-W. (1991). Blue Loops during Core Helium Burning as the Consequence of Moderate Convective Envelope Overshooting in Stars of Intermediate to High Mass., *374*, 288. https://doi.org/10.1086/170117

Sana, H., Gosset, E., Nazé, Y., Rauw, G., & Linder, N. (2008). The massive star binary fraction in young open clusters - I. NGC 6231 revisited., *386*(1), arXiv 0707.2847, 447–460. https://doi.org/10.1111/j.1365-2966.2008.13037.x

Sana, H., Gosset, E., & Evans, C. J. (2009). The massive star binary fraction in young open clusters - II. NGC6611 (Eagle Nebula)., *400*(3), arXiv 0909.0486, 1479–1492. https://doi.org/10.1111/j.1365-2966.2009.15545.x

Maíz Apellániz, J. (2010). High-resolution imaging of Galactic massive stars with AstraLux. I. 138 fields with $\delta >$ - 25., *518*arXiv 1004.5045, A1. https://doi.org/10.1051/0004-6361/201014409

Aldoretta, E. J., Caballero-Nieves, S. M., Gies, D. R., Nelan, E. P., Wallace, D. J., Hartkopf, W. I., Henry, T. J., Jao, W. C., Maíz Apellániz, J., Mason, B. D., Moffat, A. F. J., Norris, R. P., Richardson, N. D., & Williams, S. J. (2015). The Multiplicity of Massive Stars: a High Angular Resolution Survey With the Guidance Sensor., *149*(1), arXiv 1410.0021, 26. https://doi.org/10.1088/0004-6256/149/1/26

Sana, H., de Mink, S. E., de Koter, A., Langer, N., Evans, C. J., Gieles, M., Gosset, E., Izzard, R. G., Le Bouquin, J. B., & Schneider, F. R. N. (2012). Binary Interaction Dominates the Evolution of Massive Stars. *Science*, *337*(6093), arXiv 1207.6397, 444. https://doi.org/10.1126/science.1223344

Sana, H., de Koter, A., de Mink, S. E., Dunstall, P. R., Evans, C. J., Hénault-Brunet, V., Maíz Apellániz, J., Ramírez-Agudelo, O. H., Taylor, W. D., Walborn, N. R., Clark, J. S., Crowther, P. A., Herrero, A., Gieles, M., Langer, N., Lennon, D. J., & Vink, J. S. (2013). The VLT-FLAMES Tarantula Survey. VIII. Multiplicity properties of the O-type star population., *550*arXiv 1209.4638, A107. https://doi.org/10.1051/0004-6361/201219621

Hubble, E., & Sandage, A. (1953). The Brightest Variable Stars in Extragalactic Nebulae. I. M31 and M33., *118*, 353. https://doi.org/10.1086/145764

Feast, M. W., Thackeray, A. D., & Wesselink, A. J. (1960). The brightest stars in the Magellanic Clouds., *121*, 337. https://doi.org/10.1093/mnras/121.4.337

Sandage, A., & Tammann, G. A. (1974). Steps toward the Hubble constant. II. The brightest stars in late-type spiral galaxies., *191*, 603–621. https://doi.org/10.1086/153001

Humphreys, R. M. (1975). The spectra of AE Andromedae and the Hubble-Sandage variables in M31 and M33., *200*, 426–429. https://doi.org/10.1086/153806

Conti, P. S. (1984). Basic Observational Constraints on the Evolution of Massive Stars (A. Maeder & A. Renzini, Eds.). In A. Maeder & A. Renzini (Eds.), *Observational tests of the stellar evolution theory*.

Richardson, N. D., & Mehner, A. (2018). The 2018 Census of Luminous Blue Variables in the Local Group. *Research Notes of the American Astronomical Society*, *2*(3), arXiv 1807.04262, 121. https://doi.org/10.3847/2515-5172/aad1f3

Humphreys, R. M., & Davidson, K. (1994). The Luminous Blue Variables: Astrophysical Geysers., *106*, 1025. https://doi.org/10.1086/133478

Wolf, B. (1989). Empirical amplitude-luminosity relation of S Doradus variables and extragalactic distances., *217*, 87–91.

Smith, N., Vink, J. S., & de Koter, A. (2004). The Missing Luminous Blue Variables and the Bistability Jump., *615*(1), arXiv astro-ph/0407202, 475–484. https://doi.org/10.1086/424030

Lamers, H. J. G. L. M. (1986). P Cygni type stars - Evolution and physical processes (C. W. H. De Loore, A. J. Willis, & P. Laskarides, Eds.). In C. W. H. De Loore, A. J. Willis, & P. Laskarides (Eds.), *Luminous stars and associations in galaxies*.

Davidson, K. (1987). The Relation between Apparent Temperature and Mass-Loss Rate in Hypergiant Eruptions., *317*, 760. https://doi.org/10.1086/165324

van Genderen, A. M. (2001). S Doradus variables in the Galaxy and the Magellanic Clouds., *366*, 508–531. https://doi.org/10.1051/0004-6361:20000022

van Genderen, A. M., Thé, P. S., Heemskerk, M., Heynderickx, D., Larsen, I., Wanders, I., & van Weeren, N. (1989). The Optical Micro-Variations of the S Dor-Type Stars AG CAR and HR CAR. In K. Davidson, A. F. J. Moffat, & H. J. G. L. M. Lamers (Eds.), *Iau colloq. 113: Physics of luminous blue variables* (p. 273). https://doi.org/10.1007/978-94-009-1031-7_37

Smith, N. (2014). Mass Loss: Its Effect on the Evolution and Fate of High-Mass Stars., *52*arXiv 1402.1237, 487–528. https://doi.org/10.1146/annurev-astro-081913-040025

Lamers, H. J. G. L. M., Snow, T. P., & Lindholm, D. M. (1995). Terminal Velocities and the Bistability of Stellar Winds., *455*, 269. https://doi.org/10.1086/176575

Stahl, O., Jankovics, I., Kovács, J., Wolf, B., Schmutz, W., Kaufer, A., Rivinius, T., & Szeifert, T. (2001). Long-term spectroscopic monitoring of the Luminous Blue Variable AG Carinae., *375*, 54–69. https://doi.org/10.1051/0004-6361:20010824

Vink, J. S. (2012). Eta Carinae and the Luminous Blue Variables. In K. Davidson & R. M. Humphreys (Eds.), *Eta carinae and the supernova impostors* (p. 221). https://doi.org/10.1007/978-1-4614-2275-4_10

de Jager, C. (1984). The stability limit of hypergiant photospheres., *138*, 246–252.

Guzik, J. A., Cox, A. N., & Despain, K. M. (2005). Pulsation-Driven Mass Loss in Luminous Blue Variables. In R. Humphreys & K. Stanek (Eds.), *The fate of the most massive stars* (p. 267).

Lovekin, C. C., & Guzik, J. A. (2014). Pulsations as a driver for LBV variability., *445*(2), arXiv 1407.1693, 1766–1773. https://doi.org/10.1093/mnras/stu1899

Jiang, Y.-F., Cantiello, M., Bildsten, L., Quataert, E., Blaes, O., & Stone, J. (2018). Outbursts of luminous blue variable stars from variations in the helium opacity., *561*(7724), 498–501. https://doi.org/10.1038/s41586-018-0525-0

Van Dyk, S. D. (2007). Supernova impostors: LBV outbursts from the most massive stars. *Highlights of Astronomy*, *14*, 205–205. https://doi.org/10.1017/S1743921307010174

Kochanek, C. S., Szczygieł, D. M., & Stanek, K. Z. (2012). Unmasking the Supernova Impostors., *758*(2), arXiv 1202.0281, 142. https://doi.org/10.1088/0004-637X/758/2/142

de Vaucouleurs, G., & Eggen, O. J. (1952). The Brightening of η Carinae., *64*(379), 185. https://doi.org/10.1086/126457

Davidson, K. (1989). Plinian Eruptions a la Eta Carinae. In K. Davidson, A. F. J. Moffat, & H. J. G. L. M. Lamers (Eds.), *Iau colloq. 113: Physics of luminous blue variables* (p. 101). https://doi.org/10.1007/978-94-009-1031-7_11

Gomez, H. L., Vlahakis, C., Stretch, C. M., Dunne, L., Eales, S. A., Beelen, A., Gomez, E. L., & Edmunds, M. G. (2010). Submillimetre variability of Eta Carinae: cool dust within the outer ejecta., *401*(1), arXiv 0911.0176, L48–L52. https://doi.org/10.1111/j.1745-3933.2009.00784.x

Davidson, K., & Humphreys, R. M. (2012). *Eta Carinae and the Supernova Impostors* (Vol. 384). https://doi.org/10.1007/978-1-4614-2275-4

Pastorello, A., & Fraser, M. (2019). Supernova impostors and other gap transients. *Nature Astronomy*, *3*arXiv 1908.02323, 676–679. https://doi.org/10.1038/s41550-019-0809-9

Weis, K. (2001). LBV Nebulae: The Mass Lost from the Most Massive Stars. *Reviews in Modern Astronomy*, *14*arXiv astro-ph/0104214, 261.

Smith, N., & Owocki, S. P. (2006). On the Role of Continuum-driven Eruptions in the Evolution of Very Massive Stars and Population III Stars., *645*(1), arXiv astro-ph/0606174, L45–L48. https://doi.org/10.1086/506523

Weis, K. (2012). LBV Nebulae as Tracers of Stellar Instabilities (L. Drissen, C. Robert, N. St-Louis, & A. F. J. Moffat, Eds.). In L. Drissen, C. Robert, N. St-Louis, & A. F. J. Moffat (Eds.), *Proceedings of a scientific meeting in honor of anthony f. j. moffat.*

Smith, N., Rest, A., Andrews, J. E., Matheson, T., Bianco, F. B., Prieto, J. L., James, D. J., Smith, R. C., Strampelli, G. M., & Zenteno, A. (2018c). Exceptionally fast ejecta seen in light echoes of Eta Carinae's Great Eruption., *480*(2), arXiv 1808.00991, 1457–1465. https://doi.org/10.1093/mnras/sty1479

Gail, H. P., Duschl, W. J., Ferrarotti, A. S., & Weis, K. (2005). Dust formation in LBV envelopes. In R. Humphreys & K. Stanek (Eds.), *The fate of the most massive stars* (p. 323).

Mizuno, D. R., Kraemer, K. E., Flagey, N., Billot, N., Shenoy, S., Paladini, R., Ryan, E., Noriega-Crespo, A., & Carey, S. J. (2010). A Catalog of MIPSGAL Disk and Ring Sources., *139*(4), arXiv 1002.4421, 1542–1552. https://doi.org/10.1088/0004-6256/139/4/1542

Wachter, S., Mauerhan, J. C., Van Dyk, S. D., Hoard, D. W., Kafka, S., & Morris, P. W. (2010). A Hidden Population of Massive Stars with Circumstellar Shells Discovered with the Spitzer Space Telescope., *139*(6), arXiv 1004.0399, 2330–2346. https://doi.org/10.1088/0004-6256/139/6/2330

Gvaramadze, V. V., Kniazev, A. Y., & Fabrika, S. (2010). Revealing evolved massive stars with Spitzer., *405*(2), arXiv 0909.0458, 1047–1060. https://doi.org/10.1111/j.1365-2966.2010.16496.x

Smith, N. (2017). Luminous blue variables and the fates of very massive stars. *Philosophical Transactions of the Royal Society of London Series A*, *375*(2105), 20160268. https://doi.org/10.1098/rsta.2016.0268

Trundle, C., Kotak, R., Vink, J. S., & Meikle, W. P. S. (2008). SN 2005 gj: evidence for LBV supernovae progenitors?, *483*(3), arXiv 0804.2392, L47–L50. https://doi.org/10.1051/0004-6361:200809755

Smith, N., Li, W., Foley, R. J., Wheeler, J. C., Pooley, D., Chornock, R., Filippenko, A. V., Silverman, J. M., Quimby, R., Bloom, J. S., & Hansen, C. (2007b). SN 2006gy: Discovery of the Most Luminous Supernova Ever Recorded, Powered by the Death of an Extremely Massive Star like η Carinae., *666*(2), arXiv astro-ph/0612617, 1116–1128. https://doi.org/10.1086/519949

Pastorello, A., Smartt, S. J., Mattila, S., Eldridge, J. J., Young, D., Itagaki, K., Yamaoka, H., Navasardyan, H., Valenti, S., Patat, F., Agnoletto, I., Augusteijn, T., Benetti, S., Cappellaro, E., Boles, T., Bonnet-Bidaud, J. M., Botticella, M. T., Bufano, F., Cao, C., … Zampieri, L. (2007). A giant outburst two years before the core-collapse of a massive star., *447*(7146), arXiv astro-ph/0703663, 829–832. https://doi.org/10.1038/nature05825

Arnal, E. M., Cappa, C. E., Rizzo, J. R., & Cichowolski, S. (1999). The Interstellar Medium around Galactic WN Stars: WR 2, WR 128, and WR 151., *118*(4), 1798–1805. https://doi.org/10.1086/301043

Chu, Y. H. (1981). Galactic ring nebulae associated with Wolf-rayet stars. I. Introduction and classification., *249*, 195–200. https://doi.org/10.1086/159275

Miller, G. J., & Chu, Y.-H. (1993). A New Survey of Nebulae around Galactic Wolf-Rayet Stars in the Northern Sky., *85*, 137. https://doi.org/10.1086/191757

Marston, A. P. (1996). Large IRAS Shells Around Galactic Wolf-Rayet Stars and the O Star Phase of Wolf-Rayet Evolution., *112*, 2828. https://doi.org/10.1086/118223

Duncan, R. A., & White, S. M. (2002). Radio images of four luminous blue variable stars., *330*(1), 63–68. https://doi.org/10.1046/j.1365-8711.2002.05034.x

Duncan, R. A., & White, S. M. (2003). Radio evidence of recent mass ejection from η Carinae., *338*(2), 425–427. https://doi.org/10.1046/j.1365-8711.2003.06287.x

Umana, G., Buemi, C. S., Trigilio, C., & Leto, P. (2005). Current day mass loss rate for Luminous Blue Variable IRAS 18576+0341., *437*(1), L1–L5. https://doi.org/10.1051/0004-6361:200500126

Buemi, C. S., Umana, G., Trigilio, C., Leto, P., & Hora, J. L. (2010). VISIR/VLT and VLA Joint Imaging Analysis of the Circumstellar Nebula Around IRAS 18576+0341., *721*(2), arXiv 1008.0997, 1404–1411. https://doi.org/10.1088/0004-637X/721/2/1404

Umana, G., Buemi, C. S., Trigilio, C., Leto, P., Agliozzo, C., Ingallinera, A., Noriega-Crespo, A., & Hora, J. L. (2011). Expanded Very Large Array Observations of the Nebula Around G79.29+0.46., *739*(1), L11. https://doi.org/10.1088/2041-8205/739/1/L11

Schneps, M. H., Haschick, A. D., Wright, E. L., & Barrett, A. H. (1981). The stellar wind bubble NGC 2359. I. CO, VLA, and optical observations., *243*, 184–196. https://doi.org/10.1086/158582

McGregor, P. J., Hyland, A. R., & Hillier, D. J. (1988a). Atomic and Molecular Line Emission from Early-Type High-Luminosity Stars., *324*, 1071. https://doi.org/10.1086/165964

McGregor, P. J., Hillier, D. J., & Hyland, A. R. (1988b). CO Overtone Emission from Magellanic Cloud Supergiants., *334*, 639. https://doi.org/10.1086/166867

St-Louis, N., Doyon, R., Chagnon, F., & Nadeau, D. (1998). Molecular Hydrogen Emission in the Wolf-Rayet Nebula NGC 2359., *115*(6), 2475–2482. https://doi.org/10.1086/300351

Marston, A. P., Welzmiller, J., Bransford, M. A., Black, J. H., & Bergman, P. (1999). Molecular Gas Associated with the Ejecta Ring Nebula around the Wolf-Rayet Star WR 16., *518*(2), 769–777. https://doi.org/10.1086/307304

Rizzo, J. R., Martín-Pintado, J., & Mangum, J. G. (2001b). On the history of the interplay between HD 56925 and NGC 2359., *366*arXiv astro-ph/0011163, 146–156. https://doi.org/10.1051/0004-6361:20000095

Rizzo, J. R., Martín-Pintado, J., & Henkel, C. (2001a). Shocked Ammonia in the Wolf-Rayet Nebula NGC 2359., *553*(2), arXiv astro-ph/0104330, L181–L184. https://doi.org/10.1086/320695

Smith, N., & Davidson, K. (2001). The Shocking Near-Infrared Spectrum of the Homunculus Nebula Surrounding η Carinae., *551*(1), L101–L104. https://doi.org/10.1086/319846

Nota, A., Pasquali, A., Marston, A. P., Lamers, H. J. G. L. M., Clampin, M., & Schulte-Ladbeck, R. E. (2002). Detection of ^{12}CO J=1–>0 and J=2–>1 Emission from the Luminous Blue Variable AG Carinae: Circumstellar Envelope or Disk?, *124*(5), arXiv astro-ph/0208040, 2920–2930. https://doi.org/10.1086/343770

Rizzo, J. R., Martín-Pintado, J., & Desmurs, J. F. (2003a). Shocked gas layers surrounding the WR nebula NGC 2359., *411*arXiv astro-ph/0308527, 465–475. https://doi.org/10.1051/0004-6361:20031330

Rizzo, J. R., Martín-Pintado, J., & Desmurs, J.-F. (2003b). Complex molecules in Wolf-Rayet ring nebula NGC 2359 (K. van der Hucht, A. Herrero, & C. Esteban, Eds.). In K. van der Hucht, A. Herrero, & C. Esteban (Eds.), *A massive star odyssey: From main sequence to supernova*.

Verner, E., Bruhweiler, F., Nielsen, K. E., Gull, T. R., Vieira Kober, G., & Corcoran, M. (2005). Discovery of CH and OH in the -513 km s^{-1} Ejecta of η Carinae., *629*(2), arXiv astro-ph/0505353, 1034–1039. https://doi.org/10.1086/431917

Smith, N., Brooks, K. J., Koribalski, B. S., & Bally, J. (2006). Cleaning Up η Carinae: Detection of Ammonia in the Homunculus Nebula., *645*(1), arXiv astro-ph/0605543, L41–L44. https://doi.org/10.1086/505934

Loinard, L., Kamiński, T., Serra, P., Menten, K. M., Zapata, L. A., & Rodríguez, L. F. (2016). Spatial Distribution and Kinematics of the Molecular Material Associated with eta Carinae., *833*(1), arXiv 1606.04575, 48. https://doi.org/10.3847/1538-4357/833/1/48

Rizzo, J. R., Jiménez-Esteban, F. M., & Ortiz, E. (2008). Discovery of Warm and Dense Molecular Gas Surrounding the Ring Nebula G79.29+0.46., *681*(1), arXiv 0804.0266, 355–364. https://doi.org/10.1086/588455

Jiménez-Esteban, F. M., Rizzo, J. R., & Palau, A. (2010). Multiple Shells Around G79.29+0.46 Revealed from Near-IR to Millimeter Data., *713*(1), arXiv 1003.4455, 429–439. https://doi.org/10.1088/0004-637X/713/1/429

Rizzo, J. R., Palau, A., Jiménez-Esteban, F., & Henkel, C. (2014). Ammonia observations in the LBV nebula G79.29+0.46. Discovery of a cold ring and some warm spots., *564*arXiv 1401.6186, A21. https://doi.org/10.1051/0004-6361/201323170

Palau, A., Rizzo, J. R., Girart, J. M., & Henkel, C. (2014). A Luminous Blue Variable Star Interacting with a Nearby Infrared Dark Cloud., *784*(2), arXiv 1401.8248, L21. https://doi.org/10.1088/2041-8205/784/2/L21

Petriella, A., Paron, S. A., & Giacani, E. B. (2012). The molecular gas around the luminous blue variable star G24.73+0.69., *538*arXiv 1111.6043, A14. https://doi.org/10.1051/0004-6361/201118394

Paron, S., Combi, J. A., Petriella, A., & Giacani, E. (2012). Study of the luminous blue variable star candidate G26.47+0.02 and its environment., *543*arXiv 1205.1469, A23. https://doi.org/10.1051/0004-6361/201218919

Loinard, L., Menten, K. M., Güsten, R., Zapata, L. A., & Rodríguez, L. F. (2012). Molecules in η Carinae., *749*(1), arXiv 1203.1559, L4. https://doi.org/10.1088/2041-8205/749/1/L4

Smith, N., Gehrz, R. D., Hinz, P. M., Hoffmann, W. F., Mamajek, E. E., Meyer, M. R., & Hora, J. L. (2002). A Disrupted Circumstellar Torus inside η Carinae's Homunculus Nebula., *567*(1), arXiv astro-ph/0201489, L77–L80. https://doi.org/10.1086/339897

Morris, P. W., Gull, T. R., Hillier, D. J., Barlow, M. J., Royer, P., Nielsen, K., Black, J., & Swinyard, B. (2017). η Carinae's Dusty Homunculus Nebula from Near-infrared to Submillimeter Wavelengths: Mass, Composition, and Evidence for Fading Opacity., *842*(2), arXiv 1706.05112, 79. https://doi.org/10.3847/1538-4357/aa71b3

Smith, N., Ginsburg, A., & Bally, J. (2018b). A disrupted molecular torus around Eta Carinae as seen in ^{12}CO with ALMA., *474*(4), arXiv 1712.01362, 4988–4996. https://doi.org/10.1093/mnras/stx3050

Bordiu, C., Rizzo, J. R., & Ritacco, A. (2019). A slowly expanding torus associated with the candidate LBV MGE 042.0787+00.5084., *482*(2), arXiv 1810.04897, 1651–1663. https://doi.org/10.1093/mnras/sty2726

Rizzo, J. R., Ritacco, A., & Bordiu, C. (2020). NIKA2 observations around LBV stars Emission from stars and circumstellar material, In *European physical journal web of conferences*. https://doi.org/10.1051/epjconf/202022800023

Bordiu, C., Bufano, F., Cerrigone, L., Umana, G., Rizzo, J. R., Buemi, C. S., Leto, P., Cavallaro, F., Ingallinera, A., Loru, S., Trigilio, C., & Riggi, S. (2021). A warm molecular ring in AG Car: composing the mass-loss puzzle., *500*(4), arXiv 2011.08161, 5500–5514. https://doi.org/10.1093/mnras/staa3606

Bordiu, C., & Rizzo, J. R. (2019). The peculiar chemistry of the inner ejecta of Eta Carina., *490*(2), arXiv 1904.00256, 1570–1580. https://doi.org/10.1093/mnras/stz2621

Goodisman, J. (2012). *Diatomic interaction potential theory: Fundamentals*. Elsevier Science. https://books.google.es/books?id=Hx9xPYsrwBwC

Einstein, A. (1917). Zur Quantentheorie der Strahlung. *Physikalische Zeitschrift*, *18*, 121–128.

Condon, J. J., & Ransom, S. M. (2016). *Essential Radio Astronomy*.

Hildebrand, R. H. (1983). The determination of cloud masses and dust characteristics from submillimetre thermal emission., *24*, 267–282.

Ekers, R. D. (2014). Non-thermal radio astronomy. *Astroparticle Physics*, *53*, 152–159. https://doi.org/10.1016/j.astropartphys.2013.05.012

Rybicki, G. B., & Lightman, A. P. (1986). *Radiative Processes in Astrophysics*.

Burke, B. F., & Graham-Smith, F. (1997). *An introduction to radio astronomy*.

van der Hucht, K. A., Williams, P. M., Spoelstra, T. A. T., & de Bruyn, A. G. (1992). Non-thermal radio observations of Wolf-Rayet stars: a case for long-period binaries. (L. Drissen, C. Leitherer, & A. Nota, Eds.). In L. Drissen, C. Leitherer, & A. Nota (Eds.), *Nonisotropic and variable outflows from stars*.

Penzias, A. A., & Burrus, C. A. (1973). Millimeter-Wavelength Radio-Astronomy Techniques., *11*, 51. https://doi.org/10.1146/annurev.aa.11.090173.000411

Ulich, B. L., & Haas, R. W. (1976). Absolute calibration of millimeter-wavelength spectral lines., *30*, 247–258. https://doi.org/10.1086/190361

Kutner, M. L., & Ulich, B. L. (1981). Recommendations for calibration of millimeter-wavelength spectral line data., *250*, 341–348. https://doi.org/10.1086/159380

van Cittert, P. H. (1934). Die Wahrscheinliche Schwingungsverteilung in Einer von Einer Lichtquelle Direkt Oder Mittels Einer Linse Beleuchteten Ebene. *Physica*, *1*(1), 201–210. https://doi.org/10.1016/S0031-8914(34)90026-4

Zernike, F. (1938). The concept of degree of coherence and its application to optical problems. *Physica*, *5*(8), 785–795. https://doi.org/10.1016/S0031-8914(38)80203-2

Högbom, J. A. (1974). Aperture Synthesis with a Non-Regular Distribution of Interferometer Baselines., *15*, 417.

Wilson, T., & Hüttemeister, S. (2000). *Tools of radio astronomy*. https://doi.org/10.1007/978-3-642-57001-8

Mangum, J. G., & Shirley, Y. L. (2015). How to Calculate Molecular Column Density., *127*(949), arXiv 1501.01703, 266. https://doi.org/10.1086/680323

Sobolev, V. V. (1960). *Moving envelopes of stars*.

Elitzur, M. (1992). Astronomical masers., *30*, 75–112. https://doi.org/10.1146/annurev.aa.30.090192.000451

Draine, B. T., Dale, D. A., Bendo, G., Gordon, K. D., Smith, J. D. T., Armus, L., Engelbracht, C. W., Helou, G., Kennicutt, J., R. C., Li, A., Roussel, H., Walter, F., Calzetti, D., Moustakas, J., Murphy, E. J., Rieke, G. H., Bot, C., Hollenbach, D. J., Sheth, K., & Teplitz, H. I. (2007). Dust Masses, PAH Abundances, and Starlight Intensities in the SINGS Galaxy Sample., *663*(2), arXiv astro-ph/0703213, 866–894. https://doi.org/10.1086/518306

Schnee, S., Enoch, M., Noriega-Crespo, A., Sayers, J., Terebey, S., Caselli, P., Foster, J., Goodman, A., Kauffmann, J., Padgett, D., Rebull, L., Sargent, A., & Shetty, R. (2010). The Dust Emissivity Spectral Index in the Starless Core TMC-1C., *708*(1), arXiv 0911.0892, 127–136. https://doi.org/10.1088/0004-637X/708/1/127

Wright, A. E., & Barlow, M. J. (1975). The radio and infrared spectrum of early type stars undergoing mass loss., *170*, 41–51. https://doi.org/10.1093/mnras/170.1.41

Dougherty, S. M., & Williams, P. M. (2000). Non-thermal emission in Wolf-Rayet stars: are massive companions required?, *319*(4), 1005–1010. https://doi.org/10.1046/j.1365-8711.2000.03837.x

Eckart, A., Witzel, A., Biermann, P., Johnston, K. J., Simon, R., Schalinski, C., & Kuhr, H. (1986). Investigation of a complete sample of flat spectrum radio sources from the S5 Survey. I. Analysis., *168*, 17–24.

Panagia, N., & Felli, M. (1975). The spectrum of the free-free radiation from extended envelopes., *39*, 1–5.

Leitherer, C., & Robert, C. (1991). Observations of Stellar Winds from Hot Stars at 1.3 Millimeters., *377*, 629. https://doi.org/10.1086/170390

van der Tak, F. F. S., Black, J. H., Schöier, F. L., Jansen, D. J., & van Dishoeck, E. F. (2010). Radex: Fast Non-LTE Analysis of Interstellar Line Spectra.

Schöier, F. L., van der Tak, F. F. S., van Dishoeck, E. F., & Black, J. H. (2005). An atomic and molecular database for analysis of submillimetre line observations., *432*(1), arXiv astro-ph/0411110, 369–379. https://doi.org/10.1051/0004-6361:20041729

Brinch, C., & Hogerheijde, M. R. (2010). LIME - a flexible, non-LTE line excitation and radiation transfer method for millimeter and far-infrared wavelengths., *523*arXiv 1008.1492, A25. https://doi.org/10.1051/0004-6361/201015333

Ziurys, L. M. (2006). The chemistry in circumstellar envelopes of evolved stars: Following the origin of the elements to the origin of life. *Proceedings of the National Academy of Sciences*, *103*(33), https://www.pnas.org/content/103/33/12274.full.pdf, 12274–12279. https://doi.org/10.1073/pnas.0602277103

Carey, S. J., Noriega-Crespo, A., Mizuno, D. R., Shenoy, S., Paladini, R., Kraemer, K. E., Price, S. D., Flagey, N., Ryan, E., Ingalls, J. G., Kuchar, T. A., Pinheiro Gonçalves, D., Indebetouw, R., Billot, N., Marleau, F. R., Padgett, D. L., Rebull, L. M., Bressert, E., Ali, B., ... Testi, L. (2009). MIPSGAL: A Survey of the Inner Galactic Plane at 24 and 70 μm., *121*(875), 76. https://doi.org/10.1086/596581

Wachter, S., Mauerhan, J., van Dyk, S., Hoard, D. W., & Morris, P. (2011). Massive Stars with Circumstellar Shells Discovered with the Spitzer Space Telescope. *Bulletin de la Societe Royale des Sciences de Liege*, *80*, 291–296.

Flagey, N., Noriega-Crespo, A., Petric, A., & Geballe, T. R. (2014). Palomar/TripleSpec Observations of Spitzer/MIPSGAL 24 μm Circumstellar Shells: Unveiling the Natures of Their Central Sources., *148*(2), arXiv 1405.4023, 34. https://doi.org/10.1088/0004-6256/148/2/34

Ingallinera, A., Trigilio, C., Umana, G., Leto, P., Noriega-Crespo, A., Flagey, N., Paladini, R., Agliozzo, C., & Buemi, C. S. (2014). A radio characterization of Galactic compact bubbles., *437*(4), arXiv 1311.4753, 3626–3638. https://doi.org/10.1093/mnras/stt2157

Ingallinera, A., Trigilio, C., Leto, P., Umana, G., Buemi, C., Bufano, F., Agliozzo, C., Riggi, S., Flagey, N., Silva, K., Cerrigone, L., & Cavallaro, F. (2016). High-resolution Very Large Array observations of 18 MIPSGAL bubbles., *463*(1), arXiv 1609.00003, 723–739. https://doi.org/10.1093/mnras/stw2053

Adam, R., Adane, A., Ade, P. A. R., André, P., Andrianasolo, A., Aussel, H., Beelen, A., Benoît, A., Bideaud, A., Billot, N., Bourrion, O., Bracco, A., Calvo, M., Catalano, A., Coiffard, G., Comis, B., De Petris, M., Désert, F. X., Doyle, S., ... Zylka, R. (2018). The NIKA2 large-field-of-view millimetre continuum camera for the 30 m IRAM telescope., *609*arXiv 1707.00908, A115. https://doi.org/10.1051/0004-6361/201731503

Guilloteau, S., & Lucas, R. (2000). Imaging at the IRAM Plateau de Bure Interferometer (J. G. Mangum & S. J. E. Radford, Eds.). In J. G. Mangum & S. J. E. Radford (Eds.), *Imaging at radio through submillimeter wavelengths*.

Bailer-Jones, C. A. L., Rybizki, J., Fouesneau, M., Mantelet, G., & Andrae, R. (2018). Estimating Distance from Parallaxes. IV. Distances to 1.33 Billion Stars in Gaia Data Release 2., *156*(2), arXiv 1804.10121, 58. https://doi.org/10.3847/1538-3881/aacb21

Berdyugina, S. V., & Savanov, I. S. (1994). CNO abundances and $^{12}C/^{13}C$ ratios in the atmospheres of lithium-rich giants. *Astronomy Letters*, *20*(5), 639–643.

Davis, T. A. (2014). Systematic variation of the $^{12}CO/^{13}CO$ ratio as a function of star formation rate surface density., *445*(3), arXiv 1409.1732, 2378–2384. https://doi.org/10.1093/mnras/stu1850

Shimajiri, Y., Kitamura, Y., Saito, M., Momose, M., Nakamura, F., Dobashi, K., Shimoikura, T., Nishitani, H., Yamabi, A., Hara, C., Katakura, S., Tsukagoshi, T., Tanaka, T., & Kawabe, R. (2014). High abundance ratio of ^{13}CO to C^{18}O toward photon-dominated regions in the Orion-A giant molecular cloud., *564*arXiv 1403.2930, A68. https://doi.org/10.1051/0004-6361/201322912

Humphreys, R. M., Lamers, H. J. G. L. M., Hoekzema, N., & Cassatella, A. (1989). The distance and evolutionary phase of the luminous blue variable AG Car., *218*, L17–L20.

Smith, N., Aghakhanloo, M., Murphy, J. W., Drout, M. R., Stassun, K. G., & Groh, J. H. (2019). On the Gaia DR2 distances for Galactic luminous blue variables., *488*(2), arXiv 1805.03298, 1760–1778. https://doi.org/10.1093/mnras/stz1712

Groh, J. H., Hillier, D. J., & Damineli, A. (2011). On the Nature of the Prototype Luminous Blue Variable AG Carinae. II. Witnessing a Massive Star Evolving Close to the Eddington and Bistability Limits., *736*(1), arXiv 1105.0814, 46. https://doi.org/10.1088/0004-637X/736/1/46

Sterken, C. (2003). The S Dor phases of AG Carinae, In *American astronomical society meeting abstracts #202*.

Thackeray, A. D. (1950). Some southern stars involved in nebulosity., *110*, 524. https://doi.org/10.1093/mnras/110.6.524

Nota, A., Leitherer, C., Clampin, M., Greenfield, P., & Golimowski, D. A. (1992). Mapping AG Carinae: Long-Slit Spectroscopy and Coronographic Imaging of the Nebula and Jet., *398*, 621. https://doi.org/10.1086/171887

Vamvatira-Nakou, C., Hutsemékers, D., Royer, P., Cox, N. L. J., Nazé, Y., Rauw, G., Waelkens, C., & Groenewegen, M. A. T. (2015). The Herschel view of the nebula around the luminous blue variable star AG Carinae., *578*arXiv 1504.03204, A108. https://doi.org/10.1051/0004-6361/201425090

Voors, R. H. M., Waters, L. B. F. M., de Koter, A., Bouwman, J., Morris, P. W., Barlow, M. J., Sylvester, R. J., Trams, N. R., & Lamers, H. J. G. L. M. (2000). Infrared imaging and spectroscopy of the Luminous Blue Variables Wra 751 and AG Car., *356*, 501–516.

Mahy, L., Lanthermann, C., Hutsemékers, D., Kluska, J., Lobel, A., Manick, R., Miszalski, B., Reggiani, M., Sana, H., & Gosset, E. (2021). Multiplicity of Galactic Luminous Blue Variable stars. *arXiv e-prints*, arXiv 2105.12380, arXiv:2105.12380.

Portegies Zwart, S. F., & van den Heuvel, E. P. J. (2016). Was the nineteenth century giant eruption of Eta Carinae a merger event in a triple system?, *456*(4), arXiv 1511.06889, 3401–3412. https://doi.org/10.1093/mnras/stv2787

Smith, N., Andrews, J. E., Rest, A., Bianco, F. B., Prieto, J. L., Matheson, T., James, D. J., Smith, R. C., Strampelli, G. M., & Zenteno, A. (2018a). Light echoes from the plateau in Eta Carinae's Great Eruption reveal a two-stage shock-powered event., *480*(2), arXiv 1808.00992, 1466–1498. https://doi.org/10.1093/mnras/sty1500

Maeder, A., & Desjacques, V. (2001). The shape of eta Carinae and LBV nebulae., *372*arXiv astro-ph/0105053, L9–L12. https://doi.org/10.1051/0004-6361:20010539

Groh, J. H., Hillier, D. J., & Damineli, A. (2006). AG Carinae: A Luminous Blue Variable with a High Rotational Velocity., *638*(1), arXiv astro-ph/0512372, L33–L36. https://doi.org/10.1086/500928

Groh, J. H., Damineli, A., Hillier, D. J., Barbá, R., Fernández-Lajús, E., Gamen, R. C., Moisés, A. P., Solivella, G., & Teodoro, M. (2009a). Bona Fide, Strong-Variable Galactic Luminous Blue Variable Stars are Fast Rotators: Detection of a High Rotational Velocity in HR Carinae., *705*(1), arXiv 0909.4459, L25–L30. https://doi.org/10.1088/0004-637X/705/1/L25

Smith, N. (2013). A model for the 19th century eruption of Eta Carinae: CSM interaction like a scaled-down Type IIn Supernova., *429*(3), arXiv 1209.6155, 2366–2379. https://doi.org/10.1093/mnras/sts508

Groh, J. H., Hillier, D. J., Damineli, A., Whitelock, P. A., Marang, F., & Rossi, C. (2009b). On the Nature of the Prototype Luminous Blue Variable Ag Carinae. I. Fundamental Parameters During Visual Minimum Phases and Changes in the Bolometric Luminosity During the S-Dor Cycle., *698*(2), arXiv 0904.2363, 1698–1720. https://doi.org/10.1088/0004-637X/698/2/1698

Mehner, A., Davidson, K., Ferland, G. J., & Humphreys, R. M. (2010). High-excitation Emission Lines near Eta Carinae, and Its Likely Companion Star., *710*(1), arXiv 0912.1067, 729–742. https://doi.org/10.1088/0004-637X/710/1/729

Iping, R. C., Sonneborn, G., Gull, T. R., Massa, D. L., & Hillier, D. J. (2005). Detection of a Hot Binary Companion of η Carinae., *633*(1), arXiv astro-ph/0510581, L37–L40. https://doi.org/10.1086/498268

Damineli, A. (1996). The 5.52 Year Cycle of Eta Carinae., *460*, L49. https://doi.org/10.1086/309961

Davidson, K., & Humphreys, R. M. (1997). Eta Carinae and Its Environment., *35*, 1–32. https://doi.org/10.1146/annurev.astro.35.1.1

Smith, N. (2012). All Things Homunculus. In K. Davidson & R. M. Humphreys (Eds.), *Eta carinae and the supernova impostors* (p. 145). https://doi.org/10.1007/978-1-4614-2275-4_7

Gaviola, E. (1950). Eta Carinae. I. The Nebulosity., *111*, 408. https://doi.org/10.1086/145274

Allen, D. A., & Hillier, D. J. (1993). The shape of the Homunculus Nebula around Eta Carinae. *Proceedings of the Astronomical Society of Australia*, *10*, 338–341.

Smith, N. (2008). A blast wave from the 1843 eruption of η Carinae., *455*(7210), arXiv 0809.1678, 201–203. https://doi.org/10.1038/nature07269

Seward, F. D., Butt, Y. M., Karovska, M., Prestwich, A., Schlegel, E. M., & Corcoran, M. (2001). Early Chandra X-Ray Observations of η Carinae., *553*(2), arXiv astro-ph/0101206, 832–836. https://doi.org/10.1086/320961

Ishibashi, K., Gull, T. R., Davidson, K., Smith, N., Lanz, T., Lindler, D., Feggans, K., Verner, E., Woodgate, B. E., Kimble, R. A., Bowers, C. W., Kraemer, S., Heap, S. R., Danks, A. C., Maran, S. P., Joseph, C. L., Kaiser, M. E., Linsky, J. L., Roesler, F., & Weistrop, D. (2003). Discovery of a Little Homunculus within the Homunculus Nebula of η Carinae., *125*(6), 3222–3236. https://doi.org/10.1086/375306

Pittard, J. M., & Corcoran, M. F. (2002). In hot pursuit of the hidden companion of eta Carinae: An X-ray determination of the wind parameters., *383*arXiv astro-ph/0201105, 636–647. https://doi.org/10.1051/0004-6361:20020025

Corcoran, M. F., Liburd, J., Morris, D., Russell, C. M. P., Hamaguchi, K., Gull, T. R., Madura, T. I., Teodoro, M., Moffat, A. F. J., Richardson, N. D., Hillier, D. J.,

Damineli, A., & Groh, J. H. (2017). The 2014 X-Ray Minimum of η Carinae as Seen by Swift., *838*(1), 45. https://doi.org/10.3847/1538-4357/aa6347

Okazaki, A. T., Owocki, S. P., Russell, C. M. P., & Corcoran, M. F. (2008). 3-D SPH Simulations of Colliding Winds in η Carinae (F. Bresolin, P. A. Crowther, & J. Puls, Eds.). In F. Bresolin, P. A. Crowther, & J. Puls (Eds.), *Massive stars as cosmic engines*. https://doi.org/10.1017/S1743921308020413

Gull, T. R., Nielsen, K. E., Corcoran, M. F., Madura, T. I., Owocki, S. P., Russell, C. M. P., Hillier, D. J., Hamaguchi, K., Kober, G. V., Weis, K., Stahl, O., & Okazaki, A. T. (2009). The extended interacting wind structure of Eta Carinae., *396*(3), 1308–1328. https://doi.org/10.1111/j.1365-2966.2009.14854.x

Gull, T. R., Madura, T. I., Teodoro, M., Clementel, N., Corcoran, M., Damineli, A., Groh, J. H., Hamaguchi, K., Hillier, D. J., Moffat, A. F. J., Richardson, N. D., Weigelt, G., Lindler, D., & Feggans, K. (2016). The fossil wind structures of Eta Carinae: changes across one 5.54-yr cycle., *462*(3), arXiv 1608.06193, 3196–3220. https://doi.org/10.1093/mnras/stw1829

Abraham, Z., Falceta-Gonçalves, D., & Beaklini, P. P. B. (2014). η Carinae Baby Homunculus Uncovered by ALMA., *791*(2), arXiv 1406.6297, 95. https://doi.org/10.1088/0004-637X/791/2/95

Chesneau, O., Min, M., Herbst, T., Waters, L. B. F. M., Hillier, D. J., Leinert, C., de Koter, A., Pascucci, I., Jaffe, W., Köhler, R., Alvarez, C., van Boekel, R., Brandner, W., Graser, U., Lagrange, A. M., Lenzen, R., Morel, S., & Schöller, M. (2005). The sub-arcsecond dusty environment of Eta Carinae., *435*(3), arXiv astro-ph/0501159, 1043–1061. https://doi.org/10.1051/0004-6361:20041395

Weigelt, G., & Ebersberger, J. (1986). Eta Carinae resolved by speckle interferometry., *163*, L5–L6.

Koch, A., van Hemert, M. C., & van Dishoeck, E. F. (1995). Photodissociation of the HCO^+ ion. I. Two-dimensional calculations through the I $^1\Pi$ state., *103*(16), 7006–7015. https://doi.org/10.1063/1.470327

Damineli, A., Fernández-Lajús, E., Almeida, L. A., Corcoran, M. F., Damineli, D. S. C., Gull, T. R., Hamaguchi, K., Hillier, D. J., Jablonski, F. J., Madura, T. I., Moffat, A. F. J., Navarete, F., Richardson, N. D., Ruiz, G. F., Salerno, N. E., Scalia, M. C., & Weigelt, G. (2019). Distinguishing circumstellar from stellar photometric variability in Eta Carinae., *484*(1), arXiv 1901.00531, 1325–1346. https://doi.org/10.1093/mnras/stz067

Damineli, A., Navarete, F., Hillier, D. J., Moffat, A. F. J., Corcoran, M. F., Gull, T. R., Richardson, N. D., Weigelt, G., Morris, P. W., & Stevens, I. (2021). Spectroscopic Signatures of the Vanishing Natural Coronagraph of eta Carinae., arXiv 2105.00590. https://doi.org/10.1093/mnras/stab1398

Liszt, H. S. (2007). Formation, fractionation, and excitation of carbon monoxide in diffuse clouds., *476*(1), arXiv 0710.2237, 291–300. https://doi.org/10.1051/0004-6361:20078502

Hogerheijde, M. R., van Dishoeck, E. F., Blake, G. A., & van Langevelde, H. J. (1997). Tracing the Envelopes around Embedded Low-Mass Young Stellar Objects with HCO^+ and Millimeter-Continuum Observations., *489*(1), arXiv astro-ph/9706082, 293–313. https://doi.org/10.1086/304755

Abraham, Z., Beaklini, P. P. B., Cox, P., Falceta-Gonçalves, D., & Nyman, L.-Å. (2020). η Carinae: high angular resolution continuum, H30α and He30α ALMA images., *499*(2), arXiv 2009.10829, 2493–2512. https://doi.org/10.1093/mnras/staa2907

Schneider, N., Bontemps, S., Simon, R., Jakob, H., Motte, F., Miller, M., Kramer, C., & Stutzki, J. (2006). A new view of the Cygnus X region. KOSMA ^{13}CO 2 to 1, 3 to 2, and ^{12}CO 3 to 2 imaging., *458*(3), 855–871. https://doi.org/10.1051/0004-6361:20065088

Redman, R. O., Feldman, P. A., Wyrowski, F., Côté, S., Carey, S. J., & Egan, M. P. (2003). Interactions between a Bright Young Stellar Object and the Midcourse Space Experiment Infrared-dark Cloud G79.3+0.3: An Early Stage of Triggered Star Formation?, *586*(2), arXiv astro-ph/0212172, 1127–1135. https://doi.org/10.1086/367823

Higgs, L. A., Wendker, H. J., & Landecker, T. L. (1994). G 79.29+0.46: a young stellar-wind shell in Cygnus X., *291*, 295–309.

Silva, K. M., Flagey, N., Noriega-Crespo, A., Carey, S., & Ingallinera, A. (2017). VLT/SINFONI Observations of SPITZER/MIPSGAL 24 μm Circumstellar Shells: Revealing the Natures of Their Central Sources., *153*(3), 115. https://doi.org/10.3847/1538-3881/153/3/115

Garcia-Segura, G., Mac Low, M. M., & Langer, N. (1996b). The dynamical evolution of circumstellar gas around massive stars. I. The impact of the time sequence Ostar -> LBV -> WR star., *305*, 229.

Hutsemekers, D., van Drom, E., Gosset, E., & Melnick, J. (1994). A dusty nebula around the luminous blue variable candidate HD 168625., *290*, 906–914.

Pasquali, A., Nota, A., Smith, L. J., Akiyama, S., Messineo, M., & Clampin, M. (2002). Multiwavelength Study of the Nebula Associated with the Galactic LBV Candidate HD 168625., *124*(3), arXiv astro-ph/0207613, 1625–1635. https://doi.org/10.1086/341820

Nota, A., Pasquali, A., Clampin, M., Pollacco, D., Scuderi, S., & Livio, M. (1996). The Nebula around HD 168625: Morphology, Dynamics, and Physical Properties., *473*, 946. https://doi.org/10.1086/178205

Smith, N. (2007a). Discovery of a Nearby Twin of SN 1987A's Nebula around the Luminous Blue Variable HD 168625: Was Sk -69 202 an LBV?, *133*(3), arXiv astro-ph/0611544, 1034–1040. https://doi.org/10.1086/510838

Umana, G., Buemi, C. S., Trigilio, C., Leto, P., & Hora, J. L. (2010). Spitzer, Very Large Telescope, and Very Large Array Observations of the Galactic Luminous Blue Variable Candidate HD 168625., *718*(2), 1036–1045. https://doi.org/10.1088/0004-637X/718/2/1036

Chentsov, E. L. (1980). The star HD 168607 - an S Doradus object. *Soviet Astronomy Letters*, *6*, 199–201.

Chentsov, E. L., & Gorda, E. S. (2004). Spatial Closeness of the White Hypergiants HD 168607 and HD 168625. *Astronomy Letters*, *30*, 461–468. https://doi.org/10.1134/1.1774398

Kniazev, A. Y., Gvaramadze, V. V., & Berdnikov, L. N. (2016). MN48: a new Galactic bona fide luminous blue variable revealed by Spitzer and SALT., *459*(3), arXiv 1604.03942, 3068–3077. https://doi.org/10.1093/mnras/stw889

Clark, J. S., Larionov, V. M., Crowther, P. A., Egan, M. P., & Arkharov, A. (2003). Confirmation of the Luminous Blue Variable nature of <ASTROBJ>AFGL 2298</ASTROBJ>., *403*, 653–658. https://doi.org/10.1051/0004-6361:20030389

Ueta, T., Meixner, M., Dayal, A., Deutsch, L. K., Fazio, G. G., Hora, J. L., & Hoffmann, W. F. (2001). Discovery of an Extended Dust Emission around IRAS 18576+0341 (AFGL 2298) At 10.3 and 18.0 Microns: A New Luminous Blue Variable Candidate?, *548*(2), arXiv astro-ph/0010099, 1020–1028. https://doi.org/10.1086/319004

Gull, T. R., Morris, P. W., Black, J. H., Nielsen, K. E., Barlow, M. J., Royer, P., & Swinyard, B. M. (2020). Eta carinae and the homunculus: far infrared/submillimetre spectral lines detected with the Herschel Space Observatory., *499*(4), 5269–5301. https://doi.org/10.1093/mnras/staa3113

Jackson, J. M., Rathborne, J. M., Shah, R. Y., Simon, R., Bania, T. M., Clemens, D. P., Chambers, E. T., Johnson, A. M., Dormody, M., Lavoie, R., & Heyer, M. H. (2006). The Boston University-Five College Radio Astronomy Observatory Galactic Ring Survey., *163*(1), arXiv astro-ph/0602160, 145–159. https://doi.org/10.1086/500091

Morris, P. W., Waters, L. B. F. M., Barlow, M. J., Lim, T., de Koter, A., Voors, R. H. M., Cox, P., de Graauw, T., Henning, T., Hony, S., Lamers, H. J. G. L. M., Mutschke, H., & Trams, N. R. (1999). Discovery of a massive equatorial torus in the η Carinae stellar system., *402*(6761), 502–504. https://doi.org/10.1038/990048

Waters, L. B. F. M., Izumiura, H., Zaal, P. A., Geballe, T. R., Kester, D. J. M., & Bontekoe, T. R. (1996). Infrared imaging and spectroscopy of G79.29+0.46., *313*, 866–872.

Garcia-Segura, G., Langer, N., & Mac Low, M. M. (1996a). The hydrodynamic evolution of circumstellar gas around massive stars. II. The impact of the time sequence O star -> RSG -> WR star., *316*, 133–146.

Panagia, N. (1999). Distance to SN 1987 A and the LMC (Y. H. Chu, N. Suntzeff, J. Hesser, & D. Bohlender, Eds.). In Y. H. Chu, N. Suntzeff, J. Hesser, & D. Bohlender (Eds.), *New views of the magellanic clouds*.

Burrows, C. J., Krist, J., Hester, J. J., Sahai, R., Trauger, J. T., Stapelfeldt, K. R., Gallagher, I., John S., Ballester, G. E., Casertano, S., Clarke, J. T., Crisp, D., Evans, R. W., Griffiths, R. E., Hoessel, J. G., Holtzman, J. A., Mould, J. R., Scowen, P. A., Watson, A. M., & Westphal, J. A. (1995). Hubble Space Telescope Observations of the SN 1987A Triple Ring Nebula., *452*, 680. https://doi.org/10.1086/176339

McCray, R., & Fransson, C. (2016). The Remnant of Supernova 1987A., *54*, 19–52. https://doi.org/10.1146/annurev-astro-082615-105405

Wampler, E. J., & Richichi, A. (1989). Observations of nebular emission lines toward SN 1987A., *217*, 31–34.

Lundqvist, P., & Fransson, C. (1996). The Line Emission from the Circumstellar Gas around SN 1987A., *464*arXiv astro-ph/9512025, 924. https://doi.org/10.1086/177380

Meaburn, J., Bryce, M., & Holloway, A. J. (1995). The kinematics of the rings around SN 1987A$\hat{*}_{\hat{\cdot}}$, *299*, L1.

Abellán, F. J., Indebetouw, R., Marcaide, J. M., Gabler, M., Fransson, C., Spyromilio, J., Burrows, D. N., Chevalier, R., Cigan, P., Gaensler, B. M., Gomez, H. L., Janka, H. T., Kirshner, R., Larsson, J., Lundqvist, P., Matsuura, M., McCray, R., Ng, C. Y., Park, S., ... Woosley, S. E. (2017). Very Deep inside the SN 1987A Core Ejecta: Molecular Structures Seen in 3D., *842*(2), arXiv 1706.04675, L24. https://doi.org/10.3847/2041-8213/aa784c

Cigan, P., Matsuura, M., Gomez, H. L., Indebetouw, R., Abellán, F., Gabler, M., Richards, A., Alp, D., Davis, T. A., Janka, H.-T., Spyromilio, J., Barlow, M. J., Burrows, D., Dwek, E., Fransson, C., Gaensler, B., Larsson, J., Bouchet, P., Lundqvist, P., ... Zanardo, G. (2019). High Angular Resolution ALMA Images of Dust and Molecules in the SN 1987A Ejecta., *886*(1), arXiv 1910.02960, 51. https://doi.org/10.3847/1538-4357/ab4b46

Ng, C. Y., Gaensler, B. M., Murray, S. S., Slane, P. O., Park, S., Staveley-Smith, L., Manchester, R. N., & Burrows, D. N. (2009). High-Resolution X-Ray Imaging of Supernova Remnant 1987A., *706*(1), arXiv 0910.3610, L100–L105. https://doi.org/10.1088/0004-637X/706/1/L100

Hollenbach, D., & McKee, C. F. (1980). Molecule formation and infrared emission in fast interstellar shocks. II. Dissociation speeds for interstellar shock waves., *241*, L47–L50. https://doi.org/10.1086/183358

Zhekov, S. A., McCray, R., Borkowski, K. J., Burrows, D. N., & Park, S. (2005). Chandra Observations of Shock Kinematics in Supernova Remnant 1987A., *628*(2), arXiv astro-ph/0506443, L127–L130. https://doi.org/10.1086/432794

Fransson, C., Larsson, J., Migotto, K., Pesce, D., Challis, P., Chevalier, R. A., France, K., Kirshner, R. P., Leibundgut, B., Lundqvist, P., McCray, R., Spyromilio, J., Taddia, F., Jerkstrand, A., Mattila, S., Smith, N., Sollerman, J., Wheeler, J. C., Crotts, A., ... Sugerman, B. (2015). The Destruction of the Circumstellar Ring of SN 1987A., *806*(1), arXiv 1505.06669, L19. https://doi.org/10.1088/2041-8205/806/1/L19

Walborn, N. R., Lasker, B. M., Laidler, V. G., & Chu, Y.-H. (1987). The Composite Image of Sanduleak -69 degrees 202, Candidate Precursor to Supernova 1978A in the Large Magellanic Cloud., *321*, L41. https://doi.org/10.1086/185002

Groh, J. H., Meynet, G., Georgy, C., & Ekström, S. (2013b). Fundamental properties of core-collapse supernova and GRB progenitors: predicting the look of massive stars before death., *558*arXiv 1308.4681, A131. https://doi.org/10.1051/0004-6361/201321906

Muratore, M. F., Kraus, M., Oksala, M. E., Arias, M. L., Cidale, L., Borges Fernandes, M., & Liermann, A. (2015). Evidence of the Evolved Nature of the B[e] Star MWC 137., *149*(1), arXiv 1409.7550, 13. https://doi.org/10.1088/0004-6256/149/1/13

Chiotellis, A., Boumis, P., & Spetsieri, Z. T. (2021). 'Ears' formation in supernova remnants: overhearing an interaction history with bipolar circumstellar structures., *502*(1), arXiv 2011.06020, 176–187. https://doi.org/10.1093/mnras/staa3573

Weis, K. (2011). Nebulae around Luminous Blue Variables - large bipolar variety (C. Neiner, G. Wade, G. Meynet, & G. Peters, Eds.). In C. Neiner, G. Wade, G. Meynet, & G. Peters (Eds.), *Active ob stars: Structure, evolution, mass loss, and critical limits*. https://doi.org/10.1017/S1743921311010799

Maeder, A., & Meynet, G. (2000). Stellar evolution with rotation. VI. The Eddington and Omega -limits, the rotational mass loss for OB and LBV stars., *361*arXiv astro-ph/0006405, 159–166.

Owocki, S. (2008). Rotation and Mass Loss (A. de Koter, L. J. Smith, & L. B. F. M. Waters, Eds.). In A. de Koter, L. J. Smith, & L. B. F. M. Waters (Eds.), *Mass loss from stars and the evolution of stellar clusters.*

Eddington, A. S. (1926). *The Internal Constitution of the Stars.*

Langer, N. (1997). The Eddington Limit in Rotating Massive Stars (A. Nota & H. Lamers, Eds.). In A. Nota & H. Lamers (Eds.), *Luminous blue variables: Massive stars in transition.*

Pauldrach, A. W. A., & Puls, J. (1990). Radiation-driven winds of hot luminous stars. VIII. The bistable wind of the luminous blue variable P Cygni (B1 Ia+)., *237*, 409.

Lamers, H. J. G., & Pauldrach, A. W. A. (1991). The formation of outflowing disks around early-type stars by bi-stable radiation-driven winds., *244*, L5–L8.

Curé, M., Rial, D. F., & Cidale, L. (2005). Outflowing disk formation in B[e] supergiants due to rotation and bi-stability in radiation driven winds., *437*(3), arXiv astro-ph/0503359, 929–933. https://doi.org/10.1051/0004-6361:20052686

Pelupessy, I., Lamers, H. J. G. L. M., & Vink, J. S. (2000). The radiation driven winds of rotating B[e] supergiants., *359*arXiv astro-ph/0005300, 695–706.

Smith, N., Davidson, K., Gull, T. R., Ishibashi, K., & Hillier, D. J. (2003). Latitude-dependent Effects in the Stellar Wind of η Carinae., *586*(1), arXiv astro-ph/0301394, 432–450. https://doi.org/10.1086/367641

Leitherer, C., Allen, R., Altner, B., Damineli, A., Drissen, L., Idiart, T., Lupie, O., Nota, A., Robert, C., Schmutz, W., & Shore, S. N. (1994). Geometry and Physical Conditions in the Stellar Wind of AG Carinae., *428*, 292. https://doi.org/10.1086/174241

Mahy, L., Hutsemékers, D., Royer, P., & Waelkens, C. (2016). Tracing back the evolution of the candidate LBV HD 168625., *594*arXiv 1608.01087, A94. https://doi.org/10.1051/0004-6361/201628584

Gvaramadze, V. V., Kniazev, A. Y., Bestenlehner, J. M., Bodensteiner, J., Langer, N., Greiner, J., Grebel, E. K., Berdnikov, L. N., & Beletsky, Y. (2015). The blue supergiant MN18 and its bipolar circumstellar nebula., *454*(1), arXiv 1508.06288, 219–237. https://doi.org/10.1093/mnras/stv1995

Livio, M. (1997). Planetary Nebulae with binary nuclei (Invited Review) (H. J. Habing & H. J. G. L. M. Lamers, Eds.). In H. J. Habing & H. J. G. L. M. Lamers (Eds.), *Planetary nebulae.*

Soker, N. (1998). Binary Progenitor Models for Bipolar Planetary Nebulae., *496*(2), 833–841. https://doi.org/10.1086/305407

Kastner, J. H., Weintraub, D. A., Gatley, I., Merrill, K. M., & Probst, R. G. (1996). H_2 Emission from Planetary Nebulae: Signpost of Bipolar Structure., *462*, 777. https://doi.org/10.1086/177192

Smith, N., & Tombleson, R. (2015). Luminous blue variables are antisocial: their isolation implies that they are kicked mass gainers in binary evolution., *447*(1), arXiv 1406.7431, 598–617. https://doi.org/10.1093/mnras/stu2430

Justham, S., Podsiadlowski, P., & Vink, J. S. (2014). Luminous Blue Variables and Superluminous Supernovae from Binary Mergers., *796*(2), arXiv 1410.2426, 121. https://doi.org/10.1088/0004-637X/796/2/121

Aghakhanloo, M., Murphy, J. W., Smith, N., & Hložek, R. (2017). Modelling luminous-blue-variable isolation., *472*(1), arXiv 1701.05626, 591–603. https://doi.org/10.1093/mnras/stx2050

Kashi, A. (2010). Luminous Blue Variable Eruptions Triggered and Powered by Binary Interaction (V. Kalogera & M. van der Sluys, Eds.). In V. Kalogera & M. van der Sluys (Eds.), *International conference on binaries: In celebration of ron webbink's 65th birthday*. https://doi.org/10.1063/1.3536411

Kashi, A., & Soker, N. (2010). Periastron Passage Triggering of the 19th Century Eruptions of Eta Carinae., *723*(1), arXiv 0912.1439, 602–611. https://doi.org/10.1088/0004-637X/723/1/602

Smith, N., Bally, J., & Walawender, J. (2007a). And in the Darkness Bind Them: Equatorial Rings, B[e] Supergiants, and the Waists of Bipolar Nebulae., *134*(2), arXiv 0705.3054, 846–859. https://doi.org/10.1086/518563

Smith, N., Gehrz, R. D., Campbell, R., Kassis, M., Le Mignant, D., Kuluhiwa, K., & Filippenko, A. V. (2011). Episodic mass loss in binary evolution to the Wolf-Rayet phase: Keck and HST proper motions of RY Scuti's nebula., *418*(3), arXiv 1105.2329, 1959–1972. https://doi.org/10.1111/j.1365-2966.2011.19614.x

Hirai, R., Podsiadlowski, P., Owocki, S. P., Schneider, F. R. N., & Smith, N. (2021). Simulating the formation of η Carinae's surrounding nebula through unstable triple evolution and stellar merger-induced eruption., *503*(3), arXiv 2011.12434, 4276–4296. https://doi.org/10.1093/mnras/stab571

Morris, T., & Podsiadlowski, P. (2007). The Triple-Ring Nebula Around SN 1987A: Fingerprint of a Binary Merger. *Science*, *315*(5815), arXiv astro-ph/0703317, 1103. https://doi.org/10.1126/science.1136351

Velilla Prieto, L., Sánchez Contreras, C., Cernicharo, J., Agúndez, M., Quintana-Lacaci, G., Alcolea, J., Bujarrabal, V., Herpin, F., Menten, K. M., & Wyrowski, F. (2015). New N-bearing species towards OH 231.8+4.2. HNCO, HNCS, HC_3N, and NO., *575*arXiv 1412.2074, A84. https://doi.org/10.1051/0004-6361/201424768

Sánchez Contreras, C., Velilla Prieto, L., Agúndez, M., Cernicharo, J., Quintana-Lacaci, G., Bujarrabal, V., Alcolea, J., Goicoechea, J. R., Herpin, F., Menten, K. M., & Wyrowski, F. (2015). Molecular ions in the O-rich evolved star OH231.8+4.2: HCO^+, $H^{13}CO^+$ and first detection of SO^+, N_2H^+, and H_3O^+., *577*arXiv 1503.01290, A52. https://doi.org/10.1051/0004-6361/201525652

García-Hernández, D. A., & Manchado, A. (2016). On the formation of molecules and solid-state compounds from the AGB to the PN phases, In *Journal of physics conference series*. https://doi.org/10.1088/1742-6596/728/3/032009

Morris, P. W., Charnley, S. B., Corcoran, M., Cordiner, M., Damineli, A., Groh, J. H., Gull, T. R., Loinard, L., Madura, T., Mehner, A., Moffat, A., Palmer, M. Y., Rau, G., Richardson, N. D., & Weigelt, G. (2020). CO, Water, and Tentative Methanol in η Carinae Approaching Periastron., *892*(2), arXiv 2002.11053, L23. https://doi.org/10.3847/2041-8213/ab784a

Hasegawa, T., Volk, K., & Kwok, S. (2000). A Chemical Model of the Neutral Envelope of the Planetary Nebula NGC 7027., *532*(2), 994–1005. https://doi.org/10.1086/308610

Heays, A. N., Bosman, A. D., & van Dishoeck, E. F. (2017). Photodissociation and photoionisation of atoms and molecules of astrophysical interest., *602*arXiv 1701.04459, A105. https://doi.org/10.1051/0004-6361/201628742

Amano, T. (1990). The dissociative recombination rate coefficients of H^+_3, HN^+_2, and HCO^+., *92*(11), 6492–6501. https://doi.org/10.1063/1.458594

Usov, V. V. (1992). Stellar Wind Collision and X-Ray Generation in Massive Binaries., *389*, 635. https://doi.org/10.1086/171236

Eichler, D., & Usov, V. (1993). Particle Acceleration and Nonthermal Radio Emission in Binaries of Early-Type Stars., *402*, 271. https://doi.org/10.1086/172130

De Becker, M. (2007). Non-thermal emission processes in massive binaries., *14*(3-4), arXiv 0709.4220, 171–216. https://doi.org/10.1007/s00159-007-0005-2

Buemi, C. S., Trigilio, C., Leto, P., Umana, G., Ingallinera, A., Cavallaro, F., Cerrigone, L., Agliozzo, C., Bufano, F., Riggi, S., Molinari, S., & Schillirò, F. (2017). Exploring the multifaceted circumstellar environment of the luminous blue variable HR Carinae., *465*(4), arXiv 1612.05039, 4147–4158. https://doi.org/10.1093/mnras/stw3074

Farnier, C., Walter, R., & Leyder, J. C. (2011). η Carinae: a very large hadron collider., *526*, A57. https://doi.org/10.1051/0004-6361/201015590

White, R. L. (1985). Synchrotron emission from chaotic stellar winds., *289*, 698–708. https://doi.org/10.1086/162933

Puls, J. (2011). Winds from massive stars., *82*, 774.

Hirai, R., Podsiadlowski, P., Owocki, S. P., Schneider, F. R. N., & Smith, N. (2020). Modelling Eta Carinae's Great Eruption and its surrounding nebula. *arXiv e-prints*, arXiv 2011.12434, arXiv:2011.12434.

Agliozzo, C., Umana, G., Trigilio, C., Buemi, C., Leto, P., Ingallinera, A., Franzen, T., & Noriega-Crespo, A. (2012). Radio detection of nebulae around four luminous blue variable stars in the Large Magellanic Cloud., *426*(1), 181–186. https://doi.org/10.1111/j.1365-2966.2012.21791.x

Simón-Díaz, S., Herrero, A., Esteban, C., & Najarro, F. (2006). Detailed spectroscopic analysis of the Trapezium cluster stars inside the Orion nebula. Rotational velocities, stellar parameters, and oxygen abundances., *448*(1), 351–366. https://doi.org/10.1051/0004-6361:20053066

Carroll, J. A. (1933). The spectroscopic determination of stellar rotation and its effect on line profiles., *93*, 478–507. https://doi.org/10.1093/mnras/93.7.478

Dravins, D., Lindegren, L., & Torkelsson, U. (1990). The rotationally broadened line profiles of Sirius., *237*, 137.